Titre: Title:	Study of Symmetry-Breaking Instabilities in Axisymmetric Geometries
Auteur: Author:	Félix Armando Salazar Padron
Date:	2016
Type:	Mémoire ou thèse / Dissertation or Thesis
Référence: Citation:	Salazar Padron, F. A. (2016). Study of Symmetry-Breaking Instabilities in Axisymmetric Geometries [Thèse de doctorat, École Polytechnique de Montréal]. PolyPublie. https://publications.polymtl.ca/2058/

UNIVERSITÉ DE MONTRÉAL

STUDY OF SYMMETRY-BREAKING INSTABILITIES IN AXISYMMETRIC GEOMETRIES

FÉLIX ARMANDO SALAZAR PADRÓN
DÉPARTEMENT DE GÉNIE MÉCANIQUE
ÉCOLE POLYTECHNIQUE DE MONTRÉAL

THÈSE PRÉSENTÉE EN VUE DE L'OBTENTION
DU DIPLÔME DE PHILOSOPHIÆ DOCTOR
(GÉNIE MÉCANIQUE)
JANVIER 2016

UNIVERSITÉ DE MONTRÉAL

ÉCOLE POLYTECHNIQUE DE MONTRÉAL

Cette thèse intitulée :

STUDY OF SYMMETRY-BREAKING INSTABILITIES IN AXISYMMETRIC GEOMETRIES

présentée par : SALAZAR PADRÓN Félix Armando
en vue de l'obtention du diplôme de : Philosophiæ Doctor
a été dûment acceptée par le jury d'examen constitué de :

M. REGGIO Marcelo, Ph. D., président
M. GARON André, Ph. D., membre et directeur de recherche
M. VÉTEL Jérôme, Doct., membre et codirecteur de recherche
M. CAMARERO Ricardo, Ph. D., membre
M. URQUIZA José, Doct., membre externe

DEDICATION

To you, for reading it

Merci à toi,
pour prendre le temps de la lire

A mi familia, por no leerla

À
To
Para
} *Paula. Gracias*

ACKNOWLEDGEMENTS

First of all, I want to thank Dr. André Garon for his support throughout this process. His comments and recommendations were always helpful. It has been a privilege working with him, and I truly admire his remarkable formality in the treatment of numerical methods was an eye-opening experience for me, allowing the combination of applied mathematics with the practical engineering approach in a seamless manner.

I also want to thank Dr. Jérôme Vétel for his support and trust. He has been another of my heroes. The meeting and conversation were always enlightening, and his library of knowledge about fluid mechanics is impressive in both extension and depth. The balance between the numerical approach from Dr. Garon and the practical experimental understanding from Dr. Vétel has been extremely interesting and the many meetings I have the privilege to have with both of them at the same time were remarkable, with the chance of acquiring a tremendous amount of information in an extremely short time. I am grateful to both of them.

The people that has been part of the laboratory of fluid dynamics along this time. Thanks to Philippe, Marc-Etienne, Atabak, Mouhammad, Pauline, Ian, Cédric and a large etc. Great partners. Thanks for receiving this guy that barely spoke neither English nor French when he started.

The Département de Génie Mécanique. Thanks to Vivianne and Martine, and Dr. Marcelo Reggio, always willing to take a moment from his time and have an informal talk in Spanish along the hallway in the most varied topics, from fluid mechanics to Latin-American politics, touching of course the mother of all subjects: soccer. Thanks for helping me feel a little bit like home.

A huge recognition to another of my heroes: Mr. Alain Robidoux. I might caused issues with servers like no other user, and Alain was always there, in the line of duty, to address them.

I also want to thank NSERC for their financial support through the Vanier Scholarpship program. Being a Vanier Scholar has been a privilege and without their support, I doubt that this project could have progressed.

I have to mention my family in Venezuela. My parents and my sisters have always been a beacon for me, helping me to keep the north about the important things in life. Their constant nagging, especially the *when are you done?* was surprisingly helpful (not). Thank you.

The rest of my friends and family in Montréal, for keeping me grounded, and for always being

open to study the fluid dynamics of a beer glass.

Finally, I want to thank my wife. Without her, I would not have started this journey and certainly I could have not completed it. There are no words in any language that could allow me to express my gratitude for her support. So basically, thank you, for allowing me to change by your side.

F.A.S.P

Montréal, December 2015.

RÉSUMÉ

L'étude des écoulements traversant des changements de section est un problème numérique et expérimental important dans le domaine de la mécanique des fluides. En effet, les termes d'inertie dans les équations de transport étant non nuls dans les changements géométriques, cela peut générer des phénomènes complexes comme le décollement et le recollement. Ce projet de recherche se focalise sur deux types de changements de sections : un convergent-divergent et une expansion brusque, des géométries largement rencontrées dans le domaine du génie et du biomédical. Cependant, il existe des différences importantes entre les prévisions numériques et les résultats expérimentaux sur les conditions qui mènent à une rupture de symétrie. En particulier, les simulations prédisent généralement des symétries alors que les mesures montrent la présence d'asymétries. Ces caractéristiques sont étudiées ici en utilisant l'analyse de stabilité linéaire. Trois méthodes de calcul de stabilité sont exposées en détail, mises en oeuvre et validées avec des données expérimentales et numériques publiées dans la littérature. La méthode la plus utilisée dans cette étude est une technique originale développée pour les écoulements incompressibles, pour lesquels elle offre plusieurs avantages par rapport aux approches basées sur l'intégration temporelle. Les résultats pour une géométrie de sténose sont présentés et discutés de façon détaillée, y compris l'étude de l'effet d'une excentricité géométrique de la sténose sur la stabilité de l'écoulement. Plusieurs solutions sont alors obtenues, et une boucle d'hystérésis est aussi observée, où deux solutions stables coexistent au même nombre de Reynolds. L'algorithme de calcul de stabilité se comporte bien à faible nombre de Reynolds, mais des problèmes numériques se produisent aux nombres de Reynolds modérés, ce qui n'a pas permis d'étudier complètement la géométrie présentant une expansion brusque. Plusieurs améliorations possibles sont discutées.

ABSTRACT

The study of the fluid dynamics of the flow through change-of-sections constitutes an important numerical and experimental setup for the Fluid Mechanics. Indeed, the non-vanishing inertia terms due to the geometrical change in the domain might produce interesting phenomena like flow separation and reattachment. The present research focuses in two types of change-of-section: a smooth contraction-expansion and a sudden expansion, both with important application in engineering and bio-engineering. However, there are discrepancies between the experimental and numerical conditions at which the axisymmetry of the flow downstream the change of section is lost, with several numerical works describing a symmetric flow at conditions where an asymmetric flow has been reported by experiments. The present research studied these discrepancies through the use of linear stability analysis. In particular, several methods for the computation of stability are developed in detail, tested numerically and validated against data published by other authors. In particular, the method used most extensively within this research constitutes a novel approach in the computation of stability in incompressible flow, with several advantages over traditional time-integration based methods. The results for the stenotic geometry are thoroughly discussed, including differences due to the geometrical description of the constriction and the parametric study of geometric perturbations due to eccentric geometries. Several solution branches were uncovered, including an hysteresis loop where two stable solution could appear at the same Reynolds number. The linear stability algorithm is well behaved at low Reynolds number, but present numerical problems at moderate Reynolds that did not allowed a complete study of the sudden expansion. Several possible improvements are discussed.

CONTENTS

DEDICATION iii

ACKNOWLEDGEMENTS iv

RÉSUMÉ vi

ABSTRACT vii

CONTENTS viii

LIST OF TABLES xi

LIST OF FIGURES xii

LIST OF APPENDICES xvii

ABBREVIATIONS AND NOMECLATURE xviii

CHAPTER 1 Introduction 1

1.1 The problem 1

1.2 Relevance 2

1.3 Methodology 2

1.4 Objectives 3

1.5 Structure 4

CHAPTER 2 Literature Review 5

2.1 Introduction 5

2.2 Stability analysis 6

2.3 Governing Equations 6

2.4 Stability and bifurcation in fluid flow 8

2.5 The Orr-Sommerfeld problem . . . 13
2.6 Taylor-Couette flow . . . 17
2.7 Further considerations about linear stability . . . 18
2.8 Two-dimensional geometries . . . 22
2.9 Axisymmetric geometries . . . 28
2.9.1 Three-dimensional sudden expansion . . . 28
2.9.2 Smooth contraction-expansion . . . 33
2.10 Geometric perturbations . . . 37
2.11 Iterative computation of eigenvalues . . . 38
2.11.1 Example . . . 42
2.11.2 Another example . . . 44
2.11.3 Introduction to ARPACK . . . 47

CHAPTER 3 Numerical computation of Linear Stability . . . 51
3.1 Introduction . . . 51
3.2 Variational formulation . . . 51
3.2.1 Implicit matrix . . . 52
3.2.2 Method of normal modes . . . 52
3.2.3 Modified matrix-vector product . . . 54
3.3 Implementation within ARPACK . . . 58
3.4 Validation of the method . . . 59
3.4.1 Two-dimensional sudden expansion . . . 59
3.4.2 Axisymmetric contraction-expansion . . . 67
3.4.3 Results of the implicit matrix method . . . 75

CHAPTER 4 Smooth contraction-expansion . . . 79
4.1 Introduction . . . 79
4.2 Definition of the stenotic geometry . . . 79
4.3 Axisymmetric 3-arcs stenosis . . . 80

4.4 Eccentric stenoses 83
4.5 Numerical methodology 84
4.6 Mesh validation 85
4.7 Bifurcation in eccentric stenoses 95
4.7.1 Influence of Eccentricity 103
4.8 Bifurcation in the 3-arcs eccentric stenosis 105
4.9 Comparison with experiments 113

CHAPTER 5 Sudden expansion 118
5.1 Introduction 118
5.2 Axisymmetric expansion 119
5.3 Eccentric expansion 120
5.4 Geometry and grid validation 120
5.5 Eigenvalues 123
5.6 Future works 129

CHAPTER 6 Conclusions 130
6.1 Contributions 130
6.2 Limitations 130
6.3 Suggested improvements and future works 131

BIBLIOGRAPHY 132

APPENDICES 141

LIST OF TABLES

TABLE 2.1 Critical Reynolds number reported in the literature for the two-dimensional sudden expansion. 24

TABLE 2.2 Comparison of the computed eigenvalues for the example of the Arnoldi algorithm. 43

TABLE 2.3 Comparison of the computed eigenvalues for the example of the Arnoldi algorithm with the rotated matrix. 46

TABLE 2.4 Comparison of the computed eigenvalues for the example of the Arnoldi algorithm with the rotated matrix. 47

TABLE 3.1 Paramenters used for ARPACK. 58

TABLE 3.2 Meshes for the study of the influence of L_{out} in the planar sudden expansion. 62

TABLE 3.3 Meshes for the study of the influence of F_{mesh} in the planar sudden expansion. 63

TABLE 3.4 Meshes for the study of the influence of L_{out} in the axisymmetric stenosis 70

TABLE 3.5 Meshes for the study of the influence of F_{mesh} in the axisymmetric stenosis 73

TABLE 4.1 Meshes for the study of the influence of L_{out} in the eccentric stenosis. . 86

TABLE 4.2 Meshes for the study F_{mesh} in the eccentric stenosis. 87

TABLE 4.3 Linear stability analysis for the cosine stenose 99

TABLE 4.4 Linear stability analysis for the 3-arcs stenosis. 108

TABLE 5.1 Mesh used for the preliminary computations in the axisymmetric sudden expansion. 120

TABLE 5.2 Details of the different meshes used in the geometry and grid independence study for the three-dimensional sudden expansion. 123

TABLE 5.3 Eigenvalues in the sudden expansion at $Re = 1083$ 128

LIST OF FIGURES

FIGURE 1.1 Axisymmetric change-of-section. 1

FIGURE 2.1 Depiction of absolutely and convectively unstable flow regimes. 9

FIGURE 2.2 Bifurcation diagrams for several pitchfork bifurcations. Adapted from Benjamin (1976). 12

FIGURE 2.3 General Couette-Poiseuille flow. 13

FIGURE 2.4 Taylor-Couette vortex 18

FIGURE 2.5 Flow map of regimes of instabilities for Taylor-Couette flow 19

FIGURE 2.6 Instabilities in the Taylor-Couette flow as appeared on Golubitsky and Stewart (1986) 20

FIGURE 2.7 Two-dimensional sudden expansion. 23

FIGURE 2.8 Flow profile in a planar sudden expansion. 24

FIGURE 2.9 Flow map for the planar sudden expansion. Adapted from Cherdron *et al.* (1978). 25

FIGURE 2.10 Planar divergent channel, with symmetrical flow pattern depicted. . . . 26

FIGURE 2.11 Numerical and experimental bifurcation diagram for a planar sudden expansion. Adapted from Fearn *et al.* (1990). 27

FIGURE 2.12 Definition of axisymmetric geometries. 29

FIGURE 2.13 Numerical and experimental results by Macagno and Hung (1967). . . . 30

FIGURE 2.14 Selected results for the sudden expansion reproduced from Mullin *et al.* (2009). 32

FIGURE 2.15 Numerical prediction of separation zones (shown in red). Adapted from Forrester and Young (1970a). 34

FIGURE 2.16 Asymmetric flow, from Ahmed and Giddens (1983a). 34

FIGURE 2.17 Eccentricity on the stenotic geometry. 37

FIGURE 2.18 Exponential transformation of the complex plane 41

FIGURE 2.19 Influence of the number of filtering steps over the computed eigenvalues and eigenvectors. 44

FIGURE 2.20 Influence of the number of filtering steps over the computed eigenvalues and eigenvectors with the rotated matrix. 48

FIGURE 3.1 Geometry and boundary conditions for the planar sudden expansion studied. 60

FIGURE 3.2 Mesh examples for the planar sudden expansion. 61

FIGURE 3.3 Definition of the half development length for the planar sudden expansion. 61

FIGURE 3.4 Results for $X_{\frac{1}{2}}$ and X_R with $F_{\text{mesh}} = 1.00$ in a planar sudden expansion. 63

FIGURE 3.5 Results for $L_{\text{out}} = 40d_1$ in a planar sudden expansion. 64

FIGURE 3.6 Variation of the reattachment length X_R with the refinement factor F_{mesh} at $Re = 50$. 65

FIGURE 3.7 Leading eigenvalues for the planar sudden expansion. 66

FIGURE 3.8 Contours of the solution for the planar sudden expansion 68

FIGURE 3.9 Definition of $Z_{\frac{1}{2}}$ and Z_R for the geometry of the axisymmetric stenosis. 70

FIGURE 3.10 $Z_{\frac{1}{2}}$ and Z_R with for $F\text{mesh} = 1.00$. 71

FIGURE 3.11 Normalized axial velocity at $z/D = 25$ at $Re = 800$ for the different L_{out} studied. 72

FIGURE 3.12 Influence of the Reynolds number and refinement factor over the reattachment length Z_R, with $L_{\text{out}} = 25$. 74

FIGURE 3.13 Maximum eigenvalue as a function of Reynolds numbers for an axisymmetric stenose. 76

FIGURE 3.14 Axial velocity contours for the eigenfunctions at $Re = 720$. 77

FIGURE 4.1 Definition of the geometry of the stenosis. 79

FIGURE 4.2 Construction of the 3-arcs stenotic geometry. 81

FIGURE 4.3 Comparison of the 3-arcs and the cosine stenoses. 81

FIGURE 4.4 Critical eigenvalues for the 3-arcs and the cosine stenoses as a function of Re. 82

FIGURE 4.5 Eccentricity on the stenotic geometry. 83

FIGURE 4.6 Definition of lengths in the stenotic geometry 85

FIGURE 4.7 Mesh validation at $Re = 400$ and $E = 0.0025$ for both geometries. . . . 88

FIGURE 4.8 Density and distribution of elements for a stenosis. 89

FIGURE 4.9 Definition of Z_R for the geometry of the eccentric stenosis. 90

FIGURE 4.10 Reattachment length as a function of Re and F_{mesh}. 91

FIGURE 4.11 Comparison of eigenvalues at $Re = 350$ in both geometrical descrriptions of the stenosis with different meshes. 93

FIGURE 4.12 Comparison of asymmetry results from the cosine and 3-arcs stenoses against Griffith *et al.* (2013) 94

FIGURE 4.13 Maximum asymmetry $\mu_{\max}$ as a function of the Reynolds number for the cosine stenose. Increasing Reynolds number. 96

FIGURE 4.14 Slices of normalized axial velocity at $Re = 352$ and $Re = 365$ for the cosine stenosis. 97

FIGURE 4.15 Maximum asymmetry $\mu_{\max}$ as a function of Reynolds number for the cosine stenose. Increasing and decreasing Reynolds number. 98

FIGURE 4.16 Real part of the critical eigenvalues for ascending and descending Reynolds numbers in the cosine stenose. 100

FIGURE 4.17 Qualitaive comparison of the axial velocity contours for the two stable solutions at $Re = 350$ in the cosine stenosis. 101

FIGURE 4.18 Comparison of normalized asymmetry μ_r in the cosine stenose for both branches of the bifurcation (Re_{up} and Re_{down}). 102

FIGURE 4.19 Most critical velocity mode for the Re_{down} branch at $Re = 355$ for the cosine stenose. 103

FIGURE 4.20 Comparison of normalized asymmetry μ_r and the angular position of the velocity peak in the cosine stenose at $Re = 360$ for the additional branch uncovered. 104

FIGURE 4.21 Maximum asymmetry as a function of eccentricity for the cosine stenosis. 105

FIGURE 4.22 Comparison of normalized asymmetry μ_r in the 3-arcs stenose for both branches of the bifurcation (Re_{up} and Re_{down}). 106

FIGURE 4.23 Real part of the critical eigenvalues for ascending and descending Reynolds numbers in the 3-arcs stenosis. 107

FIGURE 4.24 Comparison of normalized asymmetry μ_r and the angular position of the velocity peak in the 3-arcs stenosis for the Re_{down} and the additional stable branch at $Re = 360$. 109

FIGURE 4.25 Qualitative comparison of the axial velocity contours for the two stable solutions at $Re = 348$ and $E = 0.0025$ in the 3-arcs stenosis: (a) Ascending Reynolds; (b) Descending Reynolds. 110

FIGURE 4.26 Normalized asymmetry μ_r as a function of the axial position for the 3-arcs stenose at $Re = 348$ and $E = 0.0025$. 111

FIGURE 4.27 Slices of normalized axial velocity at $Re = 360$ for the additional branch uncovered in the 3-arcs stenosis. 112

FIGURE 4.28 Comparison of μ_r at $z/D = 2.5$ for diferent numerical cases, with the experimental results of Vétel *et al.* (2008) 113

FIGURE 4.29 Comparison of μ_r at $z = 7.5D$ for diferent numerical cases, with the experimental results of Vétel *et al.* (2008) 114

FIGURE 4.30 Comparison of μ_r at $z = 2.5D$ for higher values of eccentricity in the 3-arcs stenosis against the experimental results of Vétel *et al.* (2008) . . 115

FIGURE 4.31 Comparison of μ_r at $z = 7.5D$ for higher values of eccentricity in the 3-arcs stenosis against the experimental results of Vétel *et al.* (2008) . . 116

FIGURE 5.1 Diagram of velocity profiles, to illustrate the inconvenience of the centroid as measure of asymmetry. 119

FIGURE 5.2 Boundary conditions used in the preliminary simulation of the axisymmetric sudden expansion. 119

FIGURE 5.3 Maximum eigenvalues as a function of the Reynolds number for different meshes 121

FIGURE 5.4 Eccentricity of the sudden expansion geometry 121

FIGURE 5.5 Longitudinal cut of the mesh, showing the detail of the eccentricity transition 122

FIGURE 5.6 Geometrical lengths of the sudden expansion geometry. 122

FIGURE 5.7 Maximum asymmetry $\mu_{\max}$ at different outlet lengths L_{out} for sudden expansion with $E = 0.0025$. 124

FIGURE 5.8 Maximum asymmetry $\mu_{\max}$ at different mesh densities for sudden expansion with $E = 0.0025$. 125

FIGURE 5.9 Longitudinal variation of asymmetry μ_r at $Re = 1200$ with different meshes for sudden expansion with $E = 0.0025$. 126

FIGURE 5.10 Maximum real part of the eigenvalues for the sudden expansion with $E = 0.0025$. 127

FIGURE 5.11 Axial perturbation velocity contours for the eigenmodes at $Re = 1083$. 128

LIST OF APPENDICES

APPENDIX A Computational example of Arnoldi algorithm 141

ABBREVIATIONS AND NOMECLATURE

Acronyms

CFD	Computational fluid dynamics
DNS	Direct numerical simulation
FEM	Finite element method
GERVAIS	Gradient echo rapid velocity and acceleration imaging sequence
HVAC	Heating, ventilation and air conditioning
IRAM	Implicitly restarted Arnoldi method
LDA	Laser doppler anemometry
MRI	Magnetic resonance imaging
PIV	Particle image velocimetry
RANS	Reynolds-averaged Navier-Stokes equation
RARE	Rapid acquisition with relaxation enhancements
RMS	Root mean squared
SVD	Singular value decomposition

Usual characters

d_1	
d_2	
D	Diameter
	Differential operator
E	Relative measure of geometrical eccentricity
e	Geometrical eccentricity, $e = ED$
F_{mesh}	Mesh refinement factor
H	Hilbert space
L_{in}	Length of the inlet tube
L_{out}	Length of the outlet tube
p	Pressure field
p'	Perturbation in the pressure field
P	Pressure field that is a solution to the Navier-Stokes equations
	Base pressure for decomposition $p' = p - P$

Re	Reynolds number
Re_{crit}	Critical Reynolds number
Re_{up}	Solution history with increasing Reynolds number
Re_{down}	Solution history with decreasing Reynolds number
R_{st}	Radius of the construction arc for the 3-arcs stenosis
$r(z)$	Function that describes the internal radius of the stenosis
$\mathbf{u}$	Velocity vector field
$\mathbf{u}'$	Perturbation in the velocity vector field
$\hat{\mathbf{u}}$	Velocity mode
$\mathbf{U}$	Velocity field that is a solution to the Navier-Stokes equations
	Base flow for perturbation decomposition $\mathbf{u}' = \mathbf{u} - \mathbf{U}$
$\mathbf{v}_1, \mathbf{v}_2, \ldots$	Vectors that form a base for a Krylov subspace
x,y,z	Cartesian coordinates axes or directions
$\hat{u}$,$\hat{v}$,$\hat{w}$	Amplitude of the perturbation or the velocity mode (eigenfuntion)
K	Number of eigenvalues sought

Greek letters

α, β	Angular frequencies
α	Womersley number
μ	Dynamic viscosity
μ_x	Normalized index of asymmetry in the x direction
μ_y	Normalized index of asymmetry in the y direction
μ_r	Total normalized index of asymmetry in the radial direction
$\mu_{\max}$	Maximum asymmetry
ν	Kinematic viscosity
Ω	Domain of solution
Γ	Domain boundary
Γ_D	Subset of Γ where Dirichlet boundary conditions are defined
Γ_N	Subset of Γ where Neumann boundary conditions are defined
$\boldsymbol{\sigma}$	Stress tensor
δ_i^j	Kronecker delta
ρ	Density
ξ	Normalized index of asymmetry, based on the centroid
λ	Eigenvalue
λ_{R}	Real part of the eigenvalue

λ_{I}	Imaginary part of the eigenvalue
θ_{μ}	Azimuthal position of the asymmetry

Symbols

∇	Del operator Gradient
$\nabla\cdot$	Divergence of a vectorial field
$\frac{\partial}{\partial}$	Partial derivative
$\|\ \|$	Norm
$\mathbf{L}$	Linear operator
$\mathbf{B}$	Bilinear operator

CHAPTER 1 INTRODUCTION

1.1 The problem

The aim of science is to explain the observable characteristics of a certain phenomenon through the use of known physical principles, uncover its causes or origins and eventually made predictions about this same phenomenon under a different set of conditions. The available tools to achieve these goals include theoretical analysis, experiments and numerical simulations. This is particularly true in fluid dynamics, where well established parameters are used to describe the fluid flow. However, it is quite common that the real phenomenon, observed under controlled experiments, disagrees with the conditions and patterns predicted by theoretical and/or numerical calculations.

These discrepancies appear in the study of three-dimensional axisymmetric change-of-section, like the ones shown in Figure 1.1. These geometries are quite common in industrial applications, especially as test cases and benchmarks. Particularly, Figure 1.1a is commonly used in the study of the flow through stenosed blood vessels. At certain flow rates, the flow downstream the narrowing changes its symmetric pattern into an asymmetric one. The numerical and experimental predictions of the circumstances under which this change occurs are inconsistent, with each method providing a different set of conditions for the transition. Hence, the critical Reynolds number for this flow is not clearly and uniquely defined despite the geometrical simplicity, adding also a veil of uncertainty to all the phenomena that occurs at higher Reynolds number, including the transition toward the turbulent regime. A similar situation occurs within the axisymmetric sudden expansion shown in Figure 1.1b.

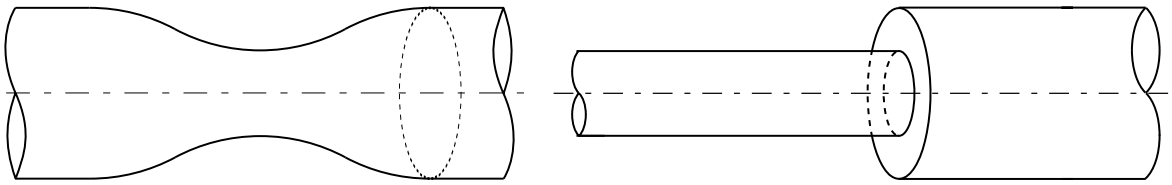

FIGURE 1.1 Axisymmetric change-of-section. (a) A smooth contraction expansion, (b) a sudden expansion.

1.2 Relevance

The fluid flow through a change-of-section in a tube provides a simple and relatively easy to reproduce setup for the study of some complex fluid phenomena. In contrast with parallel flows, the flow downstream the change-of-section undergoes a hydrodynamic development of the velocity profile and this traduces into non-zero terms in the mass conservation equation and also non-vanishing inertia terms in the other governing equations. These factors make convenient the use of these geometries as a framework for theoretical, experimental and numerical studies.

The smooth contraction-expansion shown in Figure 1.1a is used as a model to investigate the blood flow patterns within a stenosis. An accurate knowledge of the flow field downstream the narrowing is required to compute the forces over the vessel wall and based on the effect of these loads over the vascular tissue, make predictions about the evolution of the diseased vessel and the prognosis of the patient.

The sudden expansion of Figure 1.1b is frequently found in many situations in engineering, like heat exchangers, HVAC facilities, gas-turbine and rocket combustor systems (Haapanen, 2008). Its relative geometrical simplicity makes it a common setup in experimental and numerical studies. However, this case also presents the same discrepancy in the description of the transition to an asymmetric flow downstream the expansion. And again, due to this difference between experiments and simulations, the transition Reynolds number is also not clearly defined.

1.3 Methodology

The main objective of this research is to provide extensive quantitative investigations of the transient dynamics in conduits with some sort of geometric symmetry,using numerical techniques and comparison with available experimental results for validations. In the case of planar geometries with abrupt expansions (or double backward-facing step flows), it is well known that the symmetry of the flow is lost at a certain critical Reynolds number that depends of the expansion ratio. The experimental evidence for this symmetry-breaking bifurcation led to the development of theoretical and numerical tools to predict such phenomena. In particular, the transition toward an asymmetry in the planar case can be easily captured by linear stability theory, but the story is quite different with an axisymmetric geometry. The available experimental studies suggest the existence of a symmetry-breaking bifurcation that is not predicted by the linear stability computation of the axisymmetric flow. Hence, this ambiguity of symmetric/asymmetric regimes difficult the accurate computation of the flow

solution after this point. The goal of this project is to investigate the physical mechanisms responsible for these discrepancies within these axisymmetric geometries, and to explain why existing theories fail to predict critical Reynolds numbers above which flow becomes asymmetric.

For this aspect, new tools were developed, particularly regarding the linear stability analysis. This technique is based on the computation of eigenvalues for the whole flow map, constructed from the linearization of the Navier-Stokes equations. The computational cost of this task is remarkable, due to the dimensions of the matrix representation of the flow map, being proportional to the size of the mesh used for the flow solution. Moreover, this matrix is in general ill-conditioned, increasing the difficulty.

Vétel *et al.* (2008) performed an experimental work with an axisymmetric smooth contraction-expansion similar to the one depicted in Figure 1.1a. They showed that after a relatively low Reynolds number the jet emanating from the throat of the constriction is deflected toward the wall, and hence pushing the bulk of the recirculation zone to the opposite side of the tube. They were the first to experimentally measure and report this symmetry-breaking phenomenon, comparing it against the linear stability study of Sherwin and Blackburn (2005) for a similar geometric configuration. Analog observations were made by Mullin *et al.* (2009) on an axisymmetric conduit with an abrupt expansion similar to the one shown in Figure 1.1b, confirming the existence of a symmetry-breaking for this flow. As was the case for the smooth contraction-expansion, numerical studies by Cliffe *et al.* (2012) described a symmetry-breaking at a much higher Reynolds number that the one studied by Mullin *et al.*, where Cantwell *et al.* (2010) showed that the flow was linearly stable, although sensitive to perturbations. Indeed, Cantwell *et al.* observed that small perturbation in the range studied covered by the experiments of Mullin *et al.* could be amplified into finite-amplitude oscillations after the sudden expansion, affecting the topology of the observed flow but with the flow remaining linearly stable. Hence, these two geometrical setups were selected to study the symmetry breaking bifurcation through linear stability analysis.

1.4 Objectives

The aim of this research is to develop mathematical models for the accurate computation of flow instabilities, in order to reveal the physical mechanism behind the onset of symmetry breaking in an axisymmetric change of section, using theoretical and numerical approaches. The specific objectives are to:

— develop and validate a tool for the study of flow instabilities, using linear stability

analysis;
— characterize numerically and experimentally the symmetry-breaking phenomena in the smooth contraction-expansion and the sudden expansion;
— analyze the bifurcation phenomena occurring in flows through axisymmetric expansions,
— compare the predicted transition point with the available data from experimental results;
— analyze further bifurcations in the proximity of the symmetry-breaking point.

1.5 Structure

The present document is organized as follows. A thorough review of the physical and numerical studies on the geometries of interest is given, followed by the details of the linear stability theory. Afterwards, the description of the proposed numerical method for the computation of stability is exposed. The results of the application of this method are then presented and analyzed for a smooth contraction-expansion and for a sudden expansion under several flow conditions.

CHAPTER 2 LITERATURE REVIEW

2.1 Introduction

Flows through the classical geometry of sudden expansion have been studied experimentally, theoretically and numerically for a long time, in both the planar or two-dimensional case (Durst *et al.*, 1974; Cherdron *et al.*, 1978; Sobey and Drazin, 1986; Fearn *et al.*, 1990) as well as in the three-dimensional axisymmetric case (Hung and Macagno, 1966; Macagno and Hung, 1967). Despite all the accumulated knowledge and its geometrical simplicity, this flow still presents important challenging situations in both laminar and turbulent regime.

In the planar sudden expansion, an asymmetric flow was first reported experimentally by Durst *et al.* (1974), while a concordant numerical solution was obtained by Fearn *et al.* (1990). In contrast with the planar case, the 3D axisymmetric problem present several discrepancies. Mullin *et al.* (2009) reported a similar asymmetry in two different experimental setups for an axisymmetric sudden expansion, while Cantwell *et al.* (2010) concluded that this flow is linearly stable in the range studied by Mullin *et al.*. The results by Mullin *et al.* were also in disagreement with the early numerical study by Macagno and Hung (1967), who reported a fully axisymmetric flow downstream the sudden expansion. These discrepancies are not exclusive of this geometry. In 2005, Sherwin and Blackburn mentioned a predominantly symmetric flow in their numerical study of a smooth contraction-expansion in a tube similar to the one presented in Figure 1.1a, results presented as well by Cliffe *et al.* (2012). They both computed symmetry-breaking transition toward a weakly asymmetric flow downstream the constriction. However, Vétel *et al.* (2008) observed experimentally a strong asymmetric flow in a similar geometry, and at a much lower Reynolds number than the one reported by both Sherwin and Blackburn and Cliffe *et al.*. Hence, the description of this symmetry-breaking transition in axisymmetric geometries presents important contradictions between numerical and experimental studies.

This chapter present a detailed revision of the relevant concepts for the study of the transition toward an asymmetric flow. The planar and axisymmetric cases are summarized, in both numerical and experimental approaches. In particular, the work of Sherwin and Blackburn is explained in detail, making emphasis on the difficulties that need to be tackled in order to succeed in the stability analysis.

2.2 Stability analysis

The study of stability in fluid flow deals with how, under certain conditions, the state and topology of the flow is affected when it is perturbed. This perturbation could grow in space and time, changing significantly the state or pattern of the flow, or could be damped with its amplitude progressively decaying, circumstances known respectively as unstable and stable flows.

Due to the difficulties in obtaining an actual non-perturbed flow in any experimental setup, the study of stability is normally performed either theoretically or numerically. Hence, the development of the technique starting from the governing equations for the incompressible fluid flow is shown, followed by some examples of its application. The development of an algorithm for its implementation within the computational tools available for this research is explained in Chapter 3, being one of the major contributions of the present research.

2.3 Governing Equations

For a fluid dynamics problem, the flow is assumed incompressible and Newtonian. Thus, the Navier-Stokes equations are valid, given by

$$\rho\frac{\partial \mathbf{u}}{\partial t} + \rho(\mathbf{u}\cdot\nabla)\mathbf{u} = -\nabla p + \nabla\cdot\left(\mu\left(\nabla\mathbf{u} + \nabla^T\mathbf{u}\right)\right), \tag{2.1}$$

along with the mass conservation equation

$$\nabla\cdot\mathbf{u} = 0, \tag{2.2}$$

within a certain domain Ω, with boundary Γ. The body forces are left out of this analysis. The boundary conditions for the previous problem are

$$\Gamma_D : \mathbf{u} = \mathbf{U}_\Gamma \tag{2.3a}$$

$$\Gamma_N : \boldsymbol{\sigma}(p,\mathbf{u})\cdot\hat{\mathbf{n}} = \mathbf{f}, \tag{2.3b}$$

where $\mathbf{u}$ is the velocity vector field, with components u, v and w respectively along the coordinate directions x, y and z. p represents the pressure field and μ is the dynamic viscosity.

A slightly different approach was taken by Barkley and Henderson (1996), who writes (2.1) as

$$\frac{\partial \mathbf{u}}{\partial t} + \mathbf{A}(\mathbf{u}) = -\frac{1}{\rho}\nabla p + \nu\nabla^2\mathbf{u}, \tag{2.4}$$

where ν is the fluid's kinematic viscosity and $\mathbf{A}(\mathbf{u})$ represents an operator grouping the nonlinear advection terms. It could be represented in any of the following three ways:

$$\mathbf{A}(\mathbf{u}) = (\mathbf{u} \cdot \nabla)\,\mathbf{u} \tag{2.5a}$$

$$\mathbf{A}(\mathbf{u}) = \nabla \cdot (\mathbf{u} \otimes \mathbf{u}) \tag{2.5b}$$

$$\mathbf{A}(\mathbf{u}) = \frac{(\mathbf{u} \cdot \nabla)\,\mathbf{u} + \nabla \cdot (\mathbf{u} \otimes \mathbf{u})}{2}, \tag{2.5c}$$

being respectively the convective representation (2.5a), the conservative representation (2.5b) and the skew-symmetric representation (2.5c) of the advection term. The three expressions are equivalent in the continuum framework. The one most commonly used corresponds to the convective form and unless specified, will be the one used throughout the present document. However, in certain cases, the use of alternative formulations for $\mathbf{A}(\mathbf{u})$ provides some advantages. For example, Blackburn and Sherwin (2004)showed that schemes 2.5a and 2.5c provided similarcovergence in axisymmetric computations. But using the same code for full three-dimensional cylindrical coordinates DNS, Sherwin and Blackburn (2005) reported superior convergence when the skew symmetric form2.5c was used. However, they still employed the convective form 2.5a in their stability analysis.

In time-varying flows, the velocity field $\mathbf{u}$ could be decomposed into a base flow $\mathbf{U}$, and a perturbation flow $\mathbf{u}'$. The same could be done for the pressure, in the following way,

$$\mathbf{u} = \mathbf{U} + \mathbf{u}' \tag{2.6a}$$

$$p = P + p', \tag{2.6b}$$

where in general, the base flow quantities $\mathbf{U}$ and P could be steady or periodic, but they should be a solution of the Navier-Stokes equations

$$\rho\frac{\partial \mathbf{U}}{\partial t} + \rho(\mathbf{U} \cdot \nabla)\mathbf{U} = -\nabla P + \nabla \cdot \left(\mu\left(\nabla\mathbf{U} + \nabla^T\mathbf{U}\right)\right) \tag{2.7}$$

$$\nabla \cdot \mathbf{U} = 0, \tag{2.8}$$

with the appropriate boundary conditions

$$\Gamma_D : \mathbf{U} = \mathbf{U}_\Gamma \tag{2.9a}$$

$$\Gamma_N : \boldsymbol{\sigma}(P, \mathbf{U}) \cdot \hat{\mathbf{n}} = \mathbf{f}. \tag{2.9b}$$

Substituting Equations (2.6) into Equation (2.1) and subtracting Equation (2.7), the following

relations are obtained,

$$\rho\frac{\partial \mathbf{u}'}{\partial t} + \rho\left((\mathbf{u}'\cdot\nabla)\,\mathbf{U} + (\mathbf{U}\cdot\nabla)\,\mathbf{u}' + \overbrace{(\mathbf{u}'\cdot\nabla)\,\mathbf{u}'}^{\simeq 0}\right) = -\nabla p' + \nabla\cdot\left(\mu\left(\nabla\mathbf{u}' + \nabla^T\mathbf{u}'\right)\right) \quad (2.10a)$$

$$\nabla\cdot\mathbf{u}' = 0, \quad (2.10b)$$

with boundary conditions

$$\Gamma_D : \mathbf{u}' = 0$$
$$\Gamma_N : \boldsymbol{\sigma}(p', \mathbf{u}')\cdot\hat{\mathbf{n}} = 0.$$

The term $(\mathbf{u}'\cdot\nabla)\,\mathbf{u}'$ is neglected in Equation (2.10) under the assumption that the perturbations are relatively small, and consequently the second order terms could be neglected. The Equation 2.10 is then linear in $\mathbf{u}'$ and p', hence the name of *Linear Stability*. These relations govern the evolution of the perturbation variables $\mathbf{u}'$ and p', and are the starting point for studies on flow stability (Lin, 1955). The study of turbulence transition was associated to the stability of laminar solutions under perturbations, as reviewed in Schlichting (1979) and Drazin (2002). But this study also applies to the bifurcation of laminar symmetric flows toward asymmetric laminar ones, as presented in Sections 2.8 and onward. It is widely regarded that below a critical Reynolds number all these perturbations are damped, meaning that the solution $\mathbf{U}$ is stable. At Reynolds numbers over this critical threshold, the perturbations are amplified and the flow is no longer stable.

2.4 Stability and bifurcation in fluid flow

In broad terms, a fluid flow is said to be stable if all perturbations that are initially small remain small all time. In contrast, a flow is qualified as unstable if at least one perturbation that is initially small grows until eventually it stops being small. However, a more formal definition of *small* within this context is required. The study of stable and unstable system is common in dynamical systems, where the formal mathematical definition of stability is done in the sense of Lyapunov, using a metric as a measure (Drazin, 2002). A base flow is stable if, for all $\epsilon > 0$ there exists $\delta(\epsilon) > 0$ in such manner than if

$$\|\mathbf{u}'(\mathbf{x}, 0)\|, \|p'(\mathbf{x}, 0)\| < \delta$$

then

$$\|\mathbf{u}'(\mathbf{x}, t)\|, \|p'(\mathbf{x}, t)\| < \epsilon \qquad \text{for all } t > 0.$$

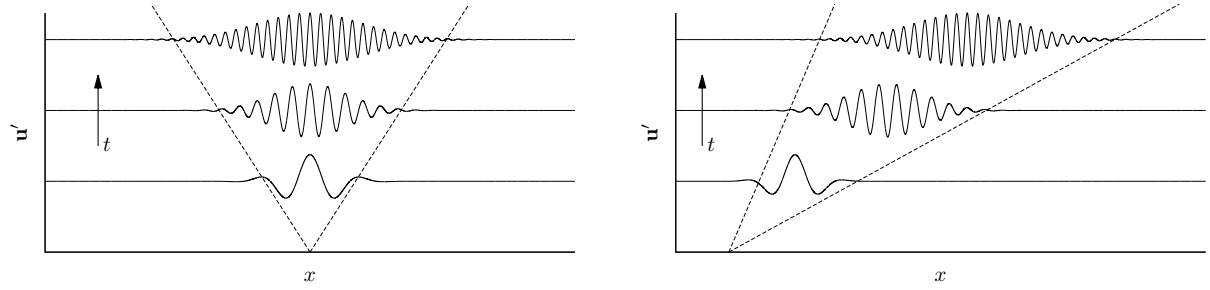

FIGURE 2.1 Depiction of (a) absolutely and (b) convectively unstable flow regimes. Adapted from Drazin (2002).

The fact that the norm $\|\cdots\|$ can be chosen in different ways may yield slightly different definitions of stability and its thresholds.

Open flows admit several kinds of instabilities. A flow is *absolutely unstable* when an initially small perturbation grows above a given threshold at a fixed point in space. As a complement to this concept, a flow is *convectively unstable* if the small perturbation grows over the threshold at a point that moves streamwise with the flow, but the magnitude of the perturbation decays at the original insertion point. These concepts are described in Figure 2.1 (Drazin, 2002).

Further considerations should be made regarding the steady base flow (*i.e.* $\partial\mathbf{U}/\partial t = 0$ in (2.7)), in order to gain insight about the physics of the development of instabilities. From Equation (2.10), in the steady flow case the coefficients for the linearized equation are time-independent. Hence, the method of separation of variables is common in this circumstance, and a general solution of the following form could be constructed

$$\mathbf{u}'(\mathbf{x},t) = \sum_i^{\infty} \hat{\mathbf{u}}_i(\mathbf{x}) \exp(\lambda_i t) \qquad p'(\mathbf{x},t) = \sum_i^{\infty} \hat{p}_i(\mathbf{x}) \exp(\lambda_i t). \tag{2.11}$$

The problem could be rewritten as a linear evolution equation in Hilbert spaces H. Considering $u(t)$ represents a "point" in H containing all of the instantaneous information for the flow at that particular time, *i.e.* the velocity field $\mathbf{u}'(\mathbf{x})$ and the pressure field $p'(\mathbf{x})$ ($u = [\mathbf{u}' \quad p']^T$). Then, Equation (2.10) takes the following form (Richtmyer, 1982; Crawford, 1991).

$$\frac{du}{dt} = \mathsf{L}_{\mathbf{U}} u, \tag{2.12}$$

with an initial condition

$$u(0) = u_0$$

and in this framework the solutions (2.11) are written as

$$u_i(t) = \varphi_i \exp(\lambda_i t),$$

which is equivalent to look for the eigenfunctions $\varphi_i = [\mathbf{u}_i' \quad p_i']^T$ and eigenvalues λ_i of the $\mathbf{L_U}$ operator, given by

$$\mathbf{L_U}\varphi = \lambda\varphi, \qquad \text{for } \varphi \neq 0.$$

Thus, in the original representation of Equation (2.11) $\hat{\mathbf{u}}_i$ and $\hat{p}_i$ also represents eigenfunctions associated to the eigenvalue λ_i, with each pair being called a *mode*. As each eigenvalue λ can have, in general, a real and an imaginary part $\lambda = \lambda_\mathrm{R} + i\lambda_\mathrm{I}$, with λ_R and λ_I respectively representing the real and imaginary part of the eigenvalue. From the Euler's exponentiation formula, the amplitude of the exponential term of (2.11) is solely determined by

$$\begin{aligned} \exp(x + iy) &= \exp(x)\exp(iy) \\ &= \exp(x)\left(\cos(y) + i\sin(y)\right), \end{aligned} \tag{2.13}$$

and hence, the evolution of these modes and the stability of the base flow is governed by the real part of the corresponding eigenvalues: according to (2.13), a negative real part of λ_i will cause that the mode φ_i decay in time, while a positive real part will produce a continuous exponential growth of the perturbation, making the flow unstable. A more thorough example is revised in the Section 2.5.

In general, a perturbation is not necessarily the most critical or fastest growing mode, but a superposition of all modes, stables and unstables. The fact that each mode is decaying or growing at different rates makes difficult to observe experimentally the exponential growth of instabilities. Indeed, it is possible that a superposition of exponentially decaying modes grow for several orders of magnitude for a definite period of time before decreasing. This is the base of the transient growth concept revised in Section 2.7.

According to the linear theory, a small perturbation that excites the fastest growing mode may grow exponentially only after a long time, when this critical mode dominates the others. However, in many practical cases, the perturbations are not very small, and nonlinearities become relevant. Due to this fact, almost all instabilities in unsteady or time-periodic flows observed in reality are due to nonlinearity. The criterion obtained through linear and normal modes allows the establishment of a threshold or reference value that is valid in most cases, except when transient growth becomes relevant or when subcritical instability occurs. But the linear theory does not only allows to estimate these critical conditions. Indeed, it is

possible to predict the flow topology beyond the critical condition, based on the nature of the instability and the characteristics of its modes. These critical points are usually known as *bifurcation points*, because the number of possible solutions changes. It is said that a solution bifurcates into separate *branches*, which could be stable or unstable. These bifurcations are usually represented using bifurcation diagrams, where a variable that characterize the flow state is plotted against a certain control parameter.

Flows are considered symmetric when they present some degree of invariability under a coordinate transformation (Golubitsky and Stewart, 1986). Under steady conditions, the symmetry of these flows is normally lost due to a pitchfork bifurcations. They have this name after the trident-like appearance on the diagram, with several solutions or branches appearing at a certain threshold value for the control parameter. Figure 2.2 presents several examples of bifurcation diagrams for pitchfork bifurcations adapted from Benjamin (1976). Figure 2.2a shows a supercritical pitchfork bifurcation, because the bifurcation develops for values of the control parameter (Reynolds number in this case) higher than a critical value. This is the case is frequent in the transition toward asymmetry in planar symmetric geometries, which are more thoroughly reviewed in Section 2.8.

Two different solutions appear for values of $Re > Re_c$ representing the asymmetric stable branches, non-null solutions to Equation (2.10). The symmetric solution is also present for $Re > Re_c$ but it is no longer stable. Hence, it is identified with an interrupted line on the bifurcation diagram. Figures 2.2b and 2.2c have subcritical pitchfork bifurcations, because at least one branch exists at $Re < Re_c$. In this example they are unstable, until a turning point $\mathcal{P}$ where they become stable again. Benjamin prefers to make the distinction between Figures 2.2b and 2.2c, calling the latter a transcritical bifurcation, given that branches appear at both $Re > Re_c$ and $Re < Re_c$.

The pitchfork bifurcation is one of the most important types studied in fluid mechanics in flows with symmetry. However it is not the only one. At the bifurcation point the purely real most critical eigenvalue of the flow change sign from negative to positive. But if this critical eigenvalue has a non-zero imaginary part, at the limit of stability it becomes purely imaginary. This case is known as a Hopf bifurcation (Hopf, 1948; Drazin, 1992). Thus, from Equation (2.13), the perturbations $\mathbf{u}'$ and p' are multiplied by an oscillation term $\exp(i\lambda_I t) = \cos(\lambda_I t) + i\sin(\lambda_I t)$, increasing their time-dependent behaviour up to the point that it dominates the base flow, turning it into a periodic flow. This is usually the type of bifurcation that a laminar flow undergoes from a steady to a periodic regime, for example in the planar flow around blunt bodies (Hopf, 1948), or the square lid-driven cavity flow (Fortin *et al.*, 1997).

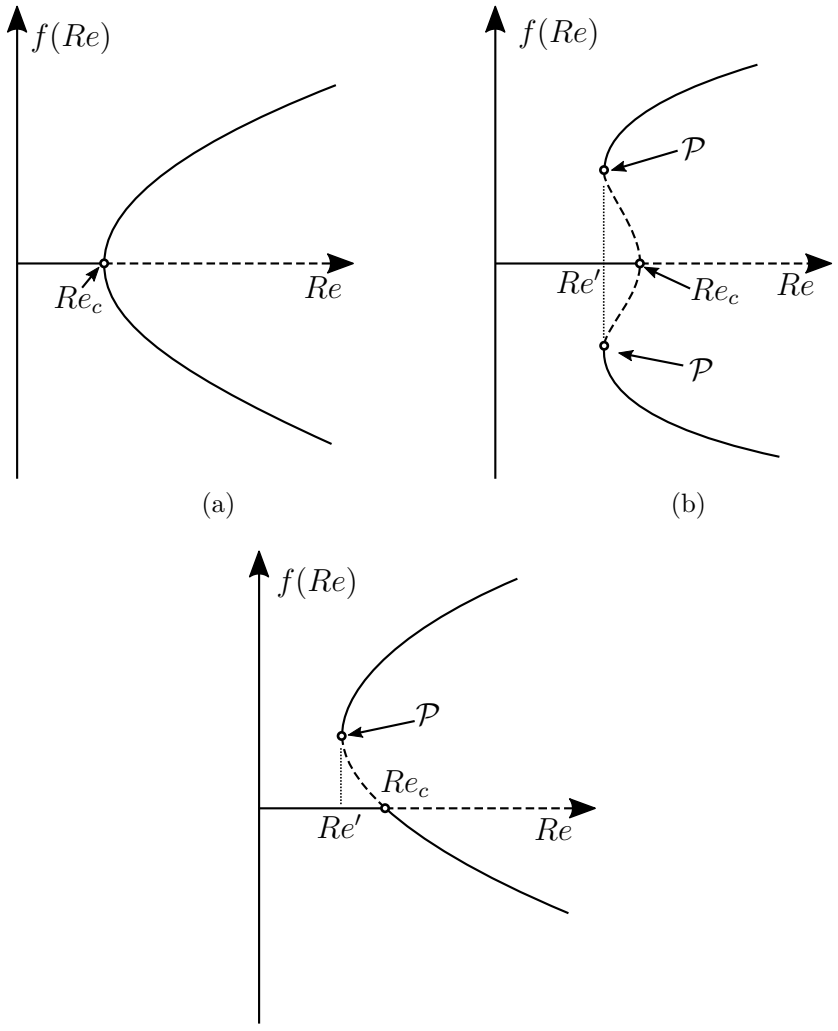

FIGURE 2.2 Bifurcation diagrams for several pitchfork bifurcations: (a) is a classical pitchfork bifurcation,(b) has a subcritical component in both branches while in (c) the bifurcation is no longer symmetric. The continuous segments (—) represent stable branches while the interrupted lines (- - -) belong to unstable ones. Adapted from Benjamin (1976).

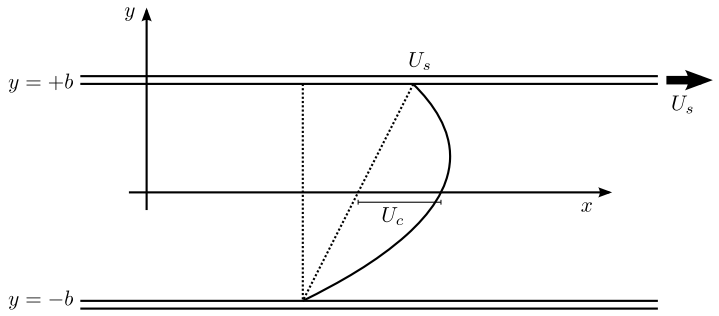

FIGURE 2.3 General Couette-Poiseuille flow.

When the real part of one eigenvalue becomes positive, the flow reach a bifurcation point. Afterwards, Equation (2.10) should be linearized around the solution corresponding to the new stable branch, in what is known as the study of the *secondary instabilities*. This justifies the computation of only a few eigenvalues in the determination of the flow instability, as after the bifurcation a new linearization, the eigenvalues and eigenmodes of the original branch become largely unimportant, at least from the point of view of the linear theory. The following sections present some of the earliest examples of calculation of instabilities and bifurcations in fluid mechanics, based on the method of normal modes introduced herein.

2.5 The Orr-Sommerfeld problem

Lin (1955) presents in detail the analysis for a general Couette-Poiseuille flow, one of the first theoretical attempts to calculate the instability onset in parallel flows. The geometry is shown in Figure 2.3. In this case, the base flow is

$$U(y) = \frac{1}{2}U_s\left(1 + \frac{y}{b}\right) + U_c\left[1 - \left(\frac{y}{b}\right)^2\right], \tag{2.14}$$

where U_s is the shear velocity of the upper plate relative to the bottom one, U_c is the velocity in the center of the channel due only to the pressure gradient (when $U_s = 0$) and $2b$ is the height of the channel.

With this simplified problem, the non-dimensional form of Equation (2.10) is

$$\begin{aligned}
\frac{\partial u'}{\partial t} + U\frac{\partial u'}{\partial x} + v'\frac{\partial U}{\partial y} &= -\frac{\partial p'}{\partial x} + \frac{1}{Re}\left(\frac{\partial^2 u'}{\partial x^2} + \frac{\partial^2 u'}{\partial y^2} + \frac{\partial^2 u'}{\partial z^2}\right) \\
\frac{\partial v'}{\partial t} + U\frac{\partial v'}{\partial x} &= -\frac{\partial p'}{\partial y} + \frac{1}{Re}\left(\frac{\partial^2 v'}{\partial x^2} + \frac{\partial^2 v'}{\partial y^2} + \frac{\partial^2 v'}{\partial z^2}\right) \\
\frac{\partial w'}{\partial t} + U\frac{\partial w'}{\partial x} &= -\frac{\partial p'}{\partial z} + \frac{1}{Re}\left(\frac{\partial^2 w'}{\partial x^2} + \frac{\partial^2 w'}{\partial y^2} + \frac{\partial^2 w'}{\partial z^2}\right) \\
\frac{\partial u'}{\partial x} + \frac{\partial v'}{\partial y} + \frac{\partial w'}{\partial z} &= 0,
\end{aligned} \tag{2.15}$$

where the Reynolds number is defined using the velocity at the midplane of the channel and half the height of the channel, as follows

$$Re = \frac{\left(\frac{1}{2}U_s + U_c\right) b}{\nu}.$$

The boundary conditions for the fluctuating components of the velocity are

$$\begin{aligned}
u'(x, \pm 1, z) &= 0 \\
v'(x, \pm 1, z) &= 0 \\
w'(x, \pm 1, z) &= 0.
\end{aligned} \tag{2.16}$$

The components of the linearized dimensionless perturbation velocity and pressure are supposed to behave according to normal modes in space and time, similar to the Equation (2.11)

$$\begin{aligned}
u'(x, y, z, t) &= \hat{u}(\mathbf{x}) \exp(\lambda t) \\
v'(x, y, z, t) &= \hat{v}(\mathbf{x}) \exp(\lambda t) \\
w'(x, y, z, t) &= \hat{w}(\mathbf{x}) \exp(\lambda t) \\
p'(x, y, z, t) &= \hat{p}(\mathbf{x}) \exp(\lambda t).
\end{aligned}$$

However, given the particularities of the geometry, it is natural to assume periodicity in the x and z directions. Thus, the amplitude of the mode is written as

$$\hat{u}(\mathbf{x}) = \breve{u}(y) \exp\left(i(\alpha x + \beta z)\right),$$

with similar equations $\breve{v}(y)$, $\breve{w}(y)$, $\breve{p}(y)$ for the other velocity components and the pressure representing the dimensionless amplitude of the perturbation. α and β are the dimensionless

wavelengths in the x and z directions. Although these expressions contain imaginary terms, this is due to the convenience of the complex notation in the Equation (2.13), as normally only the real part is deemed meaningful (Schlichting, 1979). With this in mind, the complete form of the perturbations is then

$$u'(x,y,z,t) = \check{u}(y)\exp\left[i(\alpha x+\beta z)+\lambda t\right] \tag{2.17a}$$
$$v'(x,y,z,t) = \check{v}(y)\exp\left[i(\alpha x+\beta z)+\lambda t\right] \tag{2.17b}$$
$$w'(x,y,z,t) = \check{w}(y)\exp\left[i(\alpha x+\beta z)+\lambda t\right] \tag{2.17c}$$
$$p'(x,y,z,t) = \check{p}(y)\exp\left[i(\alpha x+\beta z)+\lambda t\right]. \tag{2.17d}$$

The substitution of these expressions into the governing equations (2.15) for the perturbation yields the following systems of coupled differential equations:

$$\begin{aligned}
\left[D^2-(\alpha^2+\beta^2)-Re\,(i\alpha U+\lambda)\right]\check{u} &= Re\,DU\check{v}+i\alpha Re\,\check{p}\\
\left[D^2-(\alpha^2+\beta^2)-Re\,(i\alpha U+\lambda)\right]\check{v} &= Re\,D\check{p}\\
\left[D^2-(\alpha^2+\beta^2)-Re\,(i\alpha U+\lambda)\right]\check{w} &= i\beta Re\,\check{p}\\
i(\alpha\check{u}+\beta\check{w})+D\check{v} &= 0,
\end{aligned} \tag{2.18}$$

where the D represents differentiation with respect to y. The base flow U is known, and for a certain combination of Reynolds number and the perturbation wavelengths α and β, the previous system should allow to compute the perturbation amplitudes and the eigenvalue λ. However, in its current form, this system is not trivial to solve. But further simplifications are possible.

Given the two-dimensional nature of the base flow described by Equation (2.18) it seems natural to consider only planar perturbations. But the fact that perturbation could exist in directions where the flow is null is evident in Equation (2.15), and it is not obvious to neglect the effect of the three-dimensional perturbations. However, Squire (1933) proved that a two-dimensional flow becomes unstable at a higher Reynolds number when three-dimensional perturbations are assumed than when they are supposed two-dimensional. Hence, the two-dimensional perturbations represent a more critical case for two-dimensional flows. And in (2.18) the two-dimensional case is recovered when $\beta = 0$. To further reduce the complexity of the problem, the traditional approach is the use of the streamfunction Ψ

$$u' = \frac{\partial\Psi}{\partial y} \qquad v' = -\frac{\partial\Psi}{\partial x}.$$

The streamfunction is assumed to have a similar for to the perturbations (2.17)

$$\Psi(x, y, t) = \psi(y) \exp(i\alpha x + \lambda t),$$

and by comparison it could be established that

$$\check{u}(y) = \psi'(y) \qquad \check{v}(y) = -i\alpha\psi(y).$$

The substitution of these equation into (2.18) produces, after the elimination of the pressure

$$\psi'''' - 2\alpha^2\psi'' + \alpha^4\psi = Re\left[i\alpha\left(U\psi'' - U''\psi + \alpha^2 U\psi\right) + \lambda\left(\psi'' + \psi' + \alpha^2\psi\right)\right]. \tag{2.19}$$

with boundary conditions

$$\begin{aligned} y = +1\,; \quad u' = v' = 0 \quad &\rightarrow \quad \psi = 0\,; \quad \psi' = 0 \\ y = -1\,; \quad u' = v' = 0 \quad &\rightarrow \quad \psi = 0\,; \quad \psi' = 0. \end{aligned} \tag{2.20}$$

Equation (2.19) differs significantly from the classical Orr-Sommerfeld equation found in the literature (Orr, 1907b,a; Schlichting, 1979; Drazin, 2002). This is due to the assumed form of the perturbations and the streamfunction. The classical formulation uses

$$\Psi(x, y, t) = \psi(y) \exp(i\alpha(x - ct)),$$

which allows the cancellation of additional terms when inserted in (2.15) or in a system similar to (2.18) but obtained using perturbations $\mathbf{u'} = \check{\mathbf{u}}(y) \exp(i\alpha(x - ct)$, the same form of the streamfunction. In this case, the classical Orr-Sommerfeld equation is obtained

$$(U - c)\left(\psi'' - \alpha^2\psi\right) - U''\psi = -\frac{i}{\alpha Re}\left(\psi'''' - 2\alpha^2\psi'' + \alpha^4\psi\right), \tag{2.21}$$

with the same boundary conditions as in (2.20).

Although the base flow supposed correspond to an internal flow, the Orr-Sommerfeld equation can be used to study any two-dimensional flow where the base flow $U(y)$ is known. For example, it was employed by Tollmien (1931) to predict the apparition of the so-called Tollmien-Schlichting waves in a boundary layer, marking the beginning of the turbulence transition process. Later, during the 1960s, theoretical studies about the subcritical instabilities, *i.e.* those appearing at a lower Reynolds number than the one predicted by the Orr-Sommerfeld analysis, made by Stuart (1960), Watson (1960) and by Reynolds and Potter (1967) created interest to investigate different types of instabilities with more elaborate techniques than the

Orr-Sommerfeld equation. However, it still appears in recent research works dealing with the stability of parallel flows (Bottaro *et al.*, 2003; Skorokhodov, 2007; Walker *et al.*, 2012; Georgievskii *et al.*, 2014).

2.6 Taylor-Couette flow

As stated in the previous section, the study of stability in fluid flows was normally linked with the prediction on the turbulent transition onset (Schlichting, 1979). However, the analysis of instabilities is not exclusive to the study of turbulence transition. Within this context, the flow between rotating concentric cylinders is historically relevant. This geometry is shown in Figure 2.4a. Extensive experimentation in early years (Mallock, 1896; Taylor, 1921, 1923) showed that in the case when the outermost cilynder is kept at rest, a series of rings appears around the axis of the cylinders, as depicted in Figure 2.4b. These patterns, called the *Taylor-Couette vortices*, constituted the first laminar instability studied extensively both theoretically and experimentally. Here the flow is laminar because the velocity field is time-independent.

Using an energetic analysis, Rayleigh (1916) showed that for the particular case of cylinders with a small spacing between them, the apparition of the ring patterns requires that the centrifugal force of the inner layers overcomes the one of the outer layers. Although not widely accepted at that time, this argument was proved right by Taylor (1923), who published a complete theoretical work dealing with the instabilities in the flow between concentric cylinders. He studied the stability of this flow under axisymmetrical perturbations, independents of the azimuthal angle and with lengthwise periodicity along the axis of the cylinders, with a form analog to Equation (2.17). Instead of solving the Orr-Sommerfeld equation, he projected the supposed axisymmetric solution of the problem into a series of Bessel functions, and studied directly the values of the temporal wavelengths of the perturbation. In this framework, he determined the condition of stability for a pure shearing flow (without rings) in small spaced cylinders as $\omega_2 r_2^2 > \omega_1 r_1^2$, which is the same energetic condition proposed earlier by Rayleigh. Later, Synge (1938) rewrote the Taylor problem in a simplified form, and was able to prove the previous conditions without the approximation of small gap between cylinders. At even higher rotational speeds, the azimuthal symmetry of the vortices is lost, and additional flow patterns appear (see Figure 2.6).

Davey (1962) was the first to explain theoretically the Taylor-Couette instabilities in terms of bifurcation theory. Theoretical studies about these bifurcations were performed by Chossat and Iooss (1985) and Golubitsky and Stewart (1986). After the initial vortex rings, they predicted the apparition of additional instability modes through the bifurcation of the

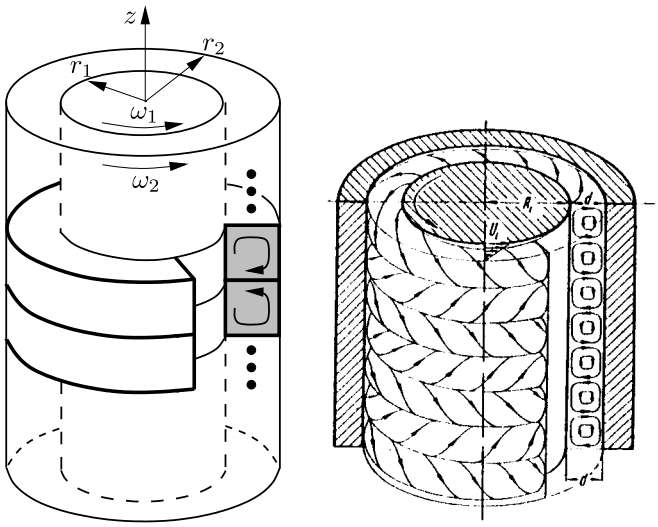

FIGURE 2.4 Taylor-Couette vortex. a) Sketch of the geometry, b) Representation of the flow pattern (from Schlichting, 1979).

approximate solution, based on the analysis of its eigenvalues. Their predictions were confirmed experimentally by Andereck *et al.* (1986), who performed their study considering different lengths of the cylinders, and also several cases for their velocity (external cylinder at rest, relative motion, and counter-rotating). Similarly to Golubitsky and Stewart, they described in detail several modes of instability, along with the conditions for their occurrence. These results were summarized in the flow map reproduced in Figure 2.5, according to the inner and outer Reynolds numbers, respectively defined as $R_\mathrm{i} = r_1(r_2 - r_1)\omega_1/\nu$ and $R_\mathrm{o} = r_2(r_2 - r_1)\omega_2/\nu$. Figure 2.6 presents several of these instability modes.

The importance of the Taylor-Couette flow is that it constitutes the first flow studied extensively in both experimental and theoretical way where the transition was not related with turbulence but instead occurred between 2 laminar regimes. Moreover, some of the additional instability regimes also present laminar characteristics, while others behave in a turbulent manner. These features make it a remarkable framework for the development of numerical and theoretical techniques for the study of flow instabilities.

2.7 Further considerations about linear stability

Some authors have criticized the linear stability method, mainly due to its inability to predict the critical Reynolds number in certain simple flows. For example, for plane Poiseuille flow, the linear stability computes a positive eigenvalue at $Re = 5772$ (Orszag, 1971), but turbulence

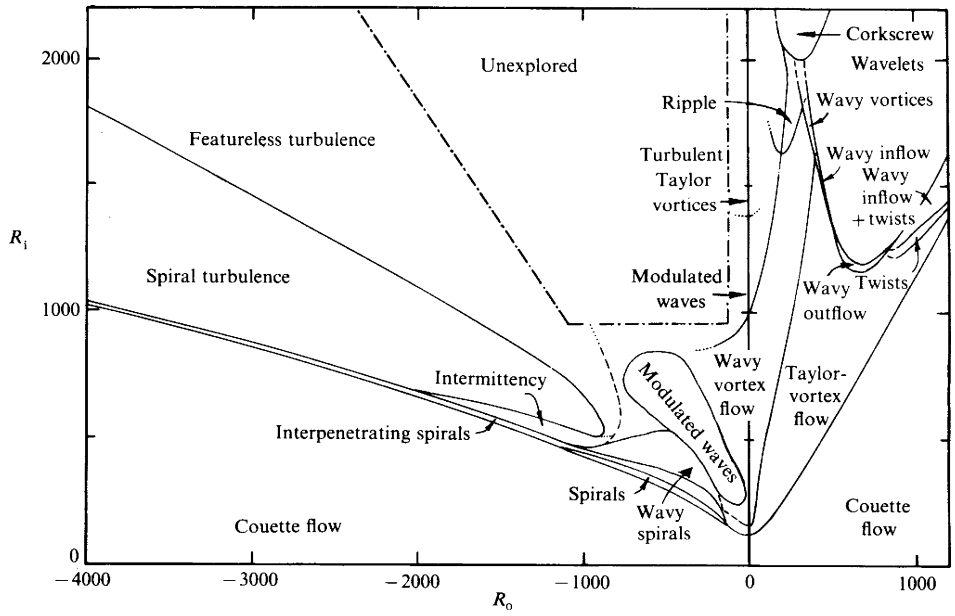

FIGURE 2.5 Flow map showing several regimes of instabilities for Taylor-Couette flow (Andereck *et al.*, 1986).

has been observed at Reynolds numbers as low as 1000 (Carlson *et al.*, 1982). The same is valid for the Hagen-Poiseuille in a tube, where it is generally accepted that turbulence occurs at $Re \simeq 2300$ but the linear stability predicts a stable flow at all Reynolds number.

Trefethen *et al.* (1993) present a thorough review of these discrepancies, stating that most critics agree that they have their origin on the linearization stage of the method, leaving outside the analysis the non-linear effects responsible for the majority of the observed phenomena. However, they also point out that in the shear dominated cases, like the cited Poiseuille examples, the evolution operator in Equation (2.12) is non-normal, meaning that the computed eigenfunctions are not mutually orthogonal. In these cases the computation of eigenvalues may produce non-satisfactory results because most iterative algorithms for the computation of eigenvalues assumes that the modes are orthogonal. Moreover, the energy associated with the fluctuating velocity components contains contributions from all the eigenfunctions of the flow and it may be possible that the energy of each mode is exponentially decaying, but the net combined effect is actually growing due to the cross terms arising from the non-orthogonality. In contrast, problems with thermal or centrifugal instabilities, like the Rayleigh-Bernard cells or the Taylor-Couette flow, the operator is normal and consequently, the linear stability analysis produce well behaved results. Similar discussions were also made by Waleffe (1995) and Baggett *et al.* (1995).

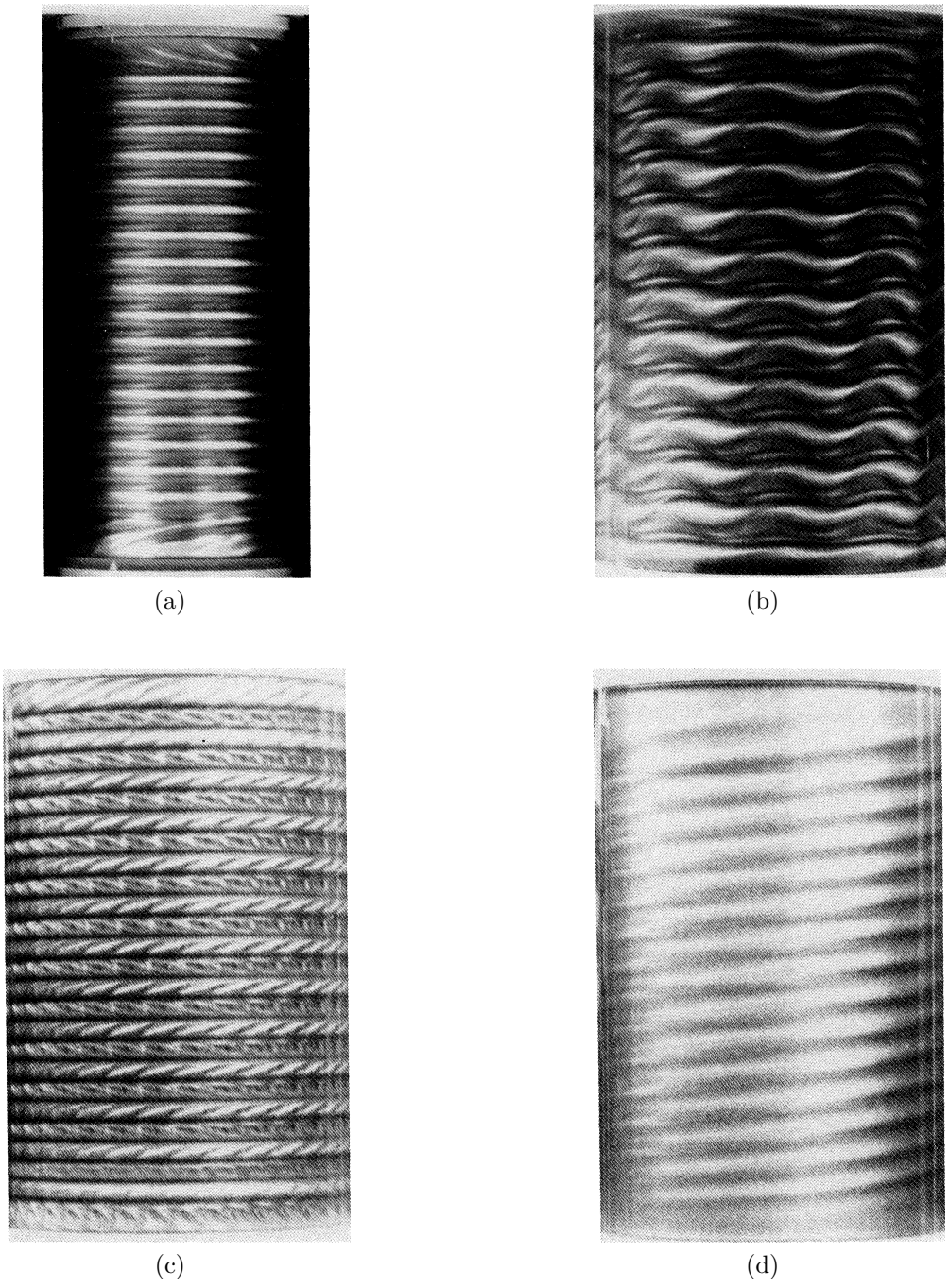

(a) (b)

(c) (d)

FIGURE 2.6 Instabilities in the Taylor-Couette flow: (a) Symmetrical vortices rings; (b) Modulated wavy vortices; (c) Twisted vortices; (d) Spiral ring. As appeared on Golubitsky and Stewart (1986).

Trefethen *et al.* argues that the non-normality of the operator makes unreliable the computation of eigenvalues as the sole criteria for stability. The non-orthogonality of the operator allows a significant amount of amplification of perturbations with three-dimensional characteristics in planar flows, a fact that has been largely overlooked due to the Squire theorem (Squire, 1933). Instead, they propose a generalization of the eigenvalue computation, using an amplification tolerance ϵ and calling the results ϵ-*pseudoeigenvalues*. They propose that this method allows the study of the transient growth phenomenon, when the effect of the perturbation is increasing in time even though all the modes are stable and exponentially decaying. Schmid and Henningson (2001) expanded on this concept, giving it coherence under an energetic point of view and establishing a nonmodal stability analysis which is still based on the linearized equation, and the use of adjoint operators and singular value decomposition (SVD) for the computation of stability thresholds.

The technique of SVD was later used by Barkley *et al.* (2008) to develop an algorithm for the computation of transient growth and optimal disturbances, based of modifications to his previously work for stability based on time integration methods (Tuckerman and Barkley, 2000). These techniques were used by Blackburn *et al.* (2008) to compute the optimal perturbation for the same stenose that was previously studied by Sherwin and Blackburn (2005) using traditional linear stability analysis. They found an optimal perturbation with a significant amount of amplification at $Re = 400$ that was previously overlooked by the linear stability analysis of Sherwin and Blackburn, and which is able to trigger important shear-layer instabilities and vortex shedding downstream the stenose. However, no symmetry-breaking instability was obtained, even though the maximum energy was found in a mode with azimuthal wavelength different from zero, meaning that it represented a non-axisymmetric perturbation. Similar results were also reported by Griffith *et al.* (2008, 2010) in a stenose with a different geometry, also finding instabilities that trigger shear layer oscillations, but no symmetry-breaking.

Cantwell *et al.* (2010) performed linear stability analysis in a sudden expansion, without success in reproducing the symmetry-breakup observed experimentally by Mullin *et al.* (2009). Additionally, they computed the optimal perturbation and transient growth for this geometry, with results analog to the ones reported by Blackburn *et al.* in the stenose. A subcritical perturbation at $Re = 600$ with a significant amount of amplification was found, able to trigger shear-layer instabilities and vortex shedding. However, as in the case of the stenose, no symmetry-breaking phenomenon was reported, even though the perturbation was not axisymmetric.

There are more elaborate techniques to the computation of stability based on the non-

orthonormality of the operator, like the nonmodal analysis (Schmid, 2007). However, they normally require the additional calculation of the adjoint operator of the Navier-Stokes equation, and given the computational cost of the classical linear stability analysis, with the methods and tools available, the memory and time requirements of these techniques would become prohibitive. Additionally, given the above mentioned results regarding this method, it provides information related to the shear-layer instabilities, but it does not capture the symmetry-breaking phenomenon that is the main objective of the present research. Thus, only the linear stability analysis is computed.

Until now, it has been mentioned the use of the stability analysis for the study of the transition to turbulence. Formally, once the turbulence regime develops, the non-linear phenomena are so relevant within the flow that it becomes impossible to find a steady or periodical solution to perform the linearization. However, the linear stability analysis has been applied to time-averaged solutions of the Reynolds-Averaged Navier-Stokes (RANS) equations using turbulence models. Iorio *et al.* (2014) used this technique to study the transition toward unsteady flow via Hopf bifurcations in two and three-dimensional airfoil geometries in transonic flow, and how this behavior is affected by the choice of turbulence model, while Mettot *et al.* (2014) employed this analysis to uncover regions of instability in the development of passive control devices in compressible flow.

The next sections present a detailed review of the relevant work in the study of symmetry-breakup in planar and axisymmetric flows.

2.8 Two-dimensional geometries

In the case of two-dimensional expansions, the classical and more widely studied example is the planar sudden expansion. A sketch of this case is depicted in Figure 2.7a, while the actual geometry used in experimental works is detailed in Figure 2.7b. Due to the geometrical symmetry in this problem, it is somewhat natural to expect a symmetrical solution, at least during laminar or steady-state conditions. Even in turbulent regime, when the fluctuations of the flow modify the instantaneous velocity field, the assumption of symmetry in the time-averaged flow field is not rare (Casey and Wintergerste, 2000). These simplifications are common in industrial applications, to cut down the size and computational cost of the problem, but they should be made carefully, given the available evidence of asymmetric average flow in turbulent regime (Monchaux *et al.*, 2006). These asymmetries also appear in the laminar regime, as discussed below.

Early experimental observations by Durst *et al.* (1972, 1974) described strong dependence of

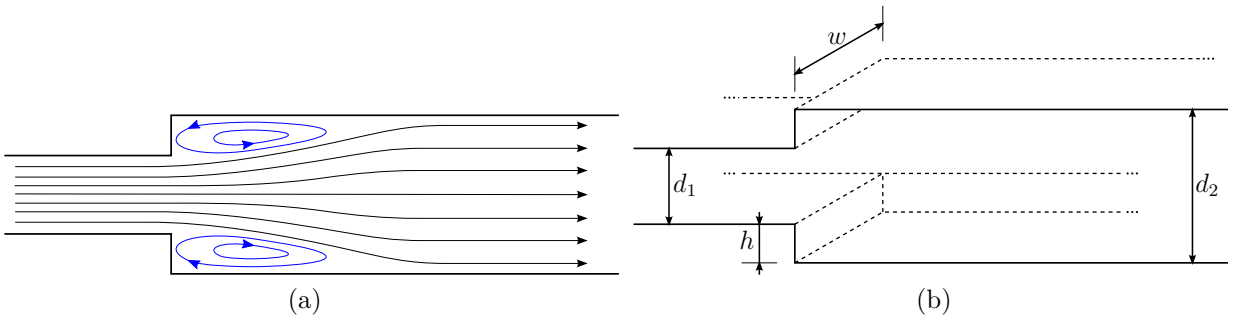

FIGURE 2.7 Two-dimensional sudden expansion: (a) schematics of the symmetric flow pattern through a planar sudden expansion; (b) geometrical parameters of the cited experimental setups (Durst *et al.*, 1974).

the visualized flow patterns with the perturbations and/or oscillations upstream the expansion. Durst *et al.* (1974) reported detached recirculation regions of equal length at both sides of a 1:3 sudden expansion at $Re = 54$ (based on the channel inlet height d_1 and the peak upstream velocity U_0), an indication of a symmetric flow pattern. The rupture of this symmetrical flow configuration occurs at some point before $Re = 114$, where the detached zones are no longer symmetrical. Additional separation zones appear at higher Reynolds numbers. The flow visualization of this asymmetrical condition is reproduced in Figures 2.8b and 2.8c, showing the attachment of the main flow to the lower wall of the channel, a phenomenon typically referred to as *Coanda effect* (Wille and Fernholz, 1965).

It is important to remark that the occurrence of the asymmetry is not only dependent of the Reynolds number, but it is also strongly dependent on the geometry of the channel, in particular the expansion ratio, *i.e.* the quotient between the upstream and downstream heights of the expansion d_1/d_2, and in experimental cases the width-to-height ratio w/h (called by some authors the aspect ratio), parameters defined in Figure 2.7b. The transition toward an asymmetry in the planar sudden expansion was also observed by Cherdron *et al.* (1978), Sobey (1985) and Fearn *et al.* (1990), with similar qualitative results. Table 2.1 summarizes the details for these experimental works. Cherdron *et al.* observed the symmetry-breaking phenomenon in setups with several width-to-height and expansion ratios, with the transition occurring at different Reynolds numbers for each combination. Their results are reproduced in Figure 2.9. Here, the influence of the expansion ratio is noticeable, with both curves presenting an asymptotic behaviour with the increase of the aspect ratio and a faster development for $d_1/d_2 = 1:3$. Similarly, for a 1:3 expansion with an aspect ratio of 15, Sobey (1985) reports the development of the asymmetry at $Re \simeq 25$, value that is also reported on Figure 2.9 for comparison.

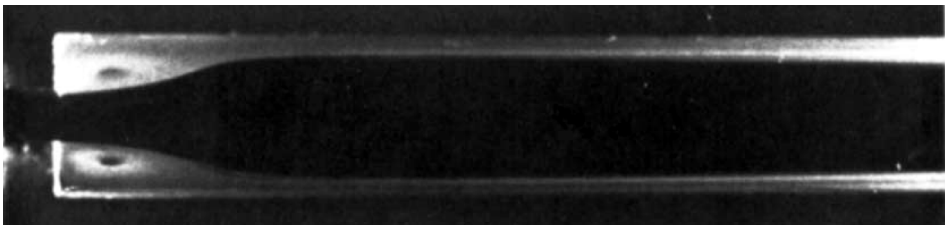

(a) $Re = 54$

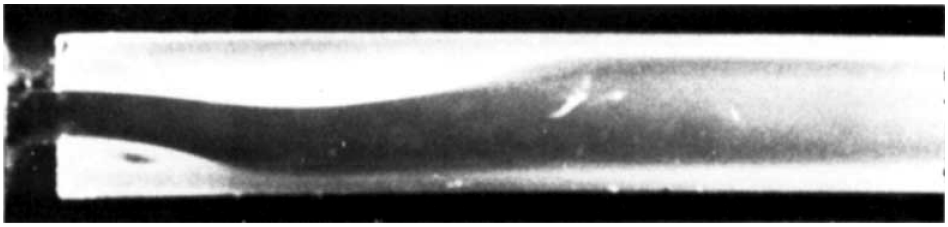

(b) $Re = 114$

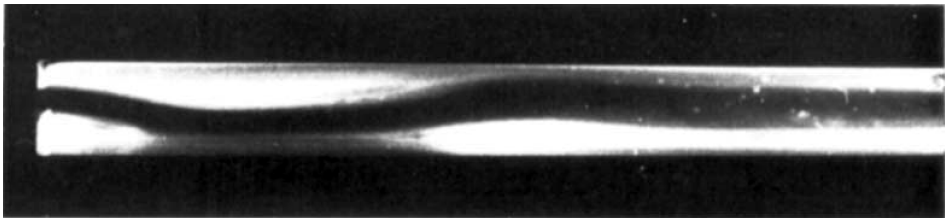

(c) $Re = 252$

FIGURE 2.8 Flow profile in a planar sudden expansion. A symmetric flow is shown in (a), which becomes asymmetric in (b), where the recirculation zones have different size. In (c) additional separated regions appear (Durst *et al.*, 1974).

TABLE 2.1 Critical Reynolds number reported in the literature for the two-dimensional sudden expansion.

Authors	d_1/d_2	w/h	Re_{crit}	Obs.
Durst *et al.* (1972)	1:2	3.75		No 2D flow obtained
Durst *et al.* (1974)	1:3	9.2	$54 < Re_{\text{crit}} < 114$	
Cherdron *et al.* (1978)	1:2, 1:3	see Fig. 2.9	see Fig. 2.9	LDA
Sobey (1985)	1:3	15	25	Reflective particles
Fearn *et al.* (1990)	1:3	8	40.25	LDA

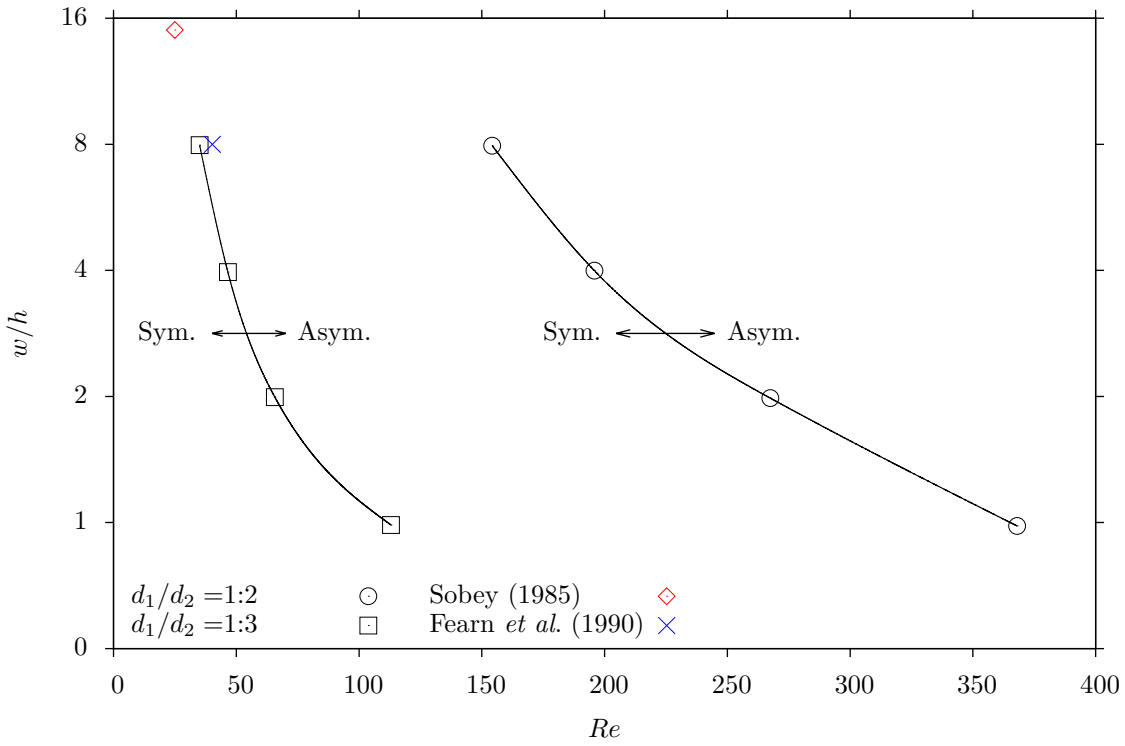

FIGURE 2.9 Flow map for the planar sudden expansion, describing the influence in the transition to asymmetry of Re, the width-to-height ratio w/h and the expansion ratio d_1/d_2. Adapted from Cherdron *et al.* (1978).

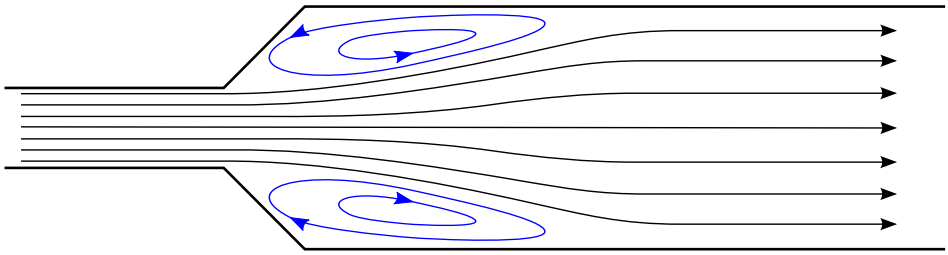

FIGURE 2.10 Planar divergent channel, with symmetrical flow pattern depicted.

In a later work, Sobey and Drazin (1986) performed a study of the flow in a two-dimensional divergent channel (sketched in Figure 2.10), in what constitutes one of the first successful applications of the bifurcation theory to parallel flows, since they confirmed through experiments the predicted symmetry-breaking phenomenon. They also observed analog asymmetries in other planar geometries, including a sudden expansion and a smooth contraction-expansion. Using techniques analogues to the ones previously implemented in the analysis of the instabilities of the classical *Taylor–Couette vortices* (Taylor, 1923; Golubitsky and Stewart, 1986), they were able to anticipate the apparition of an asymmetric flow after a critical Reynolds number that depends of the expansion ratio. Similar theoretical conclusions were made by Banks *et al.* (1988) using linear and weakly non-linear theory, confirming the symmetry-breaking through a pitchfork bifurcation and a Hopf bifurcation at higher flow rates, after which the flow becomes time dependent.

Using similar analytic techniques, Fearn *et al.* (1990) studied the symmetry breaking bifurcation in a sudden symmetric expansion with a 1:3 expansion ratio. Their bifurcation analysis indicated that the stable planar symmetric flow becomes unstable through a pitchfork bifurcation at $Re = 40.45$, based on the inlet peak velocity and half height. Above this condition, the flow has three solutions: two stable asymmetric states and the symmetrical one, which is now unstable. Each of the two asymmetrical cases represent the attachment of the main flow to either the top or the bottom channel wall. These theoretical predictions were also in good agreement with their experiments using LDA, showing a stable flow with low asymmetry for $Re < 33$, and a strong asymmetric flow above this condition. Figure 2.11 reproduces one of their bifurcation diagrams for the normalized transverse velocity component at a fixed position of the channel, along with the numerical predictions of their analysis, showing the two stable asymmetric branches. Fearn *et al.* argued that these differences arise due to the unavoidable geometrical imperfections in the experimental setup, and also the boundary effects of channel width makes any observed flow neither purely two-dimensional nor completely symmetric. Thus, one of the branches, in this case the one representing the attachment of the main flow to the upper wall, is more likely to be obtained than the other.

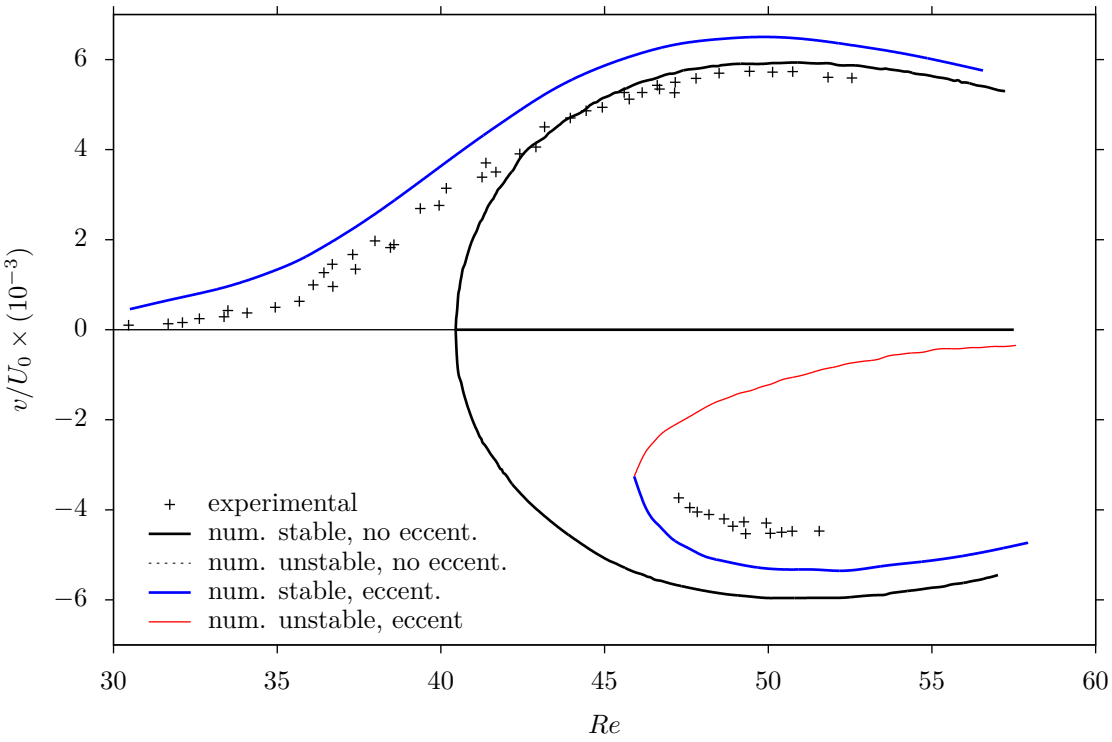

FIGURE 2.11 Numerical and experimental bifurcation diagram for a planar sudden expansion, showing the normalized vertical velocity v/U_0 at $x = 6.375\,d_1$ downstream the expansion for a symmetrical and a slightly eccentric geometry. Adapted from Fearn *et al.* (1990).

Fearn *et al.* showed that the consideration of a small eccentricity (less than 0.1% of the channel height) produced numerical results with a better match against the experimental data, as depicted in Figure 2.11. Durst *et al.* (1993), and Drikakis (1997) further expanded on these computational techniques, unveiling additional bifurcations, and establishing the possibility that the bifurcation results depend on the numerical technique used.

Further numerical calculations were carried out by Battaglia *et al.* (1997) using a time-marching finite difference method, along with stability analysis, to compare their prediction of the asymmetry threshold in the symmetric sudden expansion. Alleborn *et al.* (1997) studied the planar eccentric sudden expansion using stability analysis, uncovering several bifurcations of this flow and determining the flow solution along the different stable and unstable branches of the flow map. Later, Battaglia and Papadopoulos (2006) studied experimentally and numerically a 1:2 sudden expansion, with close agreement between their results, emphasizing the three dimensional effects due to the width of the experimental channel, with an enhancement of the stability for smaller widths, in agreement with the results of Cherdron *et al.* presented in Figure 2.9.

More recently, Fani *et al.* (2012) computed the linear stability of a flow through a sudden expansion as a previous step to the formulation of a control system to avoid the asymmetry. The symmetry- breaking threshold they computed is in agreement with all the previously cited works. And Guevel *et al.* (2014) developed an algorithm for the study of the effect of geometrical parameters on the flow stability. They evaluated it in a sudden expansion with several ranges of expansion ratio, and their results also reproduces the previously cited studies.

The different two-dimensional examples reviewed in this section show that it is possible to estimate numerically the occurrence of symmetry-breaking instabilities in planar or two-dimensional flows. This is information is useful even in cases when the computed critical condition even does not coincide exactly with the experimental value, because it allows the establishment of a reference threshold for the breakup and gives an idea of the order of magnitude of the Reynolds number at which the transition toward asymmetry will occur. However, in the following section the analog problem will be presented in the context of three-dimensional axisymmetrical geometries, where the correspondence between analytic predictions of the asymmetry and its experimental observations is harder to achieve.

2.9 Axisymmetric geometries

In the case of a planar expansion, the experimental setup has an aspect ratio high enough to approximate the two-dimensional flow state. In contrast, axisymmetrical geometries as the ones sketched in Figure 2.12 completely confines the flow, and thus limit the amplitude of the oscillations that could appear after the expansion. Consequently, it is natural to expect that the instability that triggers the asymmetrical flow appears at a higher Reynolds number than in the two-dimensional problem. The geometries that were thoroughly reviewed were the axisymmetrical sudden expansion, sometimes called in the literature *confined jet*, a common test case for several engineering applications; and the axisymmetric smooth contraction-expansion, an important setup in biomedical and biomechanical engineering, being the model case for a stenosed artery. Both geometries are presented in Figure 2.12, along with the relevant geometrical parameters.

2.9.1 Three-dimensional sudden expansion

The basic geometric description of an axisymmetric sudden expansion is shown on Figure 2.12a. As in the planar case, the most relevant parameter is the expansion ratio D_1/D_2. One of the first integrated numerical-experimental works on the flow in an axisymetrical geometry

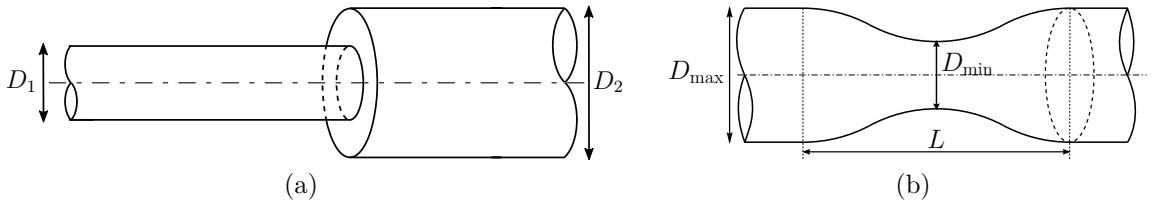

FIGURE 2.12 Definition of axisymmetric geometries. (a) a sudden expansion, (b) A smooth contraction-expansion.

was performed by Macagno and Hung (1967), who studied a 1:2 sudden expansion. Their numerical approach was based on the integration of the vorticity transport equations through finite differences, avoiding the explicit solution of the pressure field. Figure 2.13a reproduces their numerical results at $Re = 100$, based on the diameter and average velocity upstream the expansion, with the upper portion showing the vorticity contours while the lower half depicts the stream function contours. They also studied experimentally the influence of the Reynolds number until a value of 200, reporting a symmetrical profile. Figure 2.13b presents a comparison of their visualizations results with the numerical stream function at $Re = 100$, showing good agreement between them.

Later, Iribarne *et al.* (1972) studied the flow in an axisymmetric 1:2 sudden expansion through a photochromic visualization technique. Using a flat velocity profile at the inlet, they observed the characteristics of a laminar confined jet, for Reynolds numbers in the range $90-1355$, based on the inlet diameter, obtaining lengthwise fluctuations in the position of the reattachment point above $Re = 350$, and also described the shear-layer instability that generates eddies with a similar topology to the ones reported in the original Reynolds' experiment (Reynolds, 1883; Van Dyke, 1982), as described by Drazin (2002). However, as they were interested in the oscillations of the reattachment length, detailed results were presented only for $Re = 389$ and under these conditions no asymmetric flow was present.

Analog unsteady effects were also observed by Back and Roschke (1972) and by Feuerstein *et al.* (1975), although at higher Reynolds numbers, describing rapid oscillations in the reattachment length, with important fluctuations in the velocity field in its vicinity that, according to Latornell and Pollard (1986), were caused by perturbation in the upstream conditions of the experiment. This also constitutes a challenge for the accurate determination of the critical conditions for an asymmetric flow or to turbulence transition. Villermaux and Hopfinger (1994) proposed an empirical description of the oscillations in the reattachment length, as well as the shear layer instability in the recirculation region. Their model was developed for confined jet in a rectangular cavity but according to Villermaux and Hopfinger, the model

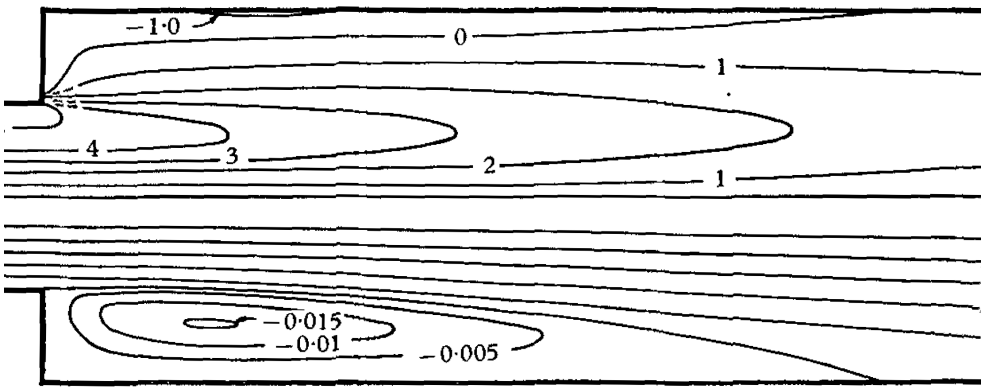

(a)

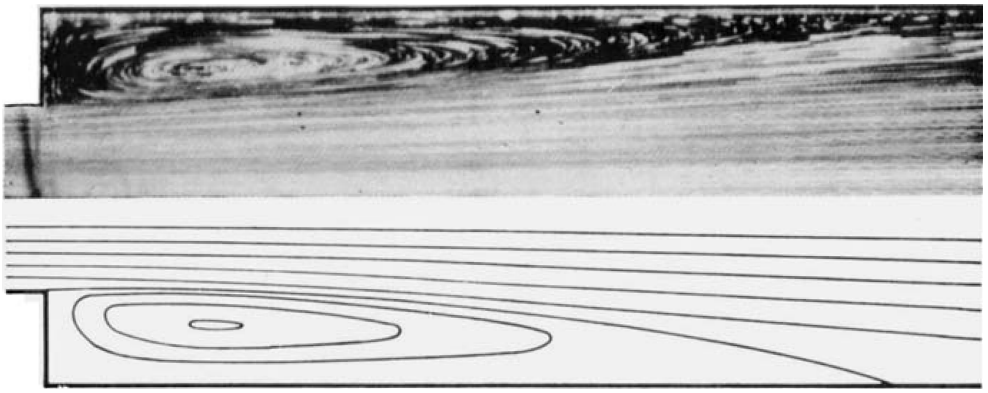

(b)

FIGURE 2.13 Numerical and experimental results in a 1:2 sudden expansion, reproduced from Macagno and Hung (1967): (a) isocontours of vorticity (upper half) and stream function (lower) for a sudden expansion at $Re = 100$; (b) comparison of the flow visualization with the stream function results at $Re = 100$.

describes these phenomena satisfactorily in an axisymmetric sudden expansion. However, it fails to explain the instabilities responsible for the asymmetric flow.

Velocity fluctuations and unsteady effects were the main focus of several experimental works in the following years. Furuichi *et al.* (2003) used a ultrasonic Doppler velocimetry (Takeda, 1995) to investigate the spatial and temporal features of the flow through an axisymmetric 1:1.8 sudden expansion, for Reynolds number in the range $Re = 500 \sim 15000$, based on the inlet diameter. They were able to identify a laminar flow regime for $Re \leq 700 \sim 1000$, a transitional regime for $1000 \leq Re \leq 3000$, and above that condition a turbulent regime. They also identify a *change in the spatial structure of the flow* for $Re \simeq 1500$, without further details, presumably due to the lack of detailed velocity information.

The first detailed description of an asymmetric flow in an axisymmetric sudden expansion was made by Mullin *et al.* (2009) via magnetic resonance imaging (MRI). Specifically, they studied a sudden expansion with a 1:2 expansion ratio using two different experimental setups in order to visualize the symmetry breaking through Rapid Acquisition with Relaxation Enhancement (RARE) imaging, and collect velocity data using Gradient Echo Rapid Velocity and Acceleration Imaging Sequence (GERVAIS). The RARE images allowed them to visualize the position of the shear layer and the shape of the recirculation region in several transverse section of their setup. They computed the centroid of the region with positive velocity in the RARE image, and used the square of its radial position as a measure of the level of asymmetry in the flow.

Figure 2.14a shows one of the RARE images captured by Mullin *et al.*, while Figure 2.14b contains their results for the asymmetry measure as a function of the Reynolds number. Here the symmetry-breaking effects manifest at $Re = 1139 \pm 10$, a value significantly higher than the one reported by Fearn *et al.* (1990) for the two-dimensional geometry. An attempt to calculate numerically this condition was made by Cantwell *et al.* (2010), using linear stability analysis. However, they failed to compute the transition to an asymmetric flow, predicting a stable symmetric flow for Reynolds number up to 1400. Thus, the computational study in this case is in disagreement with the flow pattern observed in the laboratory. These experimental and numerical thresholds for symmetric flow are of the same order of magnitude than $Re \simeq 1500$ reported by Furuichi *et al.* (2003) for his *structural change*, which was probably associated with a transition to an asymmetric velocity profile. About this issue, Mullin *et al.* (2009) states that the nature of the bifurcation in the axisymmetrical case is unlikely to be a pitchfork bifurcation as in the two-dimensional case, and that confirming their experimental results constitute an *outstanding challenge for computational fluid dynamics* (CFD).

Dawson and Blackburn (2010) performed direct numerical simulations (DNS) on a 1:5 sudden

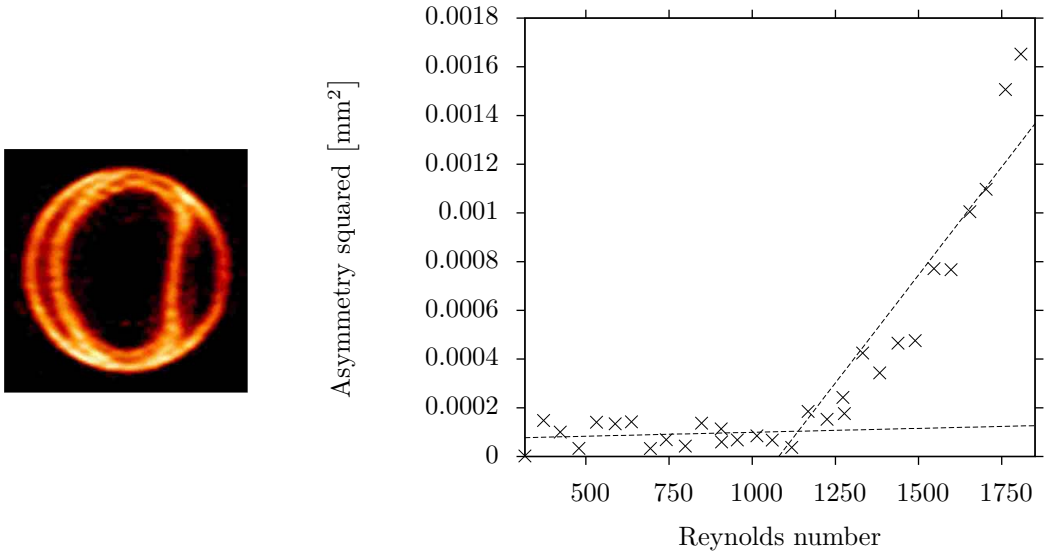

FIGURE 2.14 Selected results for the sudden expansion from Mullin *et al.* (2009): a) RARE image at 16.25 diameters dowstream of the sudden expansion at $Re = 1567$; b) Asymmetry of the flow as a function of Reynolds number.

expansion, introducing different types of high amplitude perturbations and pulsatile flow into a low Reynolds number flow ($Re = 200$, based on the average speed and diameter at the inlet). Their results showed the formation and shedding of vortex rings from the shear layer, and some degree of asymmetry is observed in the averaged fields. However, the low Reynolds number, the pulsatile nature of the base flow and the high amplitude perturbations make this asymmetry part of a different phenomenon than the one observed by Mullin *et al.*.

In a combined numerical-experimental work, Peixinho (2010); Peixinho and Besnard (2013) present the study of an axisymmetric diverging section and the transition of the Jeffery-Hammel toward a turbulent regime. Their experimental and numerical velocity profiles present only axisymmetric patterns.

Some of the challenges for CFD mentioned by Mullin *et al.* were later tackled by Sanmiguel-Rojas and Mullin (2012), who worked numerically on a 1:2 sudden expansion, adding a small transverse component to the inlet velocity profile, in order to investigate the existence of unsteady states of finite amplitude. Their results present a similar qualitative behavior to the one observed by Mullin *et al.* (2009), and they affirm that the presence of this transverse velocity at the inlet is equivalent to different geometrical imperfections, a situation that is investigated in Chapter 5. The study of these unsteady states of finite amplitude is the base of the transient growth theory mentioned in Section 2.7.

2.9.2 Smooth contraction-expansion

The study of the flow through a pipe with a smooth contraction-expansion is very important in the analysis of stenosed blood vessels. According to Young (1968), the detailed knowledge of the flow characteristics around a stenosis is valuable because there is a coupled effect between them and the growth and development rate of the vascular lesion. They are studied numerically or experimentally with usually a geometry similar to the one presented in Figure 2.12b. Here, the most important geometrical parameter are the percentage of area reduction $\%A_{\mathrm{R}}$

$$A_{\mathrm{R}} = \left[1 - \left(\frac{D_{\min}}{D_{\max}}\right)^2\right] \times 100, \tag{2.22}$$

the length-to-diameter ratio $L/D_{\max}$ of the restriction and the shape of the constriction wall, usually some sort of smooth function that match the diameters $D_{\max}$ and $D_{\min}$ at the appropriate values of the axial position.

Lee and Fung (1970) modeled their geometry with a Gaussian curve, computing the steady-flow for Reynolds numbers up to 25. Forrester and Young (1970a) performed simulations in a similar geometry with the axisymmetrical Navier-Stokes equations, characterizing the separation and recirculation zone as a function of the Reynolds number. They found that flow separation could be present even in constrictions with small reduction of transverse area. For example, for a stenosis with 55.6% of area reduction [1], they showed that for $Re \simeq 100$, there is no separation of the flow. However, at higher values of Re, a recirculation zone appears, with its size being proportional to the Reynolds number. These observations were confirmed by an accompanying experimental investigation for the same geometry (Forrester and Young, 1970b). An example of the patterns predicted by them is shown in Figure 2.15.

Young and Tsai (1973) characterized axisymmetric cosine arterial stenoses models [2] in through visualization and hot film probes, paying special attention to the separation and reattachment of the flow, mmetric recirculation zone in their results. Numerical steady-state studies for a wide range of laminar Reynolds numbers were performed by Deshpande *et al.* (1976) in a cosine stenosis with 75% of area restriction and $L/D\mathrm{max} = 2$, showing only an axisymmetric velocity profile, while later the same geometry was evaluated experimentaly by Deshpande and Giddens (1980) using LDA to investigate turbulent mean flow in stenoses. Khalifa and Giddens (1981) employed the same technique to study the evolution of disturbances downstream several cosine stenoses with $\%A_{\mathrm{R}} = 25\%, 50\%,$ and 75% with $L/D_{\max} = 2$. Further experiments using LDA were conducted by Ahmed and Giddens (1983b,a) for the same set of geometries

1. $D_{\max} = 0.75\,\mathrm{in}$, $D_{\min} = 0.50\,\mathrm{in}$, $L = 3.0\,\mathrm{in}$
2. $\%A_{\mathrm{R}}$: 56% and 89%; $L/D_{\max} = 2$ and 4.

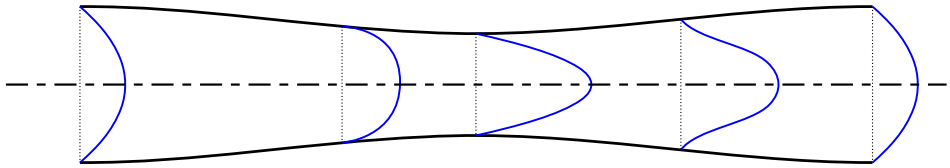

(a) $Re = 100$

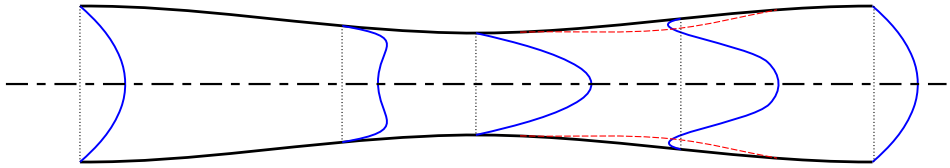

(b) $Re = 150$

FIGURE 2.15 Numerical prediction of separation zones (shown in red). Adapted from Forrester and Young (1970a).

in laminar and turbulent regimes. Although in one of their flow visualization images an asymmetric flow after the constriction could be appreciated (reproduced here in Figure 2.16), there is no mention or reference to an asymmetry in their results or analysis, reporting an axisymmetric velocity profile, as in all previously cited works.

Mallinger and Drikakis (2002) studied numerically the instabilities that occur with the pulsatile flow through a stenosis with a 75% of area reduction and $L/D_{\max} = 2$ [3]. They used a perturbed velocity profile as boundary condition, with an oscillating components parallel to the flow direction and a frequency in the phisiological range (Womersley number [4] $\alpha \approx 10$). These oscillations caused a variation of the instantaneous Reynolds number between 760 and 1245 per cycle, developing an unsteady asymmetric flow downstream the constriction.

3. Besides the fact that their geometry is axisymmetic, they did not provide details about the shape of the constriction, but from their figures it presents a sharp corner in the intection of the stenotic region and the main tube.

4. The Womersley number is the quotient between the inertial transient forces and the viscous forces, and it is important in biofluid mechanics. Usually represented as $\alpha = L\left(\frac{\omega\rho}{\mu}\right)^{\frac{1}{2}}$

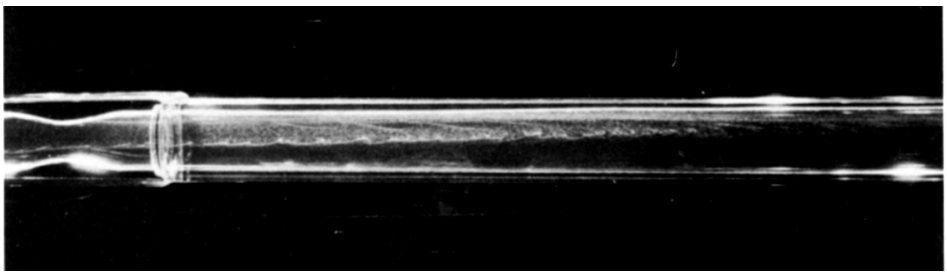

FIGURE 2.16 Asymmetric flow, from Ahmed and Giddens (1983a).

However, they described the morphology of the asymmetry only qualitatively, reporting the formation of several recirculating regions besides the one inmediately downstream the constriction, similar to what was described for the planar sudden expansion experimentally by Durst *et al.* (1974) and numerically by Alleborn *et al.* (1997). No attempt was made to correlate the observed asymmetry with the amplitude of the inlet oscillations, neither to construct a bifurcation diagram or to explain the asymmetry from the point of view of the bifurcation theory.

Sherwin and Blackburn (2005) performed a numerical study for steady and pulsatile flow within an axisymmetric stenosis with 75% or area restiction, using the spectral elements DNS code previously developed by Blackburn and Sherwin (2004) alongside a linear stability algorithm based on the work of Tuckerman and Barkley (2000). For the steady state scenario, they predicted an instability in the computed axisymmetric base flow at $Re = 722$. The perturbation velocity field associated to this critical mode cause a deflection of the symmetric flow emanating from the throat of the stenosis, and indeed describe a symmetry-breaking bifurcation. The evolution of this perturbation through DNS produced a highly unsteady flow, with a weakly asymmetric flow less remarkable than the one obtained for the two-dimensional case by Sobey and Drazin (1986), and with local transition to turbulence farther downstream. The flow also presented a subcritical behavior when the flow rate is decreased, remaining asymmetric and turbulent until $Re \approx 688$.

Similar numerical studies were carried out by Varghese *et al.* (2007) using DNS, although they did not performed any stability analysis. They worked with two geometrical descriptions of the stenosis, one axisymmetric and another with an eccentricity of 5% [5]. Their results for the axisymmetric case showed a laminar flow up to $Re = 1000$. According to the results from Sherwin and Blackburn (2005), this flow would be unstable, and instabilities will developed if perturbations were considered in the solution. And indeed, in the eccentric case, the base flow showed a significant asymmetric steady attachment at $Re = 500$, while the same turbulent structures and local transition at a similar axial position than the one reported by Sherwin and Blackburn were observed at $Re = 1000$.

In contrast, the experimental observations conducted by Vétel *et al.* (2008) using particle image velocimetry (PIV) in an axisymmetric stenosis with 75% of area reduction produced results remarkably different to these numerical works. Vétel *et al.* reported a steady asymmetric flow at Reynolds numbers as low at $Re = 250$, with unsteady behavior appearing at $Re \approx 400$, results that deviate significantly from the ones published by Sherwin and Blackburn (2005) and Varghese *et al.* (2007). First of all, the steady asymmetry obtained by Varghese *et al.* at

5. see Figure 2.17 for a sketch of the eccentricity definition.

low Re was in an eccentric stenosis, and their numerical velocity contours deviate considerably from the measurements of Vétel *et al.*. The deflection of the flow and the magnitude of the negative velocities within the recirculation pocket are larger in the DNS results than in the PIV measurements, quite likely due to the presence of the eccentricity. The asymmetry computed by Varghese *et al.* was always in the same direction of their rather large geometrical eccentricity, while in the experiments of , the asymmetry shifted its angular position over the tube with the change of flow rate. Vétel *et al.* acknowledge the existence of geometrical defects in their setup, with a manufacturing tolerance that could cause eccentricities of 0.12% of the tube diameter. This small value and the fact that the flow does not have a single preferred direction for deflection and attachment to the wall downstream the stenosis lead them to hypothesize that their symmetry-breaking mechanism does not have its main origin in geometrical defects in the experimental setup, as stated by Varghese *et al.*.

Vétel *et al.* (2008) described the occurrence of local transition to turbulence at $Re \approx 400$ with relaminarization farther downstream their setup, a phenomenon that is in agreement with the comments made by Sherwin and Blackburn (2005) and by Varghese *et al.* (2007). Nevertheless, there are important discrepancies between the numerical results of Sherwin and Blackburn (2005) and the PIV data from Vétel *et al.* (2008). First of all, Vétel *et al.* reported the shift to an asymmetric flow occurs at a much lower Reynolds number than the one predicted by the linear stability analysis of Sherwin and Blackburn (2005). Additionally, the DNS results showed a weakly asymmetric flow with local transition to turbulence, while the experimental results described a steady and noticeable asymmetry, with the flow completely attached to one side of the pipe downstream the flow restriction. It is natural to expect some differences arising from the geometrical description of the stenosis, given that both Sherwin and Blackburn and Varghese *et al.* use a sinusoidal shape for the restriction, in agreement with (Ahmed and Giddens, 1983b,a), while Vétel *et al.* use a shape constructed from the intersection of circular arcs, similarly to Cassanova and Giddens (1978). But the large amount of difference observed between these works indicate that the numerical studies fail to describe satisfactorily the behavior of this flow. In particular, the linear stability analysis is unable to capture the transition to asymmetric flow at low Reynolds number. As stated previously, the present research is focused in the elucidation of the source of these discrepancies.

2.10 Geometric perturbations

The use of perturbations is quite extended in the study of fluid flow, specially as a trigger to certain phenomena. It is common to use a small degree of noise in boundary conditions in DNS, as it provides an input for more realistic transient simulations. For example the wake

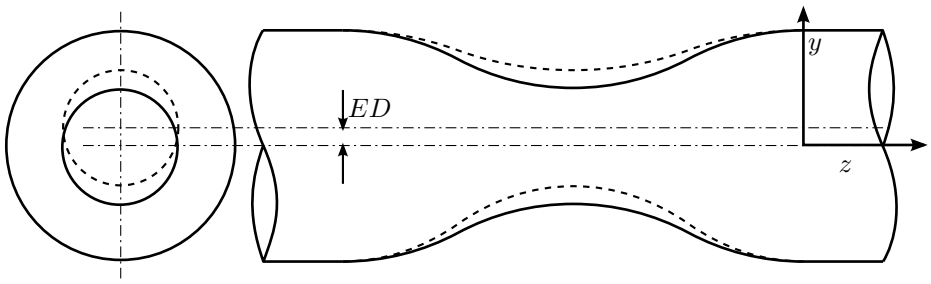

FIGURE 2.17 Eccentricity on the stenotic geometry.

around certain blunt bodies may converge to a steady state at a Reynolds number where this solution is no longer be valid (Noack and Eckelmann, 1994), and the added noise should help to avoid this situation. But sometimes is necessary an alternative way of perturbation, especially when dealing with numerical techniques that are not DNS. For example, among the several recipes available in numerical analysis and CFD textbooks to reproduce the classical Von Kármán vortex alley around a cylinder, there is the use of a slowly rotating cylinder, in order to obtain an asymmetric wake that would be then evolved in time with the cylinder in rest, or a cylinder slightly eccentric within the numerical domain (Ferziger and Perić, 2001).

For the flows of interest to this study, the use of similar geometrical perturbations, although not common, has been evaluated previously in the literature. Fearn *et al.* (1990) explained the difference between their numerical and experimental studies in the planar sudden expansion was due to the small geometrical defects in their setup (see Figure 2.11). The addition of a small vertical offset to the inlet tube in their numerical domain allowed them to reproduce the smooth transition toward the asymmetric flow obtained experimentally. Stroud *et al.* (2000) studied numerically several different irregular stenoses with a more realistic shape, contrasting their results against the ones obtained for smooth axisymmetric restrictions and finding important differences between them. The wall shear stress, employed for the assessment of risk for plaque rupture within the stenosis is particularly sensible to these geometrical irregularities, to the point that Stroud *et al.* recommend the use of more complex geometrical characterizations for stenoses than simply the percentage of area restriction.

Varghese *et al.* (2007) evaluated numerically a stenosis with a 5% of eccentricity, based on the diameter. A sketch of this additional geometrical parameter is shown on Figure 2.17 [6]. Their focus was the study to turbulence transition in the presence of asymmetry, justifying the use of a geometry with a high amount of eccentricity to force the deflection of the flow. Expanding the work of Varghese *et al.* (2007) in the stenosis, Griffith *et al.* (2013) performed a parametric

6. The eccentricity index E represents the maximum deviation fom the axisymmetric form as a fraction of the maximun diameter of the tube. Hence, an eccentricity of 5% is equivalent to $E = 0.05$

study on the effect of small eccentricities in the contraction-expansion section, in the range of 0.01% to 10% of the tube diameter, much smaller that the one studied by Varghese *et al.*. They found that the asymmetry in the flow solution downstream the stenosis is strongly dependent upon the value of eccentricity added, with a remarkable qualitative similarity between the asymmetry of the experimental results of Vétel *et al.* (2008) and their DNS simulation when the geometry had an eccentricity of 0.25% of the diameter. And Sanmiguel-Rojas and Mullin (2012) studied numerically the sudden expansion using a perturbed velocity profile as boundary condition, with a small velocity component perpendicular to the streamwise flow direction. They managed to correlate the magnitude of this small velocity component with an estimated eccentricity of the inlet tube to the expansion. However, in contrast with Varghese *et al.* (2007), no actual eccentric domain was used in their computations.

Chapters 4 and 5 of the present study deal with the effect of these geometrical imperfections in the stenosis and sudden expansion, respectively, building over the knowledge and results presented in the previous cited works, with the additional aspect of the linear stability analysis.

2.11 Iterative computation of eigenvalues

As explained previously, each point $u(t)$ in Equation (2.12) contains information about the flow in the whole domain. Thus, the size of the operator $\mathbf{L_U}$ will be large, proportional to the mesh used in the numerical solution of the flow. Hence, its explicit representation in its matrix form is largely inadequate. However, the linear stability analysis requires only the leading eigenvalues (those with the largest real part) to establish the stability condition. Hence, the direct computation of all the eigenvalues is, besides unpractical, also unnecessary. The algorithm requires the use of a numerical technique to compute only a few eigenvalues and eigenvectors of the discretized linear operator $L_{\mathbf{U}}$.

Through a series of articles, Tuckerman and Barkley present different details concerning the technique for the computation of stability they employed (Barkley, 1992; Mamun and Tuckerman, 1995; Barkley and Henderson, 1996; Barkley and Tuckerman, 1999; Tuckerman and Barkley, 2000). Their approach uses an iterative Krylov subspace method based on the Arnoldi iteration algorithm (Saad, 1980). The core of this procedure is the modified power method, which allows to compute the dominant eigenvector of a $m \times m$ matrix $\mathbf{A}$ from its repeated action over an arbitrary initial vector x_0. Indeed, the sequence

$$x_n = \mathbf{A}^n x_0$$

approximate the dominant eigenvector, the one corresponding to the eigenvalue with largest

magnitude. The eigenvalue is computed from the Rayleigh quotient

$$h_n = \frac{x_n^T \mathbf{A} x_n}{x_n^T x_n}$$

.

This power method only allows to compute one eigenpair, *i.e.* an eigenvalue and its associated eigenvector. The Arnoldi algorithm allows the simultaneous computation of several eigenpairs, being a generalization of the power method. The procedure is as follows:

1. Start with an arbitrary initial vector x_0, with the same number of elements as degrees of freedom the system has. In other words, x_0 should have m elements.
2. Construct the sequence $x_0, \mathbf{A}x_0, \mathbf{A}^2x_0, \ldots, \mathbf{A}^{k-1}x_0$. These vectors define the span of the Krylov space. Here, k is the number of eigenpairs sought, normally 4-8. k is significantly smaller than m, the size of the matrix $\mathbf{A}$.
3. The previous sequence of vectors is orthonormalized to obtain the base of the Krylov space $v_1, v_2, \ldots, v_k$. The classical Gram-Schmidt method, although simple, presents severe numerical convergence problems when performed numerically due to roundoff errors (Cheney and Kincaid, 2009). The modified or stabilized Gram-Schmidt method is recommended (Daniel *et al.*, 1976; Saad, 1980).
4. The Krylov space base vectors are assembled as the columns of a $m \times k$ matrix $\mathbf{V} = [v_1\ , v_2\ , \ldots\ , v_k]$.
5. The $k \times k$ Hessenberg matrix $\mathbf{H} = \mathbf{V}^T\mathbf{A}\mathbf{V}$ is constructed.
6. The eigenvalues and eigenvectors of $\mathbf{H}$ are computed. Given the reduced size of the matrix $\mathbf{H}$ compared with the original $\mathbf{M}$, more traditional direct methods could be used to compute these eigenpairs. Goldhirsch *et al.* (1987) recommends using the QR algorithm, already included in most computational libraries.
7. The eigenvalues of $\mathbf{H}$ approximate the first k dominant eigenvalues of $\mathbf{A}$, while its eigenvectors, multiplied by $\mathbf{V}$, approximate the associated k eigenvectors of $\mathbf{A}$.

The previous algorithm allows the computation of eigenpairs of a large $m \times m$ $\mathbf{A}$ matrix solving a reduced problem of size $k \times k$, without explicitly using the matrix $\mathbf{A}$. Indeed, the method only uses $\mathbf{A}$ implicitly, through its repeated action over a vector of size m. However, it still computes the eigenvalues with largest magnitude, not the ones with the largest real part, which are the ones of interest for the stability analysis. A modified version of the Arnoldi algorithm developed in detail by Goldhirsch *et al.* (1987) was included in the computational routine of Tuckerman and Barkley, allowing them to obtain the leading eigenpairs of the problem instead of the dominant ones. This modification was developed in general for any

large asymmetric matrix $\mathbf{A}$, but it is especially well suited when the matrix actually represents a differential operator like in Equation (2.12). Given the following problem

$$\frac{d\mathbf{x}}{dt} = \mathbf{A}\mathbf{x}, \tag{2.23}$$

with initial condition

$$\mathbf{x}(0) = \mathbf{x}_0.$$

Its solution, after integration for $0 \leq t \leq t_f$ is

$$\mathbf{x}(t_f) = \exp(\mathbf{A}t_f)\mathbf{x}_0. \tag{2.24}$$

Now, assuming that the eigenvalues of $\mathbf{A}$: λ_i are sorted according to their real parts, in decreasing order $\mathrm{Re}(\lambda_1) > \mathrm{Re}(\lambda_1) > \ldots > \mathrm{Re}(\lambda_m)$, with associated eigenvectors $\boldsymbol{\varphi}_1, \boldsymbol{\varphi}_2, \ldots, \boldsymbol{\varphi}_m$, where again m is the rank of $\mathbf{A}$. It is possible to expand the vector $\mathbf{x}_0$ as a linear combination of these eigenvectors

$$\mathbf{x}_0 = \sum_{i=1}^{m} \alpha_i \boldsymbol{\varphi}_i,$$

which after the application of the operator $\exp(\mathbf{A}t_f)$

$$\begin{aligned}\mathbf{x}(t_f) = \exp(\mathbf{A}t_f)\mathbf{x}_0 &= \sum_{i=1}^{m} \alpha_i \exp(\mathbf{A}t_f)\boldsymbol{\varphi}_i \\ &= \sum_{i=1}^{m} \alpha_i \exp(\lambda_i t_f)\boldsymbol{\varphi}_i,\end{aligned}$$

where the definition of an eigenvalue $\mathbf{A}\mathbf{e}_i = \lambda_i \boldsymbol{\varphi}_i$ has been used. It is clear that for t_f large enough the non-leading eigenvalues will decay and their contribution will be small due to the exponential terms. Because of this decay Goldhirsch *et al.* call this time integration *filtering stage*. But the exponential term in Equation (2.24) also transform the complex plane containing the eigenvalues of $\mathbf{A}$ as follows

$$\begin{aligned} z &\in \mathbb{C} \\ z &= \mathrm{Re}(z) + i\,\mathrm{Im}(z) \\ e^z &= \exp(\mathrm{Re}(z) + i\,\mathrm{Im}(z)) \\ &= \exp(\mathrm{Re}(z))\exp(i\,\mathrm{Im}(z)) \\ &= \exp(\mathrm{Re}(z))\left[\cos(\mathrm{Im}(z)) + i\sin(\mathrm{Im}(z))\right], \end{aligned}$$

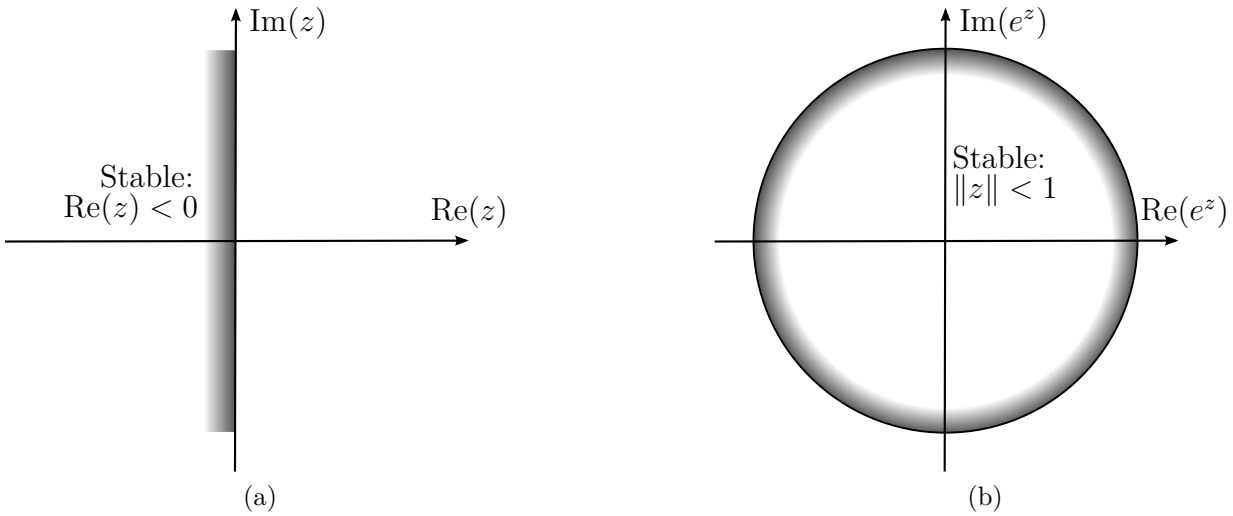

FIGURE 2.18 Exponential transformation of the complex plane. The shaded stability region goes from the half-plane with negative real part in (a), to the interior of the unit circle in (b).

and thus, the imaginary axis $\mathrm{Re}(z) = 0$ becomes the unit circle in the transformed plane, as depicted in Figure 2.18. The stable negative half of the complex plane is mapped into the interior of the circle, while the unstable half becomes the exterior. Hence, the dominant eigenvalues of the $\exp(\mathbf{A})$ are the leading ones of $\mathbf{A}$. The explicit exponentiation of the matrix $\mathbf{A}$ is never computed. Instead, the time integration of the operator (2.23) is performed, even for algebraic cases where the matrix $\mathbf{A}$ is not related with differential problems.

Instead of the exponential transformation, Cliffe *et al.* (1993) used different preconditioners to transform leading eigenvalues into dominant ones, making it suitable for an Arnoldi iteration, and using the resulting method to locate Hopf bifurcations. A hybrid approach was developed by Fortin *et al.* (1994), using a similar stability problem as the one presented in this section, and combining with it predictions from the Orr-Sommerfeld equation as input for non-linear computations, integrating directly the unsteady Navier-Stokes with perturbed boundary conditions. They applied this algorithm to the study of the plane Poiseuille flow, managing to reproduce the threshold predicted by Orszag (1971) of $Re_c = 5772$. An improved version of their algorithm was used in the detection of Hopf bifurcation in different geometries (Fortin *et al.*, 1997). Cliffe *et al.* (2012) implemented an error estimator within their linear stability code, allowing them to refine their meshes according to stability results. They applied this method to several examples, reproducing the critical Reynolds number published by Sherwin and Blackburn (2005) for their stenosis.

2.11.1 Example

The previous method was implemented in a Matlab/Octave routine as a computational example[7]. In this case, the matrix $\mathbf{A}$ is constructed with all the elements in its diagonal, according to

$$\mathbf{A}_{ii} = -i/2.$$

Thus, its eigenvalues and eigenvectors are already known *a priori*:

$$\lambda_i = -i/2 \qquad \varphi_{ij} = \delta_{ij}.$$

An implicit second-order backward differentiation formula (BDF) was used for the time filtering stage, with the first time step computed through a first-order BDF. The orthonormalization was performed using a modified Gram-Schmidt, to decrease the truncation errors introduced during the projections (Daniel *et al.*, 1976; Saad, 1980). The time integration parameters are critical, even with a matrix with a simple structure like this one. The combination and interaction of modes that grows and decay at different rates using BDF methods was studied by Stewart (1990), setting the limitations to high-order schemes. However, in this case a second-order scheme is used and the numerical convergence of the time integration is less critical. But still, an incorrect selection of the time-step size and the total time of filtration will cause wrong results to the Arnoldi algorithm.

The Arnoldi algorithm converges faster to the leading eigenvalues, but the converge rate to the other requested eigenvalues is slower. Hence, it is a common practice to compute a larger number of eigenvalues than the actual sough number, to use the extra values as an error buffer (Lehoucq *et al.*, 1998; Tuckerman and Barkley, 2000). In the present example, the four leading eigenvalues are sought. Therefore, the method is assembled to compute twice as many eigenvalues and eigenvectors ($k = 8$), but only the first four are reported and used in the computation of the errors and convergence residue.

Assuming that the matrix $\mathbf{A}$ represents a discretized linear operator that has been already expressed in its non-dimensional form. Table 2.2 contains the first four eigenvalues for a matrix $\mathbf{A}$ of 50×50 ($m = 50$). These values were computed using a filtering time step $\Delta t_f = 0.05$ and a total filtering steps of $N_f = 70$, resulting in a filtering time $t_f = 3.5$. The time step for the construction of the Krylov base is also $\Delta t_k = 0.05$. With these parameters, the first three eigenvalues present a low level of error when compared against the real value ($\lambda_i = -i/2$), with an error of less than 0.0003%, with a larger level of error obtained for the

7. The full source code of these routines is presented in Appendix A

TABLE 2.2 Comparison of the computed eigenvalues for the example of the Arnoldi algorithm with $m = 50$, $k = 8$, $\Delta t = 0.05$ and $N_f = 70$.

i	Analytic	Numerical	$\%\epsilon_\lambda$	$\%\epsilon_\varphi$
1	$-0.500\,0$	$-0.500\,0$	$1.472\,2 \times 10^{-05}\%$	$7.001\,8 \times 10^{-03}\%$
2	$-1.000\,0$	$-1.000\,0$	$1.168\,2 \times 10^{-04}\%$	$5.505\,6 \times 10^{-02}\%$
3	$-1.500\,0$	$-1.500\,0$	$2.933\,6 \times 10^{-04}\%$	$1.406\,3 \times 10^{-01}\%$
4	$-2.000\,0$	$-2.002\,9$	$1.464\,9 \times 10^{-01}\%$	$3.929\,8 \times 10^{+00}\%$

eigenvectors. The fourth eigenvalue present a significantly deviation in both the eigenvalue and eigenvactor. To further decrease these errors, a longer filtering time t_f should have been computed. The following expressions were used to compute the errors in the third and fourth column of Table 2.2.

$$\%\epsilon_\lambda = \frac{|\lambda_i - \lambda_i^{\text{num}}|}{|\lambda_i|} \times 100$$

$$\%\epsilon_\varphi = \frac{\|\boldsymbol{\varphi}_i - \boldsymbol{\varphi}_i^{\text{num}}\|}{\|\boldsymbol{\varphi}_i\|} \times 100$$

The effect of the number of filtering steps is evident in Figure 2.19. After an initial decrease of the errors and residues for low N_f, an important increase occurs, and the errors remain high as N_f increase, until a sharp drop occurs at around $N_f = 1000$. The plateau evidenced in the curves indicates that some of the larger modes of $\mathbf{A}$ have not decayed completely and indeed have an effect in the time integration of the operator 2.23, a manifestation of the transient growth phenomenon in this simple problem. The values reported in Figure 2.19 were computed using the following expressions

$$\epsilon_\lambda^{\max} = \max(\epsilon_\lambda) = \max\left(\frac{|\lambda_i - \lambda_i^{\text{num}}|}{|\lambda_i|}\right) \qquad \text{for } i = 1 \ldots k$$

$$\epsilon_\varphi^{\max} = \max(\epsilon_\varphi) = \max\left(\frac{\|\boldsymbol{\varphi}_i - \boldsymbol{\varphi}_i^{\text{num}}\|}{\|\boldsymbol{\varphi}_i\|}\right) \qquad \text{for } i = 1 \ldots k$$

$$R_\lambda^{\max} = \max\left(\frac{\left|\lambda_i^k - \lambda_i^{k-1}\right|}{0.5\left|\lambda_i^k - \lambda_i^{k-1}\right|}\right) \qquad \text{for } i = 2 \ldots k$$

$$R_\lambda^{\max} = \max\left(\frac{\left\|\boldsymbol{\varphi}_i^k - \boldsymbol{\varphi}_i^{k-1}\right\|}{0.5\left\|\boldsymbol{\varphi}_i^k - \boldsymbol{\varphi}_i^{k-1}\right\|}\right) \qquad \text{for } i = 2 \ldots k$$

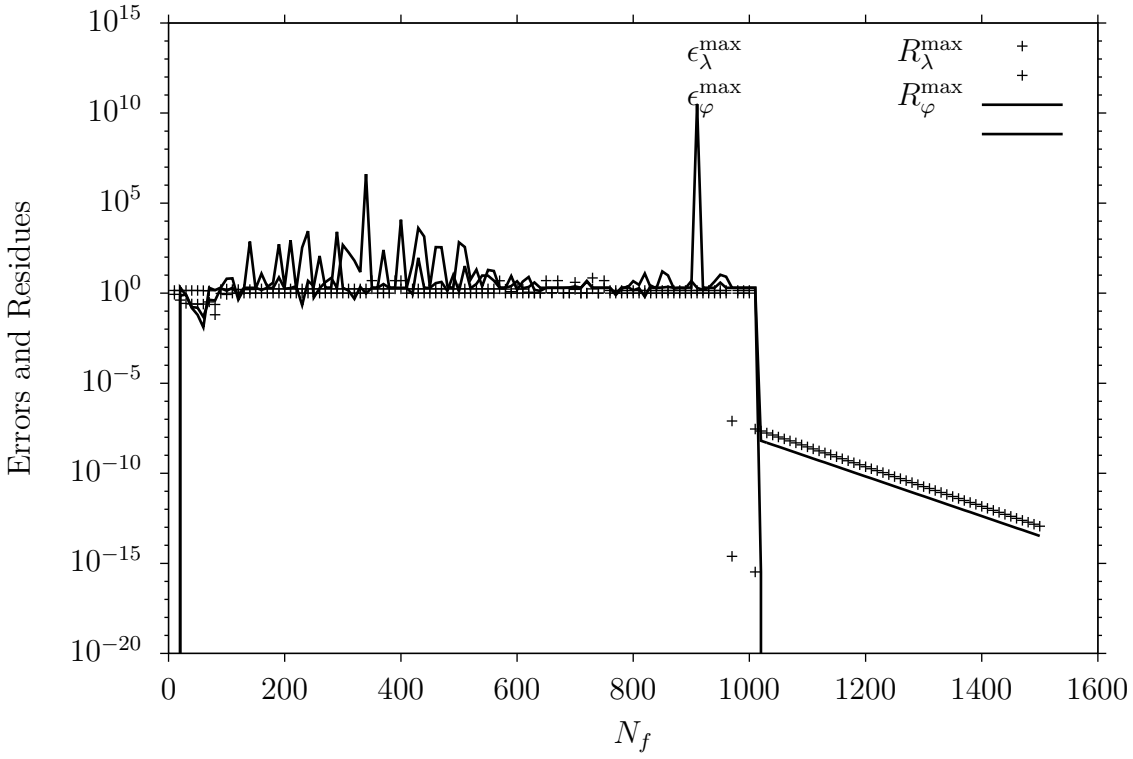

FIGURE 2.19 Influence of the number of filtering steps over the computed eigenvalues and eigenvectors. Results computed using $m = 50$, $k = 8$, $\Delta t = 0.05$, and $10 < N_f < 1500$.

2.11.2 Another example

The previous example was particularly simple due to the diagonal structure of the matrix $\mathbf{A}$. Indeed, in the formulation of the BDF operators for time integration there are terms of the following form

$$\begin{aligned} (\mathbf{I} - \Delta t\mathbf{A})\,\mathbf{x}^{[k]} &= \mathbf{x}^{[k-1]} && \text{for BDF1} \\ \left(\mathbf{I} - \frac{2}{3}\Delta t\mathbf{A}\right)\mathbf{x}^{[k]} &= \frac{4}{3}\mathbf{x}^{[k-1]} - \frac{1}{3}\mathbf{x}^{[k-2]} && \text{for BDF2,} \end{aligned}$$

and given that $\mathbf{A}$ is diagonal, the equations for the components of $\mathbf{x}$ at the step k are fully decoupled and no matrix inversion is required.

However, the BDF routines included in Appendix A are able to handle more complex matrices, solving the previous system through LU factorization [8]. Through the use of rotation matrices it is possible to modify the matrix $\mathbf{A}$ without changing its eigenvalues. The generation of a random rotation matrix of dimension m could be tackled with several elaborate techniques (Diaconis and Shahshahani, 1987; León *et al.*, 2006). However, a more direct way is using the orthogonality property. A rotation matrix $\mathbf{Q}$ is indeed an orthogonal matrix whose determinant is positive, in order to conserve the orientation of the coordinate system.

$$\begin{aligned} \|\mathbf{u}\|^2 &= \mathbf{u}^T\mathbf{u} && \text{given a vector } \mathbf{u} \\ &= (\mathbf{Q}\mathbf{u})^T(\mathbf{Q}\mathbf{u}) && \text{the rotation } \mathbf{Q} \text{ conserves its length} \\ &= \mathbf{u}^T\mathbf{Q}^T\mathbf{Q}\mathbf{u} \rightarrow \mathbf{Q}^T\mathbf{Q} = \mathbf{I} \end{aligned}$$

In Matlab, a random rotation matrix $\mathbf{Q}$ could be constructed from the QR factorization of a random matrix, changing the sign of a few of its entries in order to obtain a positive determinant. The algorithm to construct this rotation matrix in presented in Section A.1 of Appendix A and it has the following form

$$\mathbf{Q}_{[m\times m]} = \left(\begin{array}{c|c} \mathbf{Q}_{[p\times p]} & \mathbf{0}_{[p\times(m-p)]} \\ \hline \mathbf{0}_{[(m-p)\times p]} & \mathbf{I}_{[(m-p)\times(m-p)]} \end{array}\right),$$

where $\{p \in \mathbb{N} : 0 < p < m\}$. With this transformation, a new rotated matrix $\mathbf{A}'$ is constructed, with eigenvalues λ' equal to the original λ of $\mathbf{A}$ and whose eigenvectors $\boldsymbol{\varphi}'$ could be compared

8. The factorization is done using the internal Matlab function `lu`, which itself calls the library UMFPACK (Davis, 2004).

TABLE 2.3 Comparison of the computed eigenvalues for the example of the Arnoldi algorithm with the rotated matrix with $m = 50$, $k = 8$, $\Delta t = 0.05$ and $N_f = 70$ The rotation matrix used had a $p = 3m/4$.

i	Analytic	Numerical	$\%\epsilon_\lambda$	$\%\epsilon_\varphi$
1	$-0.500\,0$	$-0.452\,9$	$9.417\,9 \times 10^{+00}\%$	$1.246\,3 \times 10^{+01}\%$
2	$-1.000\,0$	$-0.984\,8$	$1.522\,2 \times 10^{+00}\%$	$1.191\,0 \times 10^{+01}\%$
3	$-1.500\,0$	$-1.500\,1$	$8.585\,7 \times 10^{-03}\%$	$8.307\,4 \times 10^{-01}\%$
4	$-2.000\,0$	$-2.000\,1$	$2.677\,9 \times 10^{-03}\%$	$6.315\,2 \times 10^{-01}\%$

against the original set $\boldsymbol{\varphi}$ through the rotation matrix.

$$\begin{aligned} \mathbf{A}' &= \mathbf{Q}^T\mathbf{A}\mathbf{Q} \\ \mathbf{A}'\boldsymbol{\varphi}' &= \lambda'\boldsymbol{\varphi}' \\ \lambda' = \lambda \qquad &\text{and} \qquad \boldsymbol{\varphi}' = \mathbf{Q}^T\boldsymbol{\varphi}. \end{aligned}$$

With this transformation, the new matrix $\mathbf{A}'$ becomes more dense, increasing the difficulty and the computational demands for the Arnoldi algorithm in this case. The results with the same parameters used in the diagonal example are presented in Table 2.3 using a $\mathbf{Q}$ matrix that affects the first 75% of the rows and columns of $\mathbf{A}$ ($p = \frac{3}{4}m$). Higher values of p were tested, decreasing the convergence of the results. The goal of this example is present the method with a matrix with a more complex structure than a diagonal matrix. The errors reported in Table 2.3 are significantly higher than the ones obtained for the diagonal case with the same parameters where it can be see a higher level of errors than in Table 2.2.

As in the previous example, to further decrease the errors in Table 2.3 it is necessary to increase the length of the filtering stage. Table 2.4 contains the results of this computation with $N_f = 80$ and $t_f = 4$, producing lower levels of errors in both the eigenvalues and eigenvectors than in the previous results.

The decrease in the quality of the convergence rate for the rotated matrix $\mathbf{A}'$ is evident in Figure 2.20, where the effect of the number of filtering steps N_f is evaluated leaving the time step fixed at $\Delta t = 0.05$. In contrast with Figure 2.19, where a sharp drop appears at around $N_f = 1000$, here the errors and residues increase and remain high up to $N_f = 10000$. It is unlikely that correct results would be obtained if further filtering steps were computed, because the components of the vector obtained after this long integration are all fairly small and are below the error margin of the BDF methods. Moreover, the error associated with the modified Gram-Schmidt algorithm and the normalization of vectors with such small

TABLE 2.4 Comparison of the computed eigenvalues for the example of the Arnoldi algorithm with the rotated matrix with $m = 50$, $k = 8$, $\Delta t = 0.05$ and $N_f = 80$ The rotation matrix had a $p = 3m/4$.

i	Analytic	Numerical	$\%\epsilon_\lambda$	$\%\epsilon_\varphi$
1	$-0.500\,0$	$-0.500\,0$	$4.634\,4 \times 10^{-03}\%$	$1.610\,4 \times 10^{-01}\%$
2	$-1.000\,0$	$-1.000\,0$	$1.846\,2 \times 10^{-05}\%$	$2.748\,6 \times 10^{-02}\%$
3	$-1.500\,0$	$-1.500\,0$	$3.825\,7 \times 10^{-05}\%$	$6.796\,8 \times 10^{-02}\%$
4	$-2.000\,0$	$-2.000\,1$	$3.864\,4 \times 10^{-03}\%$	$6.786\,9 \times 10^{-01}\%$

components are additional obstacles to obtain an actual orthogonal base. Certainly, the dense structure of $\mathbf{A}'$ puts this method outside its intended scope of sparse matrix. And for this case, more sophisticated computational methods are required, like the ones implemented inside the library ARPACK.

The goal of these examples section was presenting the capabilities of the Arnoldi algorithm and show how it is able to compute eigenvalues and eigenvectors. For practical problems, further improvements are necessary in the Arnoldi algorithm in order to tackle more general problems. For example, Goldhirsch *et al.* (1987) proposes techniques that allow to monitor dynamically if the Krylov subspace base needs to be increased due to eigenvalues with repeated multiplicity and to avoid splitting a complex pair. No attempt was made to implements these techniques in the Matlab code presented in Appendix A. The common approach is the use of external computational libraries specialized in eigenvalues and eigenvectors. Probably the one with more extended use is ARPACK (Lehoucq *et al.*, 1998). In fact, the computation of eigenpairs in Matlab and Octave uses this library for sparse matrices [9]. The following section explains the basic usage of the ARPACK library.

2.11.3 Introduction to ARPACK

The numerical methods used by the ARPACK library (Lehoucq *et al.*, 1998) is quite similar to the one presented in this section. ARPACK also uses the block power method of the Arnoldi algorithm to construct the Krylov subspace, using the matrix $\mathbf{A}$ in an implicit manner through its effect on a vector. It also performs the orthonormalization of the base each time a vector is added. The factorization of the Hessenberg matrix is computed using the QR method.

Once again, for a given matrix $\mathbf{A}$, the algorithm of ARPACK will compute its dominant

9. Implemented under the command `eigs`.

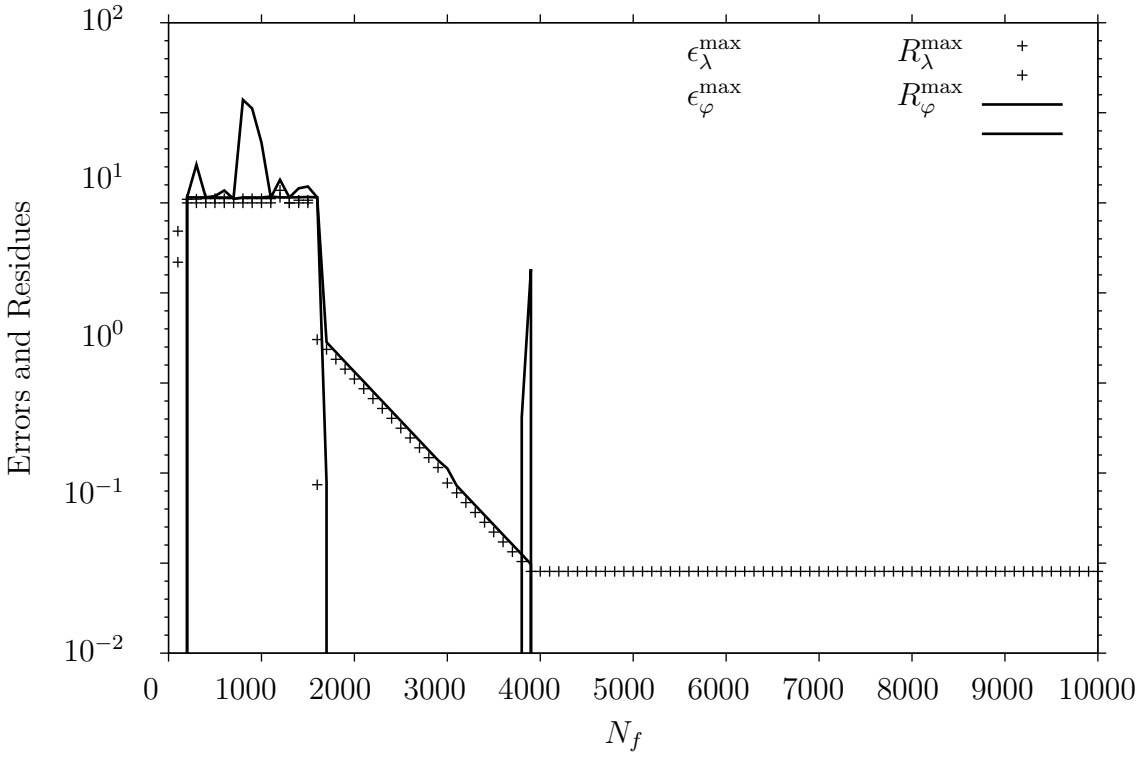

FIGURE 2.20 Influence of the number of filtering steps over the computed eigenvalues and eigenvectors with the rotated matrix. The results were computed using $m = 50$, $k = 8$, $\Delta t = 0.05$, and $100 < N_f < 10000$.

eigenvalues. However, it provides options to discriminate the type of eigenvalues sought, which avoids the explicit use of exponential transformations, time integrations or preconditioners, as in the original methodology of Tuckerman and Barkley. ARPACK's approach is based on the internal transformations of the system matrix according to Saad (1984), using Tchebyshev polynomials to resolve for the leading eigenvalues, *i.e.* those with the largest real part, and also provides similar transformations that allows it to solve for eigenvalues with the smallest real part or the smallest module.

The most useful feature of ARPACK is that, being based on the Arnoldi algorithm, it allows the solution of eigenvalue problems in an implicit manner, without working over the matrices but instead using the effect of these matrices over vectors provided by the ARPACK algorithm. In general, ARPACK is able to solve problems of the following form

$$\mathbf{A}\mathbf{x} = \lambda \mathbf{M}\mathbf{x}, \tag{2.25}$$

where $\mathbf{A}$ and $\mathbf{M}$ could be real or complex square matrices. ARPACK provides techniques to reduce or transform this generalized problem into the standard form

$$\mathbf{A}\mathbf{x} = \lambda \mathbf{x}.$$

Among the several techniques available for the solution of (2.25), the most general is the so-called *shift-inverse* transformation

$$\left(\mathbf{A} - \sigma \mathbf{M}\right)^{-1} \mathbf{M}\mathbf{x} = \nu \mathbf{x} \qquad \text{where} \quad \nu = \frac{1}{\lambda - \sigma} \quad \text{for } \sigma \neq \lambda, \tag{2.26}$$

useful for finding eigenvalues in a different region of the complex plane. Indeed, the dominant eigenvalues ν of the transformed matrix $\left(\mathbf{A} - \sigma \mathbf{M}\right)^{-1} \mathbf{M}$ correspond to the eigenvalues λ of the original problem (2.25) that are closer to the the shift σ. In other words, it solves for the less dominant eigenvalues in a complex plane where the origin is in σ. In most practical problems $\sigma \in \mathbb{R}$, which avoid unnecessary complex arithmetic when $\mathbf{A}$ and $\mathbf{M}$ are both real, but complex σ are also possible (Parlett and Saad, 1987). According to Lehoucq *et al.* (1998), the enhanced local convergence provided by the shift-inverse method is useful even in regular eigenvalue problems with $\mathbf{M} = \mathbf{I}$. The main difficulty is that ARPACK will require an external factorization method to compute the inverse of $\left(\mathbf{A} - \sigma \mathbf{M}\right)^{-1}$.

When no shift is of interest ($\sigma = 0$), ARPACK tackles the generalized eigenvalue problem (2.25) with different methods. When $\mathbf{M}$ is a well-conditioned Hermitian positive definite matrix, the computation of a Cholesky factorization is possible. Then $\mathbf{M} = \mathbf{L}\mathbf{L}^H$, where $\mathbf{L}$ is a

lower triangular matrix and H denotes the conjugate transpose operator. In this case, the generalized problem (2.25) takes the following form after transformation

$$\mathbf{A}\mathbf{x} = \lambda\mathbf{M}\mathbf{x} \quad \rightarrow \quad \left(\mathbf{L}^{-1}\mathbf{A}\mathbf{L}^{-H}\right)\mathbf{y} = \lambda\mathbf{y}, \tag{2.27}$$

and the eigenvalues of the original problem are recovered from the solution of $\mathbf{L}^{H}\mathbf{x} = \mathbf{y}$. In this case it is necessary to provide the Cholesky factorization of $\mathbf{M}$ and the matrix-vector products are evaluated taking advantage of the triangular structure of $\mathbf{L}$. If $\mathbf{M}$ is not Hermitian positive definite, it is more convenient to do a direct transformation toward the standard form (2.11.3) multiplying both sides of Equation (2.25) by $\mathbf{M}^{-1}$

$$\begin{aligned} \mathbf{A}\mathbf{x} &= \lambda\mathbf{M}\mathbf{x} \qquad \times \mathbf{M}^{-1} \text{ on both sides} \\ \mathbf{M}^{-1}\mathbf{A}\mathbf{x} &= \lambda\mathbf{M}^{-1}\mathbf{M}\mathbf{x} \\ \mathbf{M}^{-1}\mathbf{A}\mathbf{x} &= \lambda\mathbf{x}, \end{aligned}$$

known as the *inverse* transformation within ARPACK. In this case either the inverse of $\mathbf{M}$ or an appropriate factorization for it has to be provided. But if $\mathbf{M}$ is ill-conditioned, the shift-inverse transformation may provide better results.

The case when $\mathbf{M} = \mathbf{I}$ translates directly into the standard eigenvalue problem. All the previously mentioned methods have the goal to transform the problem into this case, where ARPACK only needs a method to perform the matrix-vector product in order to construct the Krylov base. Indeed, the additional requirements for matrix inversions and factorization were necessary to compute the matrix-vector product with the transformed matrices. To solve Equation (2.11.3), ARPACK uses an algorithm with a similar structure to the one used for the examples reviewed in Section 2.11.1. The actual method is known as the Implicitly Restarted Arnoldi Method (IRAM). The implicit restarted part refers to interrupt the generation of the Krylov subspace base everytime a new vector is going to be added, and multiply it by a transformation that helps to filter the unwanted eigenpairs. It is based in the work by Saad (1984). The full details of the IRAM are presented in (Lehoucq *et al.*, 1998, Chap. 4). The specific details of the implementation of the stability analysis method within ARPACK are presented in the next Chapter in Section 3.3.

CHAPTER 3 NUMERICAL COMPUTATION OF LINEAR STABILITY

3.1 Introduction

This section presents the method used within this research for the study of stability in steady solutions, along with its implementation within a finite element code and the solution of the eigenvalue problem using the external library ARPACK (Lehoucq *et al.*, 1998), along with a few examples of the computation of stability in fluid flow. The limitations of the methodology and possible improvements are also addressed.

3.2 Variational formulation

First, considering a steady-state velocity field $\mathbf{U}$, solution to the Navier-Stokes equations (2.7), the problem (2.10) is written as

$$\rho\frac{\partial \mathbf{u}'}{\partial t} + \rho\left(\left(\mathbf{u}'\cdot\nabla\right)\mathbf{U} + \left(\mathbf{U}\cdot\nabla\right)\mathbf{u}'\right) = \nabla\cdot\left(-p'\mathbf{I} + \mu\left(\nabla\mathbf{u}' + \nabla^T\mathbf{u}'\right)\right)$$
$$\nabla\cdot\mathbf{u}' = 0,$$

with boundary conditions

$$\Gamma_D : \mathbf{u}' = 0$$
$$\Gamma_N : \boldsymbol{\sigma}(p', \mathbf{u}')\cdot\hat{\mathbf{n}} = 0.$$

Now, the variational formulation for the previous problem is written as follows

$$\int_\Omega \rho\frac{\partial \mathbf{u}'}{\partial t}\cdot\mathbf{w}\, d\Omega + \int_\Omega \rho\left[\left(\mathbf{u}'\cdot\nabla\right)\mathbf{U} + \left(\mathbf{U}\cdot\nabla\right)\mathbf{u}'\right]\cdot\mathbf{w}\, d\Omega$$
$$- \int_\Omega p'\nabla\cdot\mathbf{w}\, d\Omega + \int_\Omega \mu\left(\nabla\mathbf{u}' + \nabla^T\mathbf{u}'\right) : \nabla\mathbf{w}\, d\Omega = 0 \tag{3.1a}$$
$$- \int_\Omega q\nabla\cdot\mathbf{u}'\, d\Omega = 0, \tag{3.1b}$$

with $\mathbf{w} \in H^1_{\Gamma_D}(\Omega)$, $q \in L^2(\Omega)$. It is clear that this problem has an identically zero trivial solution ($\mathbf{u}' = \mathbf{0}$). However, here the interest is to find non-null solutions. Three different approaches are discussed.

3.2.1 Implicit matrix

In it most basic form, the variational problem (3.1) could be discretized into a time-dependent finite element solution. The degrees of freedom are organized in a single vector $\mathbf{W}$ and the problem implicitly reduces to

$$\frac{d\mathbf{W}}{dt} = \mathbf{A_W}\mathbf{W},$$

where the boundary conditions are already part of the assembled system. The matrix-vector product $\mathbf{A_W}\mathbf{W}$ is understood as the solution of the time dependent finite element problem after a certain time-step using $\mathbf{W}$ as initial condition. With the initial condition to this problem is the perturbation $\mathbf{W}_0$, the solution after a time Δt could then be written as

$$W(\Delta t) = \mathbf{W}_0 \ \exp\left(\mathbf{A_W}\Delta t\right).$$

It is possible to implement this formulation within ARPACK, computing the solution of the finite element problem with an external code, and inserting the resulting vector in ARPACK, to construct the Krylov subspace base internally and complete all the steps of the Arnoldi algorithm, and each time it requires a matrix-vector product, ARPACK would need to call the finite element code to solve (3.1) using the $\mathbf{W}_0$ as initial condition.

The computational cost of these external matrix-vector product represents the larger fraction of the total cost of the method. But the main issue with this approach is the dependance of the results with the time integration parameters, a fact that was already mentioned in the examples of Section 2.11.1. This approach uses the same method proposed by Goldhirsch *et al.* (1987), performing the exponential transformation as the time integration progress. Hence, the eigenvalues with the largest module of $\mathbf{A_W}$ are the ones the largest real part of the problem (3.1). The implementation of this method within ARPACK is detailed in Section 3.3, along with the issues that arise due to the dependence on the time-integration parameters.

3.2.2 Method of normal modes

For this method, the perturbation variables $\mathbf{u}'$ and p' are decomposed in their normal mode representation according to Equation (2.11), respectively $\mathbf{u}' = e^{\lambda t}\hat{\mathbf{u}}$ and $p' = e^{\lambda t}\hat{p}$, and these

are introduced into Equation 3.1 to obtain a continue representation of the eigenvalue problem

$$\begin{aligned}\lambda \int_\Omega \rho \hat{\mathbf{u}} \cdot \mathbf{w}\, d\Omega + \int_\Omega \rho \left[(\hat{\mathbf{u}} \cdot \nabla)\, \mathbf{U} + (\mathbf{U} \cdot \nabla)\, \hat{\mathbf{u}} \right] \cdot \mathbf{w}\, d\Omega \\ - \int_\Omega \hat{p} \nabla \cdot \mathbf{w}\, d\Omega + \int_\Omega \mu \left(\nabla \hat{\mathbf{u}} + \nabla^T \hat{\mathbf{u}} \right) : \nabla \mathbf{w}\, d\Omega = 0 \\ - \int_\Omega q \nabla \cdot \hat{\mathbf{u}}\, d\Omega = 0.\end{aligned}$$

The previous system is then discretized by the finite element method, and its degrees of freedom $\hat{\mathbf{u}}$ and $\hat{p}$ are regrouped into the vectors $\mathbf{X}$ and $\hat{\mathbf{P}}$, respectively

$$\begin{aligned}\hat{\mathbf{u}} &= \sum \boldsymbol{\phi}_i X_i \\ \hat{p} &= \sum \gamma_i \hat{P}_i,\end{aligned}$$

and the system takes the following form

$$\begin{aligned}\mathbf{A}\mathbf{X} + \mathbf{B}^T \hat{\mathbf{P}} &= -\lambda \mathbf{M} \mathbf{X} \\ \mathbf{B}\mathbf{X} &= \mathbf{0},\end{aligned} \tag{3.2}$$

or in an analog manner

$$\underbrace{\begin{pmatrix} \mathbf{A} & \mathbf{B}^T \\ \mathbf{B} & 0 \end{pmatrix}}_{\hat{\mathbf{A}}} \underbrace{\begin{pmatrix} \mathbf{X} \\ \hat{\mathbf{P}} \end{pmatrix}}_{\mathbf{Z}} = -\lambda \underbrace{\begin{pmatrix} \mathbf{M} & 0 \\ 0 & 0 \end{pmatrix}}_{\hat{\mathbf{M}}} \underbrace{\begin{pmatrix} \mathbf{X} \\ \hat{\mathbf{P}} \end{pmatrix}}_{\mathbf{Z}}$$

$$\hat{\mathbf{A}}\mathbf{Z} = -\lambda \hat{\mathbf{M}} \mathbf{Z}, \tag{3.3}$$

where the matrices are given by

$$\begin{aligned}\mathbf{A}_{ij} &= \int_\Omega \rho \left[(\mathbf{U} \cdot \nabla)\, \boldsymbol{\phi}_j + \left(\boldsymbol{\phi}_j \cdot \nabla \right) \mathbf{U} \right] \cdot \boldsymbol{\phi}_i\, d\Omega + \int_\Omega \mu \left(\nabla \boldsymbol{\phi}_j + \nabla^T \boldsymbol{\phi}_j \right) : \nabla \boldsymbol{\phi}_i\, d\Omega \\ \mathbf{B}^T_{ij} &= -\int_\Omega \gamma_j \nabla \cdot \boldsymbol{\phi}_i\, d\Omega \\ \mathbf{B}_{ij} &= -\int_\Omega \gamma_i \nabla \cdot \boldsymbol{\phi}_j\, d\Omega \\ \mathbf{M}_{ij} &= \int_\Omega \rho \boldsymbol{\phi}_i \cdot \boldsymbol{\phi}_j\, d\Omega.\end{aligned} \tag{3.4}$$

Equation (3.3) represents a generalized algebraic eigenvalue problem. The minus sign on the right hand side could be incorporated into the definition of $\mathbf{M}$, but in that case it would not be

a positive definite matrix. And although $\mathbf{M}$ could be Cholesky factorized into $\mathbf{M} = \mathbf{L}\mathbf{L}^H$, $\hat{\mathbf{M}}$ is ill conditioned and the transformation described in Equation (2.27) could not be performed. The inverse method using $\hat{\mathbf{M}}^{-1}\hat{\mathbf{A}}$ or the shift-inverse with $\left(\hat{\mathbf{A}} - \sigma\hat{\mathbf{M}}\right)^{-1}\hat{\mathbf{M}}$ will also present present problems due to the block of zeros in both $\hat{\mathbf{A}}$ and $\hat{\mathbf{M}}$. Thus, the solution methods proposed by ARPACK will have issues with this approach. Hence, an alternative method is proposed in the next section.

3.2.3 Modified matrix-vector product

As in the previous method, the analysis starts with the variational formulation of Equation (3.1). Without any assumption regarding the normal modes, this system is discretized by the finite element method. Its degrees of freedom for the variables $\mathbf{u}'$ and p' are grouped this time into the vectors $\hat{\mathbf{U}}$ and $\check{\mathbf{P}}$, respectively:

$$\begin{aligned} \mathbf{M}\frac{d\hat{\mathbf{U}}}{dt} + \mathbf{A}\hat{\mathbf{U}} + \mathbf{B}^T\check{\mathbf{P}} &= \mathbf{0} \\ \mathbf{B}\hat{\mathbf{U}} &= \mathbf{0}, \end{aligned} \tag{3.5}$$

with initial conditions

$$\begin{aligned} \hat{\mathbf{U}}(t=0) &= \hat{\mathbf{U}}_0 \\ \mathbf{B}\hat{\mathbf{U}}_0 &= \mathbf{0}. \end{aligned} \tag{3.6}$$

The initial condition $\hat{\mathbf{U}}_0$ represents a perturbation introduced into the steady solution $\mathbf{U}$. The goal is the description of the evolution of the perturbed field $\hat{\mathbf{U}}(t)$ as a function of the initial perturbation $\hat{\mathbf{U}}_0$, which requires the elimination of the pressure from the equations. Several methods are available for this step (Tuckerman and Barkley, 2000; Sherwin and Blackburn, 2005), but a different approach is proposed here, through an algebraic manipulation. Multiplying the equation corresponding to the momentum balance by $\mathbf{M}^{-1}$ gives

$$\frac{d\hat{\mathbf{U}}}{dt} + \mathbf{M}^{-1}\mathbf{A}\hat{\mathbf{U}} + \mathbf{M}^{-1}\mathbf{B}^T\check{\mathbf{P}} = \mathbf{0}. \tag{3.7}$$

The previous operation is possible because $\mathbf{M}$ is symmetric and positive-definite, hence its inverse exists and it is also positive-definite. The mass conservation equation also holds its equality after differentiation in time:

$$\mathbf{B}\frac{d\hat{\mathbf{U}}}{dt} = \mathbf{0}.$$

Then, multiplying Equation (3.7) by $\mathbf{B}$

$$\begin{aligned}
\overbrace{\mathbf{B}\frac{d\hat{\mathbf{U}}}{dt}}^{=0} + \mathbf{B}\mathbf{M}^{-1}\mathbf{A}\hat{\mathbf{U}} + \mathbf{B}\mathbf{M}^{-1}\mathbf{B}^T\check{\mathbf{P}} &= \mathbf{0} \\
\mathbf{B}\mathbf{M}^{-1}\mathbf{B}^T\check{\mathbf{P}} &= -\mathbf{B}\mathbf{M}^{-1}\mathbf{A}\hat{\mathbf{U}} \\
\check{\mathbf{P}} &= -\left(\mathbf{B}\mathbf{M}^{-1}\mathbf{B}^T\right)^{-1}\left(\mathbf{B}\mathbf{M}^{-1}\mathbf{A}\right)\hat{\mathbf{U}}. \qquad (3.8)
\end{aligned}$$

The product $\left(\mathbf{B}\mathbf{M}^{-1}\mathbf{B}^T\right)$ is invertible because because $\mathbf{M}^{-1}$ is positive-definite. Hence, the previous product will represent a positive-semidefinite matrix (Horn and Johnson, 2012, Obs. 7.1.8). But $\mathbf{B}$ and $\mathbf{B}^T$ comes from a well-posed finite element discretization, with a formulation that satisfies the inf-sup or LBB condition (Ladyzhenskaya-Babuška-Brezzi Babuška (1973); Brezzi (1974); Ciarlet and Lions (1991)). Therefore, $\mathbf{B}^T$ satisfy the conditions stated by Horn and Johnson [1] and $\left(\mathbf{B}\mathbf{M}^{-1}\mathbf{B}^T\right)$ will be positive-definite and invertible.

Finally, substituting (3.8) into Equation (3.7):

$$\begin{aligned}
\frac{d\hat{\mathbf{U}}}{dt} + \mathbf{M}^{-1}\mathbf{A}\hat{\mathbf{U}} - \mathbf{M}^{-1}\mathbf{B}^T\left(\mathbf{B}\mathbf{M}^{-1}\mathbf{B}^T\right)^{-1}\left(\mathbf{B}\mathbf{M}^{-1}\mathbf{A}\right)\hat{\mathbf{U}} &= \mathbf{0} \\
\frac{d\hat{\mathbf{U}}}{dt} + \left[\mathbf{M}^{-1}\mathbf{A} - \mathbf{M}^{-1}\mathbf{B}^T\left(\mathbf{B}\mathbf{M}^{-1}\mathbf{B}^T\right)^{-1}\left(\mathbf{B}\mathbf{M}^{-1}\mathbf{A}\right)\right]\hat{\mathbf{U}} &= \mathbf{0}.
\end{aligned}$$

The solution to the previous ODE is simply:

$$\hat{\mathbf{U}}(t) = \exp\left[-\left(\mathbf{M}^{-1}\mathbf{A} - \mathbf{M}^{-1}\mathbf{B}^T\left(\mathbf{B}\mathbf{M}^{-1}\mathbf{B}^T\right)^{-1}\left(\mathbf{B}\mathbf{M}^{-1}\mathbf{A}\right)\right)t\right]\ \hat{\mathbf{U}}_0.$$

This last relation implies that the evolution of $\hat{\mathbf{U}}$ is governed by the eigenvalues of the following matrix:

$$\tilde{\mathbf{A}} = \left(\mathbf{M}^{-1}\mathbf{A}\right) - \left(\mathbf{M}^{-1}\mathbf{B}^T\right)\left(\mathbf{B}\mathbf{M}^{-1}\mathbf{B}^T\right)^{-1}\left(\mathbf{B}\mathbf{M}^{-1}\mathbf{A}\right),$$

where the eigenvalue problem is written as

$$\tilde{\mathbf{A}}\mathbf{X} = \lambda\mathbf{X} \qquad (3.9)$$

This problem could be solved iteratively through ARPACK, using its regular mode, according to the description given in Section 2.11.3. The associated computational cost of this problem would be in the calculation of the matrix-vector product $\tilde{\mathbf{A}}\mathbf{X}$.

Proposition 3.2.1 (Alternative approach for product $\tilde{\mathbf{A}}\mathbf{X}$)**.** *The solution* $\mathbf{Y}$ *of the following*

1. $\mathbf{B}^T$ should be a full rank matrix.

system

$$\begin{aligned} \mathbf{M}\mathbf{Y} + \mathbf{B}^T\check{\mathbf{P}} &= \mathbf{A}\mathbf{X} \\ \mathbf{B}\mathbf{Y} &= \mathbf{0}, \end{aligned} \tag{3.10}$$

is equivalent to the matrix-vector product $\tilde{\mathbf{A}}\mathbf{X}$.

Proof. The matrix $\mathbf{M}$ in Equation (3.10) is a symmetric and positive-definite matrix. Hence, its solution process is simpler than solving the problem (3.3), given the nature of the matrices involved.

Multiplying the first Equation (3.10) by $\mathbf{M}^{-1}$ gives

$$\mathbf{Y} + \mathbf{M}^{-1}\mathbf{B}^T\check{\mathbf{P}} = \mathbf{M}^{-1}\mathbf{A}\mathbf{X}.$$

Then, multiplying it by $\mathbf{B}$:

$$\overbrace{\mathbf{B}\mathbf{Y}}^{=0} + \mathbf{B}\mathbf{M}^{-1}\mathbf{B}^T\check{\mathbf{P}} = \mathbf{B}\mathbf{M}^{-1}\mathbf{A}\mathbf{X}.$$

Isolating the pressure:

$$\check{\mathbf{P}} = \left(\mathbf{B}\mathbf{M}^{-1}\mathbf{B}^T\right)^{-1}\left(\mathbf{B}\mathbf{M}^{-1}\mathbf{A}\right)\mathbf{X}.$$

This relation, inserted into the first equation gives:

$$\mathbf{Y} = \left(\mathbf{M}^{-1}\mathbf{A}\right)\mathbf{X} - \left(\mathrm{M}^{-1}\mathrm{B}^T\right)\left(\mathbf{B}\mathbf{M}^{-1}\mathbf{B}^T\right)^{-1}\left(\mathbf{B}\mathbf{M}^{-1}\mathbf{A}\right)\mathbf{X} = \tilde{\mathbf{A}}\mathbf{X}. \quad \square$$

Remark 3.2.1. *The matrix* $\tilde{\mathbf{A}}$ *comes from the time integration of Equation* (3.7)*. Then, as explained in Section 2.11, the solution of the eigenvalues of* $\tilde{\mathbf{A}}$ *already includes the exponential transformation in an implicit manner, but without actually performing the time integration. Hence, the dominant eigenvalues of* $\tilde{\mathbf{A}}$ *(the ones with the largest module) are the leading eigenvalues of the original stability problem* (3.1)*,* i.e. *the ones with the largest real part, precisely those that determine the onset of instability.*

Hence, to calculate the matrix-vector product $\tilde{\mathbf{A}}\mathbf{X}$, it is necessary to resolve the system (3.10). Its solution exists and is unique (Delfour, 2012). This system has the same size of the Navier-Stokes problem, but its factorization could be computed only once and used for successive stages. For this, the Krylov subspace is built using the solution $\mathbf{Y}$ of Equation (3.10)

into his right-hand side, in place of $\mathbf{X}$, as follows:

$$\begin{aligned} \mathbf{M}\mathbf{Y}^{[i]} + \mathbf{B}^T\check{\mathbf{P}} &= \mathbf{A}\mathbf{Y}^{[i-1]} \\ \mathbf{B}\mathbf{Y}^{[i]} &= \mathbf{0}, \end{aligned} \tag{3.11}$$

for $i = 1 \cdots K$. In general, all the vectors of this space would be divergence-free, with the exception of $\mathbf{Y}^{[0]}$, which is selected arbitrarily. However, the filtering stage recomended by Goldhirsch *et al.* (1987) and implemented by Tuckerman and Barkley (2000) allows to advance this arbitrary perturbation for a determinate time, to remove the fastest decaying modes and assure that all vectors of the Krylov subspace base are divergence-free. The same principle is used by Sherwin and Blackburn (2005) in their study of the stenose. Thus, a similar stage is implemented here, solving Equation (3.11) a fixed number of times before the construction of the Krylov subspace base within the ARPACK library.

This whole method allows the computation of leading eigenvalues of steady solution without the use of time integration. That would imply that the results are not conditioned to the constraints imposed by the time integration method used, like time step size or its implicit–explicit formulation. For its solution, the discretized version of the problem (3.10) is implemented inside a finite element code,

$$\underbrace{\begin{pmatrix} \mathbf{M} & \mathbf{B}^T \\ \mathbf{B} & 0 \end{pmatrix}}_{\check{\mathbf{A}}} \underbrace{\begin{pmatrix} \mathbf{Y} \\ \check{\mathbf{P}} \end{pmatrix}}_{\mathbf{Z}} = \underbrace{\begin{pmatrix} \mathbf{A}\mathbf{X} \\ 0 \end{pmatrix}}_{\mathbf{F}}$$

$$\check{\mathbf{A}}\mathbf{Z} = \mathbf{F}, \tag{3.12}$$

which is called as a subroutine within ARPACK that takes $\mathbf{X}$ (or $\mathbf{Y}^{[i-1]}$) as an argument and returns $\mathbf{Y}$ (or $\mathbf{Y}^{[i]}$). Evidently, the finite element routine also takes as an argument the steady solution around which the equations are linearized, as shown in Equations (3.4) for the matrix coefficients, but this is transparent to ARPACK. The first time the ARPACK library calls this matrix-vector routine, the LU factorization of $\check{A}$ is computed and kept in memory, for the successive calls. This factorization is calculated with the library PARDISO (Schenk and Gärtner, 2004), which is adequate for small and medium size problems. For larger problems, the implementation of an iterative method for solving the system (3.12) like GMRES could improve the performance of the method. This is an aspect that is recommended for a future research project.

TABLE 3.1 Paramenters used for ARPACK.

Parameter	Implicit	Modified
Requested Eigenvalues	$6 < N_{ev}12$	$6 < N_{ev} < 12$
Krylov subspace	$2N_{ev}$	$2N_{ev}$
Type of Eigenvalues	Largest module	Largest module
Time step	0.01-1	-
Filtering time	5-30	-
ARPACK Mode	Regular (Mode 1)	Regular (Mode 1)
Matrix **M**	**I**	**I**
ϵ_{TOL}	10^{-10}	10^{-10}
Max IRAM iterations	600	600

3.3 Implementation within ARPACK

This section summarizes the details of the implementation of the computational routines for the solution of stability in incompressible fluids within ARPACK. The methods presented in Sections 3.2.1 and 3.2.3 are linked to the ARPACK library, in such way that ARPACK provides the input to the finite element computation, taking the output of these simulation as the results of the required matrix-vector products. ARPACK requires that the user declares the memory for the arrays that are used during the computation, along with a set of parameters that sets the solution mode, the number of eigenpairs sough and the stopping criterion, based on the tolerance at which the eigenvalues are computed and the maximum number of iterations. Table 3.1 summarized the parameters used for both methods.

The only difference between the two cases was in the time integration parameters. Indeed, the modified product method presented in Section 3.2.3 did not requires any time integration, while the implicit matrix of Section 3.2.1 requires the time-step length and the total time of initial filtration. In both cases ARPACK is indicated to look for the eigenvalues with the largest module, given that the formulation of the methods already include the exponential transformation that allows to compute the eigenvalues with the largest real part. And ARPACK is indicated to operate in its regular mode (see Section 2.11.3) according to the parameter *Mode=1* and the use of an identity matrix as right hand side matrix in the general eigenvalue problem, transforming it into an standard eigenvalue problem. The results for the modified matrix-vector product are presented in the next section, while the results for the implicit matrix method are discussed in Section 3.4.3, along with the inconveniences it presents for the current research.

3.4 Validation of the method

In order to verify the accuracy of the algorithm presented in Section 3.2.3, it was used to compute the stability of the flow regime in two different setups with already published results. The first is a two-dimensional sudden expansion, based on the work of Fearn *et al.* (1990), while the second is an axisymmetric smooth convergent–divergent section, based on the results of Sherwin and Blackburn (2005).

3.4.1 Two-dimensional sudden expansion

Fearn *et al.* (1990) evaluated a symmetric sudden expansion with 1:3 expansion ratio (see Figure 2.7b). They reported that the flow loses its symmetry at $Re = 40.45$, based on the half-width of the channel and the peak velocity at the inlet. This is equivalent to $Re = 53.93$ with the Reynolds number based on the total width and average velocity at the inlet of channel, parameters selected for non-dimensionalization in the present case.

Numerical solution

An incompressible fluid flow is assumed, due to the low-Reynolds number present within the domain. Hence, the Navier-Stokes equations (2.1) are valid. The problem is discretized through the finite element method, using quadrilateral 9-nodes elements that satisfy the inf-sup condition, providing quadratic interpolation for the velocity vectors and linear interpolation for the pressure. A similar geometry to the one used by Fearn *et al.* was built, according to the parameters defined in Figure 3.1, where it is also given a summary of the boundary conditions used. In this case, the expansion ratio of 1:3 means that $d_1/d_2 = 1/3$. For the inlet, the parabolic velocity profile corresponding to a developed Poiseuille flow was imposed as a Dirichlet boundary condition

$$\mathbf{u} = u(y) = \frac{3}{2} U_{\text{avg}} \left(1 - 4 \left(\frac{y}{d_1} \right)^2 \right) \qquad \text{on } \Gamma_D^{\text{inlet}}.$$

For the outlet, a null surface force was set, through the projection of the stress tensor, which correspond to a Neumann boundary condition

$$\boldsymbol{\sigma} \cdot \hat{\mathbf{n}} = \mathbf{0} \text{ on } \Gamma_N^{\text{outlet}}.$$

Additionally, the vertical velocity components were set to zero at the outlet, to guarantee a completely parallel velocity profile. In the remaining surfaces, a null velocity vector was

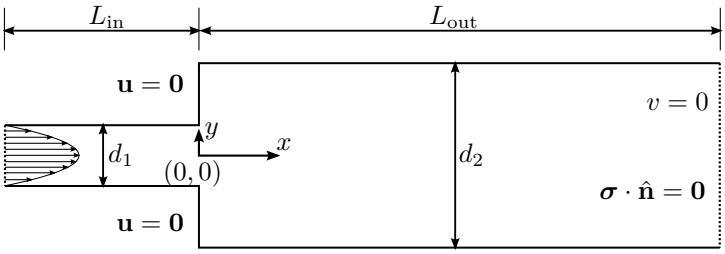

FIGURE 3.1 Geometry and boundary conditions for the planar sudden expansion studied.

imposed as Dirichlet condition

$$\mathbf{u} = \mathbf{0} \text{ on } \Gamma_D^{\text{wall}}.$$

With a value of average velocity equal to the unity and an inlet height of $d_1 = 1$, the Reynolds number definition based on the average velocity takes the form $Re = 1/\nu$. And the Reynolds number is modified decreasing the value of the viscosity ν. A steady state solution was computed at $Re = 10$, based on the average inlet velocity and the channel height d_1. Once this simulation converges, the velocity and pressure fields of this solution are used as starting point for another steady state simulation at a higher Reynolds number. This process is repeated until reaching the desired value of $Re = 100$ for this problem.

Mesh validation

For the construction of the discretized domain, two parameters were of particular relevance. The first one was the length of the outlet segment of the domain L_{out}, given that the presence of the outlet boundary condition could affect the flow upstream if it is located too close to the region of interest. The value of the inlet length L_{in} is fixed at $2d_1$, given that the velocity profile is already developed and thus, no important changes are expected in this region. The second parameter is a refinement factor denoted F_{mesh}, which controls the distribution and density of nodes along the edges of the domain. In this case the mesh was constructed to have an uniform distribution throughout the domain. Hence, a mesh $F_{\text{mesh}} = 2$ will have twice as many uniformly distributed nodes along the edges of the domain than a mesh with $F_{\text{mesh}} = 1$, while the internal nodes are defined through transfinite interpolation. Hence, a single quadrilateral element at $F_{\text{mesh}} = 1$ is split into 4 smaller quadrilaterals when $F_{\text{mesh}} = 2$, and into 16 when $F_{\text{mesh}} = 4$. Figure 3.2 depicts the mesh in the area surrounding the expansion with different values of F_{mesh}.

Two parameters are used to evaluate the velocity field of the solution computed and how it is affected by the geometric and mesh parameters L_{out} and F_{mesh}. The effect of the outlet length

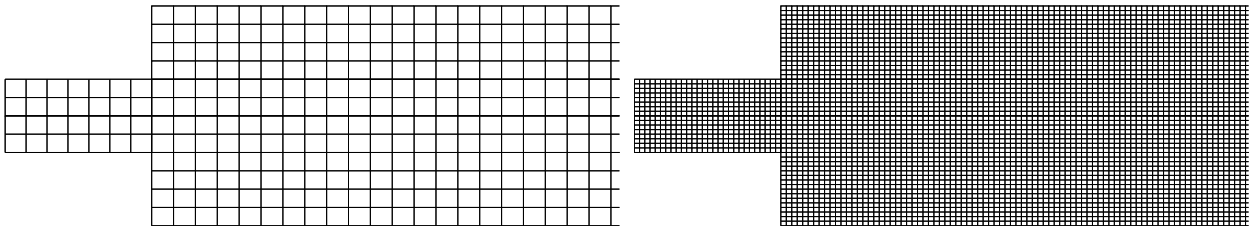

FIGURE 3.2 Mesh examples for the planar sudden expansion: (a) presents a coarse mesh with $F_{\text{mesh}} = 1.0$ while (b) is a refined one with $F_{\text{mesh}} = 4.0$.

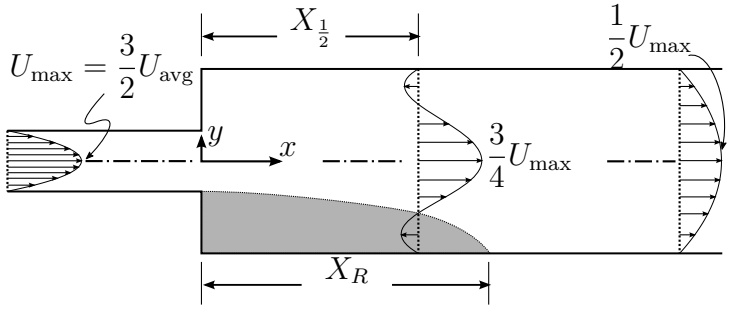

FIGURE 3.3 Definition of the half development length for the planar sudden expansion.

L_{out} is characterized through the half development length $X_{\frac{1}{2}}$, defined as the normalized distance x/d_1 at which the streamwise velocity at the centerline of the domain attain 50% of the total change between its peak value just upstream the expansion and the fully developed laminar Poiseuille velocity that will manifest in the larger section at $x \to \infty$. Equation (3.13) presents the definition of $X_{\frac{1}{2}}$, while Figure 3.3 presents a graphical sketch of its meaning.

$$X_{\frac{1}{2}}: \quad u(X_{\frac{1}{2}}d_1, y = 0) = \frac{u(x = 0, y = 0) + u(x \to \infty, y = 0)}{2}. \tag{3.13}$$

The variable $X_{\frac{1}{2}}$ defined above is more convenient than the total development length, because the computation of the latter will require domains that are too long. The refinement factor is assessed through the reattachment length, computed as the normalized distance x/d_1 at which the wall shear stress becomes zero

$$X_R: \quad \tau_{\text{wall}}(x = X_R d_1) = \mu \left.\frac{\partial u}{\partial y}\right|_{\text{wall}, x = X_R d_1} = 0. \tag{3.14}$$

Table 3.2 presents the size of the meshes used in the study of the influence of L_{out}. For this study, only L_{out} is varied, in the range $10d_1 < L_{\text{out}} < 80d_1$, while the refinement factor F_{mesh}

TABLE 3.2 Meshes used to study the influence of the downstream length L_{out} in the planar sudden expansion.

Case	Nomeclature	$\frac{L_{\text{out}}}{d_1}$	F_{mesh}	Quads	Nodes
1	$L10\_F100$	10	1.00	436	1851
2	$L20\_F100$	20	1.00	832	3501
3	$L40\_F100$	40	1.00	1636	6851
4	$L60\_F100$	60	1.00	2428	10151
5	$L80\_F100$	80	1.00	3232	13501

is kept at 1.0. Figure 3.4 shows the dependency of $X_{\frac{1}{2}}$ and X_R with the Reynolds number, where it is evident the low dispersion their values have, and for all the meshes in Table 3.2 the data points fall over the same straight line. This indicates that, at least for the current range of L_{out} studied for this geometry, both $X_{\frac{1}{2}}$ and X_R are independent of the outlet length of the domain. Also, for all the meshes, the intersection point of $Re = 0$ represents $X_{\frac{1}{2}} \simeq X_R \simeq 0$, which is logical for this geometry. Thus, $L_{\text{out}} = 40d_1$ is fixed as the outlet length of the domain for the remainder of this study.

Table 3.3 presents the size of the meshes used in the study of the influence of F_{mesh} with $L_{\text{out}} = 40d_1$. The refinement factor is varied in the range $0.25 < F_{\text{mesh}} < 5.0$. Figure 3.4 shows again the variation of X_R with the Reynolds number for all the different meshes in Table 3.3. In this case, only the reattachment length is presented, because the wall shear stress is quite sensible to the mesh resolution. The $X_{\frac{1}{2}}$ have much less dispersion, the data is not presented, for clarity in the analysis. The refinement factor has a clear influence over the computed reattachment length, at least for the coarser meshes with $F_{\text{mesh}} < 1.0$. Indeed, the data poits for $F_{\text{mesh}} = 0.25$ fail to describe the intersection point of $x = 0$ when $Re = 0$, due to the poor resolution of the recirculation region caused by the coarse mesh. For $F_{\text{mesh}} > 1$, the dispersion becomes quite small. To gain more insight of the flow behavior, the results of X_R at a fixed $Re = 50$ are presented in Figure 3.6. The condition of $Re = 50$ was selected due to its proximity to the critical point of $Re = 53.93$ reported by Fearn *et al.* (1990).

The data points in Figure 3.6 show the convergence toward an asymptote of X_R, indicating that for $F_{\text{mesh}} > 2.0$ the variation of the reattachment length with the refinement of the mesh is quite small. The error curve presents the difference against the extrapolated asymptotic value, expressed as a percentage. It is clear that a mesh of $F_{\text{mesh}} = 4.0$ produces than 1% of deviation in the reattachment length. For the present validation, this accuracy is deemed excellent, and the mesh $L40\_F400$ is selected for the remainder of this study.

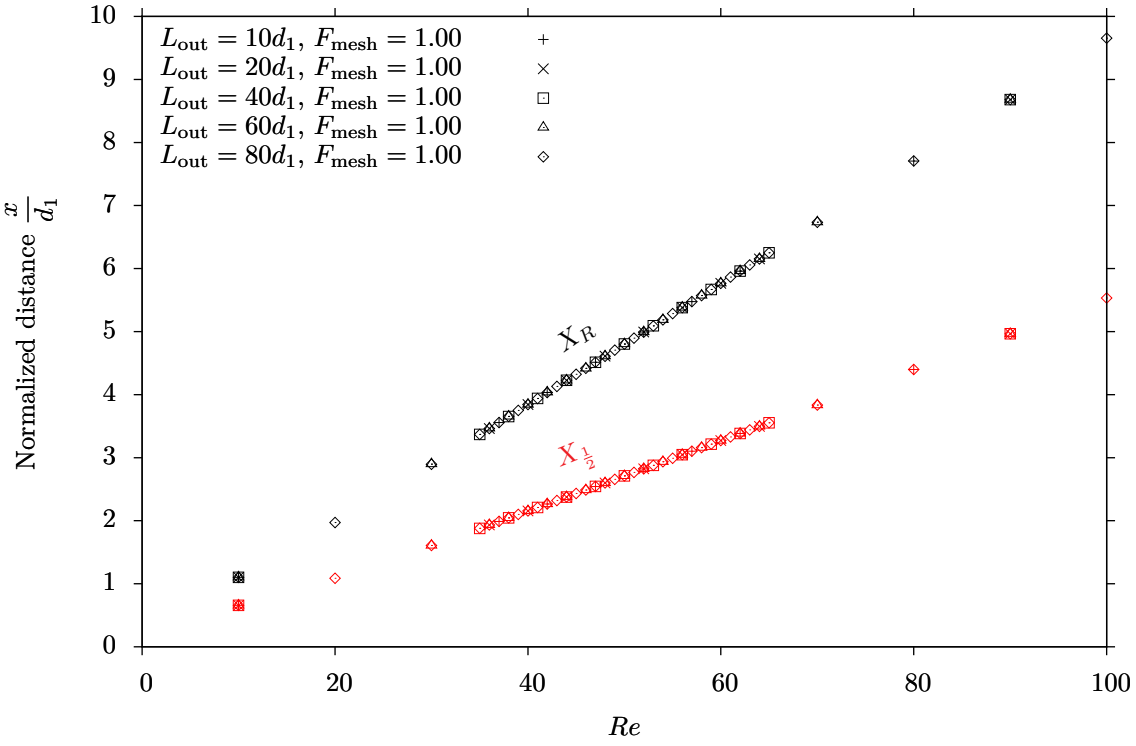

FIGURE 3.4 Half development length $X_{\frac{1}{2}}$ and reattachment length X_R as a function of the Reynolds number for $F_{\text{mesh}} = 1.00$ in the planar sudden expansion. Notice that the results are mesh independent.

TABLE 3.3 Meshes used to study the influence of the refinement factor F_{mesh} in the planar sudden expansion.

Case	Nomeclature	$\frac{L_{\text{out}}}{d_1}$	F_{mesh}	Quads	Nodes
6	$L40\_F025$	40	0.25	202	889
7	$L40\_F050$	40	0.50	408	1785
8	$L40\_F100$	40	1.00	1636	6851
9	$L40\_F125$	40	1.25	2370	9859
10	$L40\_F150$	40	1.50	3678	15171
11	$L40\_F175$	40	1.75	4752	19541
12	$L40\_F200$	40	2.00	6544	26789
13	$L40\_F300$	40	3.00	14724	59815
14	$L40\_F400$	40	4.00	26176	105959
15	$L40\_F500$	40	5.00	40900	165191

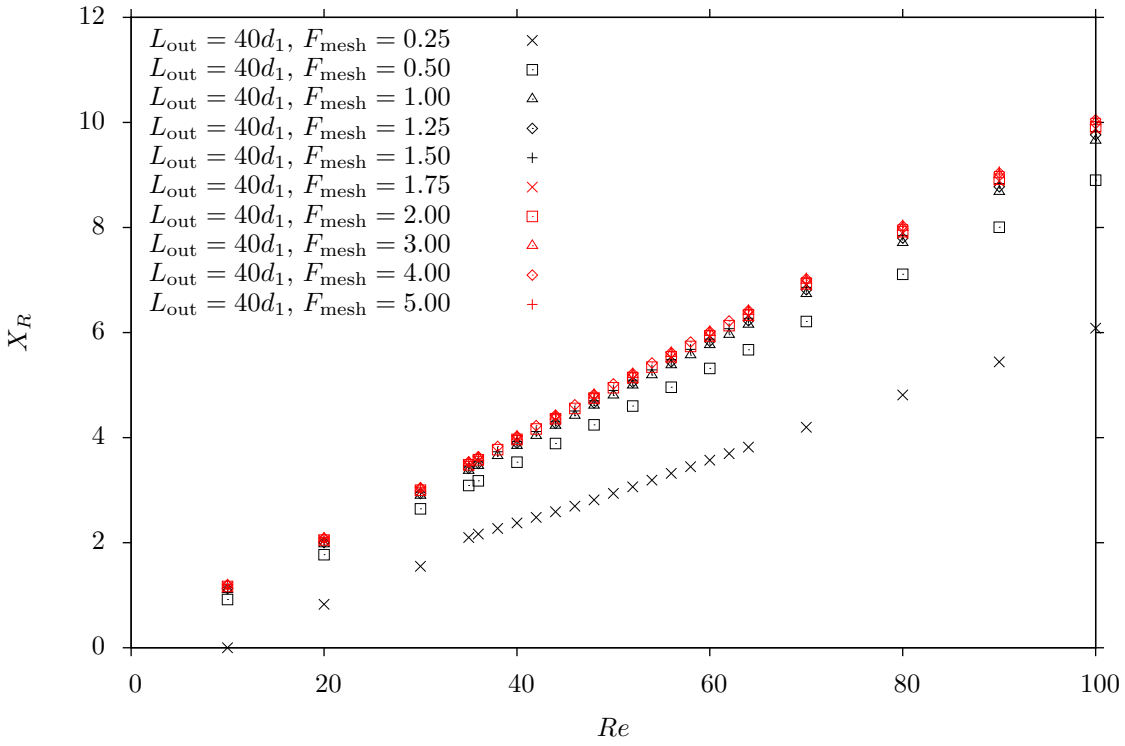

FIGURE 3.5 X_R as a function of the Reynolds number for $L_{\text{out}} = 40d_1$ in a planar sudden expansion.

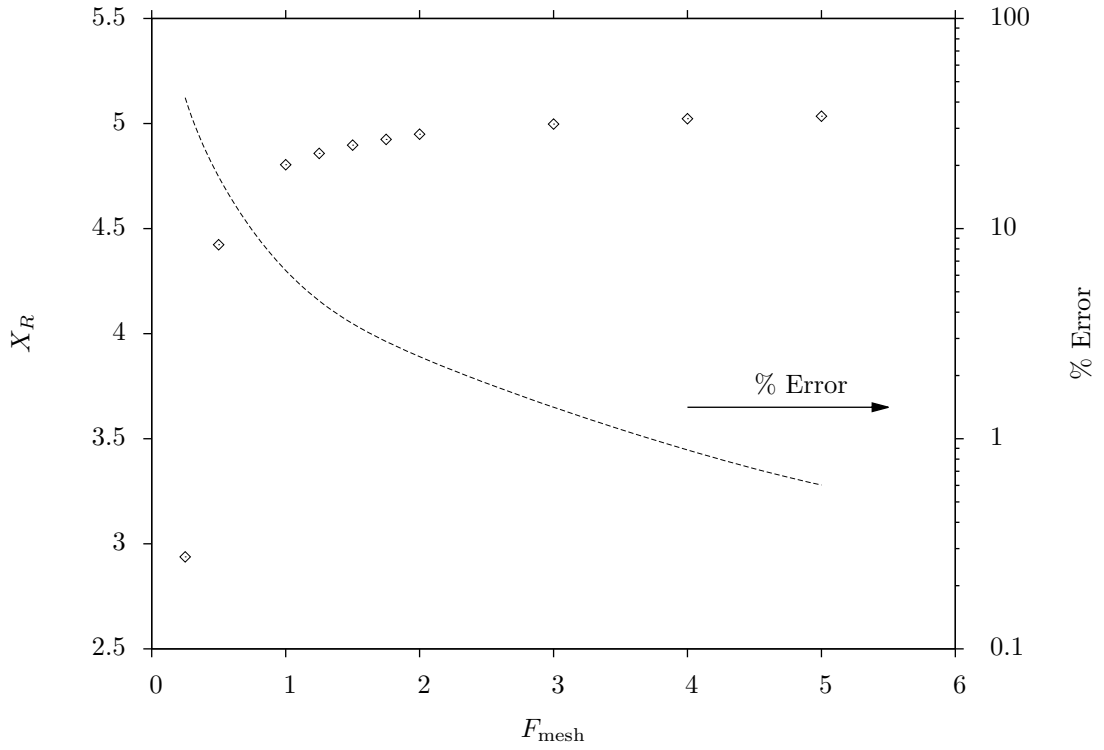

FIGURE 3.6 Variation of the reattachment length X_R with the refinement factor F_{mesh} at $Re = 50$.

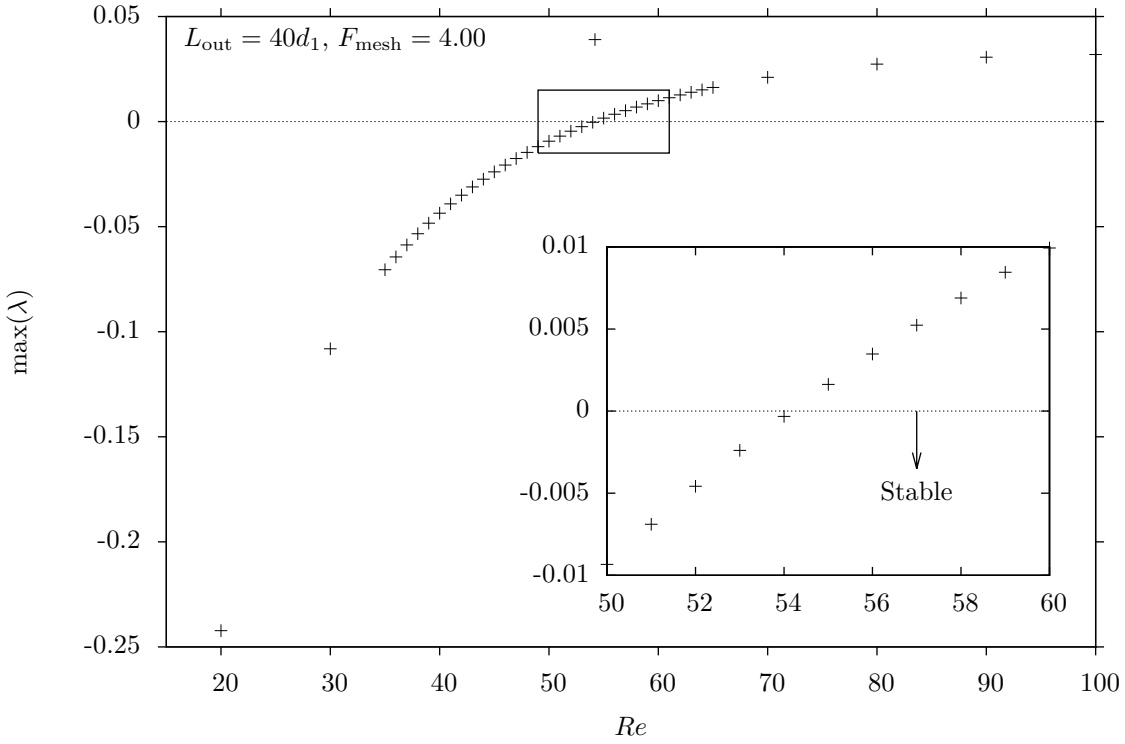

FIGURE 3.7 Leading eigenvalues as a function of the Reynolds number for the planar sudden expansion. Critical Reynolds number at $Re_{\text{cr}} = 54.17$.

Computation of stability

With the mesh of $L_{\text{out}} = 40d_1$ and $F_{\text{mesh}} = 4.0$ selected in the previous section, the stability of the symmetrical flow solution was computed, through the calculation of the eigenvalues of the linearized operator in the range $10 \leq Re \leq 100$, using the algorithm presented in Section 3.2.3. This range of Reynolds number was selected because it contains the symmetry-breaking point reported by Fearn *et al.* (1990). Figure 3.7 presents the real part of the leading eigenvalue as a function of the Reynolds number. In the inset, it is clear that a positive eigenvalue is obtained at $Re = 54.17$, a value that is less than 1% deviated from the threshold condition of $Re = 53.93$ reported by Fearn *et al.*. Thus, our current algorithm is able to reproduce satisfactorily the transition toward asymmetry in the sudden expansion according to Fearn *et al.*.

Additionally, Figure 3.8 present further information about the flow at $Re = 55$ for the sudden expansion. Figure 3.8a shows the contours of streamwise velocity of the steady-state solution, where a symmetric flow is clearly visible. As this condition occurs at a Reynolds number higher than the critical value of $Re_{\text{cr}} = 54.17$, this symmetrical flow is deemed unstable.

Figure 3.8b contains the velocity contours and streamlines for the eigenmode associated to the leading eigenvalue. These is the velocity mode that is excited and amplified after the real part of the associated critical eigenvalue becomes positive. Hence, the morphology of this mode indicates the changes that it will attempt to produce in the steady-state flow, effects that will not be damped because $Re > Re_c$. The two vortex just downstream the expansion indicates that this mode would deflect the flow from the sudden expansion toward the upper or lower side of the channel, causing the rupture of the symmetric regime.

Figure 3.8c contains the velocity contours of a perturbed velocity field, constructed as combination of the symmetrical flow from Figure 3.8a and the velocity mode from Figure 3.8b. This flow was used as an initial condition for a steady state computation at $Re = 55$. This simulation converged to the solution presented in Figure 3.8d, a flow with a small degree of asymmetry, evidenced by the different lengths between the upper and the lower recirculation regions. The computation of stability for this asymmetric solution produced only eigenvalues with a negative real part, which identify this solution as stable.

The same computation was repeated using a time integration solver based on a second-order BDF method, with a BDF1 used for the first iteration. A small perturbation obtained from the velocity mode of Figure 3.8b was injected into the steady-state solution computed for both $Re = 50$ and $Re = 60$, conditions respectively below and over the critical Reynolds number. The perturbation was damped for $Re = 50$, eventually converging to initial symmetric steady state. The unsteady simulation at $Re = 60$ presented rapid oscillations in the residuals, indicating that the solution was being significantly modified. The solution then presented progressively smaller oscillation in the residuals and the correction, asymptotically converging to an asymmetric solution similar to the one presented in Figure 3.8d.

According to the description given by Fearn *et al.* (1990), the magnitude of this asymmetry observed in Figure 3.8d will increase with Re, up to a point where this solution branch would also become unstable and additional separated regions appear downstream the channel. However, for the present case, the study is considered complete, given that for this planar geometry the stability algorithm was able to reproduce the critical value reported by Fearn *et al.* and the perturbed flow converged to an asymmetric steady-state solution. The next section presents the same study in a three dimensional axisymmetric geometry.

3.4.2 Axisymmetric contraction-expansion

Sherwin and Blackburn (2005) studied numerically an axisymmetric smooth contraction–expansion, using the spectral element code developed by Blackburn and Sherwin (2004) and a slightly refined version of the linear stability analysis algorithm proposed by Tuckerman and

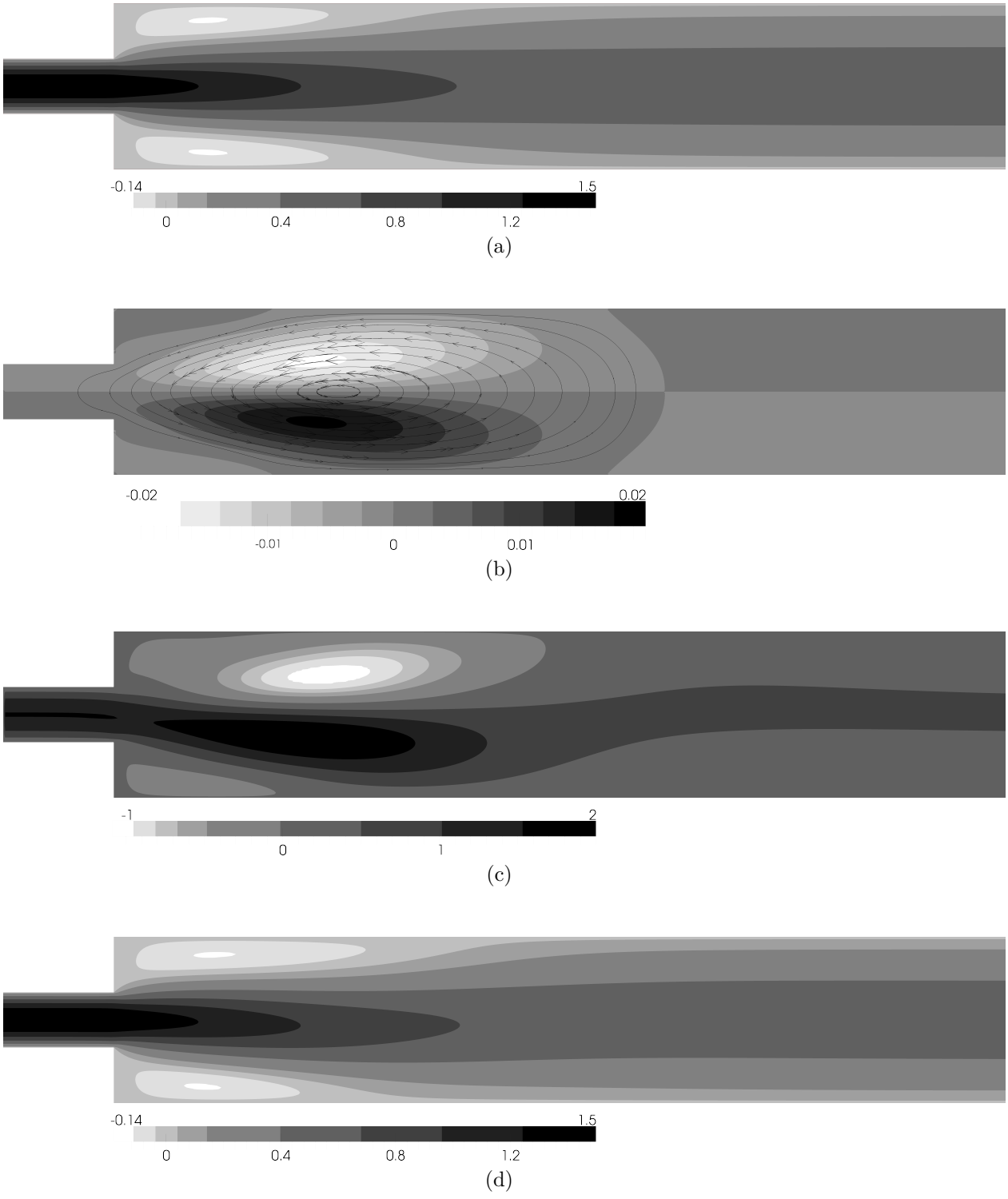

FIGURE 3.8 Contours of the solution for the planar sudden expansion at $Re = 55$. (a) longitudinal velocity, (b) longitudinal velocity of the critical mode, with an overlay of the velocity vectors due to the transverse component, (c) perturbed velocity flow used as starting point for a steady simulation at $Re = 55$, (d) converged solution describing a weakly asymmetric solution.

Barkley (2000). They found a bifurcation at $Re = 722$, where an eigenvalue with a positive real part was obtained. Afterwards, the flow remained weakly asymmetric for decreasing Reynolds numbers until a value of $Re = 688$, effectively uncovering an hysteresis loop. Here, the interest is to reproduce the results of the linear stability study. Hence, no transient calculations were performed.

Numerical solution

Once again, the flow is assumed incompressible and Navier-Stokes equations (2.1) are valid. As in the previous example, these equations are discretized through finite elements, using 27-nodes hexahedral elements with linear interpolation between the 8 pressure nodes at the corners, quadratic interpolation between the 27 velocity nodes and indeed satisfying the inf-sup condition. The geometrical coordinates x, y and z are also described through quadratic interpolation functions.

The geometry is a cylindrical tube with a smooth constriction to a minimum of 50% of the diameter or 75% of the transverse area at the throat, to then return to the original diameter. This geometry is thoroughly studied in Chapter 4, where all the details are provided. The geometry is described in Figure 4.1. The shape of the constriction is described by a cosine curve given by Equation (4.1). Figure 4.6 shows a sketch of the stenotic geometry, specifying the lengths upstream and downstream the constriction, respectively L_{in} and L_{out}, along with the boundary conditions for this problem. A parabolic Hagen-Poiseuille velocity profile is imposed as Dirichlet condition at the inlet, while at the output a natural Neumann boundary condition is used, corresponding to a null surface vector force. The velocity is set to zero at the solid boundaries of the domain, *i.e.* the walls. The solution was computed in successive increases of the Reynolds number until the condition $Re = 800$ (based on the average inlet velocity W_{avg} and the diameter of the tube D), in order to capture the critical condition reported by Sherwin and Blackburn (2005) at $Re = 722$.

Mesh validation

For the present problem, the mesh were constructed varying two parameters: the outlet length L_{out} and the refinement factor F_{mesh}. The inlet length L_{in} was kept constant during the whole study ($L_{\text{in}} = 5D$) because a developed Poiseuille velocity profile is set at the inlet, and no important changes in the velocity profile occur upstream the constriction. The process of mesh validation for the present problem follows a similar path to the one performed in the previous section for the planar sudden expansion. First, the influence of the outlet length L_{out} is studied, assessing its effect through the half development length $Z_{\frac{1}{2}}$, defined similarly to

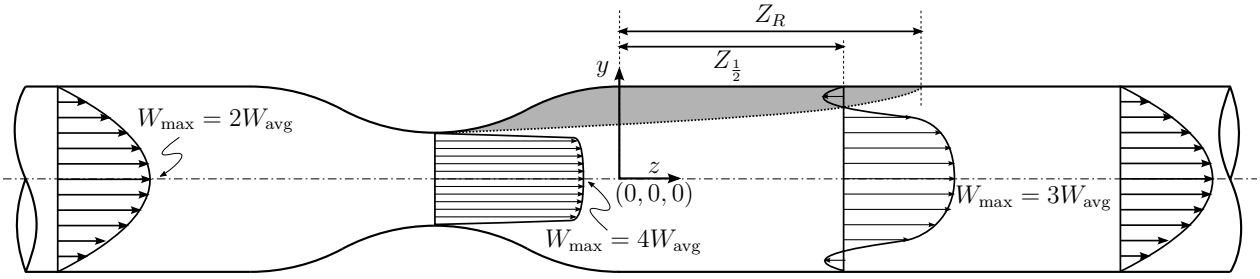

FIGURE 3.9 Definition of $Z_{\frac{1}{2}}$ and Z_R for the geometry of the axisymmetric stenosis. The shaded region represents the separated region. Notice that in this case $Z_R > Z_{\frac{1}{2}}$ but that is not necessarily true.

TABLE 3.4 Meshes used to study the influence of the downstream length L_{out} details for the axisymmetric stenosis

Case	Nomeclature	$\frac{L_{\text{out}}}{D}$	F_{mesh}	Hexas	Nodes
1	$L15\_F100$	15	1.00	24864	208119
2	$L25\_F100$	25	1.00	37536	313983
3	$L35\_F100$	35	1.00	50304	420649
4	$L45\_F100$	45	1.00	62976	526513
5	$L55\_F100$	55	1.00	75840	633981
6	$L75\_F100$	75	1.00	100992	844105

Equation (3.13), and also with the axial velocity profile at fixed distance $z/D = 25$. Figure 3.9 sketch the definition of $Z_{\frac{1}{2}}$ for this geometry. Notice that in this case the origin is placed in a different point than the separation of the boundary layer at the throat of the constriction. Hence, the behavior reported in the planar case of zero distance at zero Reynolds number would not be valid.

The refinement factor is characterized through the reattachment length Z_R. As this is a three-dimensional problem, these parameters have to be selected even more carefully than in a planar geometry, as the total number of elements and nodes increase rapidly with the extension of the geometry and the refinement of the mesh, putting constraints in the numerical solution of the problem due to its computational cost. Table 3.4 describes the characteristics of the meshes used for the study of L_{out}, keeping the refinement factor constant ($F_{\text{mesh}} = 1.0$).

Figure 3.10 presents the results for $Z_{\frac{1}{2}}$ and Z_R with the meshes of Table 3.4. As in the planar case studied previously, the data points here present very low dispersion, an indicative of the low influence of L_{out} over the half development length and the reattachment length. However,

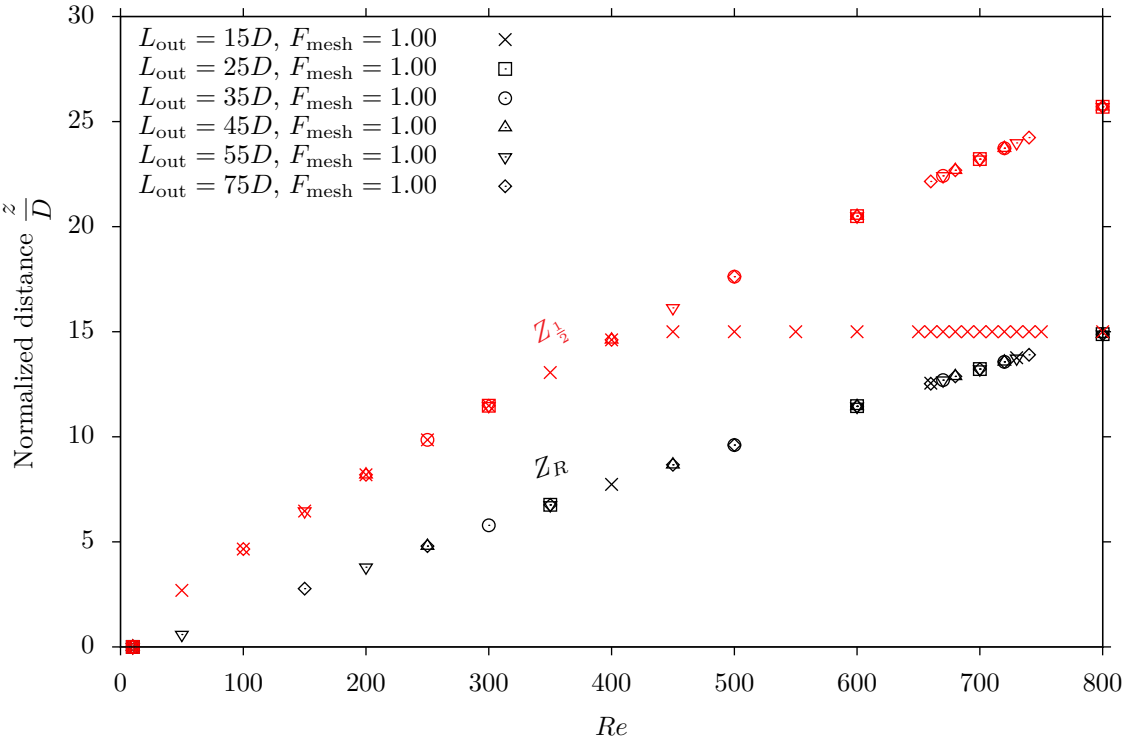

FIGURE 3.10 Evolution of half development length $Z_{\frac{1}{2}}$ and reattachment length Z_R with the Reynolds number for a constant refinement factor (F_{mesh}).

it is important to observe the plateau in $Z_{\frac{1}{2}}$ for $L_{\text{out}} = 15D$. For $Re > 400$ the data points diverge from the straight line, remaining constant at $Z_{\frac{1}{2}} = 15$. This behavior is due to the fact that the half development length is outside this numerical domain for Reynolds number over 400. Thus, this mesh of $L_{\text{out}} = 15D$ is discarded.

Figure 3.11 presents the data at $Re = 800$ for the normalized axial velocities profiles for the remaining meshes, plotted at $z/D = 25$. Once again, the data presents very low dispersion, with all the meshes describing the same velocity profile, regardless of the distance to the outlet boundary condition. Moreover, on the insert of Figure 3.11 the normalized axial velocity at the centerline of the domain is plotted against the axial coordinate, showing the same low level of dispersion. The datapoints were fitted using a Gaussian curve [2], effectively showing an horizontal asymptote at $w/W_{\text{avg}} = 2$ which represents the fully developed Poiseuille profile downstream the constriction. Thus, these meshes reproduces coherently the behavior of the flow regardless the value of of outlet length used in their construction. Consequently, the shortest domain of $L_{\text{out}} = 25D$ is selected for the rest of the study.

2. $f_{\text{G}}(z) = a_{\text{G}} + b_{\text{G}} \exp\left[-(c_{\text{G}} z + d_{\text{G}})^2\right]$, with $a_{\text{G}} = 2.01$, $b_{\text{G}} = 2.844$, $c_{\text{G}} = -0.0245$ and $d_{\text{G}} = -0.423$.

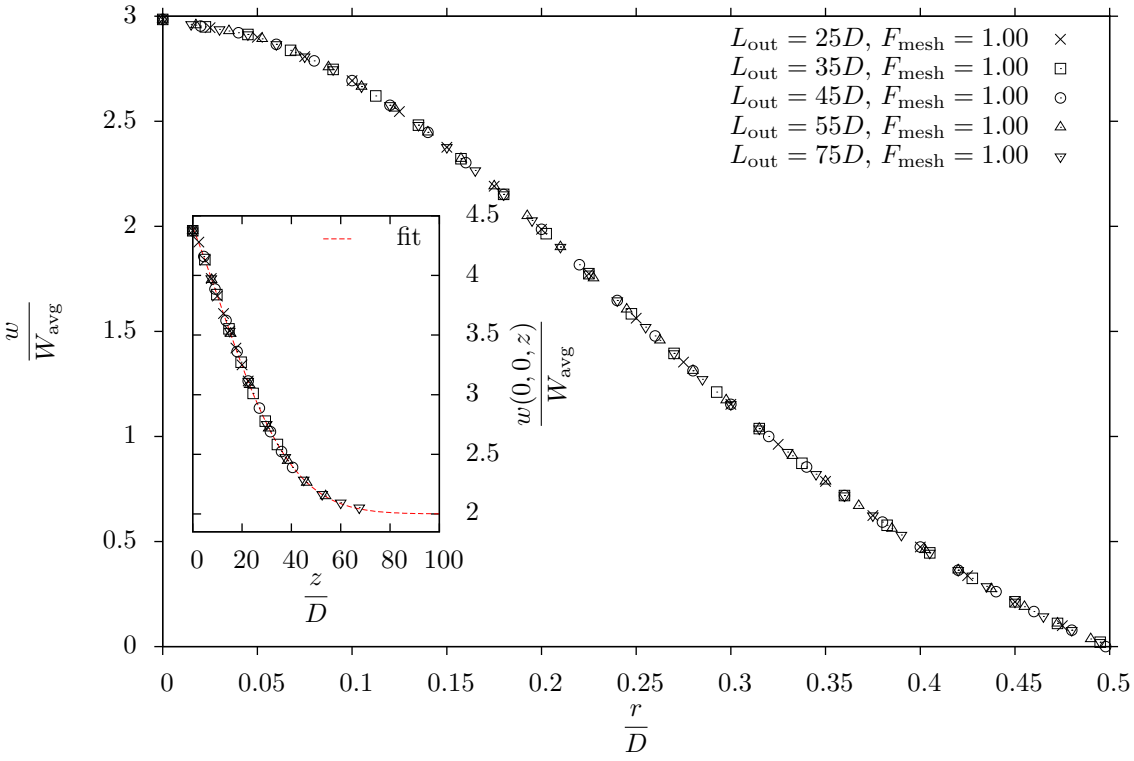

FIGURE 3.11 Normalized axial velocity at $z/D = 25$ at $Re = 800$ for the different L_{out} studied. Inset shows the evolution of the axial velocity at the centerline as a function of the axial coordinate.

TABLE 3.5 Meshes used to study the influence of the downstream length F_{mesh} details for the axisymmetric stenosis

Case	Nomeclature	$\frac{L_{\text{out}}}{D}$	F_{mesh}	Hexas	nodes
7	$L25\_F075$	25	0.75	16644	140985
8	$L25\_F100$	25	1.00	37536	313983
9	$L25\_F120$	25	1.20	67860	563137
10	$L25\_F150$	25	1.50	130872	1076613
11	$L25\_F175$	25	1.75	201369	1650987
12	$L25\_F200$	25	2.00	295296	2414691
13	$L25\_F250$	25	2.50	590240	4802505

Table 3.5 describes the characteristics of the meshes used for the study of the refinement factor, keeping the output length constant at the selected value of $L_{\text{out}} = 25D$. In this geometry, a non-uniform distribution was used, with an increased radial resolution near the domain walls and with smaller elements near the constriction. The distribution of nodes for this geometry is presented again with more details in the next Chapter. For example, Figure 4.8 presents the structure of the mesh constructed for this stenotic geometry, showing the effect of the increase of the refinement factor F_{mesh}. Figure 3.12 presents the results for the reattachment length Z_R, where significant dispersion is appreciated at higher Reynolds numbers. Hence, the refinement factor has an important effect on the prediction of the separation point. Indeed, as the node density near the wall increase with F_{mesh}, the accuracy in the computation of the velocity gradient at the wall will also increase.

The inset plot of Figure 3.12 shows the influence of the refinement length F_{mesh} over the reattachment length Z_R at $Re = 800$, showing the same asymptotic behavior for the reattachment length observed in the planar expansion as F_{mesh} increases. However, the curve for the error presents a sharp corner at $F_{\text{mesh}} = 1.5$ due to a very small local maximum in Z_R. This is probably due to truncation errors during the projections and numerical differentiation required to compute the velocity gradient at the wall. With this mesh of $F_{\text{mesh}} = 1.5$ the error is below 1%. Hence, the mesh $L25\_F150$, constructed with $L_{\text{out}} = 25D$ and $F_{\text{mesh}} = 1.5$, is selected for the stability analysis. However, the stability of the symmetric regime would also be computed with the coarser $L25\_F120$ mesh, to evaluate the effect of mesh resolution over the results of the linear stability analysis.

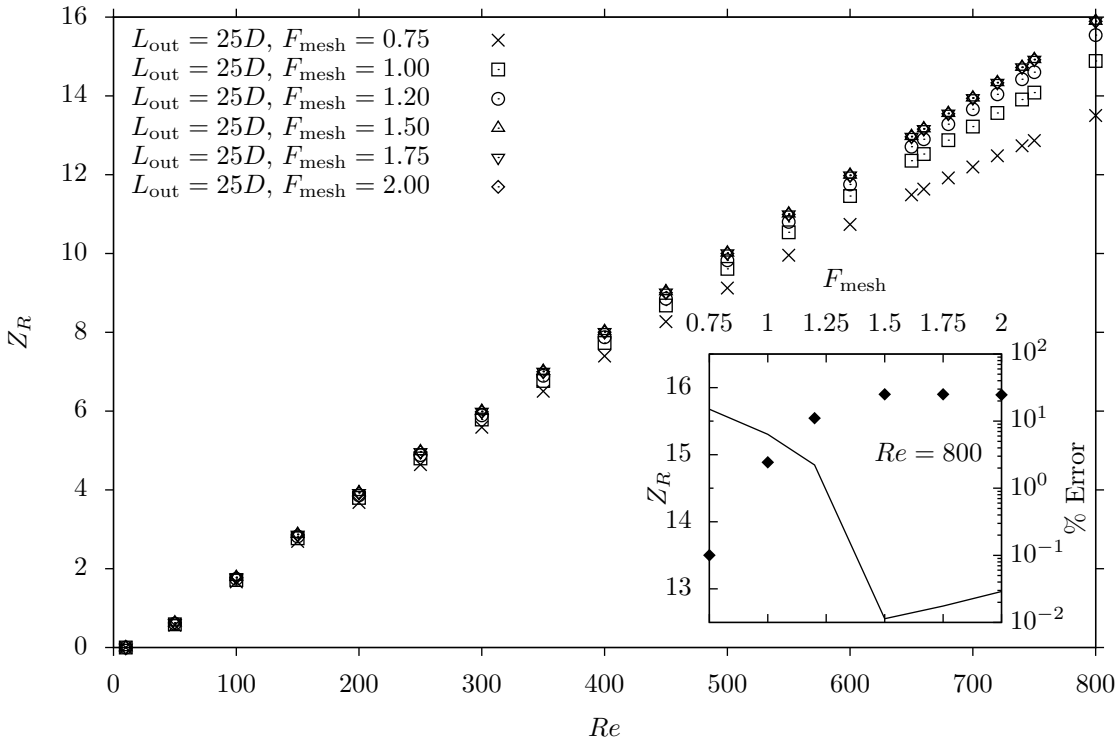

FIGURE 3.12 Influence of the Reynolds number and refinement factor over the reattachment length Z_R, with $L_{\text{out}} = 25$. Inset plot shows the reattachment length Z_R as a function of F_{mesh} at $Re = 800$, along with the error when compared to the horizontal asymptotic value.

Computation of stability

The modified product method described in Section 3.2.3 for calculation of stability was used to study the axisymmetric regime in this stenotic geometry, for the range $300 < Re < 800$. The computed leading eigenvalues are plotted in Figure 3.13 for different Reynolds number, using the two selected meshes. It is noticeable that the eigenvalues slightly decrease in their values when the mesh is refined. This causes that the critical Reynolds number for the refined mesh has a higher value. For the finer mesh, a positive eigenvalue was obtained at $Re \simeq 720.2$, representing a 0.25% of deviation from the value of $Re_{\text{cr}} = 722$ reported by Sherwin and Blackburn (2005). The coarser mesh produces an estimate of the critical Reynolds number of $Re \simeq 709.8$, a value that deviates 1.7% from the Re_{cr} described by Sherwin and Blackburn. Thus, for this case, the use of a coarser mesh provides a first useful estimate of the critical Reynolds number. And it is also conservative, from an engineering perspective, meaning that the critical threshold is reported at a magnitude smaller than the one occurring in reality. Hence, under some circumstances the use of coarse mesh might provides useful stability results, specially when computational constraints exist due to the size of the numerical problem or when only a preliminary estimate is required.

Additionally, Figure 3.14 contains the axial velocity contours for the four most critical modes at $Re = 720$. The most critical mode is a symmetry-breaking mode, similar to the one presented in Figure 3.8b for the planar sudden expansion. Regarding the less critical modes, they are equivalent to the modes with azimuthal wavenumber larger than 1 reported by Sherwin and Blackburn (2005). Thus, several streamwise vortical structures are observed, representing azymuthal wavenumbers of 2, 3 and 4. No further computations were made to check the effect of these modes over the axisymmetrical solution.

As in the previous section, the axisymmetrical solution was perturbed using the most critical velocity mode, but no convergence to an asymmetric steady state solution could be reached for $Re > Re_{\text{c}}$. This is in agreement with the observations of Sherwin and Blackburn (2005), who described transient phenomena and local turbulence transition for $Re > 725$ in this geometry, phenomena that were later confirmed by Blackburn and Sherwin (2007) to be related with convective instabilities in the shear layer downstream the stenosis.

3.4.3 Results of the implicit matrix method

The implicit matrix method presented in Section 3.4.3 was also evaluated for the two geometries presented previously. identical geometrical parameters were employed, using the same steady solutions decompose the perturbed stability problem. The time integration was computed

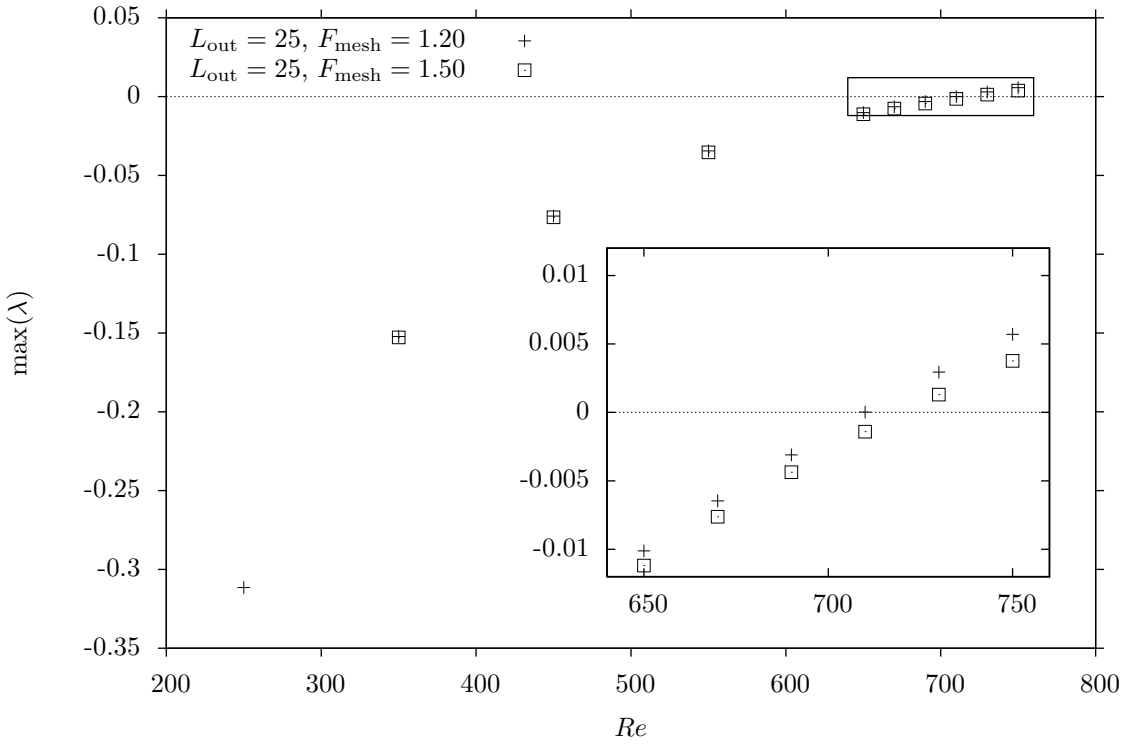

FIGURE 3.13 Maximum eigenvalue for different Reynolds numbers for an axisymmetric stenose. From the insert, a positive eigenvalue occurs at $Re \simeq 709.8$ for $F_{\text{mesh}} = 1.20$ and at $Re \simeq 720.2$ for $F_{\text{mesh}} = 1.50$.

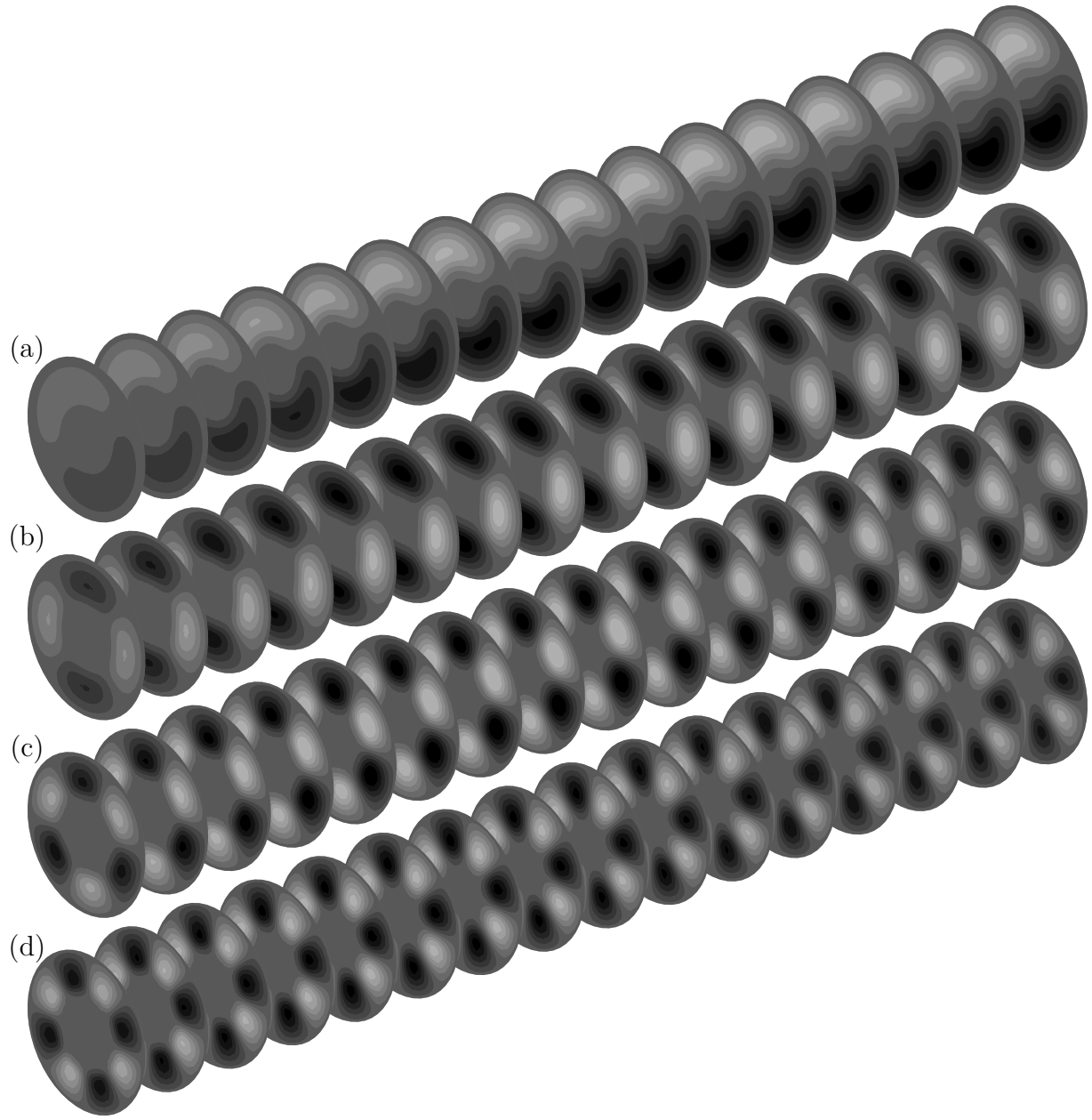

FIGURE 3.14 Axial velocity contours for the eigenfunctions at $Re = 720$. The four most critical eigenmodes are shown. The most critical is a symmetry-breaking mode, similar to the one shown in Figure 3.8b for the sudden expansion.

using the same scheme discussed in the examples of Section 2.11.1, with a first-order BDF method to compute the first time-step, and the subsequent integrations were completed using a 2nd-order BDF, leaving the time-step size constant. This is approach was only executed during the initial filtering stage of the algorithm. For the construction of the Krylov subspace base, the first order BDF method was used, because it uses a single vector as input, which is what ARPACK supplies for the implicit matrix-vector products.

As described in Table 3.1, different time parameters were used, to evaluate the sensibility of the computed spectra to these values. The method was able to reproduce the results presented in the previous section in both cases, the planar sudden expansion and the axisymmetric stenosis. In particular, for simulation cases deemed satisfactory, the critical Reynolds number deviated a maximum of 5% from the values computed with the modified product method of Section 3.2.3.

However, the use of fixed time parameters proved inefficient. The total computational time that the calculation took to complete a certain Reynolds number and combination of time-step and filtering time was between 2 and 10 times higher than the time it took the modified product method to compute eigenvalues for the same conditions. Moreover, an additional study was conducted to determine the sensibility of the solution to the time integration and filtering parameters used, leaving the total expected of filtering steps constant. Certain combination of time-step and filtering time caused and increase in the computational time up to levels extremely high to be deemed practical, while other caused a total failure in the convergence of the method at several Reynolds number. A set of eigenvalues at a certain Reynolds for the planar sudden expansion could be computed in a few minutes with the modified product method, while it took a couple of hours in certain cases with the implicit matrix method. Even more difference was observed in the axisymmetric stenosis, with the modified product method taking between 5 to 8 hours at each Reynolds number to complete the computation of eigenvalues, while they took up to a week with the implicit method. And the behavior changed with the Reynolds number. A set of parameters that functioned reasonably well at low-Reynolds numbers could present convergence problems at higher Reynolds number for the same solution branch.

Hence the selection of practical general time-integration parameters is not evident and quite likely not possible, at least not with the mixed first and second order BDF scheme. It is possible that a more sophisticated time integration algorithm capable to variate the time-step size could produce more satisfactory results. But under the current circumstances, the implicit matrix was not further evaluated.

CHAPTER 4 SMOOTH CONTRACTION-EXPANSION

4.1 Introduction

The present chapter contains the results of the numerical method presented in the previous section for the computation of stability, for the test case of the smooth contraction-expansion, also called stenosis. In order to study the effect of the geometry over the stability regime and the symmetry-breaking thresholds, two different configurations were evaluated: a stenosis constructed with arcs of circumference, identical to the one studied experimentally by Vétel *et al.* (2008), and a sinusoidal stenosis, analog to the one used in many numerical studies (Sherwin and Blackburn, 2005; Griffith *et al.*, 2013).

4.2 Definition of the stenotic geometry

A smooth contraction-expansion, with a 75% of area restriction at the throat of the stenosis, equivalent of a 50% in the reduction of the diameter, is used in both cases. The total length of the restriction is $2D$, where D is the internal diameter of the main tube, as described in Figure 4.1. These parameters are common in the study of vascular geometries. The origin of coordinates is placed at the downstream plane of the stenosis. The shape of the stenosis is described with the variation of the internal diameter of the stenosis as a function of the axial coordinate within the constriction. This geometrical characterization has been done in several ways in the literature (Khalifa and Giddens, 1981; Mallinger and Drikakis, 2002; Vétel *et al.*, 2008). Here, two different constructions of the smooth stenosis were evaluated: a sinusoidal constriction proposed by the one by Khalifa and Giddens and an alternate shape based on circunference arcs, proposed by Vétel *et al.*.

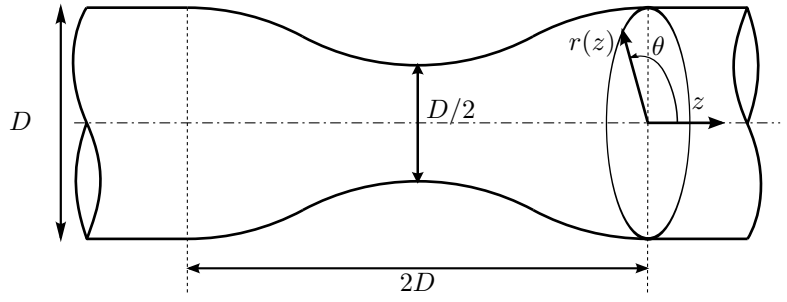

FIGURE 4.1 Definition of the geometry of the stenosis.

In their experimental study, Khalifa and Giddens used a stenosis where the diameter varied according to a *cosine* curve, a geometry that was later used by (Ahmed and Giddens, 1983b) in their experimental study, and by Sherwin and Blackburn (2005) in their stability study. Varghese *et al.* (2007) also employed the cosine description in their numerical study. For the cosine stenosis, the internal radius $r(z)$ varies according to Equation (4.1):

$$r(z) = 0.5D\left\{1 - 0.25\left[1 - \cos\left(\frac{\pi z}{D}\right)\right]\right\} \quad \text{for } z \in [-2D, 0], \tag{4.1}$$

while other authors provide an equivalent expression but using a sine function instead of a cosine. In these cases, the origin of coordinates is usually placed at the throat of the stenosis.

Vétel *et al.* used a stenosis where the internal diameter varies according to three different segments of circumference, tangents in their intersections. This geometry, which in the following will be called *3-arcs stenosis*, is depicted in Figure 4.2, where the details about the construction of the primitive curve are given. The intersection between the circumference arcs should at points where the curves are tangent among them. This condition implies that the radius of the three arcs is $R_{\text{st}} = 17D/16$.

The small geometrical differences between the 3-arcs and the cosine stenoses are displayed in Figure 4.3.

4.3 Axisymmetric 3-arcs stenosis

The method for the computation of stability presented in Section 3.2.3 was validated in Section 3.4.2 using a cosine stenosis. In order to compare the effects that the geometrical differences depicted in Figure 4.3 may have over the stability, the same analysis carried out in Section 3.4.2 was repeated but for a 3-arcs stenosis. The same numerical parameters were used, to solve a mesh with identical element density and node distribution. Figure 4.4 presents a comparison between the real part of the leading eigenvalue as a function of the Reynolds number for both geometrical description of the geometry.

The critical condition at which the real part of the eigenvalues becomes positive is different in both geometries. Indeed, $Re_{\text{c}} \simeq 709.8$ for the cosine stenosis, while $Re_{\text{c}} \simeq 726.72$ for the 3-arcs stenosis. The only source of difference between these two data sets is the description of the stenosis shape, all the other factors being as described in Section 3.4.2. Also in that Section, it was shown that a more refined mesh will produce a value of the critical Reynolds number of $Re_{\text{c}} \simeq 722$ for the cosine stenosis. A similar behavior is expected with the 3-arcs stenosis, and hence mesh refinement, although might reduce the width of the gap between the critical conditions for both geometries, it will not disappear. Hence, the small geometrical

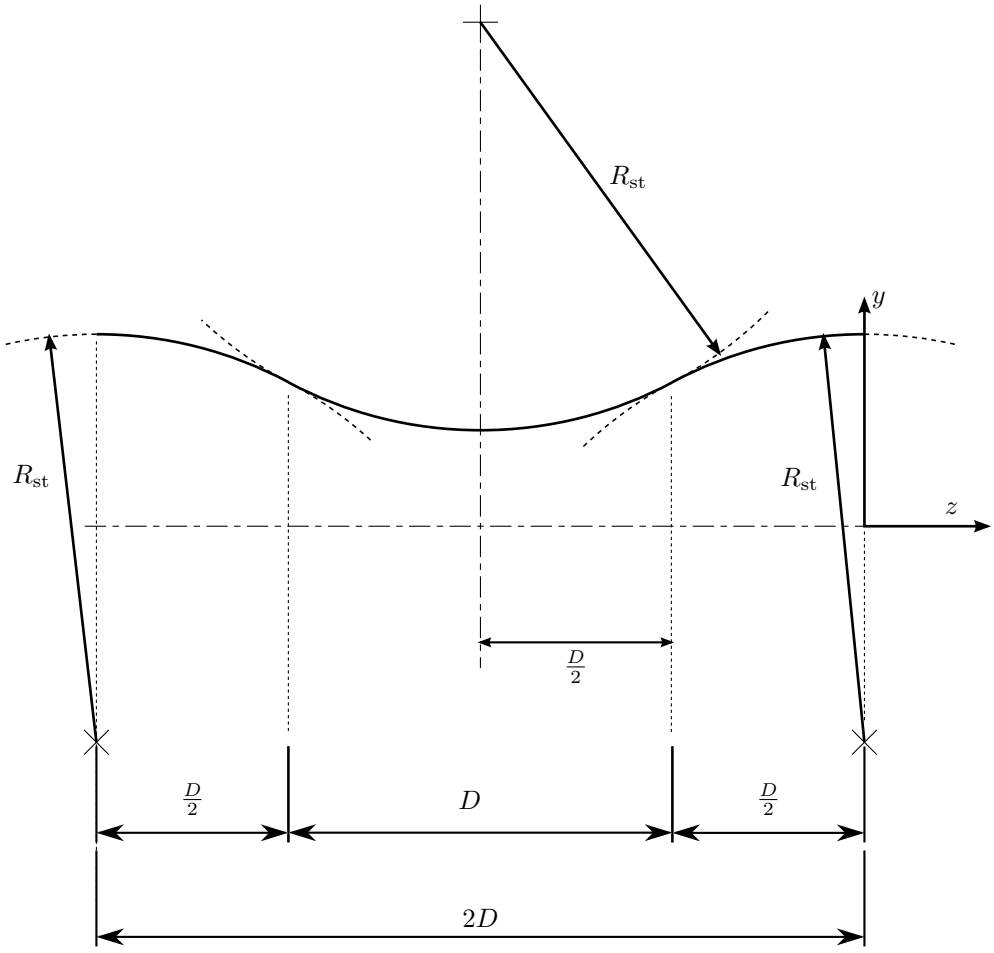

FIGURE 4.2 Construction of the 3-arcs stenotic geometry.

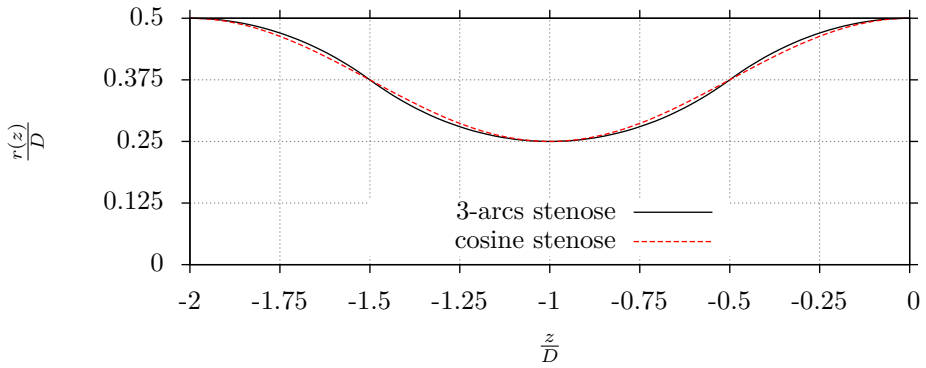

FIGURE 4.3 Comparison of the 3-arcs and the cosine stenoses.

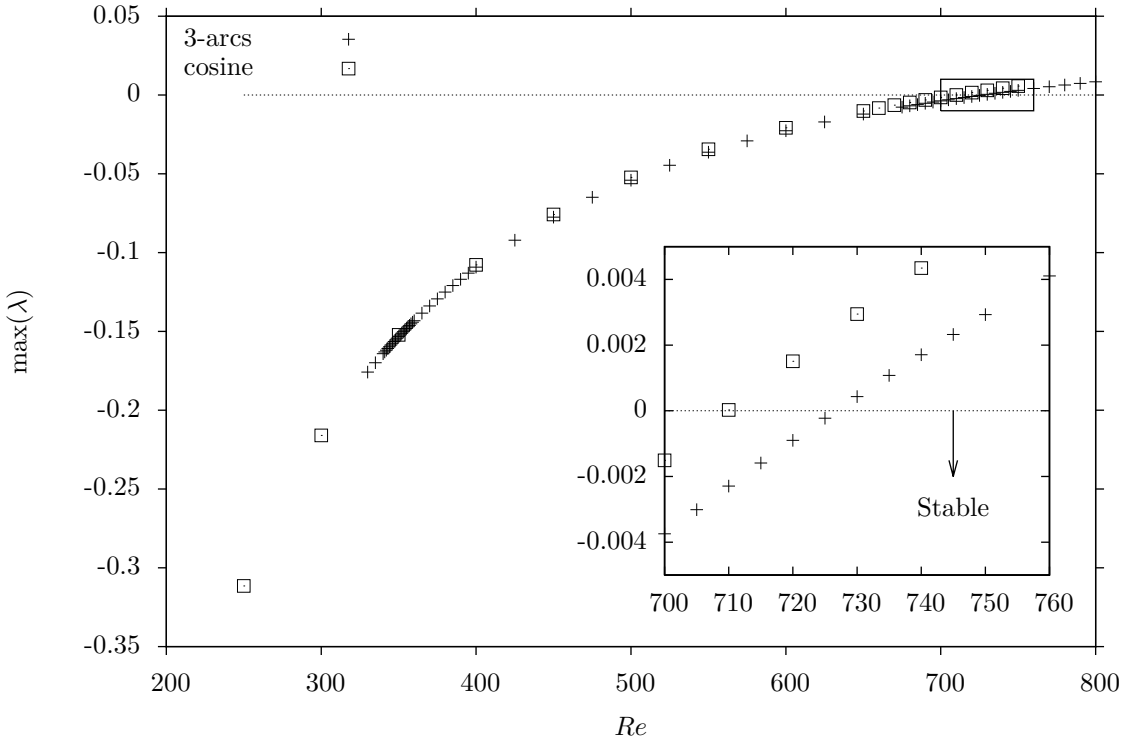

FIGURE 4.4 Critical eigenvalues for the 3-arcs and the cosine stenoses as a function of Re. The critical Reynolds number $Re_c \simeq 709.8$ for the cosine stenosis, while $Re_c \simeq 726.72$ for the 3-arcs stenosis.

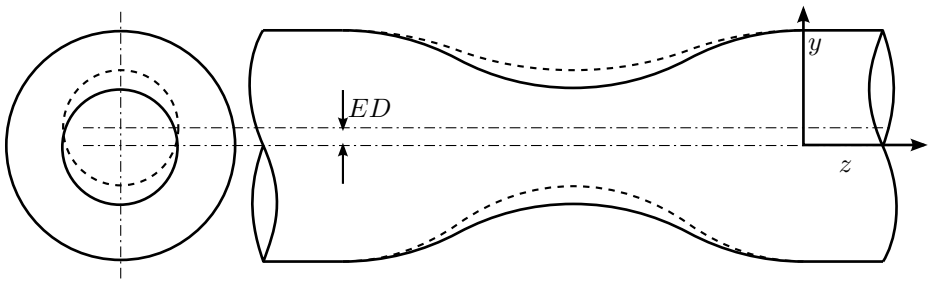

FIGURE 4.5 Eccentricity on the stenotic geometry.

differences signaled in Figure 4.3 have an effect on the critical condition for the axisymmetric stenosis. These differences increase when geometrical eccentricities are added to the area of the constriction, as presented in the next Section.

4.4 Eccentric stenoses

The existence of imperfections in the geometry and their effect on the flow as a type of perturbation was first studied numerically by Varghese *et al.* (2007) through an eccentricity inside a cosine stenosis, as depicted in Figure 4.5. The E parameter is a measure of the maximum deviation of the stenosis wall from the axis of the rest of the tube. Varghese *et al.* used a fixed value of 5% of eccentricity, equivalent to $E = 0.05$, obtaining an asymmetric solution. Later, Griffith *et al.* (2013) performed a numerical study where smaller eccentricities were evaluated ($0 \leq E \leq 0.05$) in a cosine stenosis, establishing a relation between the parameter E and the asymmetry of the flow.

In the present study, the relation between this eccentricity and the asymmetric flow is thoroughly evaluated, using a similar methodology to the one presented by Griffith *et al.* (2013), and the addition of the linear stability analysis. A small eccentricity e_y in the y direction was added to the geometry within the stenotic region, with its magnitude varying with the axial position according to Equation (4.2)

$$e_y(z) = 0.5ED\left[1 - \cos\left(\frac{\pi z}{D}\right)\right] \quad \text{for } z \in [-2D, 0], \tag{4.2}$$

where E is again a measure of the maximum eccentricity at the throat of the stenose, as shown in Figure 4.5. As mentioned in Section 2.10, Griffith *et al.* reported that with $E = 0.0025$, the asymmetry obtained presented qualitative similitude with the one observed experimentally by Vétel *et al.* (2008). In their experimental study, Vétel *et al.* used a pipe of $D = 20.5$ mm with a geometric tolerance of 25 μm. This could account for an eccentricity of the order $E = 0.0012$,

which is of the same order of magnitude as the $E = 0.0025$ described by Griffith *et al.*, and is within the range of their study. Hence, the study of these geometrical perturbations is relevant in this case.

As part of their numerical study, Griffith *et al.* developed a convenient way to compare the level of asymmetry in a flow at a certain axial position, through the normalized first moment of the axial component of the velocity vectors, according to

$$\mu_y = \frac{\int_\Omega \frac{y}{D_z}\frac{w}{W_{\text{avg}}}\, d\Omega}{\int_\Omega \frac{w}{W_{\text{avg}}}\, d\Omega}, \tag{4.3}$$

where D_z is the local internal diameter of the pipe, equivalent to $2r(z)$ from Equation (4.1), and W_{avg} is the average velocity in the pipe. The integration domain Ω correspond to the transverse section of the domain where the asymmetry is being studied. Hence, μ_y is defined as a function of the axial coordinate z. Equation (4.3) provides a measure of the deflection toward the y direction, were larger flow deflections are expected, due to the alignment of the eccentricity with y. However, this alignment is not necessarily true, and a similar formula for μ_x in the x axis was also employed, and the total normalized asymmetry μ_r was obtained using

$$\mu_r = \sqrt{(\mu_x)^2 + (\mu_y)^2}, \tag{4.4}$$

while the azymuthal position of the asymmetry could be determined through

$$\tan(\theta_\mu) = \frac{\mu_y}{\mu_x}. \tag{4.5}$$

4.5 Numerical methodology

Following the simulations presented in Section 3.4.2 for the axisymmetric stenosis and the reproduction of the stability threshold reported by Sherwin and Blackburn (2005), this section describes the study of the flow within an eccentric stenosis, based on the work of Griffith *et al.* (2013), with the additional geometry of the cosine stenosis, and the computation of the stability regime in both cases. Again, the boundary conditions are similar to the ones presented in Section 3.4.2. An incompressible fluid flow is assumed and hence, the Navier-Stokes equations (2.1) are valid. The problem is discretized through the finite element method, using 27-nodes hexahedral elements that satisfy the inf-sup condition, providing quadratic interpolation for the velocity vectors and linear interpolation for the pressure. The structured mesh was constructed using Gmsh (Geuzaine and Remacle, 2009). A parabolic Hagen-Poiseuille velocity

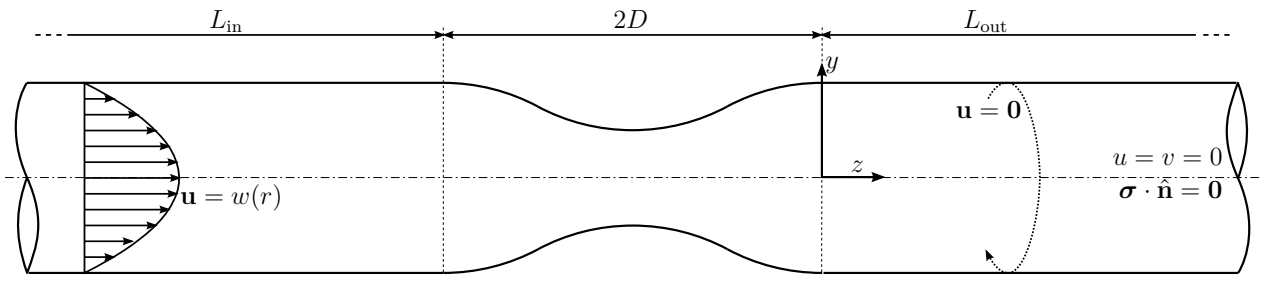

FIGURE 4.6 Definition of the inlet and outlet lengths in the stenotic geometry.

profile is used as boundary condition at the inlet of the domain, while at the outlet a null surface force vector was imposed. Additionally, the velocity at the outlet was forced to be completely axial. Most simulations were carried out in steady state, except where indicated. The boundary conditions are summarized in Figure 4.6, where the inlet and outlet lengths are also defined.

The Reynolds number was increased in successive steps of steady state convergence, decreasing the viscosity of the flow. The transient cases were computed using an implicit second order backward differentiation formula for the time integration.

4.6 Mesh validation

To carry out the simulations, the both geometrical descriptions for the stenosis were discretized with a hexahedral mesh, and an eccentricity of $E = 0.0025$ was added. The meshes were constructed using two parameters, similarly to Section 3.4.2: the length of the segment downstream the stenosis L_{out} and the refinement factor F_{mesh}. However, the addition of a geometrical eccentricity radically changes the results, because asymmetric flows are expected from the beginning. Hence, the value of the mesh parameters computed for the axisymmetric mesh no longer applies in this eccentric geometry, and the mesh independence study has to be repeated with the new geometry.

As the velocity profiles are not symmetric, new variables has to be used to monitor the meshing parameters. Indeed, the centerline velocity in not representative of the development of the flow, because the peak velocity no longer lies over the z-axis and the half development length cannot be computed through an expression similar to Equation (3.13). Hence, the simpler approach is to evaluate primitive variables, comparing velocity profiles at fixed axial positions within the domain. As the geometrical eccentricity is contained within the plane yz, the velocity profiles on this plane at two different axial positions are ($z/D = 5$ and $z/D = 24$)

TABLE 4.1 Meshes used to study the influence of the downstream length L_{out} in the eccentric stenosis with $E = 0.0025$.

				Cosine		3-arcs	
Case	Nomeclature	$\frac{L_{\text{out}}}{D}$	F_{mesh}	Hexas	Nodes	Hexas	Nodes
1	$L25\_F100$	25	1.00	37536	313983	37536	313983
2	$L35\_F100$	35	1.00	50304	420649	50304	420649
3	$L45\_F100$	45	1.00	62976	526513	62976	526513
4	$L55\_F100$	55	1.00	75840	633981	75840	633981
5	$L75\_F100$	75	1.00	100992	844105	100992	844105

are employed to characterize the influence of the outlet length L_{out}. $z/D = 24$ is just upstream of the outlet surface of the mesh selected in Section 3.4.2 with $L_{\text{out}} = 25D$, which is also the shortest domain revised in this study. Monitoring the velocity profile at $z/D = 24$ allows to compare how the flow at the outlet of the shortest domain studied is affected when the downstream geometry is extended. Additionally, it will also allow to check the validity of the fully axial outlet flow condition depicted in Figure 4.6. On the other hand, the position $z/D = 5$ is in the middle of the domain, and due to the proximity to the stenosis, asymmetric velocity profiles are expected. Thus, this position allows to quantify the effect of L_{out} over the asymmetric flow downstream the stenosis.

Until this point, the reattachment length has been used to study the effect of the refinement factor F_{mesh}. This still applies in the present case. But the asymmetry in the velocity profiles creates an azimuthal dependency of the reattachment length that did not occurred in the axisymmetric geometry. Hence, the maximum reattachment length computed over the domain is the one used as Z_R.

Table 4.1 shows the parameters used in the generation of the meshes for the validation of the outlet length L_{out} and its influence over the velocity profiles in the plane yz, keeping the refinement factor at $F_{\text{mesh}} = 1.0$. The values for the cosine and the 3-arcs descriptions for the stenosis are both shown, evidencing that in both cases the meshes have the same number of elements and nodes.

Figure 4.7 presents the velocity profiles for the meshes detailed in Table 4.1, at the two axial positions $z/D = 5$ and $z/D = 24$. Figure 4.7a corresponds to the cosine stenosis while Figure 4.7b contains the results for the 3-arcs stenosis. It is important to observe that in this eccentric case, the small geometrical differences in the description of the shape of the geometry also causes differences in the flow within both geometries, specially closer to the

TABLE 4.2 Meshes for the study of the refinement factor F_{mesh} in the eccentric stenosis with $E = 0.0025$.

				Cosine		3-arcs	
Case	Nomeclature	$\frac{L_{\text{out}}}{D}$	F_{mesh}	Hexas	Nodes	Hexas	Nodes
6	$L25\_F075$	25	0.75	16644	140985	16644	140985
7	$L25\_F100$	25	1.00	37536	313983	37536	313983
8	$L25\_F120$	25	1.20	67860	563137	67860	563137
9	$L25\_F150$	25	1.50	130872	1076613	130872	1076613
10	$L25\_F175$	25	1.75	201369	1650987	201369	1650987

stenosis. The peak velocity at $z/D = 5$ in the 3-arcs stenosis is 1% larger than the one in the cosine stenosis, a value that seems small enough to justify the establishment of analogies between both stenosis. But as presented in Section 4.3, the shape of the constriction affects the stability threshold. It remains to check if the added eccentricity will wash away these differences because its effect over the stability of the flow is far larger, or if in contrast, the differences appreciated in the axisymmetric case will be somewhat amplified due to the eccentricity.

Additionally, for both geometries, the level of dispersion in the data points is remarkable low, even at close to the stenosis at $z/D = 5$, where important asymmetries and recirculation occurs. Indeed, in all the meshes the positions and values of velocity of the local maxima and minima deviates by less than 0.0001%. Hence, due to the independence of these velocity profile to the length of the domain, the shortest $L_{\text{out}} = 25D$ is selected.

With the outlet length fixed, the effect of the refinement factor is studied, using the meshes presented in Table 4.2, where for both the cosine and 3-arcs stenosis, the refinement factor is varied in the range $0.75 < F_{\text{mesh}} < 1.75$. Figure 4.8 shows the effect of these different values of refinement factor over the distribution and density of elements within the numerical domain. Figures 4.8a and 4.8c are transversal and meridional cuts of the mesh at $F_{\text{mesh}} = 0.75$, while Figures 4.8b and 4.8d shows the transversal and meridional cuts at $F_{\text{mesh}} = 1.75$. The distribution of the elements for both the cosine and 3-arcs geometries is identical, only varying in the exact position of the nodes over the stenosis wall, due to the deviations between both shapes, as depicted in Figure 4.3.

The effect of refinement is studied through the reattachment length Z_R. In this eccentric geometry, the recirculation region will not have an uniform length due to the flow deflection. Hence, the point at which τ_{wall} becomes zero will have an azymuthal dependence. The

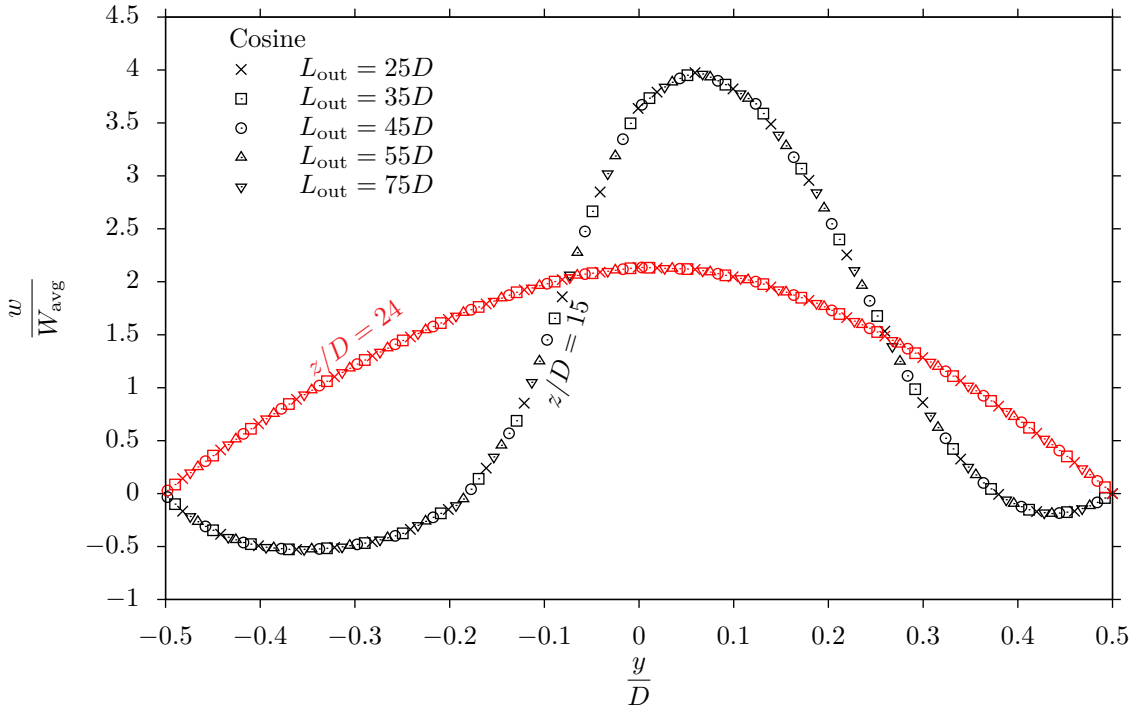

(a)

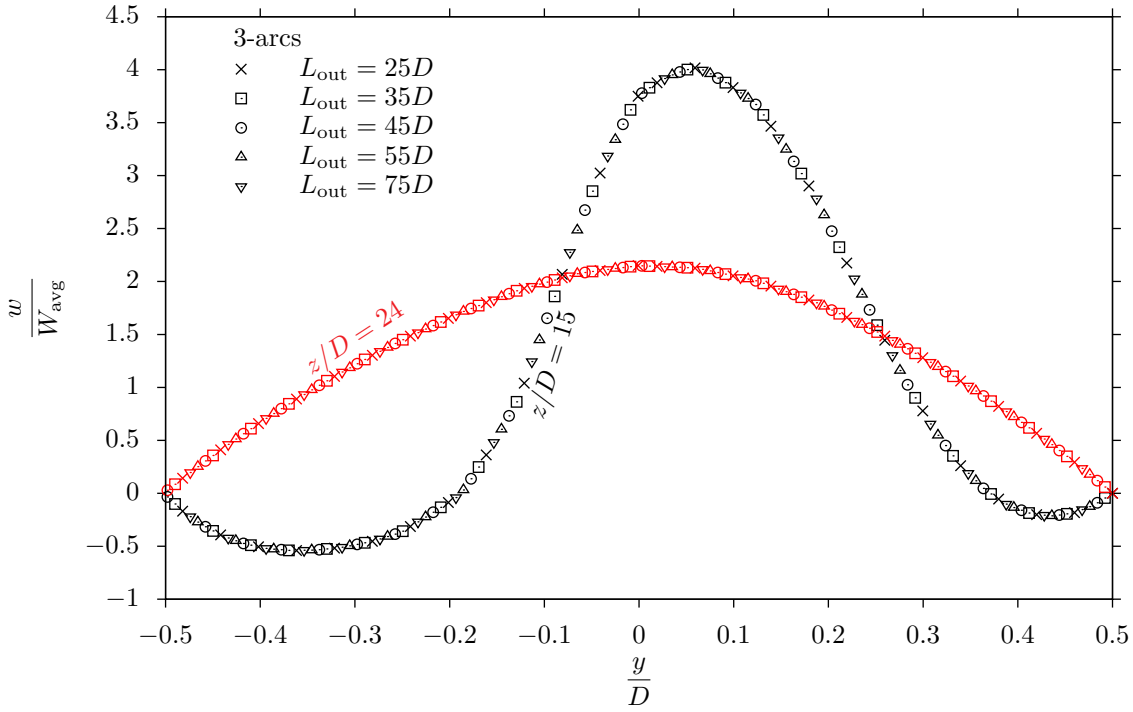

(b)

FIGURE 4.7 Axial velocity profiles in the longitudinal plane yz at $Re = 400$ and $E = 0.0025$ for both geometries: (a) cosine stenosis; (b) 3-arcs stenosis. Two axial positions are presented: $z/D = 5$ (black symbols) and $z/D = 24$ (red symbols).

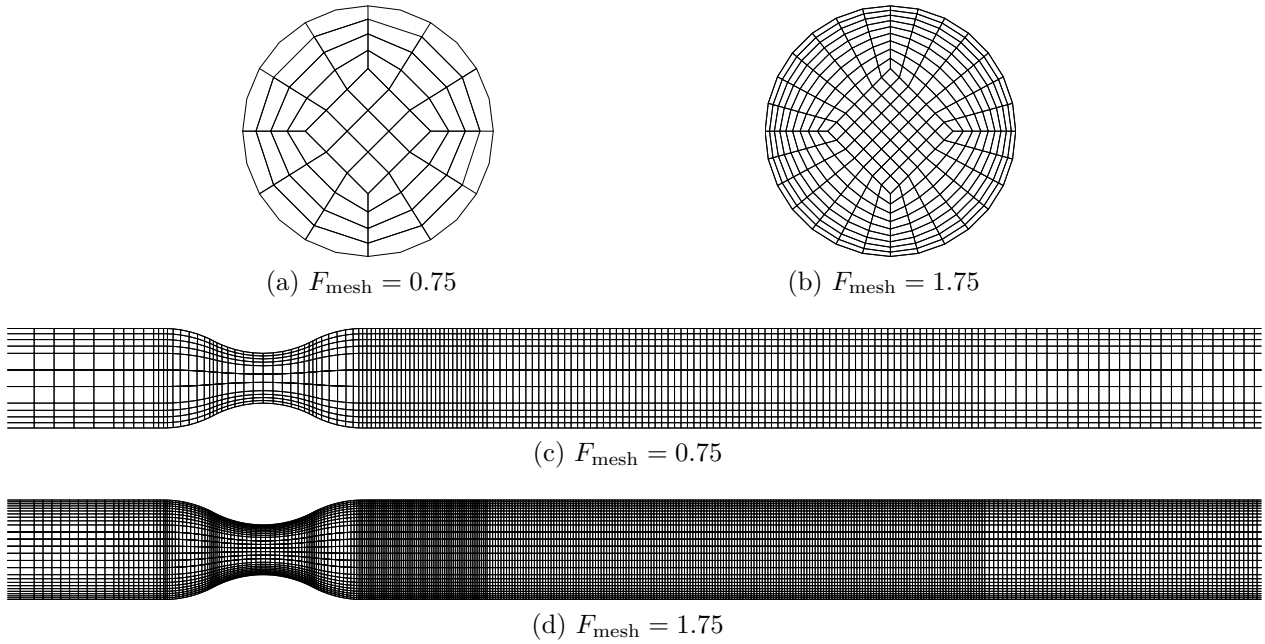

(a) $F_{\text{mesh}} = 0.75$ (b) $F_{\text{mesh}} = 1.75$

(c) $F_{\text{mesh}} = 0.75$

(d) $F_{\text{mesh}} = 1.75$

FIGURE 4.8 Effects of the refinement factor F_{mesh} over the density and distribution of elements in an stenosis. (a) and (b) are transversal views of the mesh at respectively $F_{\text{mesh}} = 0.75$ and $F_{\text{mesh}} = 1.75$. (c) and (d) are longitudinal cuts at respectively $F_{\text{mesh}} = 0.75$ and $F_{\text{mesh}} = 1.75$.

reattachment length Z_R is defined as the maximum of all these coordinates, *i.e.* the maximum length of the recirculation region. Figure 4.9 depicts graphically this definition for Z_R when neither the velocity profiles nor the separated region are non-axisymmetric.

Figure 4.10 exposes the relation between the refinement factor and the reattachment length for the meshes presented in Table 4.2. For both geometries, there is a significant amount of dispersion for the whole range of Reynolds number. This behaviour contrasts with the correlation observed in the axisymmetric stenosis in Figure 3.12, where low dispersion is observed at low Reynolds, and this dispersion progressively increases with the Reynolds number. Moreover, for the axisymmetric stenose, the reattachment length increased almost linearly with Re, but here for both geometrical descriptions of the eccentric stenosis, Z_R increases in a steeply manner, to then stabilize in an almost asymptotic way. This change in the relation between the reattachment length and the Reynolds number is a well known phenomena after transition to the turbulent regime (Armaly *et al.*, 1983; Yang *et al.*, 1994). Herein, as it is a laminar regime, it certainly occurs due to the presence of the eccentricity within the stenosis. Hence, it is natural to expect a dependency of the horizontal asymptote of Z_R with the level of eccentricity E.

At $Re \simeq 350$ some meshes present a discontinuity in the data. Indeed, in some cases it was

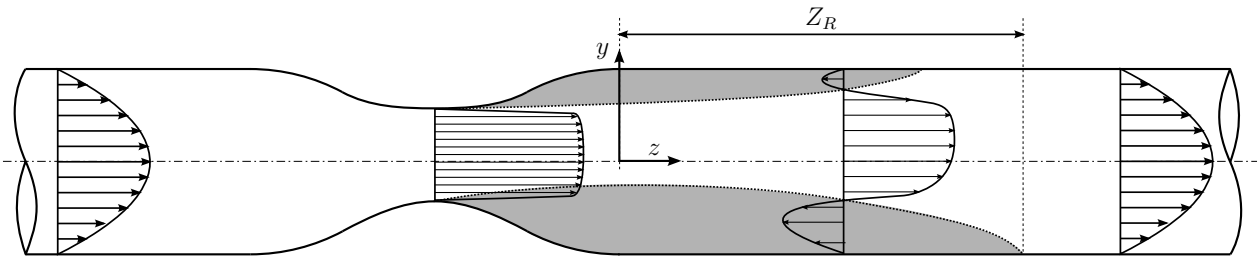

FIGURE 4.9 Definition of the reatttachment length Z_R for the geometry of the eccentric stenosis. The shaded region represents the separated region. Z_R represents a measure of the maximum length of the separated region.

not possible to reach a converged steady-state solution during the process of computation through incremental Reynolds number. The fact that these discontinuity occurs at a similar Reynolds number where Vétel *et al.* (2008) reported their asymmetric phenomena is discussed thoroughly in Section 4.8.

The insets of Figure 4.10 present the variation of the reattachment length with the refinement factor at a constant Reynolds number of $Re = 400$. Firstly, the value of Z_R at $F_{\text{mesh}} = 0.75$ is way off the tendency described by the other meshes. The reattachment length requires an accurate prediction of the wall shear stress to produce reliable results. And considering that the resolution of the mesh with $F_{\text{mesh}} = 0.75$ is quite low, this off-point is ignored. With the remaining data, in both geometries the reattachment length reaches a plateau for $F_{\text{mesh}} > 1.50$, an observation consistent with the results of Section 3.4.2 for the axisymmetric stenosis. However, the value of Z_R with $F_{\text{mesh}} = 1.2$ has less than 1% of deviation from the value at $F_{\text{mesh}} = 1.75$. Hence, selecting $F_{\text{mesh}} = 1.2$ is still reasonable, given that it represents about 50% less nodes than the mesh with $F_{\text{mesh}} = 1.5$. Besides, in Section 3.4.2 it was also established that within a stenosis, the computation of stability with a coarser mesh predicts a critical Reynolds number at about 2% lower than the actual value. But is is important to check the effect of the geometrical eccentricity over the eigenvalues, to confirm that the previously established relation in axisymmentric geometries remains valid when an eccentricity is added.

For both the cosine and the 3-arcs stenosis, Figure 4.11 presents the computation of eigenvalues at $Re = 350$ with the meshes in the range $1.2 < F_{\text{mesh}} < 1.75$ from Table 4.2. The results are quite similar, especially concerning the first few eigenvalues. Tuckerman and Barkley (2000) recommends the computation of more eigenvalues than the required number, to increase the size of the Krylov subspace and decrease the error in the leading eigenvalues. Hence, differences beyond the third or fourth eigenvalue are expected. That's the case of the complex

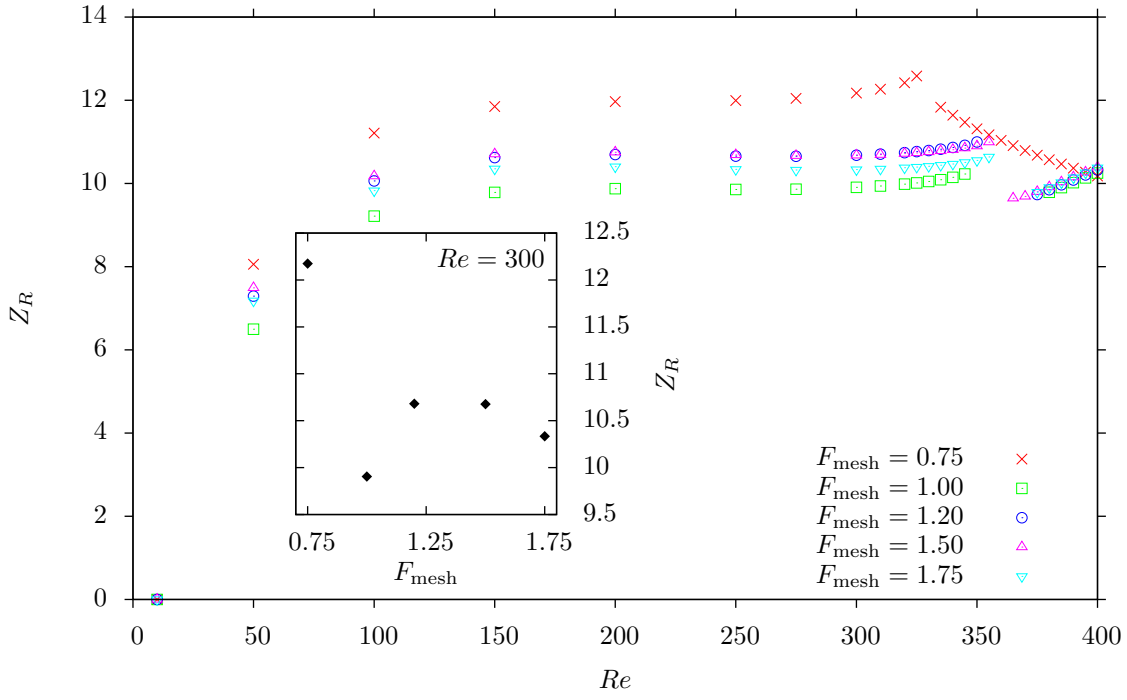

(a)

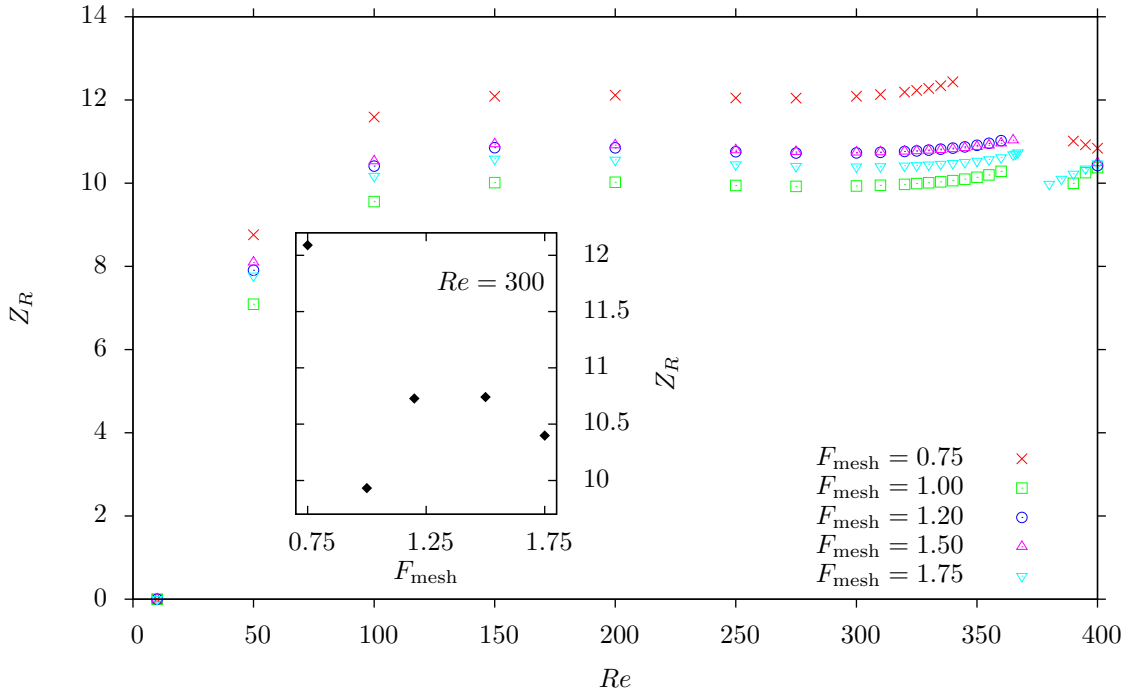

(b)

FIGURE 4.10 Effect of the refinement factor F_{mesh} over the reattachment length at different Reynolds numbers. The insets present this variation at $Re = 400$. (a) shows the data for a cosine stenosis and (b) presents the results in the 3-arcs stenosis.

pair of eigenvalues observed in Figure 4.11a for the cosine stenosis. But for the leading eigenvalue, good agreement is obtained between the results of the different meshes.

Figure 4.11c shows the dependency between the real part of the leading eigenvalue for each mesh as a function of the refinement factor F_{mesh}. And similarly to the case of the axisymmetric stenosis from Section 3.4.2, the coarser mesh produces a more critical eigenvalue, but still close to the value obtained with a more refined mesh. The inclusion of eccentricity produced a smaller difference in the leading eigenvalue between the meshes with $F_{\text{mesh}} = 1.2$ and $F_{\text{mesh}} = 1.75$, being smaller that in the axisymmetric case. Consequently, due to these similitude and the low deviation in the reattachment length obtained with the mesh of $F_{\text{mesh}} = 1.2$, this mesh is selected to compute the simulations that are presented in the following sections, saving memory and time due to the reduced computational cost of this mesh.

Figure 4.12 present the comparison of the results of Griffith *et al.* (2013) against both stenosis with $F_{\text{mesh}} = 1.2$ and $F_{\text{mesh}} = 1.75$, in terms of the normalized asymmetry index μ_r. In all cases, the data follow the same tendency, with the local maximum deviation placed at the same axial position z/D. The asymmetry index however presents slower convergence than the velocity profiles previously analyzed. Indeed, in the cosine stenosis the refinement of the mesh produces μ_r results that are closer to the curve of Griffith *et al.*, but still, the maximum divergence between them is about 2% and hence, an even more refined mesh would be required to further close this gap. However, the mesh convergence analysis already conducted determined that further refinements would not produce important changes in the results. Hence, although attractive, the asymmetry index would be a much more restrictive variable to check the accuracy of the results, specially when comparing with the results computed by Griffith *et al.*. In their research they used a high-order spectral element technique, and any attempt to reproduce the accuracy of their results using quadratic finite elements would require a mesh whose computational cost will exceed the currently available capabilities of this research group.

Regarding the 3-arcs geometry, the difference in magnitude of the asymmetry index μ_r between the 3-arcs and the cosine stenosis are quite significant. It was previously stated in Figure 4.7 that the peak velocity at $z/D = 5$ was 1% higher in the 3-arcs geometry. This difference is again enhanced in the μ_r data to about 20%. Hence, the relatively large difference in the peak of μ_r do not represent a radically different flow field between the two geometries. However, the asymmetry index μ_r proved helpful to characterize differences observed in the stability regime between the two geometries, as presented in what follows.

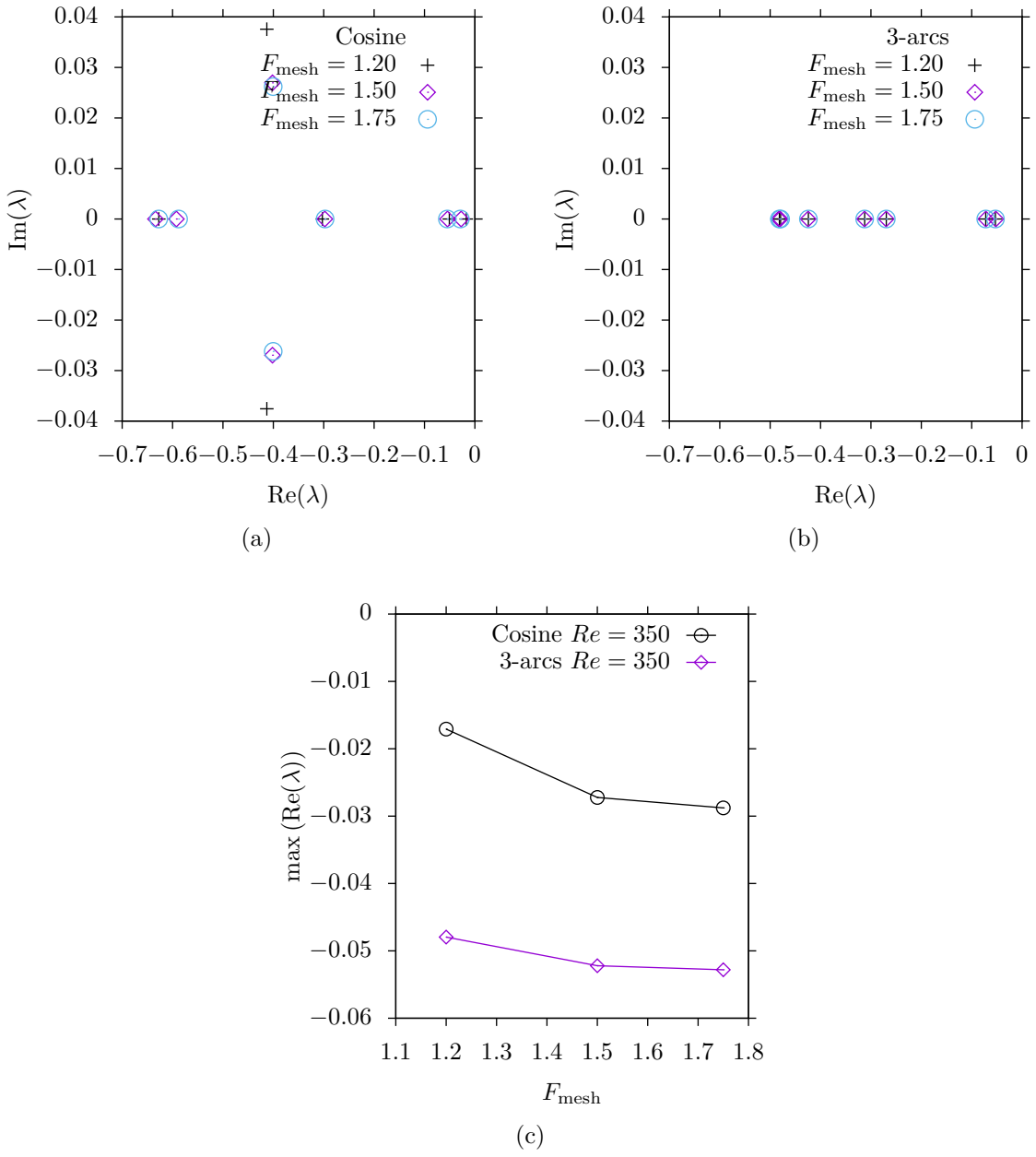

FIGURE 4.11 Comparison of eigenvalues at $Re = 350$ in both geometrical descrriptions of the stenosis with different meshes. (a) and (b) show respectively the cosine and the 3-arcs stenosis. (c) is the plot the leading eigenvalue as a function of the refinement factor.

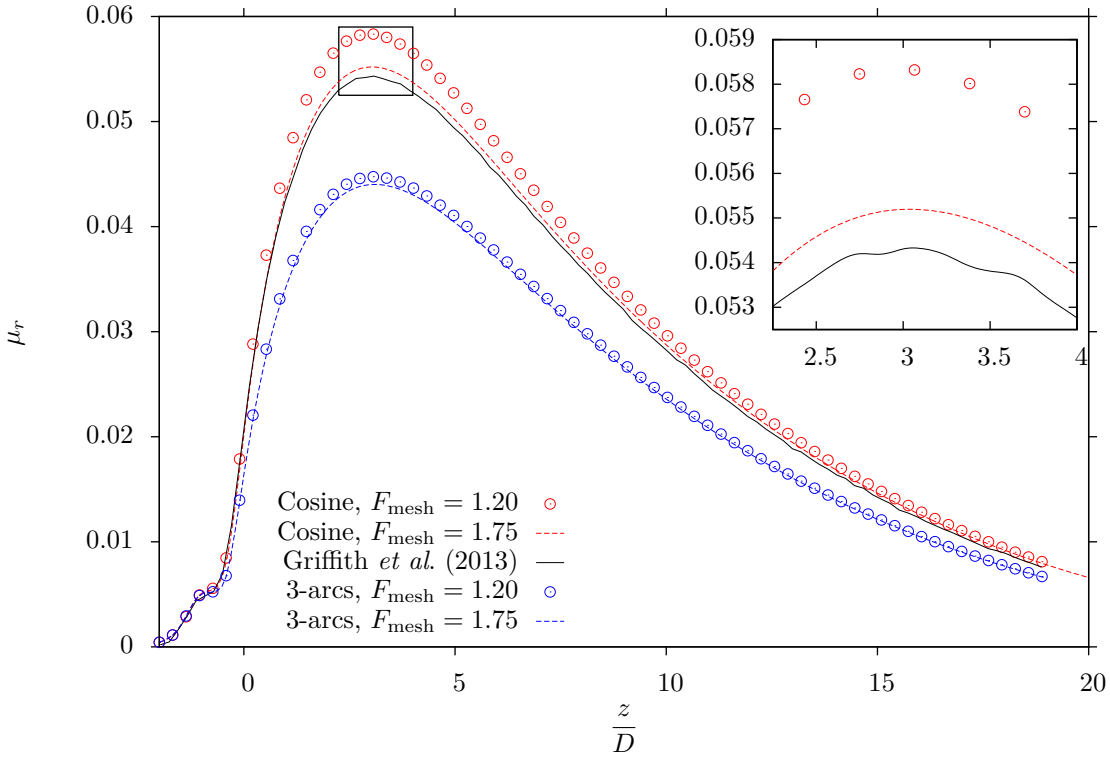

FIGURE 4.12 Comparison of μ_r from the cosine and 3-arcs stenoses against the results of Griffith *et al.* (2013) at $Re = 350$ and $E = 0.0025$ with $F_{\text{mesh}} = 1.20$ and 1.75.

4.7 Bifurcation in eccentric stenoses

In Figure 4.10 it was already discussed the presence of a bifurcation at around $Re \simeq 350$, when the flow is characterized though the reattachment length. However, in this case it is more convenient to use the normalized asymmetry index μ_r proposed by Griffith *et al.* (2013) and defined by Equation (4.4). This variable provides a local cross-sectional measure of the level of asymmetry in the flow. The process to obtain the bifurcation diagram is presented in the cosine stenosis with $E = 0.0025$, and then is repeated with the 3-arcs stenosis. Comparisons and conclusions are presented afterwards.

As explained earlier, to obtain a steady solution at $Re = 350$, the viscosity used in the simulation was progressively decreased in successive stages to effectively increase the Reynolds number, and a converged steady solution for each step was obtained that was then used as initial approximation of the solution for the next Reynolds number. However, non converged solutions appeared in the range of $350 \leq Re \leq 400$. An increased number of Reynols steps were computed within this range, until a smaller range of non-convergence was obtained ($352 < Re < 365$). This procedure of solution for increasing Reynolds number is denoted Re_{up}. The maximum value of asymmetry ($\mu_{\max}$) at each Reynolds number is presented in Figure 4.13. This constitutes a bifurcation diagram, given that it presents a variable characteristic of the flow ($\mu_{\max}$) as a function of an input parameter (Re). The abrupt increase in the behavior of $\mu_{\max}$ in the region covered by the inset plot is remarkable, until the solution eventually stops converging for $Re > 352$. The convergergence is then recovered for $Re \geq 365$, with a significant higher value of asymmetry and change in the slope of the curve. All of this indicates a strong change in the topology of the solution, as shown in Figure 4.14. Here, the velocity contours at $Re = 365$ show a larger degree of asymmetry that at $Re = 352$. The spatial structure of this flow is remarkably similar to the one reported experimentally by Vétel *et al.* (2008). It is then possible to speak about a bifurcation point at $Re = 352$, with the solution at $Re = 365$ belonging to a different branch of the bifurcation diagram. This affirmation will be confirmed later through the stability analysis.

Afterwards, the same solution process is repeated, but in the opposite direction, decreasing the Reynolds number in successive steps, using as initial solution the one obtained at higher Re, in a process denoted Re_{down}. In this case, the solutions followed a different path, as presented in Figure 4.15. An hysteresis phenomena appears, where two steady solutions could be obtained under the same conditions in the range $343 \leq Re \leq 352$, depending on the integration and solution history, whether increasing or decreasing Reynolds number.

The linear stability analysis produces interesting results about these solutions. The leading

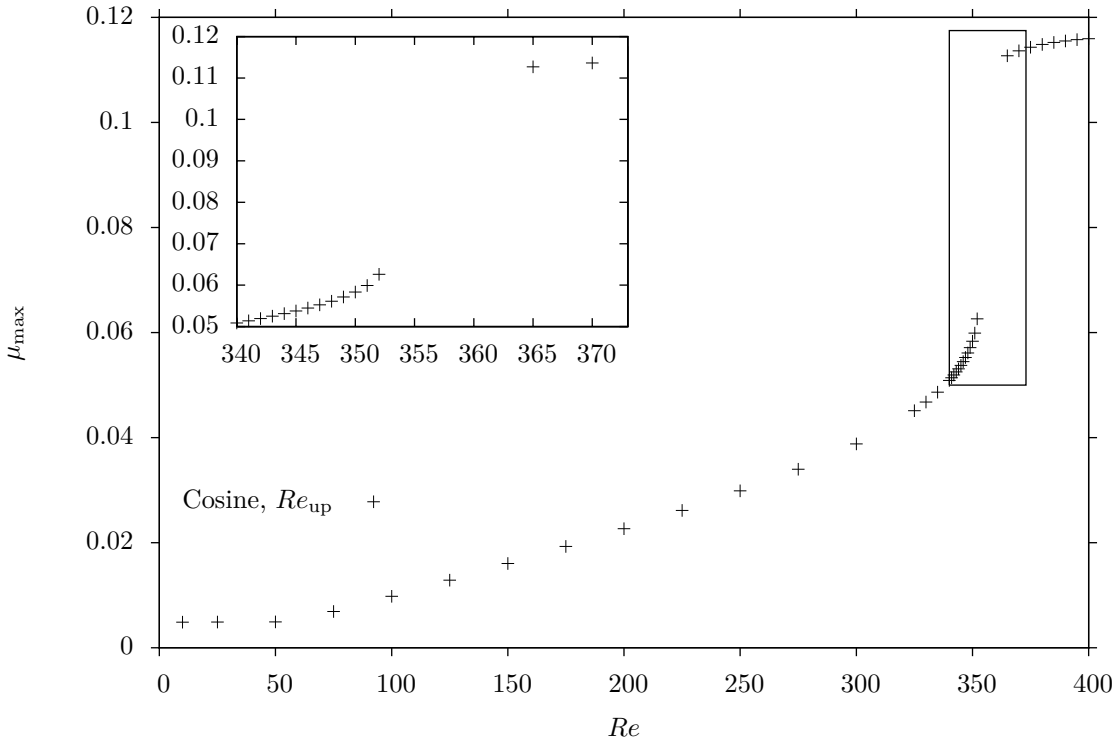

FIGURE 4.13 Maximum asymmetry $\mu_{\max}$ as a function of the Reynolds number for the cosine stenose. Increasing Reynolds number.

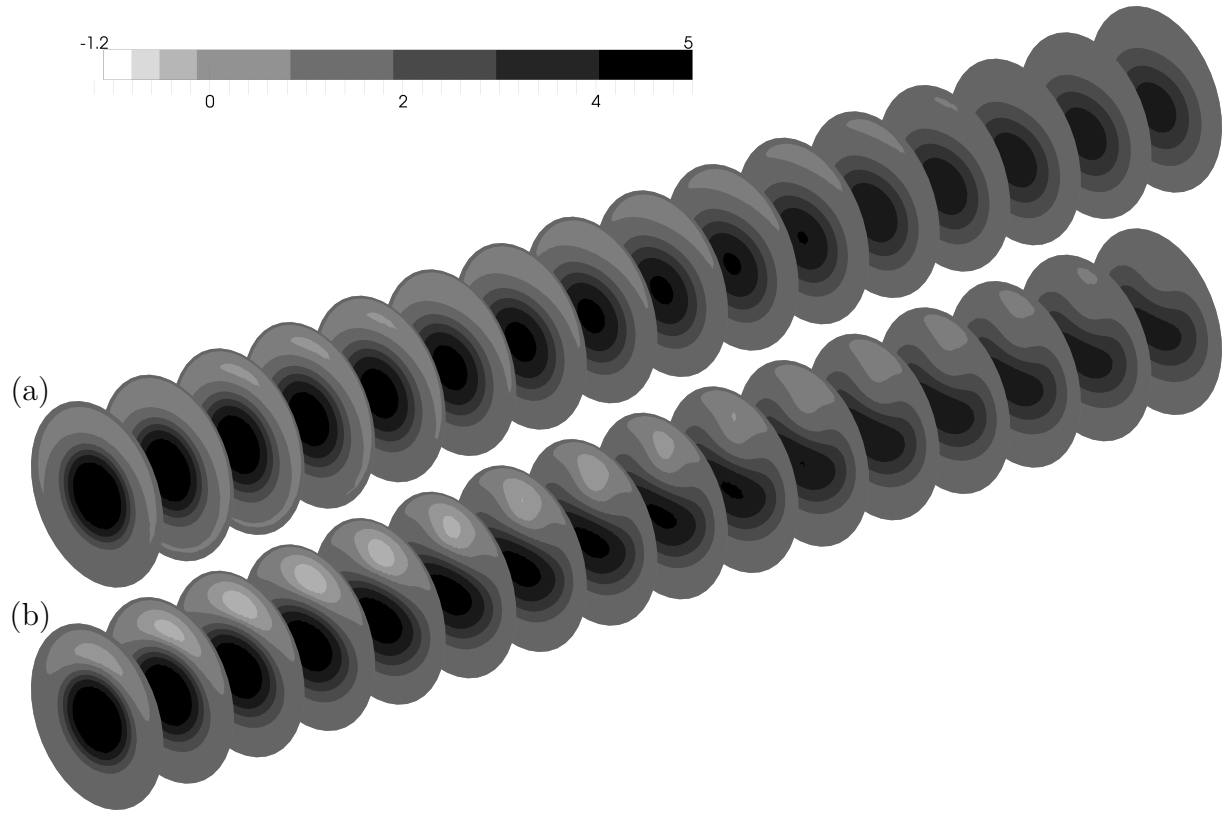

FIGURE 4.14 Slices of normalized axial velocity for the cosine stenosis at: (a) $Re = 352$ and (b) $Re = 365$, showing a remarkable difference in the structure of the flow.

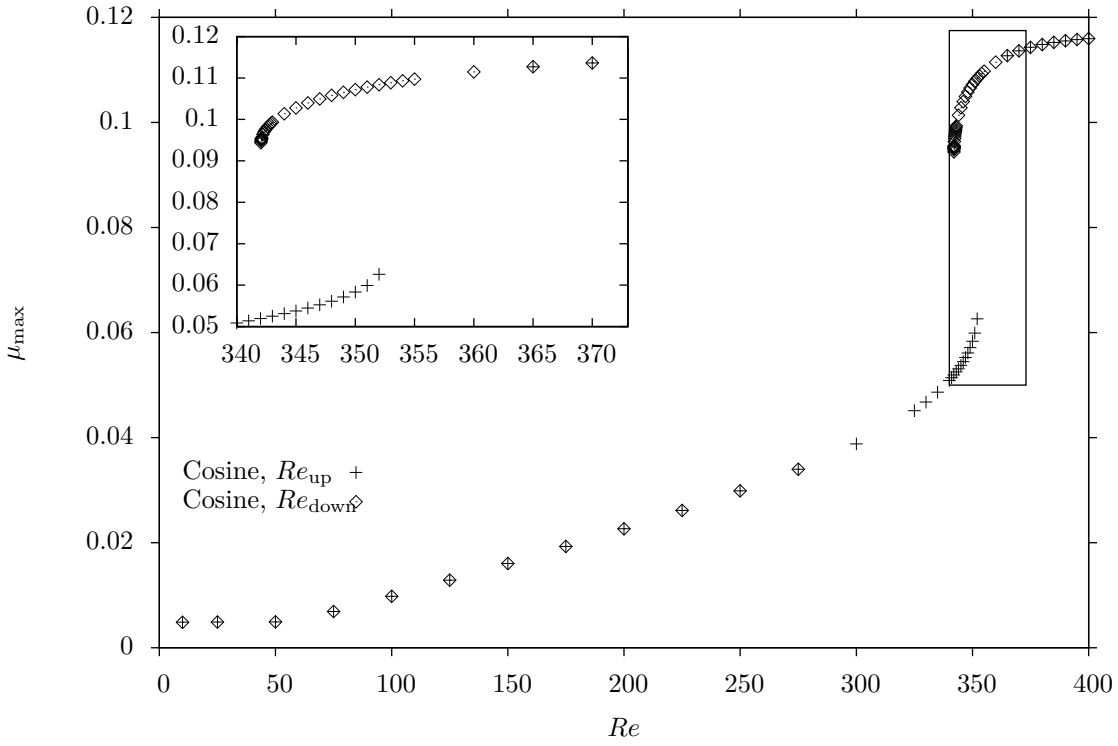

FIGURE 4.15 Maximum asymmetry $\mu_{\max}$ as a function of Reynolds number for the cosine stenose. Increasing and decreasing Reynolds number.

TABLE 4.3 Selected eigenvalues from the linear stability analysis for the cosine stenose.

	Integration Path			Integration Path	
Re	Re_{up}	Re_{down}	Re	Re_{up}	Re_{down}
342	-0.041019	$^{n/a}$	348	-0.024432	-0.002603
342.04	$^{n/c}$	-0.000527	349	-0.020978	-0.002229
343	-0.038545	-0.005651	350	-0.017074	-0.001886
344	-0.035986	-0.004708	351	-0.012354	-0.001566
345	-0.033325	-0.004031	352	-0.005181	-0.001266
346	-0.030538	-0.003484	353	$^{n/a}$	-0.000983
347	-0.02759	-0.003017	365	0.001706	0.001706

$^{n/a}$ The result is not available. A steady state solution could not be obtained at this condition.

$^{n/c}$ The eigenvalues were not computed, given that the solutions at $Re = 342$ and $Re = 343$ are both stables.

eigenvalues for each solution are presented in graphical form in Figure 4.16, while some selected values are tabulated in Table 4.3. It is clear that within the range of the hysteresis loop of Figure 4.15 ($343 \leq Re \leq 352$), there are two *linearly stable* solutions for each Reynolds number. This confirms the remarks made by Sherwin and Blackburn (2005), who regarded the symmetry-breaking phenomena as a subcritical bifurcation, only that in the present case it is a steady solution. The added geometrical eccentricity forces the flow towards one of the branches, and according to the classification of Benjamin (1976), in the present case this would be a *transcritical* or *asymmetric subcritical* bifurcation (see Figure 2.2c).

The real part of the leading eigenvalues for the decelerating branch Re_{down} decreased with the Reynolds number in the range where the two stable solutions exist. However, they increased in a sudden manner as the Reynolds approach $Re = 342$, effectively causing this solution branch to becomes unstable. The theory indicates that an unstable branch should exists joining the two branches on the bifurcation diagram shown on Figure 4.16, from the pitchfork bifurcation at $Re_{\text{up}} = 352$ to the turning point at $Re_{\text{down}} = 342.04$. Several attempts were made to compute it, using steady and unsteady solvers, without success. In both cases, the computation converged to either the top or the bottom stable branch. Thus, no further remarks about this unstable branch could be inferred.

As discussed previously with Figure 4.14, the asymmetric velocity fields in the two branches present important differences, a fact that it is evident from the huge jump of almost 100%

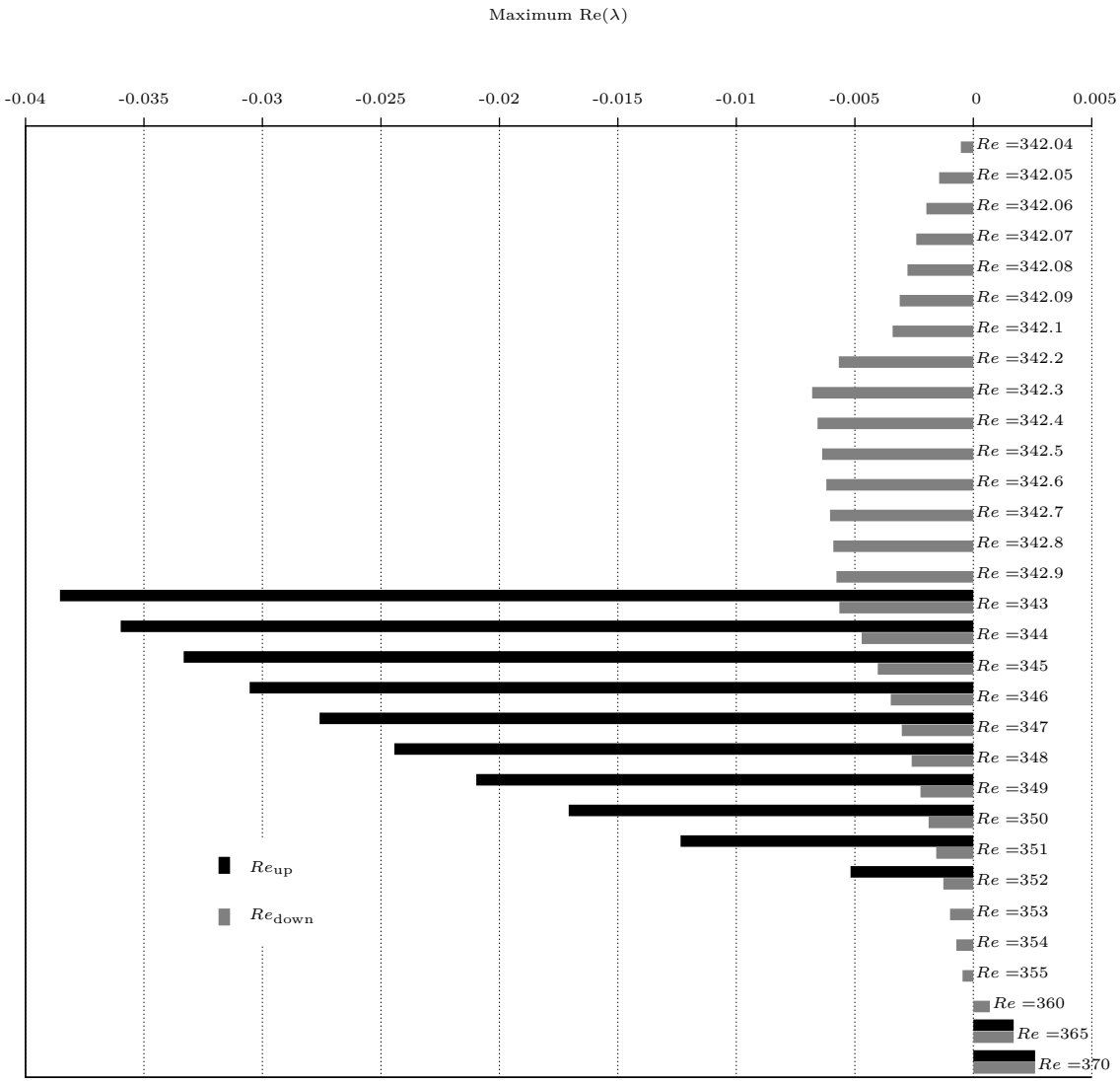

FIGURE 4.16 Real part of the critical eigenvalues for ascending and descending Reynolds numbers in the cosine stenose.

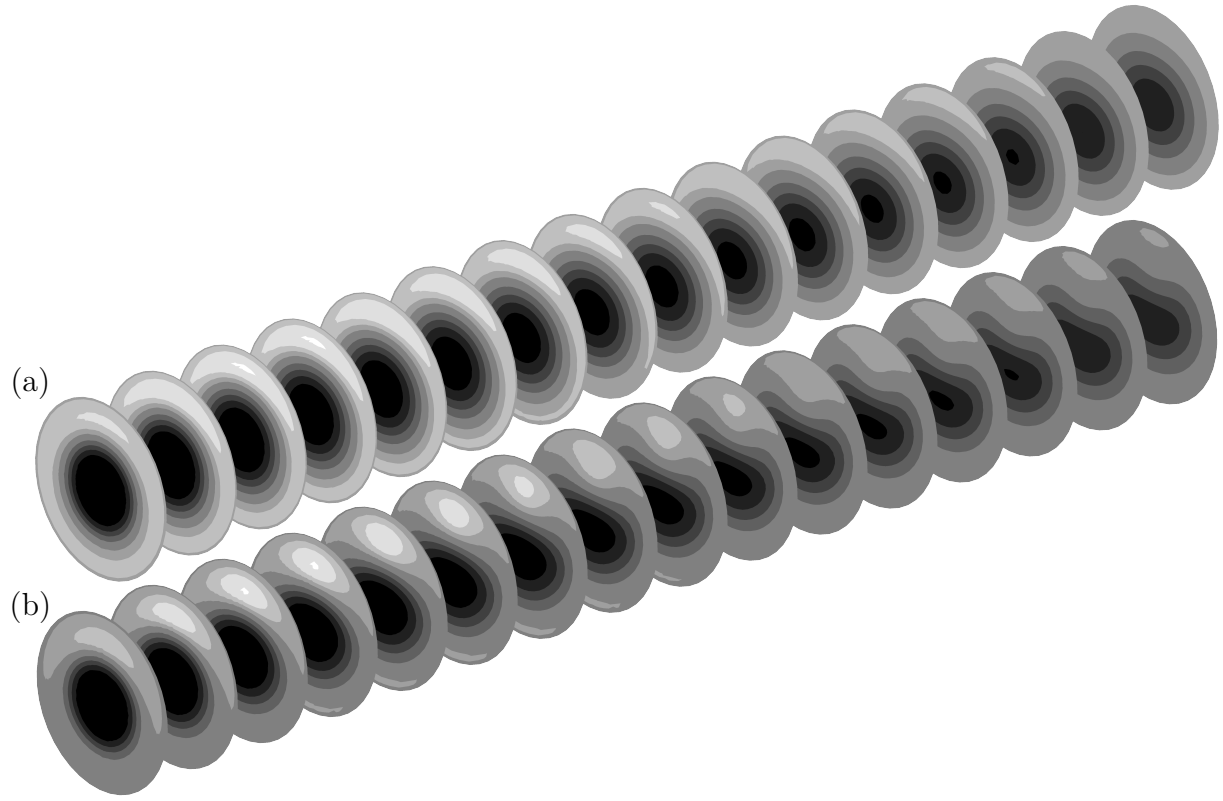

FIGURE 4.17 Qualitative comparison of the axial velocity contours for the two stable solutions at $Re = 350$ in the cosine stenosis: a) ascending Reynolds number; b) descending Reynolds number.

in the bifurcation diagram for $\mu_{\max}$. Figure 4.17 shows the transverse slices of axial velocity in the downstream region of the cosine stenosis at $Re = 350$ for the two stable branches of ascending and descending Reynolds numbers. The velocity contours of Figure 4.17b present great resemblance to the ones reported by Vétel *et al.* (2008), although they used a 3-arcs stenosis instead of a cosine one.

From the point of view of the μ_r coefficient, a comparison between the two steady stable solutions at $Re = 350$ is plotted in Figure 4.18. Additionally, the Griffith *et al.* (2013) results were included as a reference, which have a similar level of μ_r to the Re_{up} branch. Thus, they reported results before the occurrence of the pitchfork bifurcation bifurcation.

Another important remark could be made regarding these solution branches. Both solutions Re_{up} and Re_{down} have identical leading eigenvalues at $Re = 365$. However, this is a positive value, meaning that this solution is already unstable. From Figure 4.16 it can be seen that Re_{down} becomes unstable at $Re \simeq 357$. Thus, another bifurcation point exists for this asymmetrical branch at this condition. Using the velocity modes at $Re = 355$ and shown

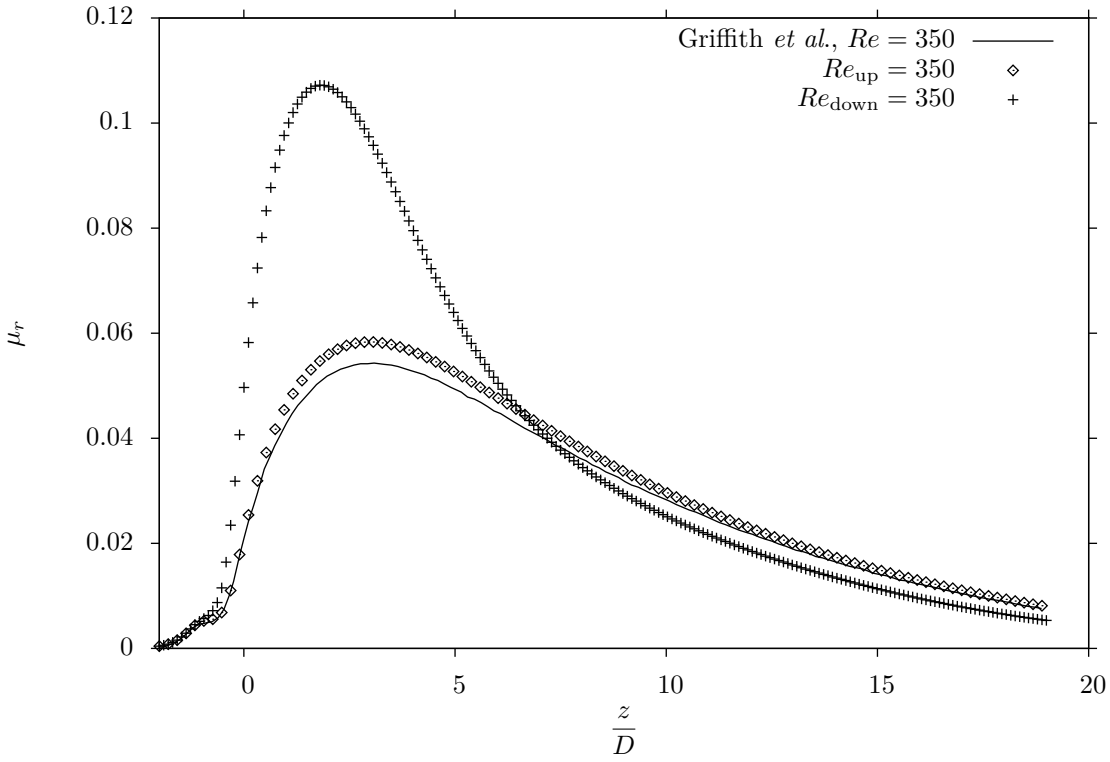

FIGURE 4.18 Comparison of normalized asymmetry μ_r in the cosine stenose for both branches of the bifurcation (Re_{up} and Re_{down}).

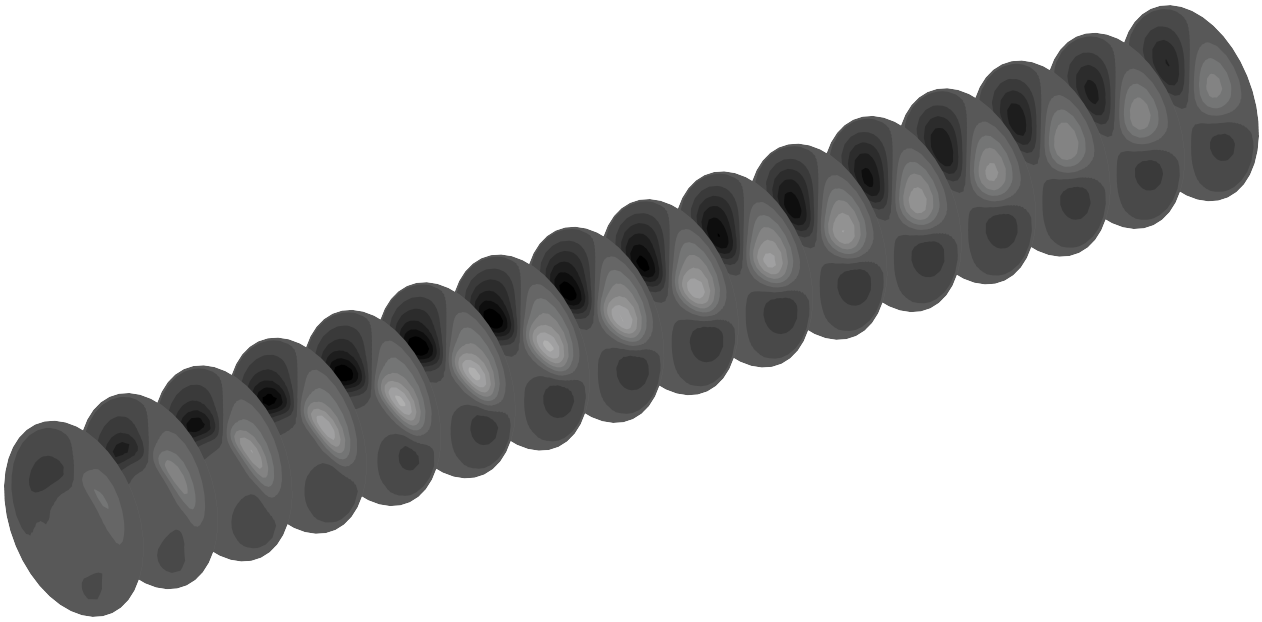

FIGURE 4.19 Most critical velocity mode for the Re_{down} branch at $Re = 355$ for the cosine stenose.

on Figure 4.19 as perturbation for the already unstable Re_{down} solution at $Re = 360$, it was possible to converge to a stable solution. From the velocity modes, it is possible to discern that this unstable mode would contribute to the development of an azymuthal component in the flow. Indeed, Figure 4.20 shows that the new stable solution at $Re = 360$ presents an identical axial behaviour of μ_r, but the azymuthal position of the point of maximum asymmetry θ_μ, given by Equation (4.5), varies with the axial position z/D, which means that the solution has developed an helical component. This rotation is very weak, and is not evident in the contours of velocity. But the change in the velocity field is enough to stabilize this new solution.

Griffith *et al.* (2013) constructed their bifurcation diagram using the normalized eccentricity E as parameter, instead of the Re number. Hence, for completeness a similar study is presented in the next section.

4.7.1 Influence of Eccentricity

In contrast with the work of Varghese *et al.* (2007), who used one fixed large value of eccentricity in their study ($E = 0.05$), Griffith *et al.* (2013) evaluated the effects that a wide range of eccentricities within the stenosis have over the flow asymmetry. To achieve that, they studied values of $E \in [0.0001, 0.1]$, reporting the maximum asymmetry $\mu_{\max}$ as a function

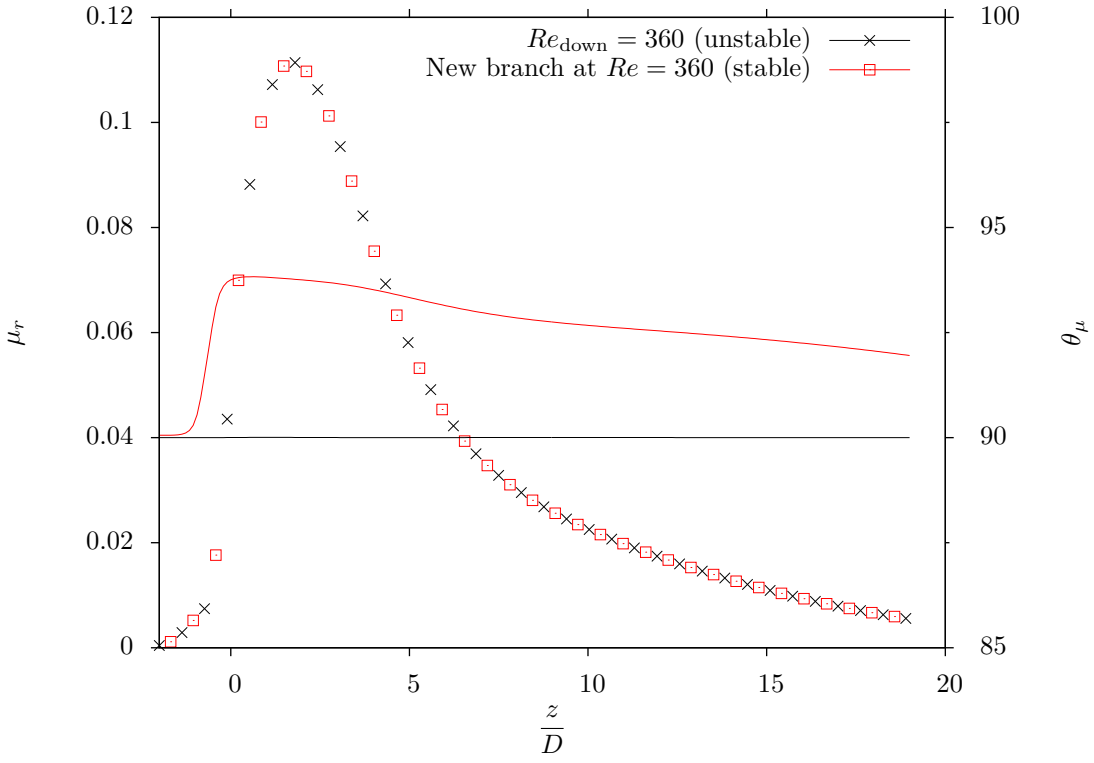

FIGURE 4.20 Comparison of normalized asymmetry μ_r and the angular position of the velocity peak in the cosine stenose at $Re = 360$ for the additional branch uncovered.

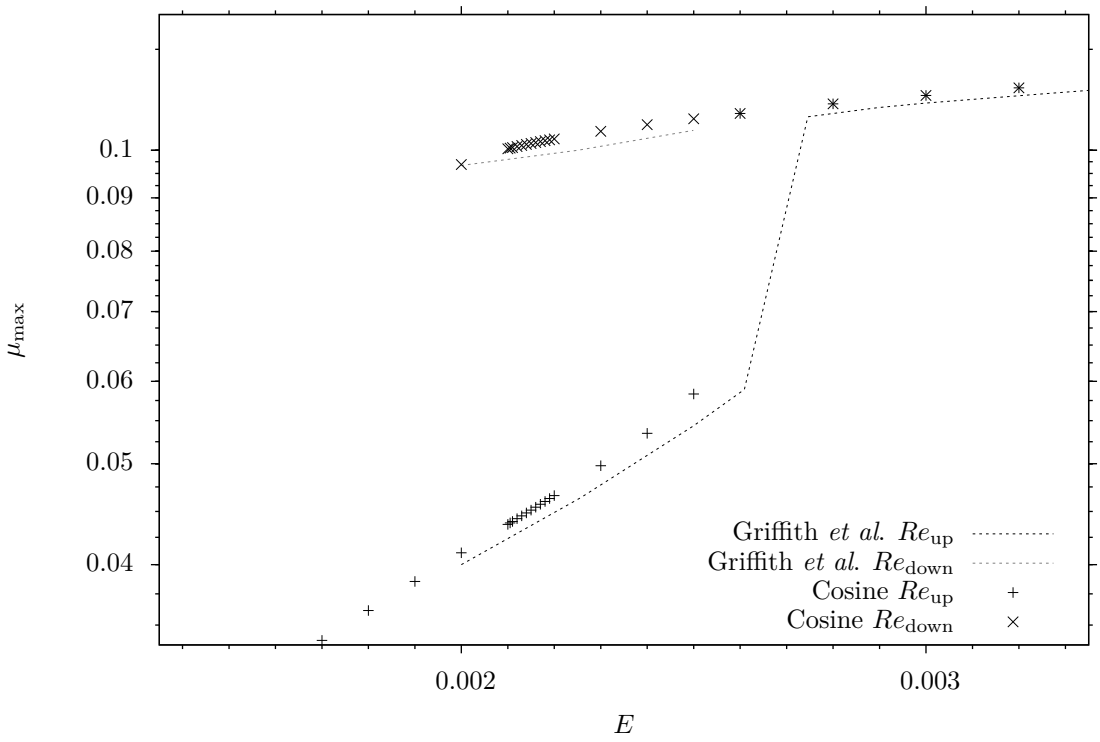

FIGURE 4.21 Maximum asymmetry $\mu_{\max}$ as a function of eccentricity E at $Re = 350$ for the cosine stenosis, and comparison against Griffith *et al.* (2013).

of E for different Reynolds numbers. That is actually the only way in which they present the hysteresis phenomenon. A similar study is performed in the present work, within the reduced range of $E \in [0.0005, 0.005]$, where Griffith *et al.* presented detailed results. These are reproduced in Figure 4.21, along with the results obtained within the current research at $Re = 350$. Here, the numerical results obtained followed closely the data reported by Griffith *et al.*. The only difference is the point for Re_{up} at $E = 0.0026$, where Griffith *et al.* reports a value that could not be reproduced. Given that this mesh ($F_{\text{mesh}} = 1.20$) produced results that were on the conservative side, slightly over-predicting the asymmetry index and critical eigenvalue, a flow at $Re_{\text{up}} = 350$ and $E = 0.0026$ could probably be above the critical point for this mesh.

4.8 Bifurcation in the 3-arcs eccentric stenosis

Given that the study of eigenvalues and integration history for the eccentic cosine stenosis produced interesting results regarding the subcritical bifurcation and its related hysteresis loop, an analog study was carried out in the 3-arcs stenosis studied by Vétel *et al.* (2008) and

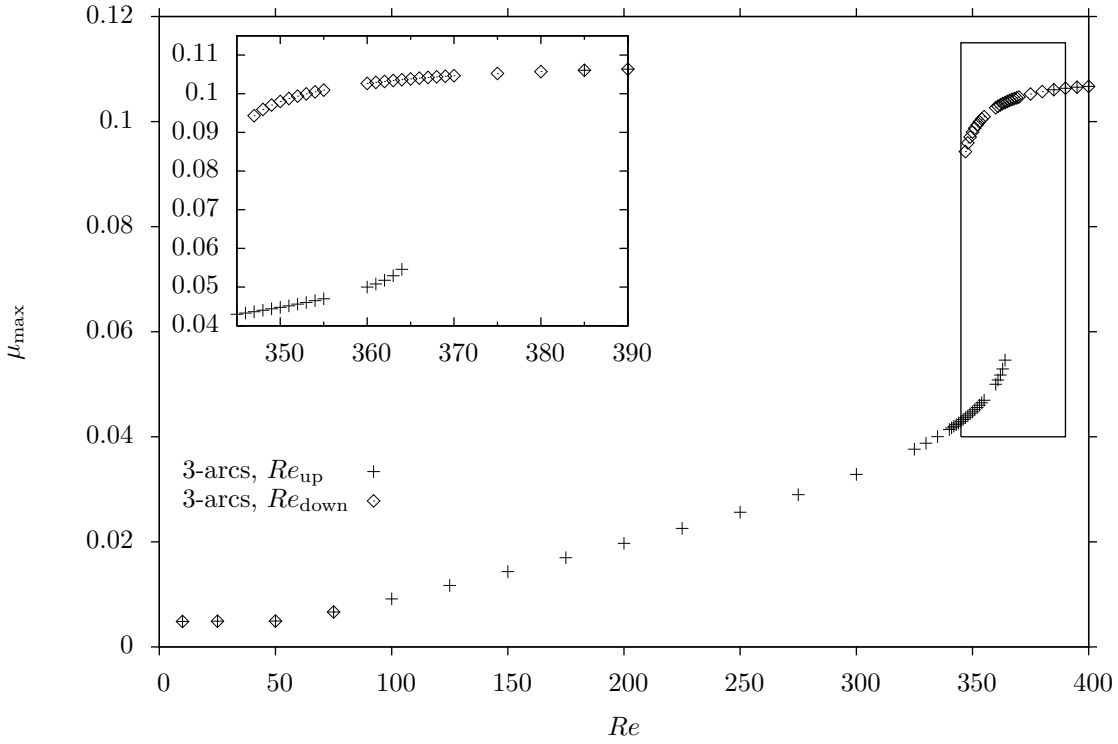

FIGURE 4.22 Comparison of normalized asymmetry μ_r in the 3-arcs stenose for both branches of the bifurcation (Re_{up} and Re_{down}).

whose symmetry-breaking phenomena served as a motivation for the present research.

Using the 3-arcs eccentric stenosis mesh selected in Section 4.6 ($L_{\text{out}} = 25D$, $F_{\text{mesh}} = 1.20$ and $E = 0.0025$) and following an identical approach as the one described in Section 4.7, a range of Re was found where the steady state convergence was not possible for increasing Reynolds numbers. Subsequently, the solutions computed using a decreasing Reynolds number (Re_{down}) followed a different path, as in the case of the cosine stenosis. These solutions are presented in Figure 4.22, comparing the value of $\mu_{\max}$ for increasing and decreasing Reynolds numbers, and where the hysteresis loop is also present, although in the range $347 \leq Re \leq 364$, much narrower than for the cosine stenosis.

Both branches of the solution present sudden changes in the slope in the proximities of the bifurcation point. The Re_{up} solution rises sharply at around $Re = 345$, and stops converging at $Re = 364$. Similarly, the Re_{down} drops at $Re = 360$, stopping its convergence at $Re = 347$. Initially, the hysteresis would be present within this range ($347 \leq Re \leq 364$). However, the computation of the eigenvalues provides further information about the stability of these solutions. The critical eigenvalues for each branch are presented graphically in Figure 4.23,

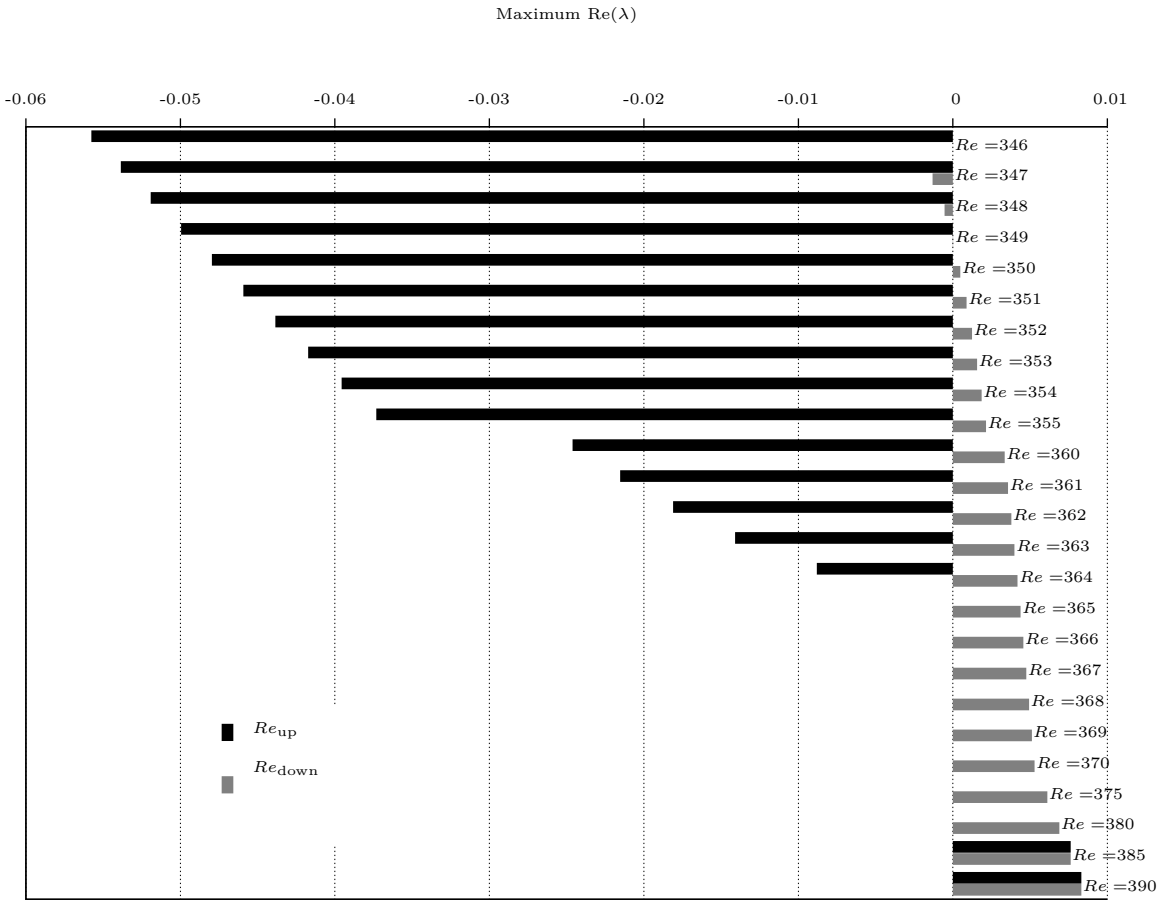

FIGURE 4.23 Real part of the critical eigenvalues for ascending and descending Reynolds numbers in the 3-arcs stenosis.

while selected values are shown in Table 4.4. The axial velocity contours of these two solutions at $Re = 348$ are presented in Figure 4.25.

Several analogies could be established with the case of the cosine stenose. Firstly, the existence of two branches of the solution, with remarkable differences in the flow field, according to the velocity contours presented in Figure 4.25 and values of $\mu_{\max}$ shown in Figure 4.22. There is also a pitchfork bifurcation for the ascending Reynolds branch Re_{up}, in this case at $Re = 364$. And besides these observations, Figure 4.23 also indicates that there exists a Reynolds number range where two solutions branches are linearly stable under the same conditions. However, this range is significantly narrower in the current case: $347 \leq Re < 349$ (given that the eigenvalue at $Re = 349$ for the Re_{down} branch is positive but with a very small value). For the upper branch of the bifurcation diagram (the decreasing Reynolds number Re_{down}), the flow becomes unstable at $Re = 347$, with an additional bifurcation for $Re \geq 349$. This

TABLE 4.4 Selected eigenvalues from the linear stability analysis for the 3-arcs stenosis.

	Integration Path			Integration Path	
Re	Re_{up}	Re_{down}	Re	Re_{up}	Re_{down}
346	-0.055766	$^{n/a}$	350	-0.047958	0.000485
347	-0.053855	-0.001315	364	-0.008806	0.004185
348	-0.051918	-0.000539	365	$^{n/a}$	0.004378
349	-0.049954	0.000019	385	0.007623	0.007623

$^{n/a}$ The result is not available. A steady state solution could not be obtained at this Reynolds.

branch was computed at $Re = 360$ using the most critical velocity mode as perturbation for the asymmetric velocity field. As in the cosine stenosis, this steady solution to the Re_{down} branch with a small azymuthal velocity component. The values of μ_r and θ_μ are presented in Figure 4.24. In this case, the angular displacement of the asymmetry is about twice as big as in the cosine stenosis.

From Figure 4.25, there are evident differences between the Re_{up} and Re_{down} solutions at $Re = 348$. As with the cosine stenosis, the decreasing Reynolds number branch, Re_{down} has a larger asymmetry and recirculation region than the increasing Re_{up} branch. The comparison of the two solutions of Figure 4.25, from the point-of-view of the normalized asymmetry index μ_r, is presented in Figure 4.26, where a remarkable similitude with Figure 4.18 is observed.

The small geometrical differences between the 3-arcs and cosine stenoses have important effects on the topology of the flow, shifting the position of the bifurcation points and changing significantly the range where within the hysteresis loop, the two branches Re_{up} and Re_{down} are both stable. The combination of the pitchfork bifurcation and turning point bifurcation allows the existence of two very distinct solutions at $Re \simeq 350$ for both geometries. Hence, the qualitative behavior is similar. The reduced range of stability for the Re_{down} in both cases also generates a new branch with an azymuthal velocity component. This helical flow arises much earlier in the 3-arcs stenosis ($Re = 347$ vs. $Re = 357$). As evidenced in Figures 4.20 and 4.24, the azymuthal displacement begins inside the stenosis ($z/D < 0$), and thus, the geometrical differences between both geometries become quite relevant in the development of the helical flow, showing a larger intensity at $Re = 360$ in the 3-arcs geometry. Figure 4.27 contains the slices of z-velocity at $Re = 360$ for the 3-arcs stenosis with $E = 0.0025$. A line parallel to the z axis was added to the recirculation region, to help visualize the small

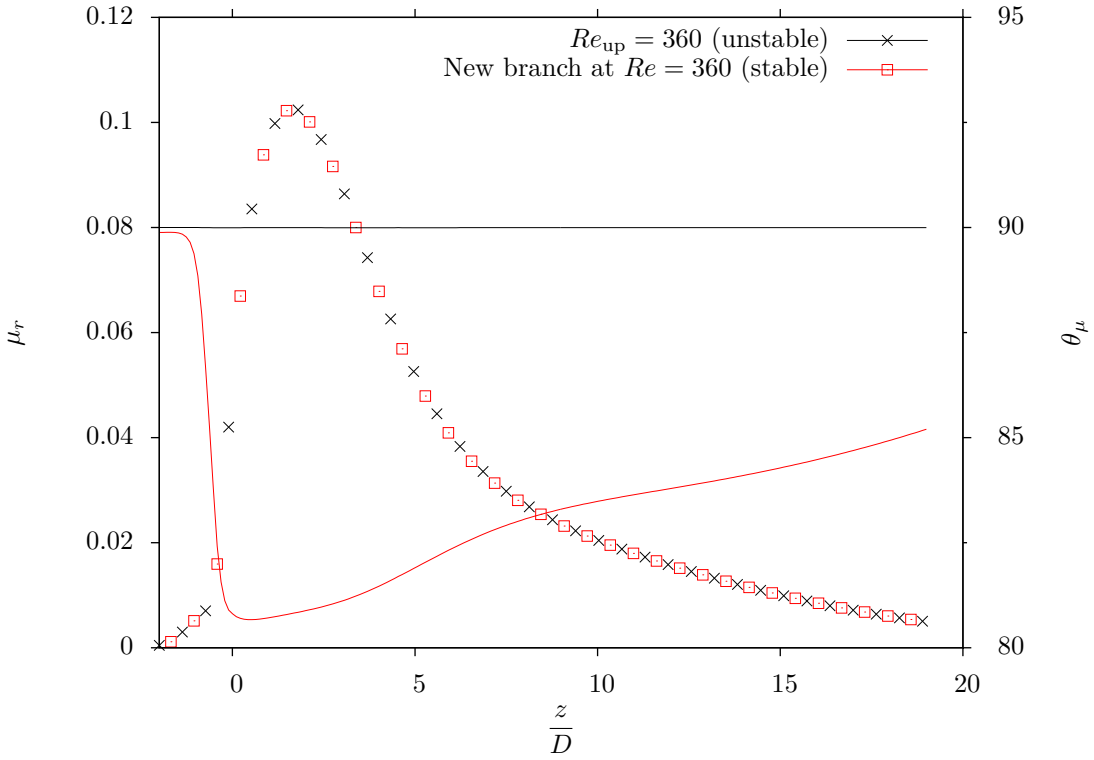

FIGURE 4.24 Comparison of normalized asymmetry μ_r and the angular position of the velocity peak in the 3-arcs stenosis for the Re_{down} and the additional stable branch at $Re = 360$.

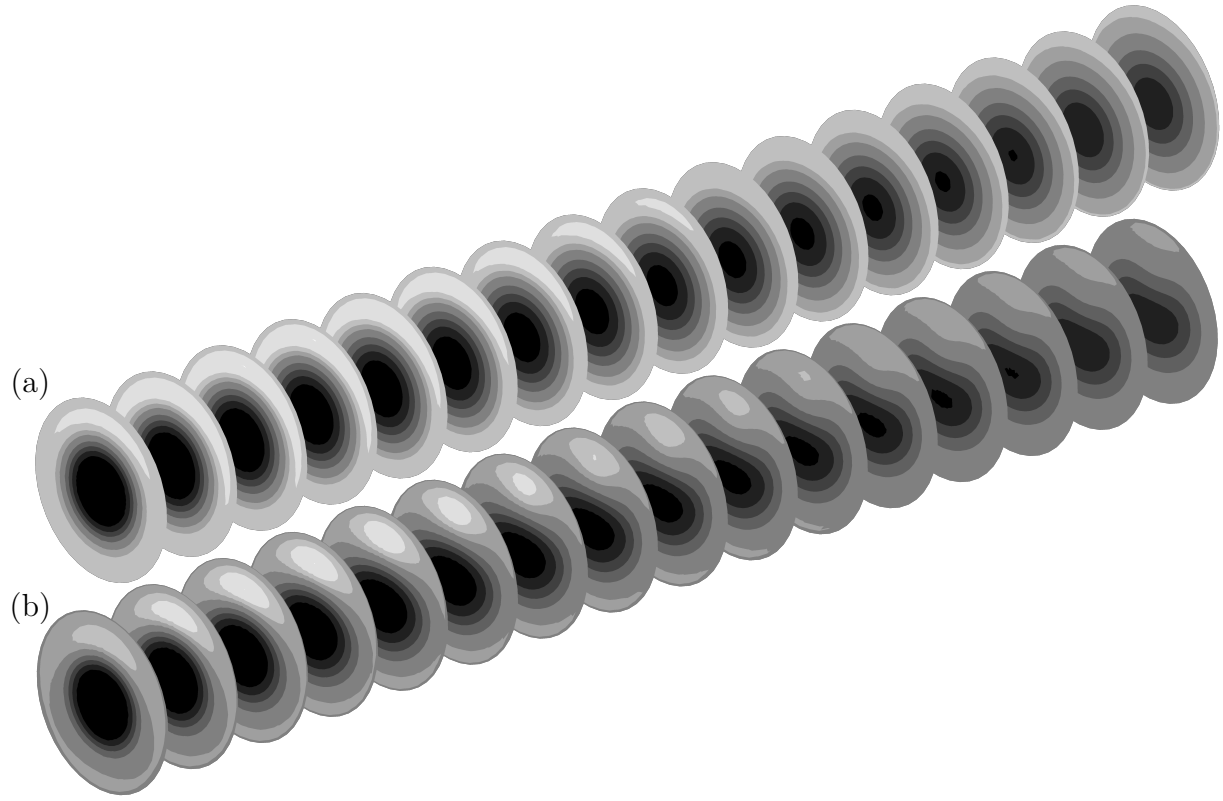

FIGURE 4.25 Qualitative comparison of the axial velocity contours for the two stable solutions at $Re = 348$ and $E = 0.0025$ in the 3-arcs stenosis: (a) Ascending Reynolds; (b) Descending Reynolds.

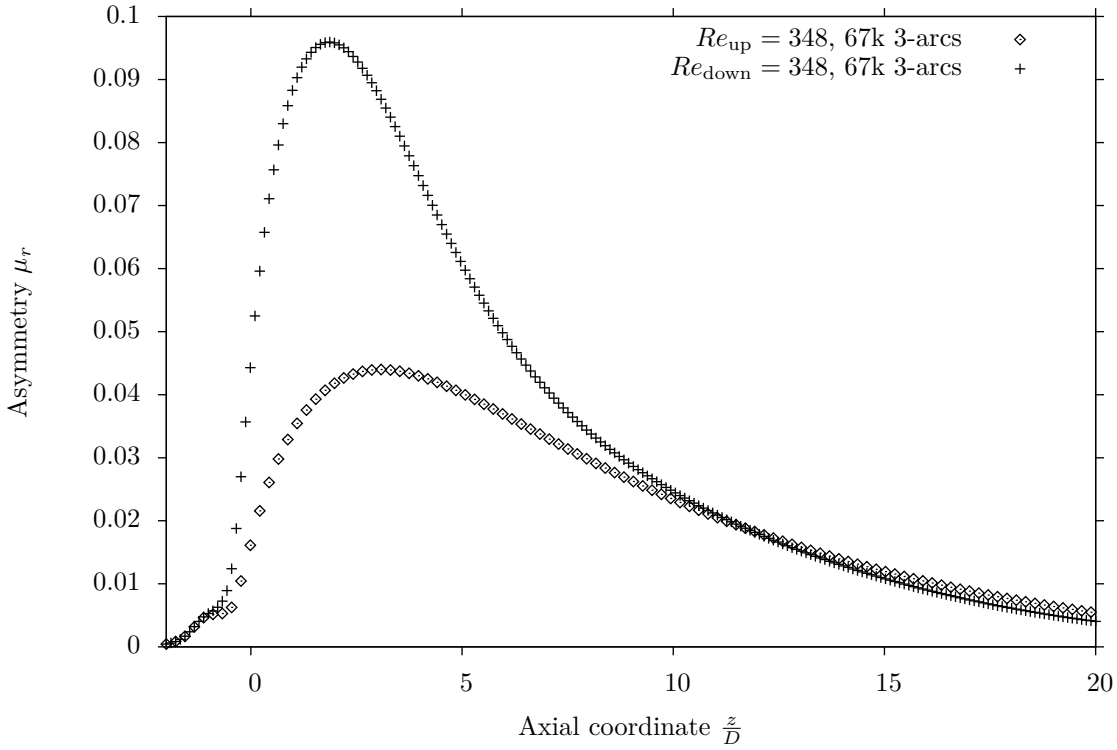

FIGURE 4.26 Normalized asymmetry μ_r as a function of the axial position for the 3-arcs stenose at $Re = 348$ and $E = 0.0025$.

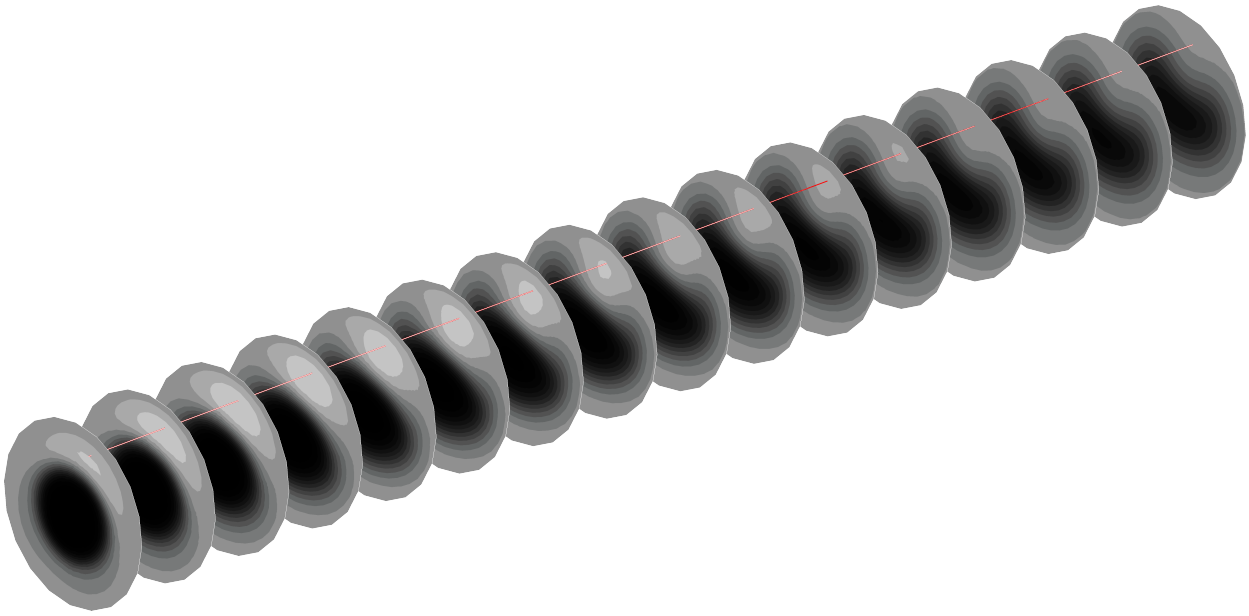

FIGURE 4.27 Slices of normalized axial velocity at $Re = 360$ for the additional branch uncovered in the 3-arcs stenosis with $E = 0.0025$. A line parallel to the axis Z is included, as a reference to observe the rotation of the recirculation zone due to the weak helical flow.

azymuthal rotation of the separated region due to the weak helical components of this stable flow.

Figure 4.21, as in the original results of Griffith *et al.*, shows that the hysteresis phenomena, and consequently the subcritical behavior of the solutions, occurs only at certain levels of eccentricity E. Lower levels of eccentricity are not large enough to trigger a strong asymmetric flow, or to the deform the branches of the first pitchfork bifurcation in such a way that two stable solutions are possible. Different mechanism with a steeper transition toward asymmetry could be present for higher values of eccentricity.

All of these results, the transitions and bifurcations uncovered were possible after the consideration of an eccentric geometry. A value of $E = 0.0025$, which is within the same order of magnitude than the manufacturing tolerance for the experimental stenosis studied by Vétel *et al.* (2008), is able to explain the qualitative behaviour observed by them at low Reynolds number. This is consistent with the observations made by Griffith *et al.* (2013) and by Sanmiguel-Rojas and Mullin (2012) regarding the geometrical defects. However, the study of stability for this flow, the side-by-side comparison of the cosine and the 3-arcs stenoses and the uncovering of further bifurcation, to the authors knowledge, has not been published before.

The following section presents a comparison of the computed asymmetry with the experimental

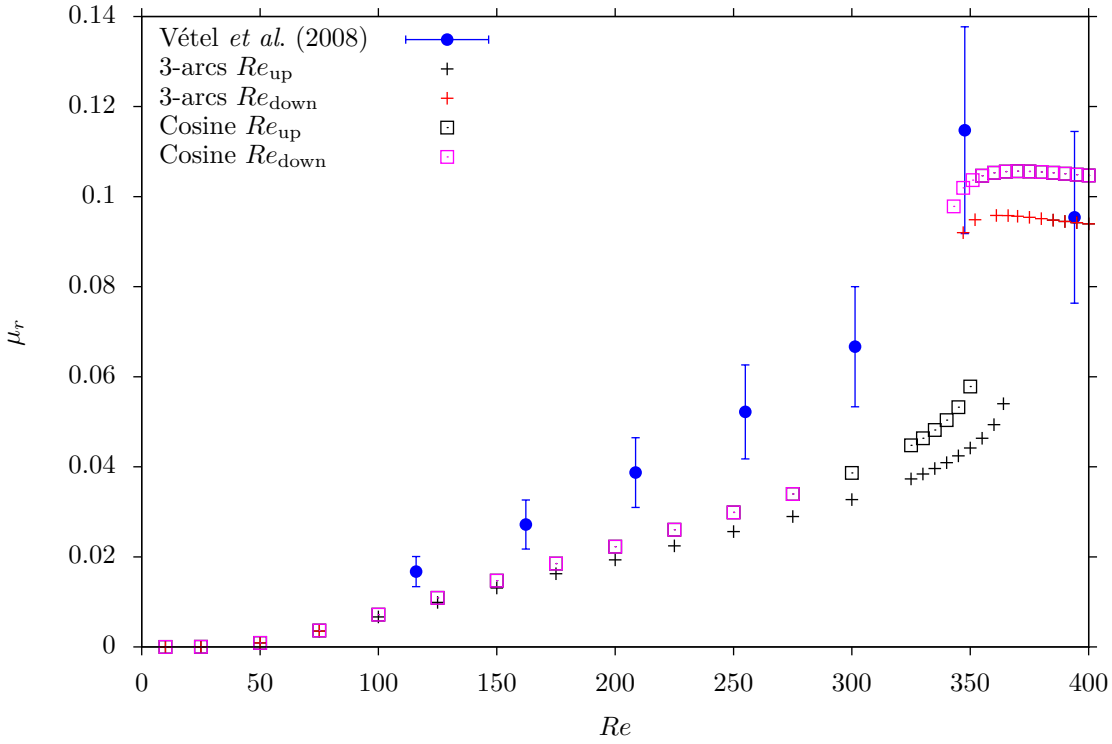

FIGURE 4.28 Comparison of μ_r at $z/D = 2.5$ for diferent numerical cases, with the experimental results of Vétel *et al.* (2008)

results from Vétel *et al.* (2008).

4.9 Comparison with experiments

The normalized asymmetry index μ_r for the 3-arcs stenosis with $E = 0.0025$ computed with the $L25\_F120$ mesh were compared with experimental results obtained by Vétel *et al.* (2008), who provided asymmetry data at two axial positions, $z/D = 2.5$ and $z/D = 7.5$. Thus, the value of μ_r was calculated for different Reynolds numbers, and compared with the experimental value of μ_r based on the PIV measurements from Vétel *et al.*[1]. Figures 4.28 and 4.29 present these comparisons at $z/D = 2.5$ and at $z/D = 7.5$, respectively. These plots constitutes both bifurcation diagrams, but with the value of μ_r monitored at a fixed axial position, instead of taking the global maximum, as in the rest of the results presented in this chapter.

The numerical data in Figure 4.28 presents a similar behavior to the bifurcation diagram

1. Error bars of ±20% were added to the experimental points, to emphasize the level of uncertainty that they carry.

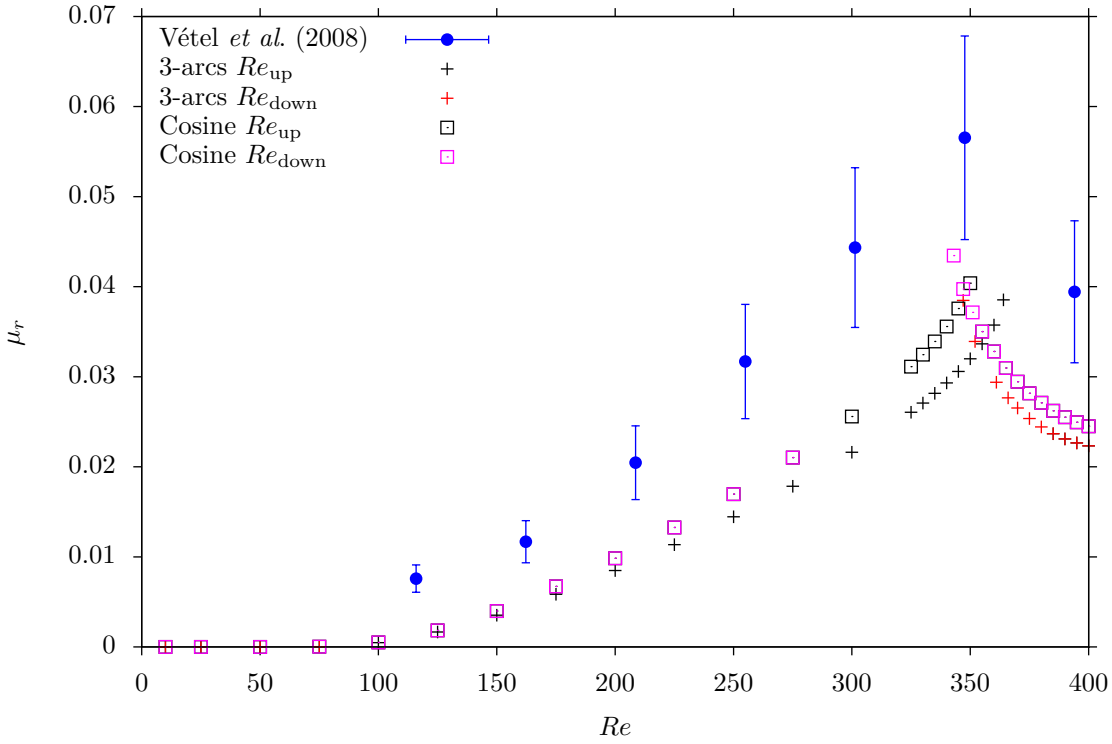

FIGURE 4.29 Comparison of μ_r at $z = 7.5D$ for diferent numerical cases, with the experimental results of Vétel *et al.* (2008)

of Figure 4.26, a fact that is not surprising, given that $z/D = 2.5$ is quite close to region where the maximum values of μ_r occur near $Re \simeq 350$, and indeed, is a good approximation to the $\mu_{\max}$ in the proximities of the bifurcations points. In general, the experimental data follows a similar qualitative route to the one computed numerically. It presents a higher level of asymmetry than the numerical values for $Re \lesssim 348$, but as already discussed, the index μ_r is prone to amplify small differences in the velocity field, plus the addition of experimental errors in this case. This condition of $Re = 348$ is precisely within the narrow range where the computed Re_{down} is linearly stable and the two branches coexists. The next experimental condition available is $Re = 394$, with the point falling directly over the numerical data for the decreasing Reynolds number branch. Formally, this branch is already unstable at this condition. But the additional branch with the small helical component has an identical value of μ_r. The magnitude of the azymuthal velocity is very weak, and was probably filtered out in the averaging and signal processing involved in the experimental process.

An analog situation occurs with Figure 4.29 for $z/D = 7.5$, with the experimental and numerical data presenting similar qualitative behavior. The constant gap that exists between numerical and experimental data could be explained with the interaction of an additional geo-

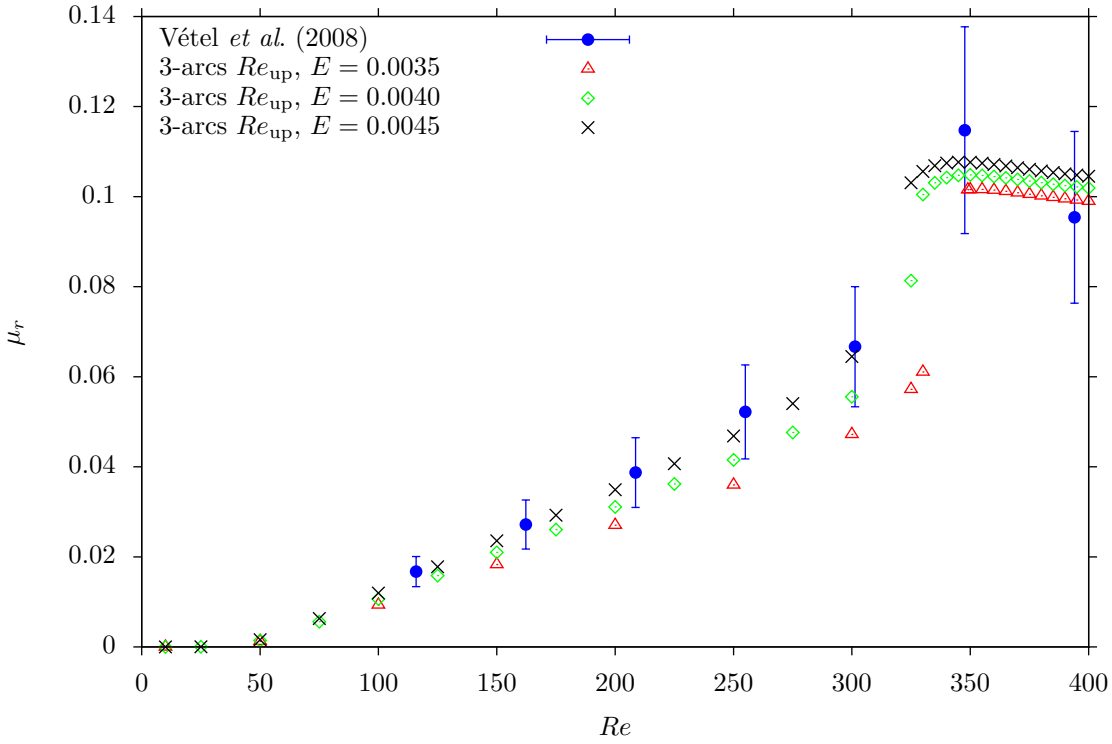

FIGURE 4.30 Comparison of μ_r at $z = 2.5D$ for higher values of eccentricity in the 3-arcs stenosis against the experimental results of Vétel *et al.* (2008)

metrical perturbation within the experimental setup.The effect of higher levels of eccentricity in the 3-arcs stenosis is evaluated in Figure 4.30 for $z = 2.5D$. As expected, the asymmetry of the flow increases with the eccentricity, with the asymmetry obtained at $E = 0.0045$ matching very closely the experimental values reported by Vétel *et al.* (2008).

However, further downstream, at $z = 7.5D$, a different effect is observed. First, the increase in eccentricity has a smaller effect on the observed level asymmetry at low Reynolds numbers. At $Re > 300$, the effect is reverted, and the increase in eccentricity causes a decrease in the asymmetry index μ. Hence, this indicates that geometrical perturbations could indeed cause the asymmetric pattern observed by Vétel *et al.*, in the real case it might have been more than just eccentricity.

Although the values of eccentricity studied so far were higher than the machining tolerance for the geometry used by Vétel *et al.*, their actual value is still quite small. It has shown that these small perturbation produce important changes in the physics of the flow. Hence, it is likely that the combination of another small geometrical perturbation, like irregularities in the shape of the stenosis added during the surface polishing, or a small misalignment in the

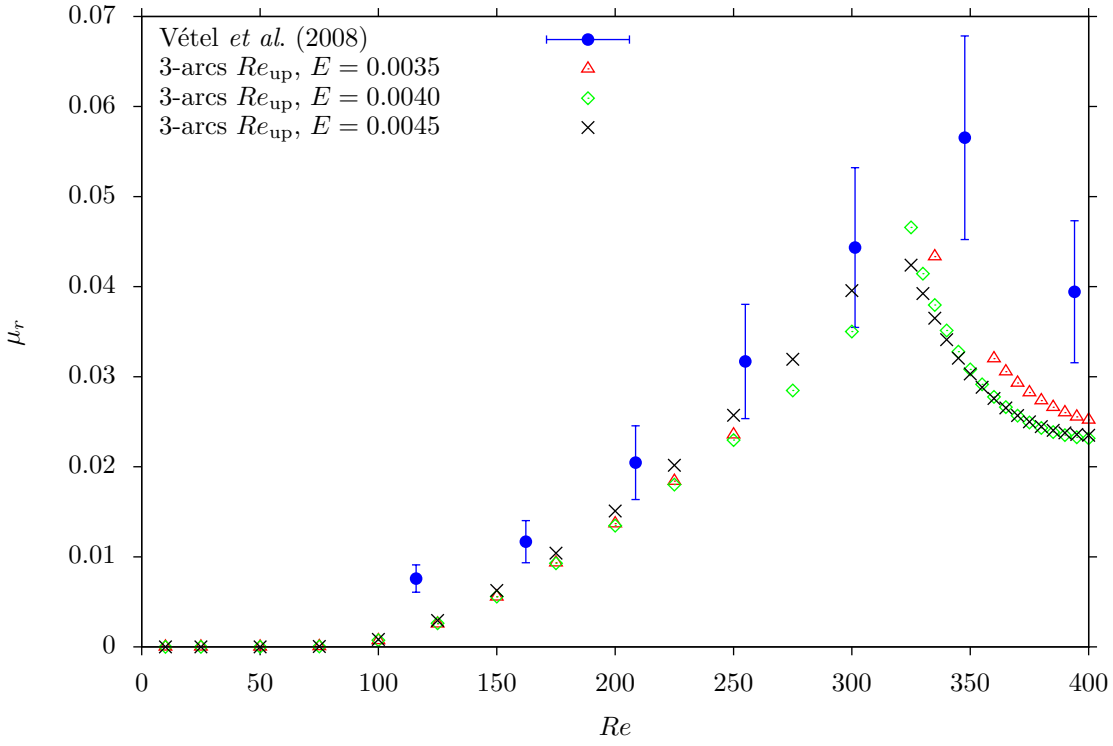

FIGURE 4.31 Comparison of μ_r at $z = 7.5D$ for higher values of eccentricity in the 3-arcs stenosis against the experimental results of Vétel *et al.* (2008)

between the inlet and outlet tubes of the experimental, could cause the observed pattern.

CHAPTER 5 SUDDEN EXPANSION

5.1 Introduction

This chapter contains the numerical results for the bifurcation analysis on a sudden expansion, using a similar methodology to the one exposed in Chapter 4 for the smooth contraction-expansion. An axisymmetric sudden expansion with an expansion ratio of 1:2 was studied, with the intention of reproducing the qualitative characteristics of the asymmetry reported by Mullin *et al.* (2009). As in the previous chapter, an eccentricity was added to the inlet tube of the geometry, to account for possible geometrical defects in the setup. This study was performed in the planar expansion by Fearn *et al.* (1990), while the eccentric thee-dimensional case was suggested by Sanmiguel-Rojas and Mullin (2012). However, this last study used perturbed velocity profile to model the eccentricity, and only performed one computation on an eccentric domain ($E = 0.0025$), as a proof of concept, to compare with their perturbed velocity results.

As mentioned earlier in Section 2.9.1, Mullin *et al.* quantify the level of asymmetry in their experimental results through the centroid of their RARE images (see Figure 2.14). They claim that this is a global measure of the asymmetry at the whole transverse section of the flow, with several advantages over the use of local velocity components, as they could add distortions into the bifurcation diagrams. However, the nature of RARE images only allows the identification of shear layers and areas of low velocity, based on their threshold of 12 mm/s (see Mullin *et al.*, 2009). Thus, velocity values (in magnitude) over this threshold are presented as black regions in their RARE images. Any change of the velocity profile within these black areas will only affect the centroid index if they modify the shape and position of the velocity isocontour at the threshold value, and this is not always true.

As Mullin *et al.* present their results in millimeters (see Figure 2.14b), it is convenient to normalize them for comparison purposes, using the inlet diameter to the sudden expansion (8 mm in the case of their setup). This new normalized measure of the asymmetry based on the centroid is denoted ξ. Figure 5.1 present 3 different velocity profiles that would have the same RARE velocity and will have the same measure of asymmetry and the same ξ, which makes it an ambiguous measure for the asymmetry. Consequently, unless stated otherwise, the quantification of the asymmetry in the present chapter is made using the μ_r index given by Equation (4.4).

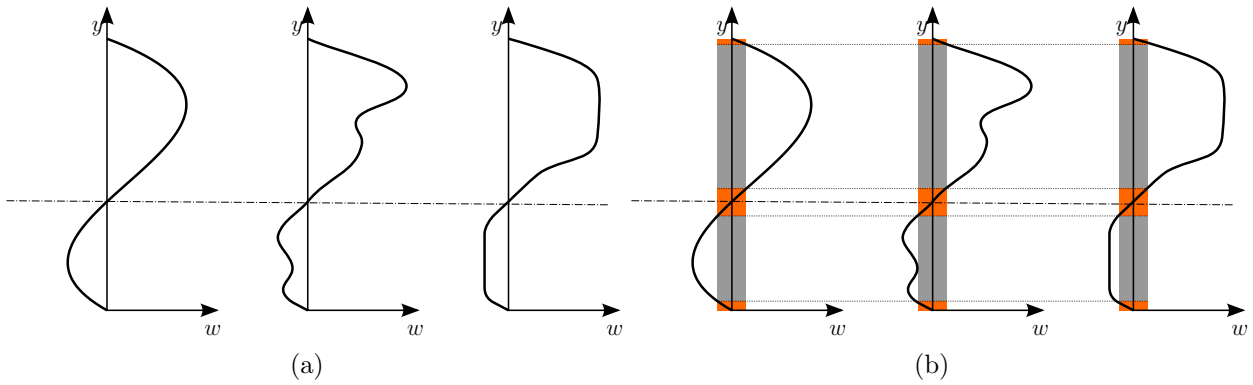

FIGURE 5.1 Diagram of velocity profiles, to illustrate the inconvenience of the centroid (or ξ) as measure of asymmetry. (a) presents the three different velocity profiles, and in (b) the threshold criteria is applied with a narrow gray band. The velocities outside this band appear black in the RARE image like the ones in Figure 2.14, while the ones inside this band appear orange.

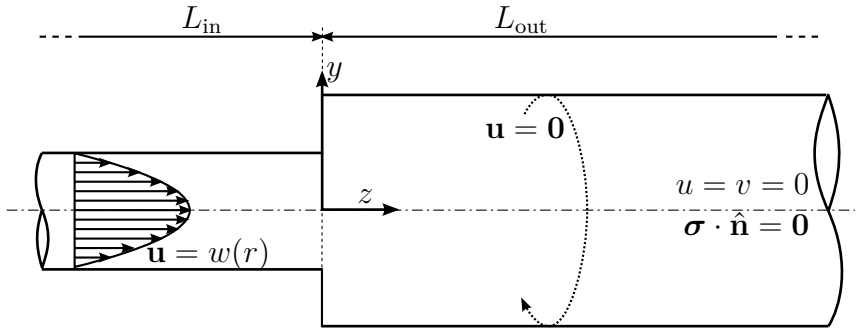

FIGURE 5.2 Boundary conditions used in the preliminary simulation of the axisymmetric sudden expansion.

5.2 Axisymmetric expansion

Preliminary simulations were conducted in the geometry of the axisymmetric sudden expansion. The boundary conditions and geometrical parameters are presented in Figure 5.2. The inlet length was kept constant at $L_{\text{in}} = 5D$ because the inlet velocity was a developed parabolic flow. The outlet length selected is $L_{\text{out}} = 75D$, which is the longest domain evaluated by Cantwell *et al.* (2010) in their numerical study.

The same numerical methodology used this research was also applied to this case. An incompressible flo is assumed, due to the low range of Reynolds number studied by Mullin *et al.* (2009) ($Re < 1400$). The boundary conditions are as presented in Figure 5.2. The numerical domain was discretized using through the finite element method, using 27-nodes

TABLE 5.1 Mesh used for the preliminary computations in the axisymmetric sudden expansion.

Case	Nodes	Elements
1	220845	26784
2	413235	50208
3	877077	106688
4	1166157	141888

hexahedral elements that satisfy the inf-sup condition, providing quadratic interpolation for the velocity vectors and linear interpolation for the pressure. Table 5.1 contains the sizes of the meshes used for this numerical preliminary study.

The computation of stability was carried out according to the method of modified product, introduced in Section 3.2.3. The real part of the leading eigenvalue computed for each mesh case as a function of Reynolds number is shown in Figure 5.3. All the values are below zero, and hence, no critical condition is observed in the Reynolds range studied by Mullin *et al.*, agreeing with the work of Cantwell *et al.* (2010). Hence, as with the case of the stenosis, an eccentricity was added to the inlet tube, with the goal of triggering the asymmetric flow reported by Mullin *et al.*, study that is presented in the following sections.

5.3 Eccentric expansion

The definition of the eccentricity parameter is shown in Figure 5.4. Special care was taken to guarantee the continuity and smoothness of the structured mesh between the inlet and the outlet tubes, through a transition region between the concentric O-grid structures of the inlet and outlet tubes, as presented in Figure 5.5. The goal of this transition is to avoid the perturbation introduced by sharp changes of direction within the mesh. The value of E was exaggerated, to show the displacement of the internal mesh elements due to the eccentricity, keeping the mesh structured. For the first part of this study, a value of $E = 0.0025$ is used, given that it is the value suggested by Sanmiguel-Rojas and Mullin (2012) and it produced interesting results in the previous chapter with the stenotic geometry.

5.4 Geometry and grid validation

The relevant geometric parameters are the lengths of the inlet and outlet segments of the expansion, L_{in} and L_{out} respectively, according to their specification as in Figure 5.6. However, as the inlet flow is still laminar in the work of Mullin *et al.*, a short inlet length is enough with

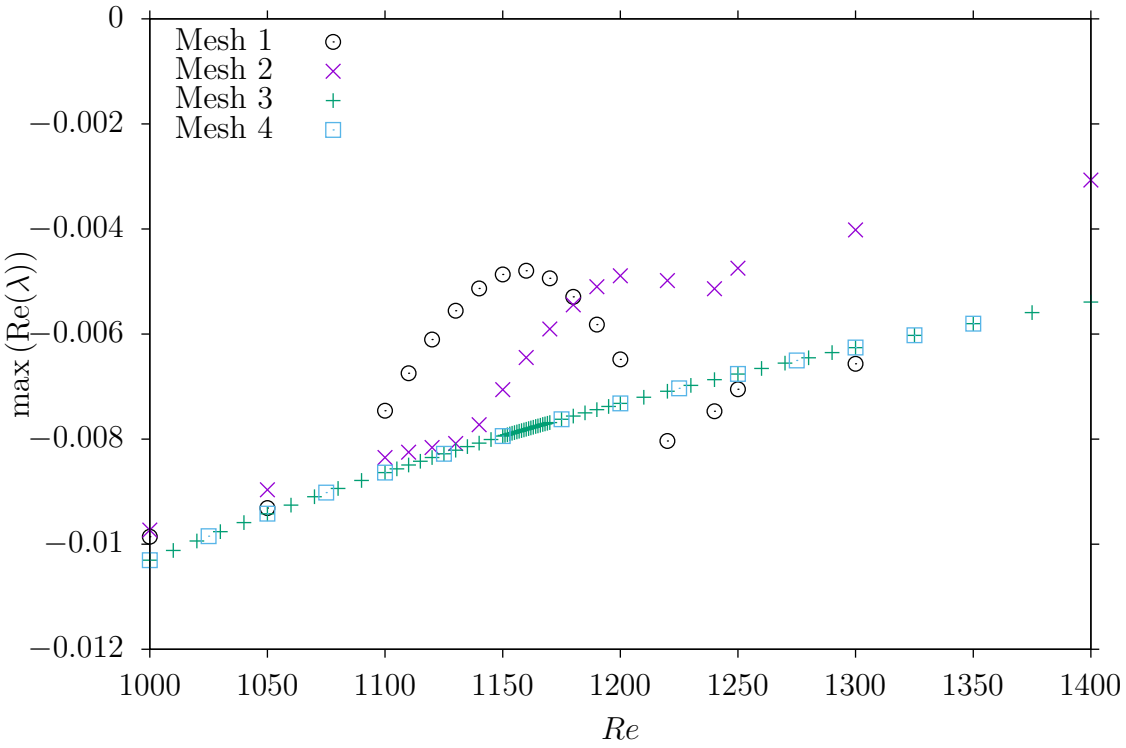

FIGURE 5.3 Maximum eigenvalues as a function of the Reynolds number for different meshes

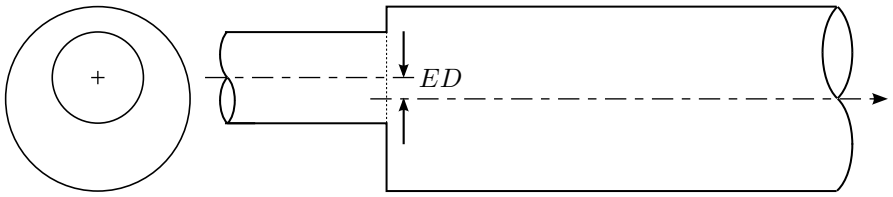

FIGURE 5.4 Eccentricity of the sudden expansion geometry

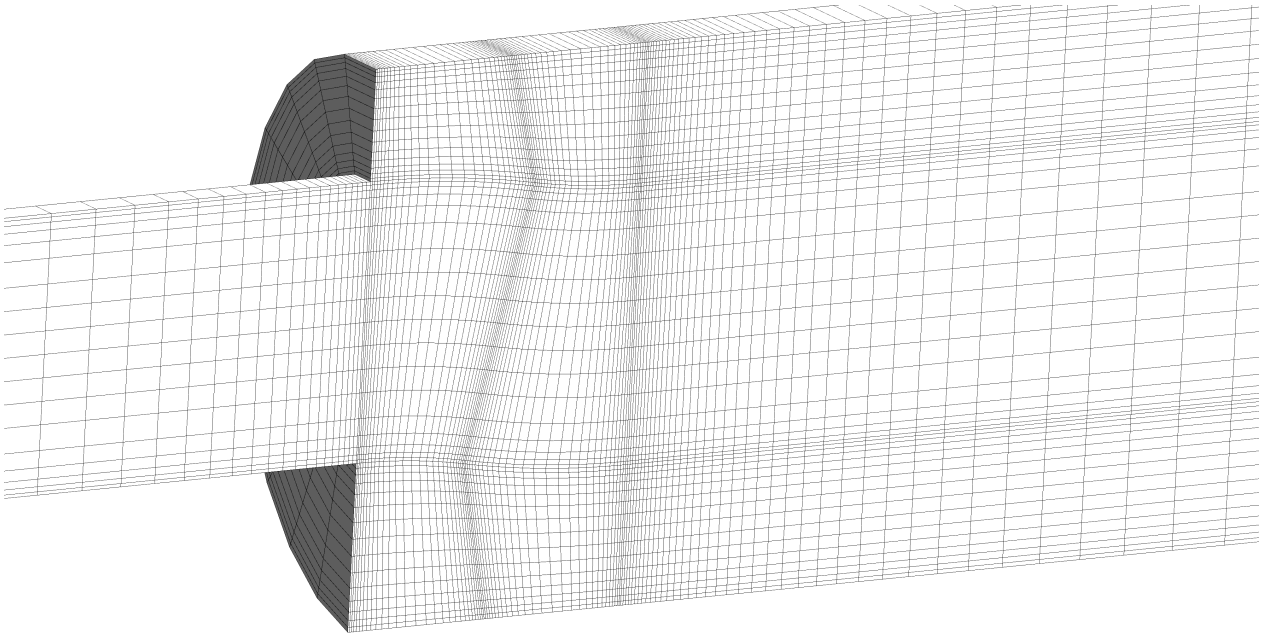

FIGURE 5.5 Longitudinal cut of the mesh, showing the detail of the eccentricity transition

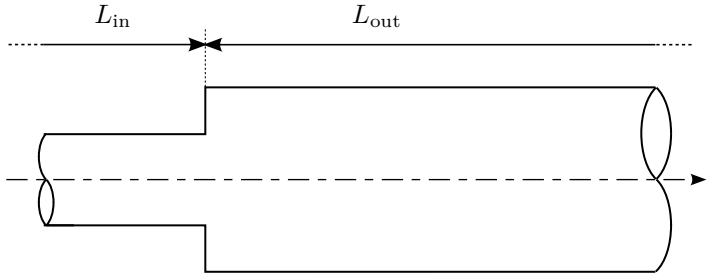

FIGURE 5.6 Geometrical lengths of the sudden expansion geometry.

the use of a developed Hagen-Poiseuille velocity profile. Hence, a constant value of $L_{\text{in}} = 5D$ was used.

The construction of the geometry and meshes with GMSH allows to control the density and grading of the mesh using a single parameter F_{mesh}. Its default value of 1.0 translates into a coarse mesh, which was used to study the effect of the outlet length over the flow field, according to the meshes detailed in the top part of Table 5.2.

In the range of Reynolds numbers $10 < Re < 1200$, the maximum value of the asymmetry index μ_r were computed, according to Equation (4.4). These results are plotted in Figure 5.7. Given that the 3 data series have essentially the same values of $\mu_{\max}$, the flow field solution is independent of variations of the outlet length L_{out} in the range analyzed. Consequently,

TABLE 5.2 Details of the different meshes used in the geometry and grid independence study for the three-dimensional sudden expansion.

Name	Hexas	F_{mesh}	$\frac{L_{\text{out}}}{D}$
$L_{\text{out}}200\_F_{\text{mesh}}100$	17472	1.00	200
$L_{\text{out}}250\_F_{\text{mesh}}100$	17920	1.00	250
$L_{\text{out}}300\_F_{\text{mesh}}100$	18368	1.00	300
$L_{\text{out}}200\_F_{\text{mesh}}100$	17472	1.00	200
$L_{\text{out}}200\_F_{\text{mesh}}110$	57140	1.10	200
$L_{\text{out}}200\_F_{\text{mesh}}120$	67880	1.20	200
$L_{\text{out}}200\_F_{\text{mesh}}130$	198960	1.30	200
$L_{\text{out}}200\_F_{\text{mesh}}140$	262416	1.40	200

the shorter domain with $L_{\text{out}} = 200D$ was selected for the remaining of the study. With this geometrical parameter fixed, the domain is then refined, using progressively higher values of F_{mesh}, as shown on the lower portion of Table 5.2. This parameter controls the number and distribution of nodes over the edges of the domain, from where a structured mesh is built using a transfinite algorithm. Hence, no linear dependence is expected between F_{mesh} and the size of the resulting mesh.

In Figure 5.7, the dispersion of the results for $\mu_{\max}$ with different values of F_{mesh} is relatively low. Further information could be extracted from the longitudinal variation of the asymmetry index for these meshes, reported on Figure 5.9. The μ_r profile is remarkably similar for all the studied meshes. However, the inset plot in Figure 5.9 shows that with the exception of the data for $F_{\text{mesh}} = 1.0$, the peak in μ_r increases with F_{mesh}. Hence, the refinements from $F_{\text{mesh}} = 1.1$ to 1.4 increase monotonically the asymmetry of the flow, while the data points for $F_{\text{mesh}} = 1.0$ has a more arbitrary behavior, intersecting the other lines. Thus, this is a sign that the mesh with $F_{\text{mesh}} = 1.0$ does not have enough resolution. The increase in μ_r observed between $F_{\text{mesh}} = 1.1$ and 1.4 is quite small. Thus, to save computational time for the stage of eigenvalue calculation, the mesh with $F_{\text{mesh}} = 1.1$ was selected for the calculations presented in the remaining of this chapter.

5.5 Eigenvalues

The previous section showed that the selected mesh produced well behaved results for the hydrodynamic solution. Despite this, the use of the same methodology developed in Chapter 3 and used in the computation of stability for the stenosis in Chapter 4 produced irregular results in the present case. Figure 5.10 shows the real part of the rightmost eigenvalues for

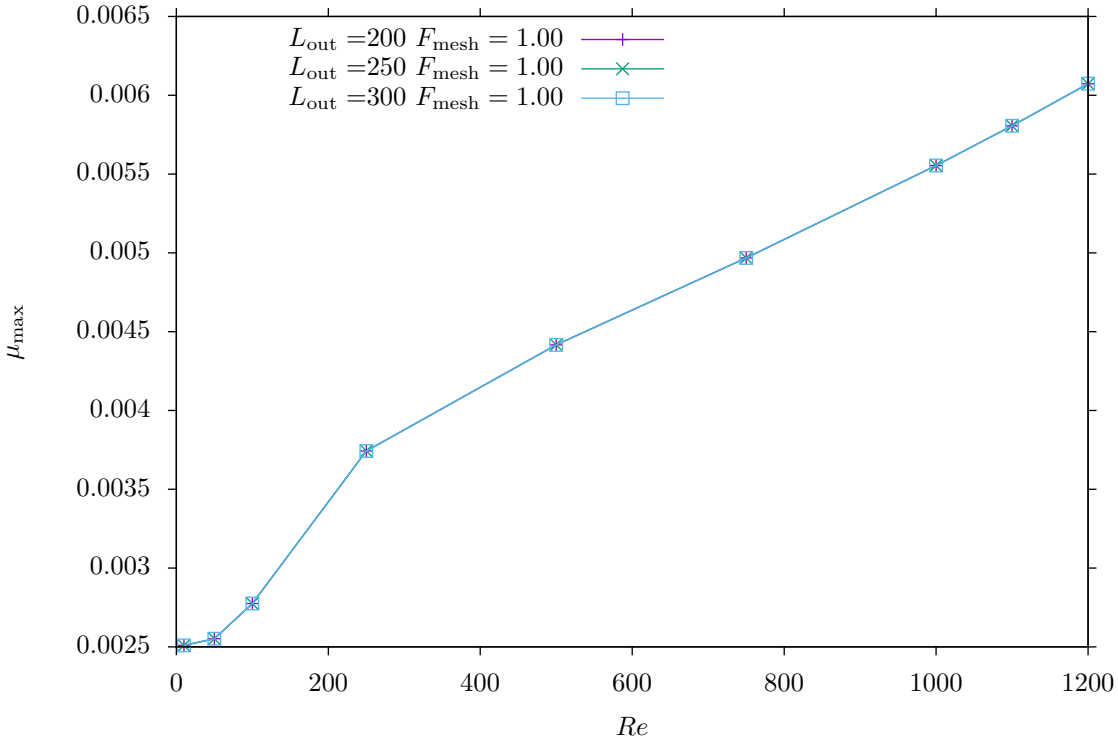

FIGURE 5.7 Maximum asymmetry μ_{max} at different outlet lengths L_{out} for sudden expansion with $E = 0.0025$.

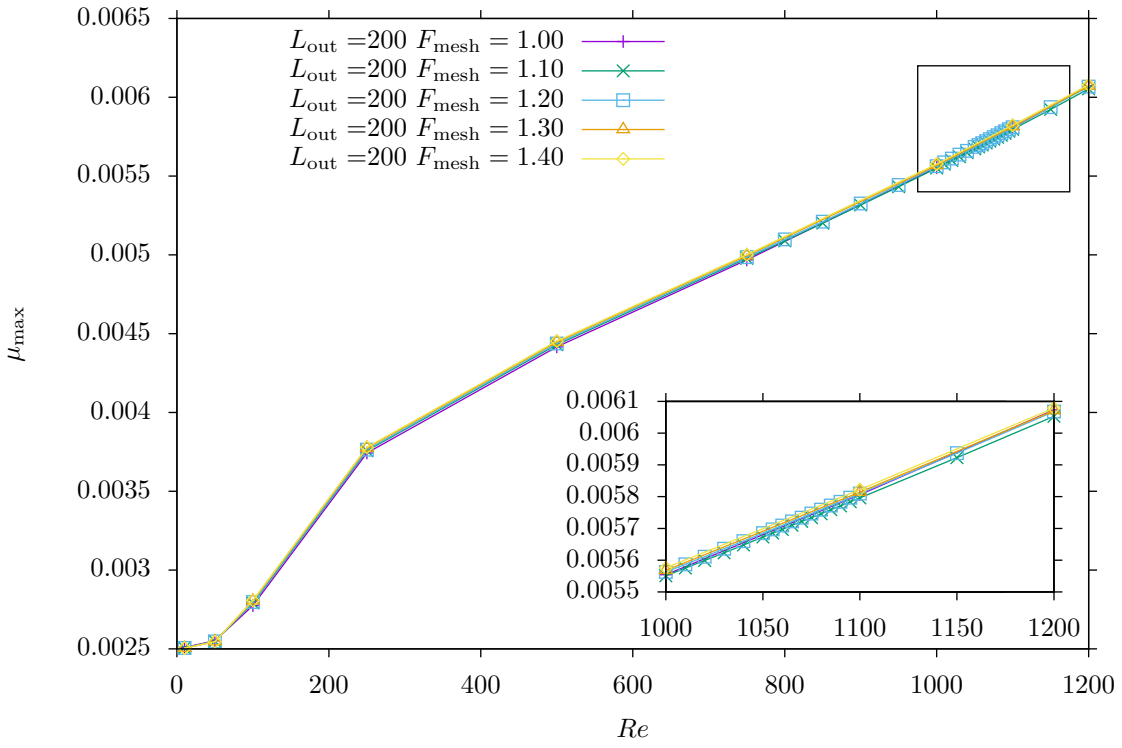

FIGURE 5.8 Maximum asymmetry $\mu_{\max}$ at different mesh densities for sudden expansion with $E = 0.0025$.

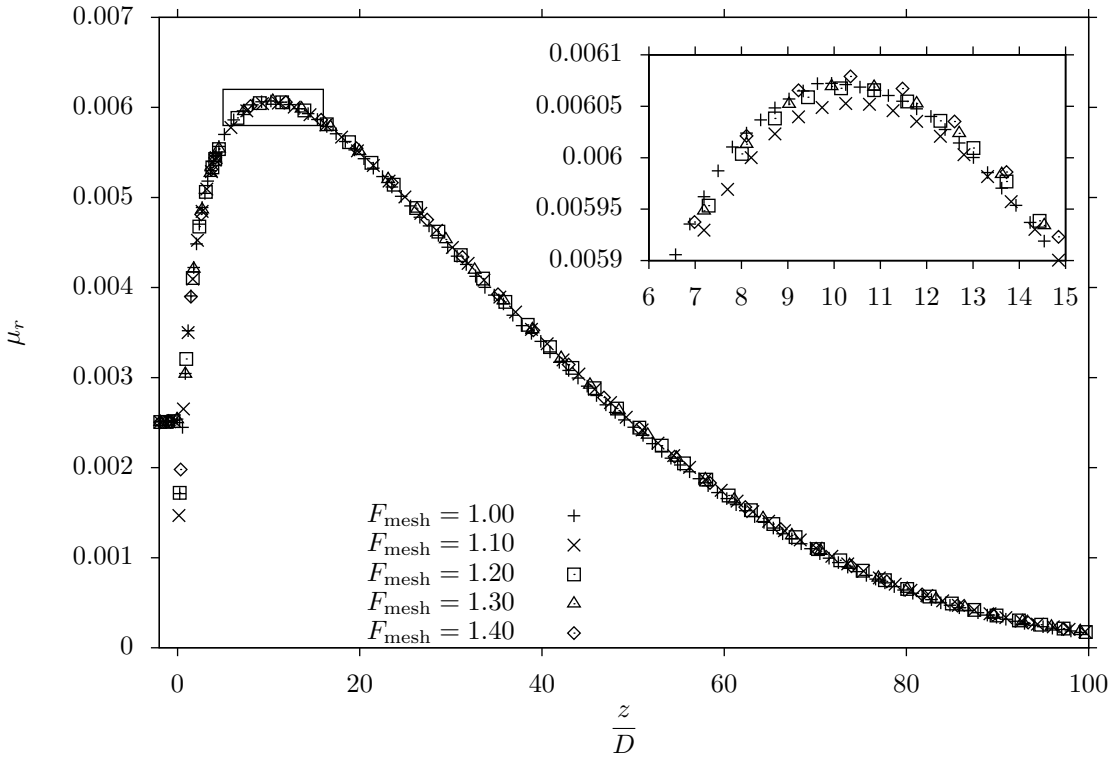

FIGURE 5.9 Longitudinal variation of asymmetry μ_r at $Re = 1200$ with different meshes for sudden expansion with $E = 0.0025$.

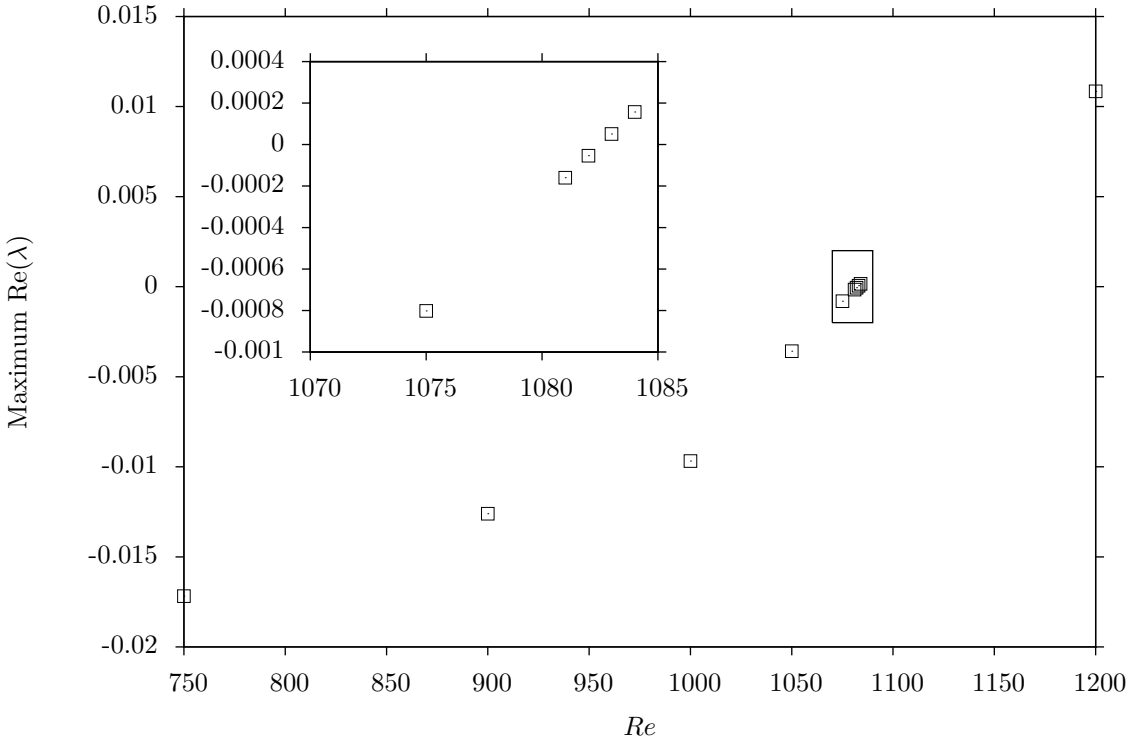

FIGURE 5.10 Maximum real part of the eigenvalues for the sudden expansion with $E = 0.0025$.

different Reynolds number conditions. Mullin *et al.* (2009) reported their transition point toward asymmetry at $Re = 1139$, which is not very far to the critical point of $Re = 1083$ observed in Figure 5.10. The whole range of computed eigenvalues at $Re = 1083$ is given in Table 5.3. However, a closer inspection to the velocity modes associated with these eigenvalues reveals patterns of $\mathbf{u}'$ that were not observed before in the case of the stenosis.

Figure 5.11a shows a longitudinal slice through the domain, with the contours of the axial velocity for the mode associated with the first eigenvalue at $Re = 1083$. These contours show a remarkable fluctuation that was not observed in the modes computed in Chapter 4. Moreover, the local maximum and minimum of these fluctuations occur at the longitudinal position of the mesh nodes, in the region where the elements are more stretched to save memory.

The aforementioned fluctuations appear in several of the other computed modes of Table 5.3, as well as at different Reynolds number. Nevertheless, in some cases the modes presented a clearly defined contour with relatively low oscillation. As an example, the velocity contours of the second and third eigenvalues of Table 5.3 are shown in Figures 5.11b and 5.11c, respectively. Figure 5.11b represents a symmetry-breaking mode, very much alike the one computed for

TABLE 5.3 Computed eigenvalues for the eccentric sudden expansion ($E = 0.0025$) at $Re = 1083$

eig	Real	Imaginary
1	$5.140\,53 \times 10^{-5}$	$0.000\,00 \times 10^{+0}$
2	$-9.057\,17 \times 10^{-3}$	$0.000\,00 \times 10^{+0}$
3	$-9.112\,89 \times 10^{-3}$	$0.000\,00 \times 10^{+0}$
4	$-9.187\,99 \times 10^{-3}$	$0.000\,00 \times 10^{+0}$
5	$-1.152\,94 \times 10^{-2}$	$0.000\,00 \times 10^{+0}$
6	$-1.439\,38 \times 10^{-2}$	$0.000\,00 \times 10^{+0}$
7	$-1.439\,92 \times 10^{-2}$	$0.000\,00 \times 10^{+0}$
8	$-2.045\,29 \times 10^{-2}$	$-6.263\,22 \times 10^{-3}$
9	$-2.045\,29 \times 10^{-2}$	$6.263\,22 \times 10^{-3}$
10	$-2.055\,88 \times 10^{-2}$	$0.000\,00 \times 10^{+0}$
11	$-2.074\,92 \times 10^{-2}$	$0.000\,00 \times 10^{+0}$

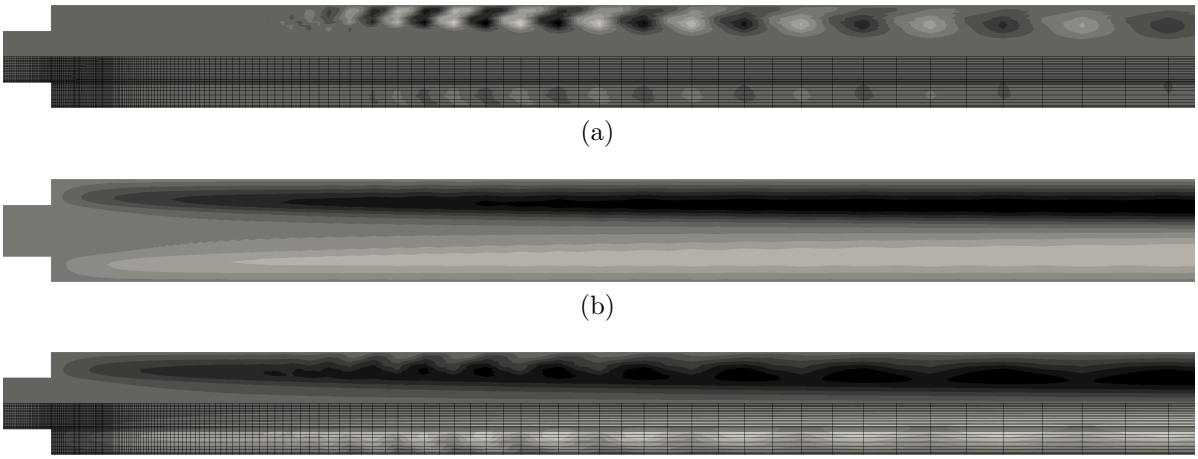

(a)

(b)

(c)

FIGURE 5.11 Axial perturbation velocity contours for the eigenmodes at $Re = 1083$ in the sudden expansion with $E = 0.0025$. (a) corresponds to the first eigenvalue of Table 5.3, (b) is the second and (c) is the third.

the planar sudden expansion (see Figure 3.8a), because the velocity components associated with the mode will deflect the flow from the inlet expansion toward the wall of the outlet tube once this mode is amplified by perturbations. However, in this case, its associated eigenvalue is negative and the flow is deemed stable. The mode presented in Figure 5.11c have similar characteristics to the Figure 5.11b, having also a symmetry-breaking topology. However, it also contains a fluctuating component at the axial nodes, analog to the one presented in Figure 5.11a.

The computations were repeated, using an increased size of the Krylov subspace, but the fluctuations in the velocity modes remained there. In some cases, the eigenvalues associated with these fluctuating modes simple not appeared between the results at one Reynolds number and the previous or following. And the use of a more refined mesh created a significant shift in the position of the eigenvalues associated to several of these irregular modes, while the eigenvalues associated with the more regular remained at roughly the same position. However, even with a finer mesh, these irregularities still appear.

It is interesting that in all the meshes, when eigenvalues are computed at low Reynolds number, these irregularities did not appeared. And certainly they were not present in the results for the different stenoses studied so far. They only appear at $Re > 1000$. Thus, this indicates that this oscilations are numerical instabilities associated with the advection term in the governing equations (Equations (2.10)). To remove them, a finer mesh could be used, but that will increase the total computational cost of the analysis to level that are unmanageable. The second option is the use of an advection-stabilized scheme in the discretization of the stability problem (3.1).

5.6 Future works

The implementation of this scheme would require an important effort, because the independence of the eigenvalues and eigenvector from the stabilization scheme has to be assessed. In the current research, that will require, for example, repeat the stability calculations presented in the previous chapter for the stenosis, but using the selected stabilized scheme, and then test its effect at higher Reynolds numbers where the advection instabilities become relevant. This process, although important for the present geometry due to its higher Reynolds numbers, was not performed, due to time constraints. Hence, this aspect of this research is left for a future research project.

CHAPTER 6 CONCLUSIONS

The present research provided a thorough study of the first symmetry breaking instability in two important setups: the smooth contraction-expansion and the sudden expansion. Additionally, several important contributions were made, listed in the following section.

6.1 Contributions

Probably the most significant contribution of the present research is the method for the computation of stability analysis. The modifications proposed to the matrix operations detailed in Section 3.2.3 are original, to the author's knowledge, and provide a way of computing the spectra of the solution without the use of time integration algorithms.

The study of effect of the eccentricity in the stenosis allowed the repetition of the Griffith *et al.* (2013) results, with the additional computation of stability. This allowed to explain the results of Vétel *et al.* (2008) under the assumption of small geometrical perturbation in the setup. The hysteresis loop was uncovered, allowing the computation of two linearly stable solutions under the same conditions. Moreover, an additional bifurcation was detected with the eigenvalues, resulting in a new stable branch with a weak helical component that shift the separated region in the azymuthal direction.

Similarly, in the sudden expansion it was demonstrated that eccentric geometries can shift the spectra of eigenvalues, and probably causing the asymmetry observed by Mullin *et al.* (2009). No further remarks can be made about this case, due to the advection instabilities that appeared in the solution of this problem.

6.2 Limitations

The present research was motivated by the study of steady asymmetries. Thus, the use of linear stability analysis was enough to fulfill the objectives. However, given that in many practical cases in the literature the transition observed were subcritical, it is convenient the inclusion of a transient growth routine within the available set of computational tools for future research. These are specially useful in the computation of periodic solutions, another situation where the current version of the computational code employed is not suitable.

At the Reynolds number of interest for the symmetry breaking phenomenon, the computation of stability in the sudden expansion presented difficulties, due to the mesh employed. These

problems were due to convective instabilities due to the advection terms in the governing equations. Hence, the computation of stability could only be computed at Reynolds numbers were this numerical instabilities, seriously limiting its applicability. The use of an stabilized scheme for the computation of stability is discussed in the next section.

6.3 Suggested improvements and future works

The computational cost of the computation of linear stability problem was discussed. It is possible to use less expensive algorithms, given the characteristics of the problem matrix. The implementation and validation of the methodology with the use of an iterative solver becomes relevant, especially to compute the stability in three dimensional geometries. Another approach to increase accuracy and decrease the total number of degrees of freedom is through the use of spectral elements.

The evaluation of further geometric imperfections in the stenosis problem could produce a closer match with the experimental results. Among the suggested source of perturbation is the use of misalignment in the stenotic geometry, and imperfections in the description of the shape of the constriction.

Finally, the issues uncovered in the sudden expansion at moderate Reynolds indicate the presence of convective instabilities, which seriously limit the range of applicability of the proposed method for the computation of stability. The implementation of an stabilized scheme is recommended for future works, helping to extend the applicability of the proposed algorithm.

BIBLIOGRAPHY

AHMED, S. A. and GIDDENS, D. P. (1983a). Flow disturbance measurements through a constricted tube at moderate Reynolds numbers. *J. Biomech.*, 16, 955–963.

AHMED, S. A. and GIDDENS, D. P. (1983b). Velocity measurements in steady flow through axisymmetric stenoses at moderate Reynolds numbers. *J. Biomech.*, 16, 505–516.

ALLEBORN, N., NANDAKUMAR, K., RASZILLIER, H. and DURST, F. (1997). Further contributions on the two-dimensional flow in a sudden expansion. *J. Fluid Mech.*, 330, 169–188.

ANDERECK, C. D., LIU, S. S. and SWINNEY, H. L. (1986). Flow regimes in a circular Couette system with independently rotating cylinders. *J. Fluid Mech.*, 164, 155–183.

ARMALY, B. F., DURST, F., PEREIRA, J. C. F. and SCHÖNUNG, B. (1983). Experimental and theoretical investigation of backward-facing step flow. *J. Fluid Mech.*, 127, 473–496.

BABUŠKA, I. (1973). The finite element method with Lagrangian multipliers. *Numerische Mathematik*, 20, 179–192.

BACK, L. H. and ROSCHKE, E. J. (1972). Shear-layer flow regimes and wave instabilities and reattachment lengths downstream of an abrupt circular channel expansion. *J. Appl. Mech.*, 39, 677–681.

BAGGETT, J. S., DRISCOLL, T. A. and TREFETHEN, L. N. (1995). A mostly linear model of transition to turbulence. *Phys. Fluids*, 7, 833–838.

BANKS, W. H. H., DRAZIN, P. G. and ZATURSKA, M. B. (1988). On perturbations of Jeffery–Hamel flow. *J. Fluid Mech.*, 186, 559–581.

BARKLEY, D. (1992). Linear stability analysis of rotating spiral waves in excitable media. *Phys. Rev. Lett.*, 68, 2090–2093.

BARKLEY, D., BLACKBURN, H. M. and SHERWIN, S. J. (2008). Direct optimal growth analysis for timesteppers. *Int. J. Numer. Meth. Fl.*, 57, 1435–1458.

BARKLEY, D. and HENDERSON, R. D. (1996). Three-dimensional Floquet stability analysis of the wake of a circular cylinder. *J. Fluid Mech.*, 322, 215–241.

BARKLEY, D. and TUCKERMAN, L. S. (1999). Stability analysis of perturbed plane Couette flow. *Phys. Fluids*, 5, 1187–1195.

BATTAGLIA, F. and PAPADOPOULOS, G. (2006). Bifurcation characteristics of flows in rectangular sudden expansion channels. *J. Fluid. Eng.*, 128, 671–679.

BATTAGLIA, F., TAVENER, S. J., KULKARNI, A. K. and MERKLE, C. L. (1997). Bifurcation of low Reynolds number flows in symmetric channels. *AIAA J.*, 35, 99–105.

BENJAMIN, T. B. (1976). Applications of Leray–Schauder degree theory to problems of hydrodynamic stability. *Math. Proc. Cambridge*, 79, 373–392.

BLACKBURN, H. M. and SHERWIN, S. J. (2004). Formulation of a Galerkin spectral element–Fourier method for three-dimensional incompressible flows in cylindrical geometries. *J. Comput. Phys.*, 197, 759–778.

BLACKBURN, H. M. and SHERWIN, S. J. (2007). Instability modes and transition of pulsatile stenotic flow: pulse-period dependence. *J. Fluid Mech.*, 573, 57–88.

BLACKBURN, H. M., SHERWIN, S. J. and BARKLEY, D. (2008). Convective instability and transient growth in steady and pulsatile stenotic flows. *J. Fluid Mech.*, 607, 267–277.

BOTTARO, A., CORBETT, P. and LUCHINI, P. (2003). The effect of base flow variation on flow stability. *J. Fluid Mech.*, 476, 293–302.

BREZZI, F. (1974). On the existence, uniqueness and approximation of saddle-point problems arising from Lagrangian multipliers. *Rev. Fr. Automat. Infor.*, 8, 129–151.

CANTWELL, C. D., BARKLEY, D. and BLACKBURN, H. M. (2010). Transient growth analysis of flow through a sudden expansion in a circular pipe. *Phys. Fluids*, 22, 034101.

CARLSON, D. R., WIDNALL, S. E. and PEETERS, M. F. (1982). A flow-visualization study of transition in plane poiseuille flow. *J. Fluid Mech.*, 121, 487–505.

CASEY, M. and WINTERGERSTE, T., editors (2000). *Best Practice Guidelines: Special Interest Group on "Quality and Trust in Industrial CFD of Single-Phase Flows"*. ERCOFTAC: European Research Community on Flow Turbulence and Combustion.

CASSANOVA, R. and GIDDENS, D. (1978). Disorder distal to modeled stenoses in steady and pulsatile flow. *J. Biomech.*, 11, 441–453.

CHENEY, E. W. and KINCAID, D. R. (2009). *Linear Algebra: Theory and Applications*. Jones and Bartlett Publishers.

CHERDRON, W., DURST, F. and WHITELAW, J. H. (1978). Asymmetric flows and instabilities in symmetric ducts with sudden expansions. *J. Fluid Mech.*, 84, 13–31.

CHOSSAT, P. and IOOSS, G. (1985). Primary and secondary bifurcations in the Couette–Taylor problem. *Japan Journal of Applied Mathematics*, 2, 37–68.

CIARLET, P. and LIONS, J., editors (1991). *Handbook of Numerical Analysis: Finite Element Methods (part 1)*, vol. II of *Handbook of Numerical Analysis*. North–Holland.

CLIFFE, K., HALL, E., HOUSTON, P., PHIPPS, E. and SALINGER, A. (2012). Adaptivity and a posteriori error control for bifurcation problems iii: Incompressible fluid flow in open systems with o(2) symmetry. *J. Sci. Comput.*, 52, 153–179.

CLIFFE, K. A., GARRATT, T. J. and SPENCE, A. (1993). Eigenvalues of the discretized Navier–Stokes equation with application to the detection of Hopf bifurcations. *Adv. Comput. Math.*, 1, 337–356.

CRAWFORD, J. D. (1991). Introduction to bifurcation theory. *Rev. Mod. Phys.*, 63, 991–1037.

DANIEL, J. W., GRAGG, W. B., KAUFMAN, L. and STEWART, G. W. (1976). Reorthogonalization and stable algorithms for updating the Gram-Schmidt QR factorization. *Math. Comput.*, 30, 772–795.

DAVEY, A. (1962). The growth of Taylor vortices in flow between rotating cylinders. *J. Fluid Mech.*, 14, 336–368.

DAVIS, T. A. (2004). Algorithm 832: Umfpack v4. 3—an unsymmetric-pattern multifrontal method. *ACM T. Math. Software (TOMS)*, 30, 196–199.

DAWSON, S. T. M. and BLACKBURN, H. M. (2010). Numerical simulation of a bifurcating jet within a radially confined domain. *17th. Australasian Fluid Mechanics Conference*.

DELFOUR, M. C. (2012). *4. Optimality Conditions*, SIAM, chapter 4. MOS-SIAM Series on Optimization. 153–239.

DESHPANDE, M. D. and GIDDENS, D. P. (1980). Turbulence measurements in a constricted tube. *J. Fluid Mech.*, 97, 65–89.

DESHPANDE, M. D., GIDDENS, D. P. and MABON, R. F. (1976). Steady laminar flow through modelled vascular stenoses. *J. Biomech.*, 9, 165–174.

DIACONIS, P. and SHAHSHAHANI, M. (1987). The subgroup algorithm for generating uniform random variables. *Probab. Eng. Inform. Sc.*, 1, 15–32.

DRAZIN, P. (1992). *Nonlinear Systems*. Cambridge Texts in Applied Mathematics. Cambridge University Press.

DRAZIN, P. G. (2002). *Introduction to Hydrodynamic Stability (Cambridge Texts in Applied Mathematics)*. Cambridge University Press.

DRIKAKIS, D. (1997). Bifurcation phenomena in incompressible sudden expansion flows. *Phys. Fluids*, 9, 76–87.

DURST, F., MELLING, A. and WHITELAW, J. H. (1972). Optical anemometer measurements in recirculating flows and flames. *Fluid Dynamic Measurements in the Industrial and Medical Environments. Proc. D I S A Conf.* Leicester University Press, vol. 1, paper II. 2–2.

DURST, F., MELLING, A. and WHITELAW, J. H. (1974). Low Reynolds number flow over a plane symmetric sudden expansion. *J. Fluid Mech.*, 64, 111–128.

DURST, F., PEREIRA, J. C. F. and TROPEA, C. (1993). The plane symmetric sudden-expansion flow at low reynolds numbers. *J. Fluid Mech.*, 248, 567–581.

FANI, A., CAMARRI, S. and SALVETTI, M. V. (2012). Stability analysis and control of the flow in a symmetric channel with a sudden expansion. *Phys. Fluids*, 24, 084102.

FEARN, R. M., MULLIN, T. and CLIFFE, K. A. (1990). Nonlinear flow phenomena in a symmetric sudden expansion. *J. Fluid Mech.*, 211, 595–608.

FERZIGER, J. H. and PERIĆ, M. (2001). *Computational Methods for Fluid Dynamics*. Springer.

FEUERSTEIN, I. A., PIKE, G. K. and ROUND, G. F. (1975). Flow in an abrupt expansion as a model for biological mass transfer experiments. *J. Biomech.*, 8, 41–51.

FORRESTER, J. H. and YOUNG, D. F. (1970a). Flow through a converging–diverging tube and its implications in occlusive vascular disease – I: Theoretical development. *J. Biomech.*, 3, 297–305.

FORRESTER, J. H. and YOUNG, D. F. (1970b). Flow through a converging–diverging tube and its implications in occlusive vascular disease – II: Theoretical and experimental results and their implications. *J. Biomech.*, 3, 307–316.

FORTIN, A., JARDAK, M., GERVAIS, J. and PIERRE, R. (1994). Old and new results on the two-dimensional poiseuille flow. *J. Comput. Phys.*, 115, 455 – 469.

FORTIN, A., JARDAK, M., GERVAIS, J. J. and PIERRE, R. (1997). Localization of Hopf bifurcations in fluid flow problems. *Int. J. Numer. Meth. Fl.*, 24, 1185–1210.

FURUICHI, N., TAKEDA, Y. and KUMADA, M. (2003). Spatial structure of the flow through an axisymmetric sudden expansion. *Exp. Fluids*, 34, 643–650.

GEORGIEVSKII, D., MÜLLER, W. and ABALI, B. (2014). Generalizations of the Orr-Sommerfeld problem for the case in which the unperturbed shear motion is nonsteady. *Russ. J. Math. Phys.*, 21, 189–196.

GEUZAINE, C. and REMACLE, J.-F. (2009). Gmsh: A 3-D finite element mesh generator with built-in pre- and post-processing facilities. *Int. J. Numer. Meth. Eng.*, 79, 1309–1331.

GOLDHIRSCH, I., ORSZAG, S. A. and MAULIK, B. K. (1987). An efficient method for computating leading eigenvalues and eigenvectors of large asymmetric matrices. *J. Sci. Comput.*, 2, 33–58.

GOLUBITSKY, M. and STEWART, I. (1986). Symmetry and stability in Taylor–Couette flow. *SIAM J. Math. Anal.*, 17, 249–288.

GRIFFITH, M. D., LEWEKE, T., THOMPSON, M. C. and HOURIGAN, K. (2008). Steady inlet flow in stenotic geometries: convective and absolute instabilities. *J. Fluid Mech.*, 616, 111–133.

GRIFFITH, M. D., LEWEKE, T., THOMPSON, M. C. and HOURIGAN, K. (2013). Effect of small asymmetries on axisymmetric stenotic flow. *J. Fluid Mech.*, 721, R1.

GRIFFITH, M. D., THOMPSON, M. C., LEWEKE, T. and HOURIGAN, K. (2010). Convective instability in steady stenotic flow: optimal transient growth and experimental observation. *J. Fluid Mech.*, 655, 504–514.

GUEVEL, Y., GIRAULT, G. and CADOU, J. (2014). Parametric analysis of steady bifurcations in 2d incompressible viscous flow with high order algorithm. *Comput. Fluids*, 100, 185–195.

HAAPANEN, S. I. (2008). *Linear stability analysis and direct numerical simulation of a miscible two-fluid channel flow*. PhD thesis, Stanford University.

HOPF, E. (1948). A mathematical example displaying features of turbulence. *Commun. Pure Appl. Math.*, 1, 303–322.

HORN, R. A. and JOHNSON, C. R. (2012). *Matrix analysis*. Cambridge University Press.

HUNG, T.-K. and MACAGNO, E. O. (1966). Laminar eddies in a two-dimensional conduit expansion. *La Houille Blanche*, 4, 391–401.

IORIO, M. C., GONZÁLEZ, L. M. and FERRER, E. (2014). Direct and adjoint global stability analysis of turbulent transonic flows over a NACA0012 profile. *Int. J. Numer. Meth. Fl.*, 76, 147–168.

IRIBARNE, A., FRANTISAK, F., HUMMEL, R. L. and SMITH, J. W. (1972). An experimental study of instabilities and other flow properties of a laminar pipe jet. *AIChE J.*, 18, 689–698.

KHALIFA, A. M. A. and GIDDENS, D. P. (1981). Characterization and evolution of poststenotic flow disturbances. *J. Biomech.*, 14, 279–296.

LATORNELL, D. J. and POLLARD, A. (1986). Some observations on the evolution of shear layer instabilities in laminar flow through axisymmetric sudden expansion. *Phys. Fluids*, 29, 2828–2835.

LEE, J. S. and FUNG, Y. C. (1970). Flow in locally constricted tubes at low Reynolds numbers. *J. Appl. Mech.*, 37, 9–16.

LEHOUCQ, R. B., SORENSEN, D. C. and YANG, C. (1998). *ARPACK User's Guide: Solution of Large-Scale Eigenvalue Problems With Implicitly Restarted Arnoldi Methods*. SIAM.

LEÓN, C. A., MASSÉ, J.-C. and RIVEST, L.-P. (2006). A statistical model for random rotations. *J. Multivariate Anal.*, 97, 412 – 430.

LIN, C. (1955). *The theory of hydrodynamic stability*. Cambridge University Press.

MACAGNO, E. O. and HUNG, T.-K. (1967). Computational and experimental study of a captive annular eddy. *J. Fluid Mech.*, 28, 43–64.

MALLINGER, F. and DRIKAKIS, D. (2002). Instability in three-dimensional, unsteady, stenotic flows. *Int. J. Heat Fluid Fl.*, 23, 657–663.

MALLOCK, A. (1896). Experiments on fluid viscosity. *Philos. T. R. Soc. A*, 187, 41–56.

MAMUN, C. K. and TUCKERMAN, L. S. (1995). Asymmetry and Hopf bifurcation in spherical Couette flow. *Phys. Fluids*, 7, 80–91.

METTOT, C., RENAC, F. and SIPP, D. (2014). Computation of eigenvalue sensitivity to base flow modifications in a discrete framework: Application to open-loop control. *J. Comput. Phys.*, 269, 234–258.

MONCHAUX, R., RAVELET, F., DUBRULLE, B., CHIFFAUDEL, A. and DAVIAUD, F. (2006). Properties of steady states in turbulent axisymmetric flows. *Phys. Rev. Lett.*, 96, 124502.

MULLIN, T., SEDDON, J. R. T., MANTLE, M. D. and SEDERMAN, A. J. (2009). Bifurcation phenomena in the flow through a sudden expansion in a circular pipe. *Phys. Fluids*, 21, 014110.

NOACK, B. R. and ECKELMANN, H. (1994). A global stability analysis of the steady and periodic cylinder wake. *J. Fluid Mech.*, 270, 297–330.

ORR, W. (1907a). The stability or instability of the steady motions of a perfect liquid and of a viscous liquid. *P. Roy. Irish Acad. A*, 27, 69–138.

ORR, W. M. (1907b). The stability or instability of the steady motions of a perfect liquid and of a viscous liquid. part i: A perfect liquid. *P. Roy. Irish Acad. A*, 27, 9–68.

ORSZAG, S. A. (1971). Accurate solution of the orr–sommerfeld stability equation. *J. Fluid Mech.*, 50, 689–703.

PARLETT, B. N. and SAAD, Y. (1987). Complex shift and invert strategies for real matrices. *Linear Algebra Appl.*, 88, 575 – 595.

PEIXINHO, J. (2010). Flow in a slowly divergent pipe section. *Seventh IUTAM Symposium on Laminar-Turbulent Transition*. Springer, 307–312.

PEIXINHO, J. and BESNARD, H. (2013). Transition to turbulence in slowly divergent pipe flow. *Phys. Fluids*, 25, 111702.

RAYLEIGH, L. (1916). On the dynamics of revolving fluids. *Philos. T. R. Soc. A*, 648, 148–154.

REYNOLDS, O. (1883). An experimental investigation of the circumstances which determine whether the motion of water shall be direct or sinuous, and of the law of resistance in parallel channels. *Philos. T. R. Soc. A*, 174, 935–982.

REYNOLDS, W. C. and POTTER, M. C. (1967). Finite-amplitude instability of parallel shear flows. *J. Fluid Mech.*, 27, 465–492.

RICHTMYER, R. D. (1982). *Principles of Advanced Mathematical Physics, Vol. 2*. Springer.

SAAD, Y. (1980). Variations on Arnoldi's method for computing eigenelements of large unsymmetric matrices. *Linear Algebra Appl.*, 34, 269–295.

SAAD, Y. (1984). Chebyshev acceleration techniques for solving nonsymmetric eigenvalue problems. *Math. Comput.*, 42, 567–588.

SANMIGUEL-ROJAS, E. and MULLIN, T. (2012). Finite-amplitude solutions in the flow through a sudden expansion in a circular pipe. *J. Fluid Mech.*, 691, 201–213.

SCHENK, O. and GÄRTNER, K. (2004). Solving unsymmetric sparse systems of linear equations with PARDISO. *Future Gen. Comp. Sy.*, 20, 475–487. Selected numerical algorithms.

SCHLICHTING, H. (1979). *Boundary-Layer Theory*. McGraw-Hill, 7th edition.

SCHMID, P. J. (2007). Nonmodal stability theory. *Annu. Rev. Fluid Mech.*, 39, 129–162.

SCHMID, P. J. and HENNINGSON, D. S. (2001). *Stability and Transition in Shear Flows*, vol. 142 of *Applied Mathematical Sciences*. Springer.

SHERWIN, S. J. and BLACKBURN, H. M. (2005). Three-dimensional instabilities and transition of steady and pulsatile axisymmetric stenotic flows. *J. Fluid Mech.*, 533, 297–327.

SKOROKHODOV, S. L. (2007). Numerical analysis of the spectrum of the orr-sommerfeld problem. *Comp. Math. Math. Phys*, 47, 1603–1621. Copyright - Nauka/Interperiodica 2007; Last updated - 2014-07-26.

SOBEY, I. J. (1985). Observation of waves during oscillatory channel flow. *J. Fluid Mech.*, 151, 395–426.

SOBEY, I. J. and DRAZIN, P. G. (1986). Bifurcations of two-dimensional channel flows. *J. Fluid Mech.*, 171, 263–287.

SQUIRE, H. B. (1933). On the stability for three-dimensional disturbances of viscous fluid flow between parallel wallslayed. *Philos. T. R. Soc. A*, 142, 621–628.

STEWART, K. (1990). Avoiding stability-induced inefficiencies in BDF methods. *J. Comput. Appl. Math.*, 29, 357 – 367.

STROUD, J., BERGER, S. and SALONER, D. (2000). Influence of stenosis morphology on flow through severely stenotic vessels: implications for plaque rupture. *J. Biomech.*, 33, 443–455.

STUART, J. T. (1960). On the non-linear mechanics of wave disturbances in stable and unstable parallel flows. part 1. the basic behaviour in plane Poiseuille flow. *J. Fluid Mech.*, 9, 353–370.

SYNGE, J. L. (1938). On the stability of a viscous liquid between rotating coaxial cylinders. *Philos. T. R. Soc. A*, 167, 250–256.

TAKEDA, Y. (1995). Velocity profile measurement by ultrasonic doppler method. *Exp. Therm. Fluid Sci.*, 10, 444–453. Experimental methods in Thermal and Fluid Science.

TAYLOR, G. (1923). Stability of a viscous liquid contained between two rotating cylinders. *Philos. T. R. Soc. A*, 223, 289–343.

TAYLOR, G. I. (1921). Experiments with rotating fluids. *Philos. T. R. Soc. A*, 100, 114–121.

TOLLMIEN, W. (1931). The production of turbulence. Technical repport NACA TM-609, NACA. Original in German: "Uber die Entstehung der Turbulenz" (1929), from: *Nachrichten.* Gesellschaft der Wissenschaften. Göttingen Mathematisch-Naturwissenschaftliche Klasse.

TREFETHEN, L. N., TREFETHEN, A. E., REDDY, S. C. and DRISCOLL, T. A. (1993). Hydrodynamic stability without eigenvalues. *Science*, 261, 578–584.

TUCKERMAN, L. S. and BARKLEY, D. (2000). Bifurcation analysis for timesteppers. E. Doedel and L. S. Tuckerman, editors, *Numerical Methods for Bifurcation Problems and Large-Scale Dynamical Systems.* Springer, vol. 119, 453–466.

VAN DYKE, M. (1982). *An Album of Fluid Motion.* Parabolic Press, Inc.

VARGHESE, S. S., FRANKEL, S. H. and FISCHER, P. F. (2007). Direct numerical simulation of stenotic flows. part 1. steady flow. *J. Fluid Mech.*, 582, 253–280.

VÉTEL, J., GARON, A., PELLETIER, D. and FARINAS, M.-I. (2008). Asymmetry and transition to turbulence in a smooth axisymmetric constriction. *J. Fluid Mech.*, 607, 351–386.

VILLERMAUX, E. and HOPFINGER, E. (1994). Self-sustained oscillations of a confined jet: a case study for the non-linear delayed saturation model. *Physica D*, 72, 230–243.

WALEFFE, F. (1995). Transition in shear flows. nonlinear normality versus non-normal linearity. *Phys. Fluids*, 7, 3060–3066.

WALKER, I. J., TORAIN II, D. S. and MORGAN III, M. H. (2012). An eigenvalue search method using the Orr–Sommerfeld equation for shear flow. *J. Comput. Appl. Math.*, 236, 2795 – 2802.

WATSON, J. (1960). On the non-linear mechanics of wave disturbances in stable and unstable parallel flows. part 2. the development of a solution for plane Poiseuille flow and for plane Couette flow. *J. Fluid Mech.*, 9, 371–389.

WILLE, R. and FERNHOLZ, H. (1965). Report on the first European Mechanics Colloquium, on the Coanda effect. *J. Fluid Mech.*, 23, 801–819.

YANG, J.-T., TSAI, B.-B. and TSAI, G.-L. (1994). Separated-reattaching flow over a backstep with uniform normal mass bleed. *J. Fluid. Eng.*, 116, 29–35.

YOUNG, D. (1968). Effect of time-dependent stenosis on flow through a tube. *J. Eng. Ind.*, 90, 248–254.

YOUNG, D. F. and TSAI, F. Y. (1973). Flow characteristics in models of arterial stenoses. – I. steady flow. *J. Biomech.*, 6, 395–410.

APPENDIX A COMPUTATIONAL EXAMPLE OF ARNOLDI ALGORITHM

The present appendix contains the Matlab/Octave source code for the computational example of the Arnoldi algorithm presented in Section 2.11.1.

Main routine

Calls all the different subroutines in the required order to compute the eigenvalues and eigenvectors of a diagonal matrix $\mathbf{M}_{ii} = -i/2$. In this case, the size of the matrix is $m = 50$ and four eigenpairs are requested, but twice as many are actually computed but not reported, to reduce the error, as recommended by Tuckerman and Barkley (2000).

```
close all
clear all
clc()

global m;       %size of the matrix
global nev;     %number of requested eigenpairs
global k;       %total number of eigenpairs to compute
global vecDiag; %size m vector with the elements in the diagonal
global A;       %sparse matrix where eigenpairs are sought
global X0;      %initial vector, or perturbation
global Q;       %rotation matrix
global L1;      %L matrix from BDF1 factorization
global L2;      %L matrix from BDF2 factorization
global U1;      %U matrix from BDF1 factorization
global U2;      %U matrix from BDF2 factorization
global P1;      %P matrix (pivots) from BDF1 factorization
global P2;      %P matrix (pivots) from BDF2 factorization
global lu1;     %Boolean variables to check if LU factorization
global lu2;     %       were already computed, to reuse them

%%
% INITIALIZE VARIABLES
%%
m   = 50;       %size of the matrix
nev = 4;        %requested eigenvalues
k   = 2*nev;    %computed eigenvalues, to reduce error
dTf = 0.05;     %filtering timestep
dTk = 0.05;     %timestep for BDF
```

```
Nf  = 70;       %number of filtering steps
lu1=false;lu2=false     %initialized to false so the
                        %LU factorization is computed
%initialize and fill vector with diagonal of the matrix
vecDiag = zeros(1,m);
for i=1:m
    vecDiag(i)=-i/2.;   %-0.5, -1.0, -1.5, ...
end
%Create sparse matrix with diagonal elements
A = CreateDiagMatrix(vecDiag);
Q = false;      %no rotation
%Random perturbation
X0 = CreatePerturb;
%Filter
Xf  = timeFilter(X0,dTf,Nf);
%Reuse factorizations?
if dTf==dTk
    lu1 = false;lu2 = false;
end
%Construction of Krylov base
U = krylovMatrix(Xf,dTk);
%Orthonormalization
V = stabGramSchmidt(U);
%Solution
[Z,L]=computeEig(A,V);
%Compute errors
[errLambda,errGamma]=errorEig(Z,L,true);
printf('i\tAnalytical\tNumerical\terrLambda\terrGamma\n')
for i=1:nev
    printf('%d\t%f\t%f\t%.5e%%\t%.5e%%\n',
        i,vecDiag(i),Z(i),errLambda(i)*100,errGamma(i)*100)
end
printf('   error:%.5e%%\n',errLambda(nev+1)*100)
writeTable('diagonal.tex',Z,errLambda,errGamma);
```

Diagonal matrix

The diagonal matrix is created, based on the elements on its diagonal.

```
function M = CreateDiagMatrix( diagVec )
%CreateDiagMatrix:
%
%   Creates a diagonal sparse matrix,
```

```
%   filling the elements on its diagonal
%   according to an input vector.
%
%   The input is a row vector "diagVec"
%   The output is a sparse matrix "M"
%
    global m;
    % Creates sparse identity matrix
    M = speye(m);
    % Loop to fill diagonal
    for i=1:m
      M(i,i) = diagVec(i);
    end
end
```

Create perturbation

A random perturbation is created to strat the Arnoldi iteration. This vector is normalized.

```
function x = CreatePerturb
%CreatePerturb: Creates random column vector
%
%   Creates a column vector of m elements
%   filled with random numbers in the range
%   (-1.0 : +1.0)
%   This vector is then normalized
%
%   The input is None
%   The output is the random vector "X"
%
    clc()
    % Takes the size m from the global variable
    global m;

    % Random vector in -1.0:+1.0
    x = randn(m,1);
    % Normalization
    x = x/sqrt(dot(x,x));
end
```

Filtering stage

The initial perturbation is advanced in time a certain number of steps. This eliminate the contribution of the fastest decaying modes to the final computed spectra. Initially, 70 integration steps are computed, but this number changes afterwards, to check its effect on the computed eigenpairs.

```
function x2 = timeFilter(x,dT,Nf)
%timeFilter:
%
%   Routine to perform the filtering stage
%   using a 2nd-order time integration.
%   Calls the soubroutine BDF1 or BDF2
%   according to the time step (BDF1 only for the first)
%   The vector "x" is integrated using a time step "dT"
%   and the process is repeated a number of steps "Nf"
%
%   The inputs are the vector "x"
%       the time step "dT"
%       the number of steps "Nf"
%   The output is the final vector "x2"
%
    clc()
    % global size
    global m;
    % Intialize the vectors
    x1 = zeros(m,1);
    x2 = zeros(m,1);
    % Integration loop
    for i=1:Nf
        % First order for the first step
        if i==1
            x1 = BDF1gen(x,dT);
        else
            x2 = BDF2gen(x,x1,dT);
            x  = x1;
            x1 = x2;
        end
    end
end
```

Time integration

First and second order BDF methods are used. The first order is only used in the first iteration, and once two solutions are available, the second order is used.

```
function x1 = BDF1gen(x,dT)
%BDF1:
%
%   First order time integration through
%   backward differentiation formula
%
%   The inputs are the vector to integrate "x"
%       the time step "dT"
%   The output is the integrated vector "y"
%
    clc()
    % global variables
    global m;
    global A;
    global L1;
    global U1;
    global P1;
    global lu1;
    % initialize output vector
    x1 = zeros(m,1);
    px = zeros(m,1);
    % compute LU factorizarion
    if lu1==false
        % compute system matrix B
        % for 1st order BDF
        B=speye(m)-dT*A;
        [L1,U1,P1]=lu(B);   %P*B=L*U
    end
    % solving routine L1*y=P1*x
    px = P1*x;      %reorganize RHS according to pivots
    opts.LT=true;   %lower triangular matrix
    y = linsolve(L1,px,opts);
    % solving routine U1*x1=y
    opts.LT=false;
    opts.UT=true;   %upper triangular matrix
    x1 = linsolve(U1,y,opts);
end
```

```
function x2 = BDF2gen(x,x1,dT)
```

```
%BDF2:
%
%   Second order time integration through
%   backward differentiation formula
%
%   The inputs are the vector to integrate "x"
%       the solution at the previous time step "x1"
%       the time step "dT"
%   The output is the integrated vector "x2"
%
    clc()
    % global variables
    global m;
    global A;
    global L2;
    global U2;
    global P2;
    global lu2;
    % intialization
    x2 = zeros(m,1);
    px = zeros(m,1);
    % compute LU factorizarion
    if lu2==false
        % compute system matrix B
        % for 2nd order BDF
        B=speye(m)-(2./3.)*dT*A;
        [L2,U2,P2]=lu(B);   %P*B=L*U
    end
    % solving routine L1*y=P1*x
    %reorganize RHS according to pivots
    px = P2*((4./3.)*x1-(1./3.)*x);
    opts.LT=true;   %lower triangular matrix
    y = linsolve(L2,px,opts);
    % solving routine U1*x1=y
    opts.LT=false;
    opts.UT=true;   %upper triangular matrix
    x2 = linsolve(U2,y,opts);
end
```

Krylov subspace

Routine that perform the matrix-vector product after the filtering stage, saving the vectors as columns of a matrix, constructing the base of the Krylov subspace.

```
function M = krylovMatrix(x,dT)
%krylovMatrix:
%
%   Construct the Krylov subspace base,
%   calling BDF1 or BDF2.
%
%   The input is a row vector "x"
%       the time step "dT"
%   The output is a sparse matrix "M"
%
    clc()
    % global variables
    global m;
    global k;
    % initialization
    M = zeros(m,k);
    % fills first column
    M(:,1) = x;
    % loop for each column
    for i=2:k
        % compute first column using BDF1
        % the others with BDF2
        if i>2
            tmp = BDF2gen(M(:,i-2),M(:,i-1),dT);
            % normalization
            %M(:,i) = tmp/sqrt(dot(tmp,tmp));
            M(:,i) = tmp;
        else
            tmp = BDF1gen(M(:,i-1),dT);
            % normalization
            %M(:,i) = tmp/sqrt(dot(tmp,tmp));
            M(:,i) = tmp;
        end
    end
end
```

Orthonormalization

The vectors of the Krylov subspace base are orthonormalized using the stabilized version of the Gram-Schmidt method (Daniel *et al.*, 1976; Saad, 1980).

```
function K = stabGramSchmidt(K)
%stabGramSchmidt:
%
%   Compute the orthonomalization of a given base "K"
%   where each vectors is one of the columns of "K"
%   The orthonormalization uses the stabilized version
%   of the Gram-Schmidt algorithm
%
%   The input is the original base "K"
%   The output is the modified base "K"
    clc()
    % global variables
    global m;
    global k;
    % loop
    for i=1:k
        K(:,i)=K(:,i)/sqrt(dot(K(:,i),K(:,i)));
        for j=i+1:k
            K(:,j)=K(:,j)-ProjGramSchmidt(K(:,i),K(:,j));
        end
    end
end
```

Results

The next routine computes the eigenvalues of the size-reduced problem, using the internal Matlab/Octave algorithms.

```
function [Lambda,EigArray] = computeEig(Mmatrix,Vmatrix)
%computeEig:
%
%   Compute the "k" eigenvalues of the reduced problem
%   using the orthonormal base and the original
%   matrix operator
%
%   The inputs are the original matrix "Mmatrix"
%       the orthonormal base "Vmatrix"
%   The output is a vector "Lambda" with the first "k" eigenvalues
%       an array "EigArray" with the "k" eigenvectors as columns
```

```
%
    clc()
    % global variables
    global k;
    global Q;
    % Hessenberg matrix
    Hmatrix = Vmatrix'*Mmatrix*Vmatrix;
    % compute eigenvalues (Matlab routine)
    [G,Lambda]=eig(Hmatrix);
    % sorting and sampling arrays
    Lambda=(Lambda*ones(k,1))';
    B=sortrows([Lambda;G]',1)';
    Lambda=B(1,:);  %eigenvalues
    G=B(2:length(B),:);
    % reverse order or rows
    revLambda=Lambda(end:-1:1);
    revG=G(:,end:-1:1);
    Lambda = revLambda;
    G = revG;
    EigArray=Vmatrix*G; %eigenvectors
    % check sign of the eigenvectors
    % FROM HERE: NOT GENERAL ROUTINE
    % CODE ONLY VALID FOR THESE EXAMPLES
    for i=1:k
        %rotate eigenvectors if Q~=false
        if (Q~=false)
            EigArray(:,i)=r*EigArray(:,i);
        end
        if EigArray(i,i) > 0
            EigArray(:,i) = -EigArray(:,i);
        end
    end
end
```

The errors of the computational values are computed, comparing them against the expected theoretical values.

```
function [errL,errG]=errorEig(Lambda,EigArray,bool)
%errorEig:
%
%   Compute errors with the eigenvalues
%   and eigenvectors
%
%   The inputs are the vector with eigenvalues "Lambda"
```

```
%       the array with the eigenvectors (as columns) "EigArray"
%       a boolean variable to decide if the results are reported
%       individually per component
%   The outputs are the respectively the errors with the
%       eigenvalues and eigenvectors: ef these are errL and errG.
%       The value of bool decides if these are escalars or vectors
%
    clc()
    % global variables
    global nev;
    global m;
    global vecDiag;
    % initialization
    if bool==true
        errG = zeros(1,nev+1);
        errL = zeros(1,nev+1);
    else
        errG = 0;
        errL = 0;
    end
    vecDiag=sort(vecDiag,"descend");
    % loop
    for i=1:nev
        eL=0;eG=0;
        % normalized contribution per eigenvalue
        eL =sqrt((vecDiag(i)-Lambda(i))^2/vecDiag(i)^2);
        % normalized contribution per component of the ith-eigenvector
        eG=norm(-eye(m)(:,i)-EigArray(:,i),2);
        if bool==true
            errL(i)=eL;
            errG(i)=eG;
            errL(nev+1)=max(eL,errL(nev+1));
            errG(nev+1)=max(eG,errG(nev+1));
        else
            errL=max(eL,errL);
            errG=max(eG,errG);
        end
    end
end
```

Prints the results in a table, directly in LaTeXformat for inclusion in this document.

```
function writeTable(filename,V,eL,eG)
    global nev;
```

```
    global vecDiag;
    fp=fopen(filename,'w');
    fprintf(fp,'\\begin{tabular}{cn{3}{4}n{3}{4}n{3}{4}n{3}{4}}\n');
    fprintf(fp,'\\toprule\n');
    fprintf(fp,'i & \\multicolumn{1}{c}{Analytic} & \\multicolumn{1}{c}{Numerical} & \\
    multicolumn{1}{c}{$\\%%\\epsilon_\\lambda$} & \\multicolumn{1}{c}{$\\%%\\epsilon_\\
    varphi$} \\\\ \n');
    fprintf(fp,'\\midrule\n');
    for i=1:nev
        fprintf(fp,'%d & %f & %f & %.5e\\%% & %.5e\\%% \\\\ \n',i,vecDiag(i),
        V(i),eL(i)*100,eG(i)*100);
    end
    fprintf(fp,'\\bottomrule\n');
    fprintf(fp,'\\end{tabular}\n');
    fclose(fp);
end
```

A.1 Rotation

For the example in Section 2.11.2, the basic algorithm is used. The main difference is the requirement of a rotation matrix, constructed from the QR factorization of a random matrix.

Main routine

The same main routine as in the previous example, but calling the matrix-rotation routines to modify the diagonal matrix before the filtering stage.

```
close all
clear all
clc()

global m;       %size of the matrix
global nev;     %number of requested eigenpairs
global k;       %total number of eigenpairs to compute
global vecDiag; %size m vector with the elements in the diagonal
global A;       %sparse matrix where eigenpairs are sought
global X0;      %initial vector, or perturbation
global Q;       %rotation matrix
global L1;      %L matrix from BDF1 factorization
global L2;      %L matrix from BDF2 factorization
global U1;      %U matrix from BDF1 factorization
global U2;      %U matrix from BDF2 factorization
```

```
global P1;      %P matrix (pivots) from BDF1 factorization
global P2;      %P matrix (pivots) from BDF2 factorization
global lu1;     %Boolean variables to check if LU factorization
global lu2;     %       were already computed, to reuse them

%%
% INITIALIZE VARIABLES
%%
m   = 50;       %size of the matrix
nev = 4;        %requested eigenvalues
k   = 2*nev;    %computed eigenvalues, to decrease error
dTf = 0.05;     %filtering timestep
dTk = 0.05;     %timestep for BDF
Nf  = 70;       %number of filtering steps
lu1=false;lu2=false     %initialized to false so the
                        %LU factorization is computed
%initialize and fill vector with diagonal of the matrix
vecDiag = zeros(1,m);
for i=1:m
    vecDiag(i)=-i/2.;
end
%Create sparse matrix with diagonal elements and modify it through
% matrix rotations without changing the eigenvalues
A = CreateDiagMatrix(vecDiag);
Q = randRotation;   %random rotation
A = Q'*A*Q;
%Random perturbation
X0 = CreatePerturb;
%Filter
Xf  = timeFilter(X0,dTf,Nf);
%Reuse factorizations?
if dTf==dTk
    lu1 = false;lu2 = false;
end
%Construction of Krylov base
U = krylovMatrix(Xf,dTk);
%Orthonormalization
V = stabGramSchmidt(U);
%Solution
[Z,L]=computeEig(A,V);
%Compute errors
[errLambda,errGamma]=errorEig(Z,L,true);
printf('i\tAnalytical\tNumerical\terrLambda\terrGamma\n')
for i=1:nev
```

```
    printf('%d\t%f\t%f\t%.5e%%\t%.5e%%\n',
        i,vecDiag(i),Z(i),errLambda(i)*100,errGamma(i)*100)
end
printf('   error:%.5e%%\n',errLambda(nev+1)*100)
writeTable('rotated.tex',Z,errLambda,errGamma);
```

Matrix rotation

An orthogonal matrix is constructed using the the QR factorization of a random matrix. This orthogonal matrix is used as rotation matrix. Only the first 75% of the rows and columns of the diagonal matrix are rotated. Beyond this limit, the performance of the algorithm decreases notably.

```
function Q = randRotation()
%randRotation:
%
%   Constructs a random rotation matrix
%   for the first "p" dimensions, the others
%   remaining an identity matrix
%
%   There are no inputs
%   The output is the rotation matrix "Q"
%
    global m;
    p=floor(3*m/4);     %partial rotation, p=75% of "m"
    [Q,~]=qr(randn(p)); %QR factorization of random matrix
    %check if the rotation conserves the axis orientation
    if det(Q)<0
        Im=speye(p);
        index=floor(rand*p);
        Im(index,index)=-1; %random -1 in diagonal
        Q=Q*Im;
    end
    %assembly of full m-sized matrix
    Q=[Q,zeros(p,m-p);zeros(m-p,p),eye(m-p)];
end
```